Hetero-Atom Containing Functional Polymers:

Synthesis, Characterization and Applications

A Dissertation Presented for the

Doctor of Philosophy

Degree

The University of Tennessee, Knoxville

Hongbo Feng

May 2017

DEDICATION

This thesis is dedicated to my beloved family.

ACKNOWLEDGEMENTS

First of all, I would like to thank my advisor, Dr. Jimmy Mays for his guidance, encouragement, and constant support throughout my research. I also appreciate this valuable opportunity to study and research in this wonderful laboratory. I feel proud and honored to work with world-class experts in living anionic polymerization.

I also thank Dr. Alexi Sokolov, Dr. Brain Long, Dr. Xue Ben, and Dr. Joshua Sangoro for their valuable time and for serving as my committee members.

I also want to thank Dr. Nam-goo Kang for being not only a mentor but also a good friend. I wouldn't be able to perform any living anionic polymerization without him. He taught me important glass-blowing and high vacuum techniques. My research wouldn't be completed without Dr. Kunlun Hong's kind help. He is a wonderful friend and mentor.

I thank Dr. Yangyang Wang, Dr. Fei Fan for helping me with characterizations. Dr. Weiyu Wang is a true friend. I thank him for helpful discussions from time to time. I couldn't not forget how we encourage each other when facing failures and frustrations. I would like to thank my fellow colleagues, Mr. Wei Lu, Dr. Xinyi Lu, Miss Huiqun Wang and previous group members for making the lab time enjoyable.

Finally, I want to thank my family. All of this wouldn't be possible without their support and love.

ABSTRACT

A mission to manage ever increased energy demands and reduce carbon foot print has challenged scientists and engineers to develop new materials with superior characteristics. In this scenario, lithium-ion batteries have been the dominating technology for not only applications in consumer electronics but also are essential for clean energy storage. On the other hand, the capture and separation of CO_2 [carbon dioxide] in power generation and in industrial processes is considered to be a key to reduce the carbon footprint.

Living anionic polymerization along with controlled polymerization techniques has realized the preparation of a wide variety of functional polymers with tunable properties. In this dissertation, we will present preparation of hetero-atom containing polymers using various polymerization techniques and post-polymerization modifications. We also want to explore: how can we employ these functional polymers to solve the current challenging problems?

In chapter 1, we present the review of the state of the art polymer electrolytes for next-generation lithium ion batteries followed by the introduction of current CO_2 [carbon dioxide] fixation and CO_2/N_2 [carbon dioxide/ nitrogen] gas separation techniques.

In chapter 2, we discuss the synthetic methodology and experimental techniques including living anionic polymerization using high vacuum techniques, cationic ring opening polymerization techniques and hydrosilylation.

In chapter 3 and chapter 4, we discuss the preparation of ambipolar polymer electrolytes and polymerized ionic liquids based on polydimethylsiloxane. The characterization, lithium ionic conductivity and structure-properties relationship are discussed.

Chapter 5 describes a novel method to obtain living anionic polymerization of 2-isopropenyl-2-oxazoline. Through our modified synthetic conditions, block copolymers of IPOx are also prepared and microphase separations are studied.

In chapter 6, we investigate the synthesis gold nanoparticle using PIPOx as template. The size of god nanoparticles will be analyzed using TEM [transmission electron microscopy] and AFM [atomic force microscopy]. Furthermore, the interactions between PIPOx [poly(2-isopropenyl-2-oxazoline)] template and AuNPs [gold nano particles] is studied using XPS [X-ray photoelectron spectroscopy].

In chapter 7, we introduce the preparation of amidoxime-modified PTMSP [poly(1-trimethylsilyl-1-propyne)] and its applications on CO_2/N_2 [carbon dioxide/ nitrogen] separation.

Finally, the research in this dissertation is summarized and future work is presented in chapter 8.

TABLE OF CONTENTS

LIST OF TABLES

LIST OF FIGURES

LIST OF ABBREVIATIONS

CO_2	Carbon dioxide
N_2	Nitrogen
EC	Ethylene carbonate
DMC	Dimethyl carbonate
EMC	Ethyl methyl carbonate
DEC	Diethyl carbonate
PVdF-HFP	Poly(vinyldienefluoride-hexfluoropropylene)
GO	Graphene oxide
PEI	Polyethyleneimine
PPEGMA	Poly [poly(ethylene glycol) methyl ethyl methacrylate]
PVC	Polyvinylene carbonate
PTMC	Polytrimethylene carbonate
$MMPIPF_6$	1-Propyl-2,3-dimethylimidazolium hexafluorophosphate
Emi	Ethyl methylimidazolium
TFSI	Bis(trifluoromethanesulfonyl)imide
MEA	Mono-ethanolamine
MCM-41	Mesostructured silica
MOFs	Metal-Organic Frameworks
PIM	Polymer of Intrinsic Microporosity
PTMSP	Poly(1-trimethylsilyl-1-propyne)

PHMS	Polyhydromethylsiloxane
ACS	2-Allyltetrahydrothiophene 1,1-dioxide
TES	Tris(2-methoxyethoxy)vinylsilane
VEC	Vinylethylene carbonate
D3	Hexamethylcyclotrisiloane
D4	Octamethylcyclotetrasiloxane
D4H	Tetramethylcyclotetrasiloxane
Pt[dvs]	Platinum (0)-1,3-divinyl-1,1,3,3-tetramethyldisiloxane
TFA	Trifluoromethanesulfonic acid
HDS	Hexamethyldisiloxane
B5B	5-Bromo-1-pentene
Imi-Br	3-Methyl-1-(pent-4-en-1-yl)-1h-imidazol-3-ium Bromide
PEtOx	Poly(2-ethyl-2-oxazoline)
B3Imi-PF_6	1-Butyl-3-methyl-imidazolium hexafluorophosphate
IPOx	2-Isopropenyl-2-oxazoline
PIPOx	Poly(2-isopropenyl-2-oxazoline)
DMP-K	Diphenyl methyl potassium
AuNPs	Gold nano particles
AO	Amidoxime
CN-S	4-(Chlorodimethylsilyl) butanenitrile

Chapter 1 Introduction

1.1 Motivation

Since the beginning of industrial revolution in the mid-1800s, the life of human society has been transformed dramatically. Steam-powered trains and ships, internal combustion engines have changed the way human move and produce goods around the globe. The second-industrial revolution along with related technology shaped our life significantly. It empowers us with capabilities from electricity-powered light bulb to computer chips, advanced space aircraft. However, along with these amazing revolutions, the energy is largely derived from burning of fossil fuels. According to International Energy Agency (IEA), the world's energy demand will increase from about 12 billion ton oil equivalents (t.o.e.) in 2009 to 18 billion t.o.e. by 2035 under their "current policies".[1] As a byproduct, carbon dioxide (CO_2) emissions are expected to increase from 29 gigatons per year (Gt yr^{-1}) to 43 Gt yr^{-1}.[2] The concentration of CO_2 in the atmosphere has risen from 278 ppm at the beginning of the industrial revolution to > 400 ppm today.[3] This massive CO_2 emission along with other gaseous emissions such as sulfur oxides (SO_x) and nitrogen oxides (NO_x) from burning of fossil fuels and biomass are not only polluting the air but also generating global warming with alarming consequences (Figure 1.1).[4-6] For example, the sea temperature has increased over 0.7°C and the rate of this elevation is even higher for the last century than the last 420,000 years.[7]

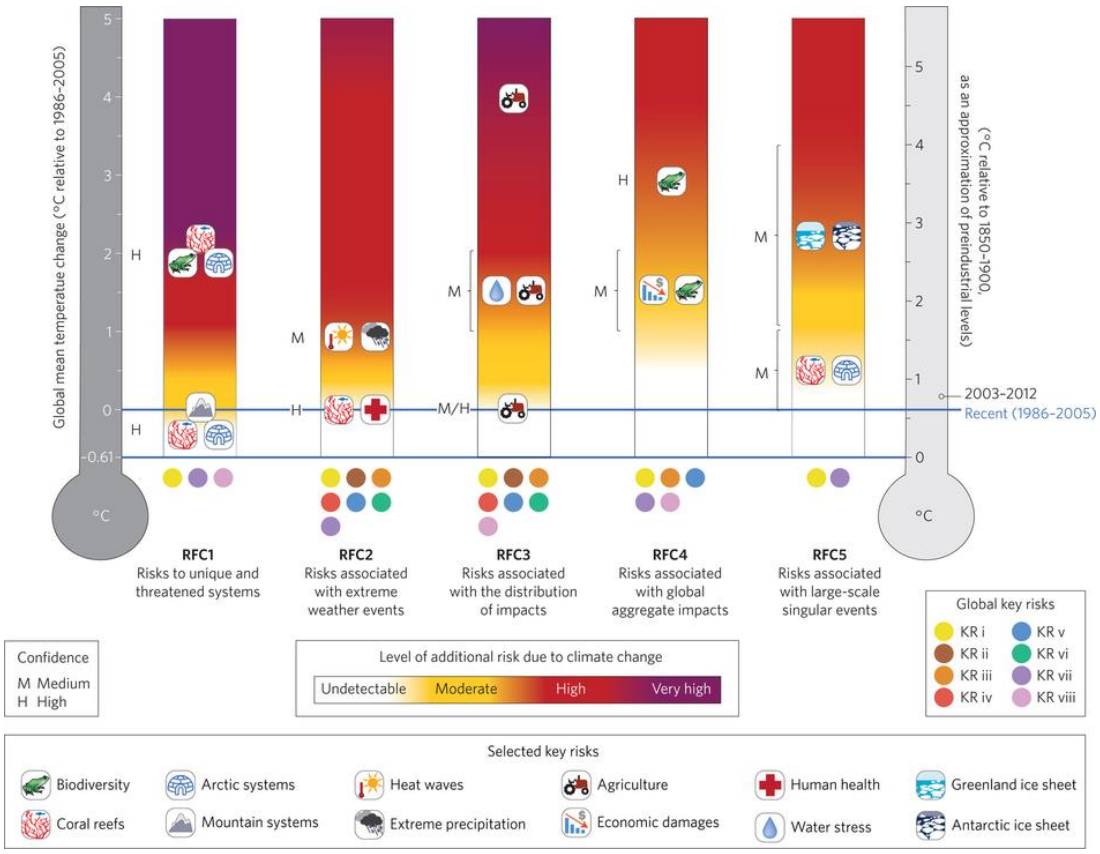

Figure 1.1. Impact of global warming on climate-related risks, reprinted from ref.[5].

To manage the ever-increasing energy demands and reduce carbon emissions, the research on new clean energy sources such as solar power, wind power, wave and geothermal energy has attracted massive attention for the last decades.[8] These important and yet challenging research areas have brought another issue, how do we store these energies? Unfortunately, there is only ~1% of the energy consumed worldwide that could be stored, most of which (98%) is through pumped-storage hydroelectricity.[9] There is clearly a demanding need to improve our ability to store energy. It is now generally accepted that among the various possible choices, the most suitable are batteries, which are capable of delivering the stored chemical energy with high conversion efficiency and without any gaseous emissions.[10] In this scenario, rechargeable batteries with high specific energy, high rate capability, high safety and low cost are desirable. Among the existing battery technologies, lithium-ion batteries (LIBs) have been the dominating technology for not only applications in consumer electronics but also are essential for clean energy storage due to their unique features.[11]On the other hand, the capture and separation of CO_2 in power generation and in industrial processes is a necessary part to reduce the carbon footprint and to deep decarbonization.[12-13]

1.1.1 Energy Storage- Lithium Ion Battery

Battery technology based on lithium has relied on the fact that Li is the most electropositive (3.04V vs standard H electrode) and lightest metal ($0.53 g/cm^3$).[14] It is therefore could serve as promising candidate for high energy density storage devices. In

fact, lithium ion batteries (LIBs) offer higher energy density compared with other battery types such as lead acid and Ni-MH batteries (Figure 1.2).

A LIB is composed of several lithium ion cells. A typical lithium ion cell consists of two electrodes, anode and cathode, and electrolyte (Figure 1.3). The negative electrode provides the intercalation sites for lithium ion during charging and recharging cycle and generally is graphite. The positive electrode is lithium metal oxide, e.g. $LiCoO_2$.

Two metallic current collector attached the two electrodes deliver the electrons from the anode to cathode through external circuit in the discharging process (reverse direction for the charging process). The electrolyte, on the other hand, acts as an electric insulator and only allows the lithium ions to transport between electrodes inside the cell so that a battery cell can do work. Traditional lithium-ion batteries are based on liquid electrolytes, which consist of lithium salts such as $LiPF_6$, $LiBF_4$ or $LiClO_4$ and organic solvents e.g. ethylene carbonate (EC), dimethyl carbonate (DMC), ethyl methyl carbonate (EMC), and diethyl carbonate (DEC).These cyclic carbonates are frequently used because they have high dielectric constants so that they can create an effective solvation shell around lithium ions.[15] In this way, lithium ions could efficiently transport between the positive and negative electrodes during charge/discharge circles. The advantage of these liquid electrolytes is that they are able to offer rather high ionic conductivity, in the range of 10^{-2} S/cm at room temperature. Since the first LIB was commercialized by SONY in the 1990s, the performance and volumetric energy density of LIB cell have been increased significantly (e.g. >3.0Ah in 18650 cell).[16]

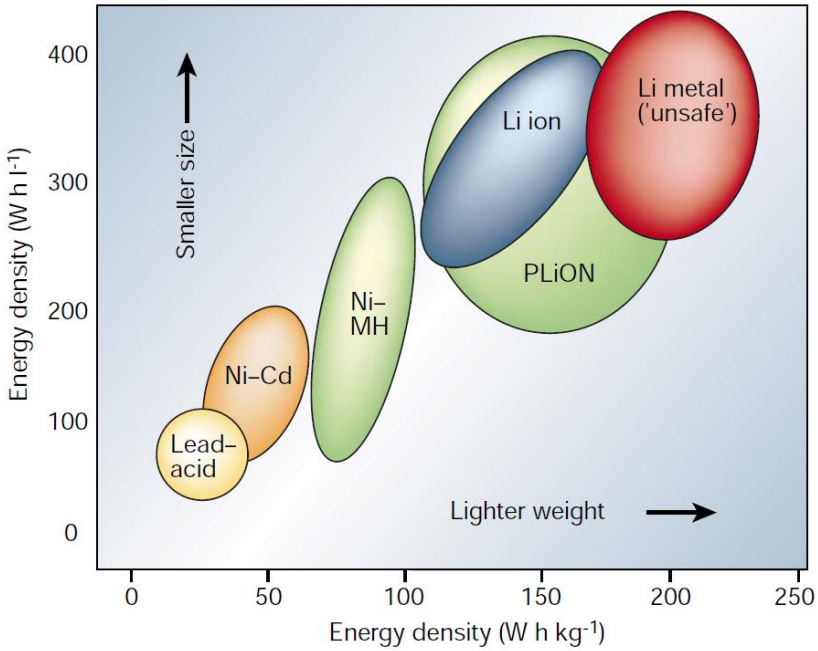

Figure 1.2. Comparison of different battery technologies. The lead–acid batteries is mainly used in automobiles, whereas Ni–Cd batteries remain the most suitable technologies for high-power applications. Adapted from ref.[14].

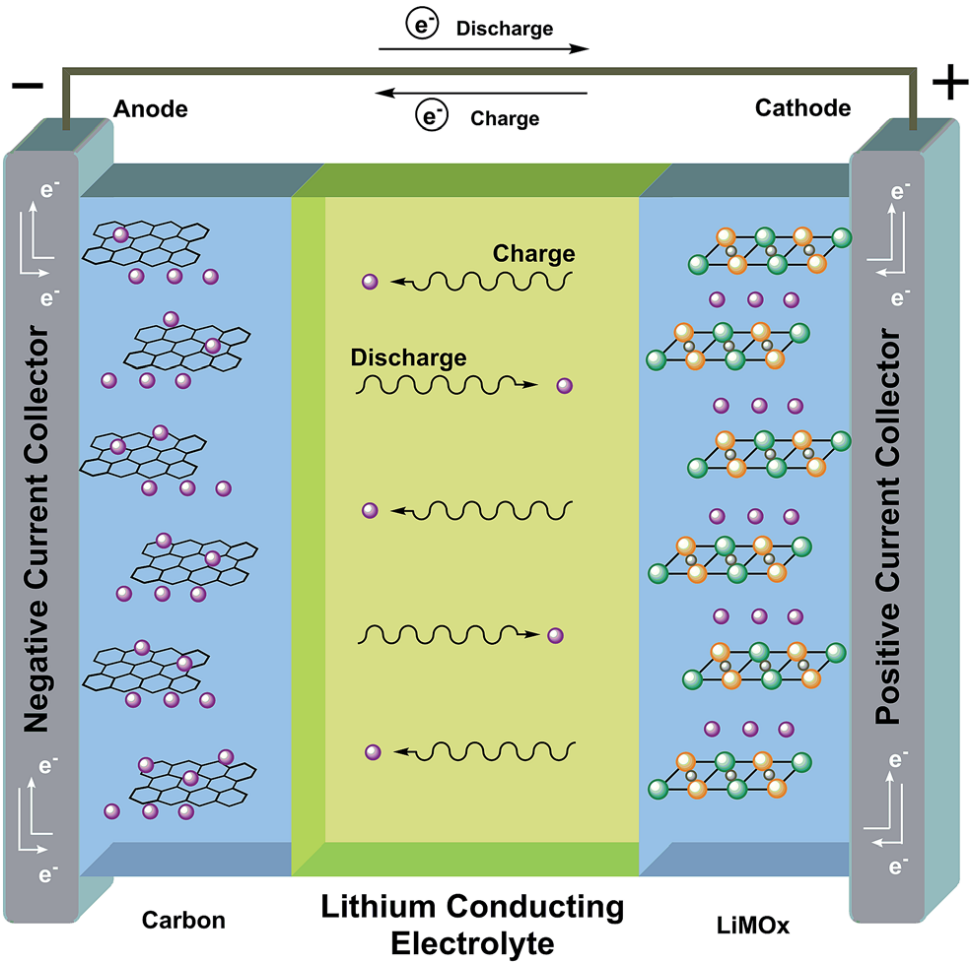

Figure 1.3. Schematic illustration of a typical lithium ion battery. Adapted from ref.[17]

The advancement of LIB technology has been vital to great changes in modern civilization. However, when conventional LIBs are operated at extreme conditions, such as at the upper limit of the charge process, oxygen may be released from the layered $LiCoO_2$ cathode and it may react with the flammable organic liquid electrolyte.

In 1972, Exxon embarked on a large project using TiS_2 as the positive electrode, Li metal as the negative electrode and lithium perchlorate in dioxolane as the electrolyte.[18-20] TiS_2 was the best intercalation compound available at the time, having a very favorable layered-type structure. However, shortcomings such as dendritic Li growth was observed on the Li-metal/liquid electrolyte interphase, which eventually could lead to an explosion.

Furthermore, because both cation and anion are transported through the polymer matrix during the charging and discharging cycles, the lithium ion can be inserted in to the nano-sized holes in the electrodes.[21] However, there is no reaction for anions on the electrodes, resulting in an accumulation of the anion at the electrodes. If the diffusion coefficient of anion is not sufficiently high for the accumulation layer to relax, the internal impedance will increase and consequently cause the battery failure (Figure 1.4). Various fire incidents have been in fact reported during LIB manufacturing and/or for battery-operated devices.[22-23] Therefore, further breakthroughs in material sciences are critical for safe and reliable energy storage devices. Numerous investigators studied the new metals and metal alloys for anodes and cathodes to improve cycle life, higher charge/discharge rate, and higher power.

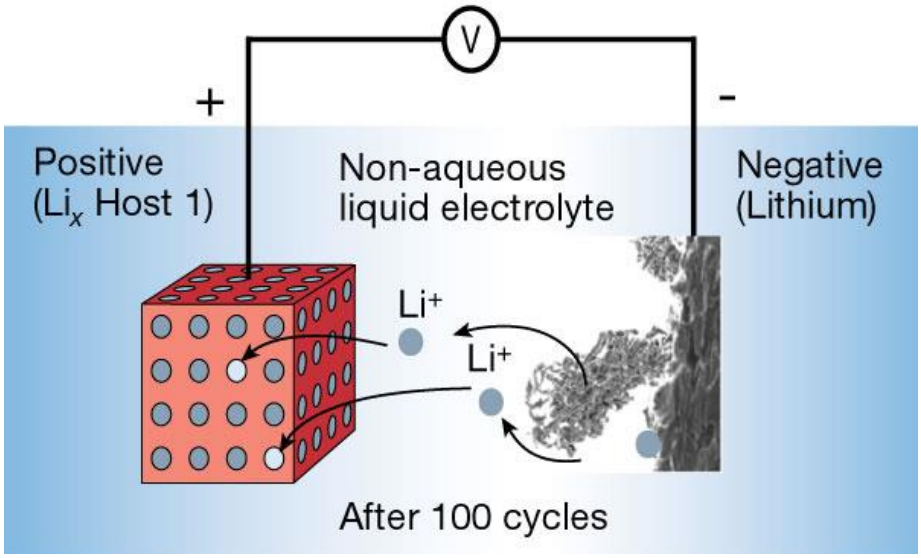

Figure 1.4. *In situ* scanning electron microscopy image of the dendrite growth at the Li surface on a Li-metal.

Researchers have found that when lithium silicon alloy was used as an anode, the energy density was enhanced significantly. For example, $Li_{4.4}Si$, is capable of offering a very high specific capacity of 4200 mAh/g compared with 372 mAh/g for graphite.[24] Moreover, nanopillars of V_2O_5 have been prepared using a porous polycarbonate as template and showed ability to support high rates of intercalation and reduce the volume change.[25] The advancement of lithium batteries also relies on improvements in the electrolyte as it does on the electrodes. In this thesis, we will focus on the design, synthesis, and characterization of polymer electrolytes.

1.1.2 Reduce Carbon Footprint-CO_2 Capture, fixation and Separation

The steady growth of CO_2 emission in the atmosphere is mostly from burning of fossil fuels, power plant, and human activity.[26] The increased CO_2 concentration in the atmosphere has caused the elevation of air temperature along with escalation in the number and strength of natural disasters such as floods, hurricanes, wide spread melting of ice and snow, and an increase in average sea levels.[5] These alarming consequences have driven researcher to find methods to reduce carbon footprint. There are mainly three phases to reduce total CO_2 emission into the atmosphere: pre-combustion, post-combustion, oxy-fuel combustion, and electrochemical separation (Figure 1.5).[27]

Pre-combustion capture utilizes new gasification technology to create combustible gas and then capture the CO_2 before burning for power. However, extensive equipment is necessary in this capture process.[28]

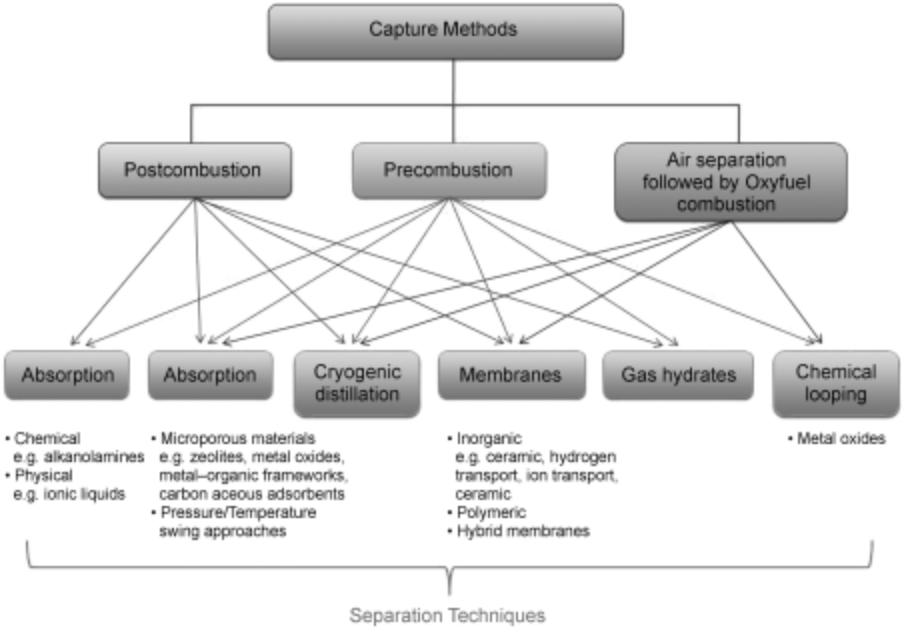

Figure 1.5. Methods for carbon capture and separation. Reprinted form ref.[29]

Oxy-fuel combustion is burning fossil fuel in an oxygen-rich gas, resulting in high concentration of CO_2 and steam.[30] Among these technologies, the post-combustion process has the highest potential to be employed to the current coal power plants.[31-32] The hot flue gases coming out of the boiler in a typical power plant are comprised mostly of N_2 and CO_2 with smaller concentrations of water vapor, SO_x and NOx.[33] Thus, CO_2/N_2 separation has been the subject of massive efforts. Figure 1.6 illustrates the CO_2 capture and separation techniques that can potentially be commercialized. The state-of-the-art review of the current membrane separation technology for CO_2/N_2 will be presented in the following section.

1.2 Literature Review- State of The Art in The Field of Polymer Electrolyte for Lithium Conduction

1.2.1 Types of Lithium-Conducting Polymer Electrolytes

There are several types of polymer based electrolytes that have been developed including composite polymer electrolytes (CPEs), gel polymer electrolytes (GPEs), and dry solid polymer electrolytes (SPEs). These three types of electrolytes offer different advantages and disadvantages (Figure 1.7).

The concept of CPEs was first reported by Weston and Steele.[34] They incorporated electrochemically inert nano-fillers into polymer matrix to increase the mechanical properties of polymer. Surprisingly, it was found that not only the mechanical strength but

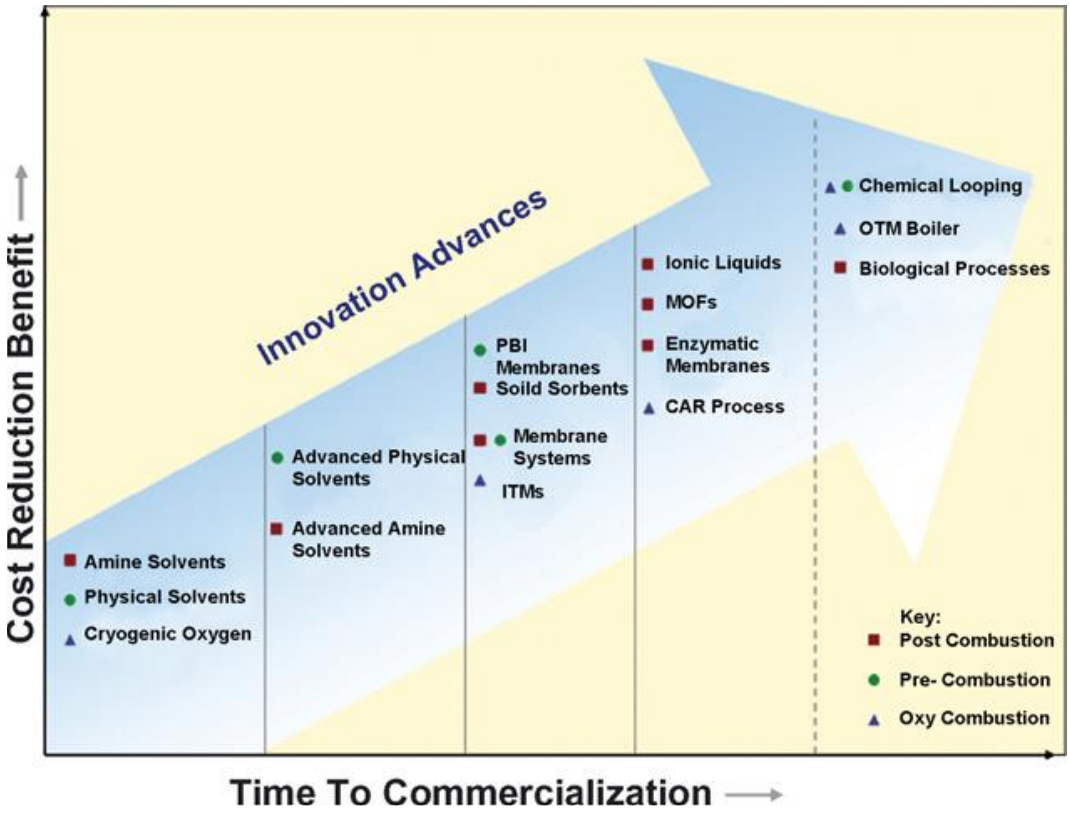

Figure 1.6. Cost-reduction benefits of CO_2 capture technologies against time to commercialization. Reprinted from ref.[35]

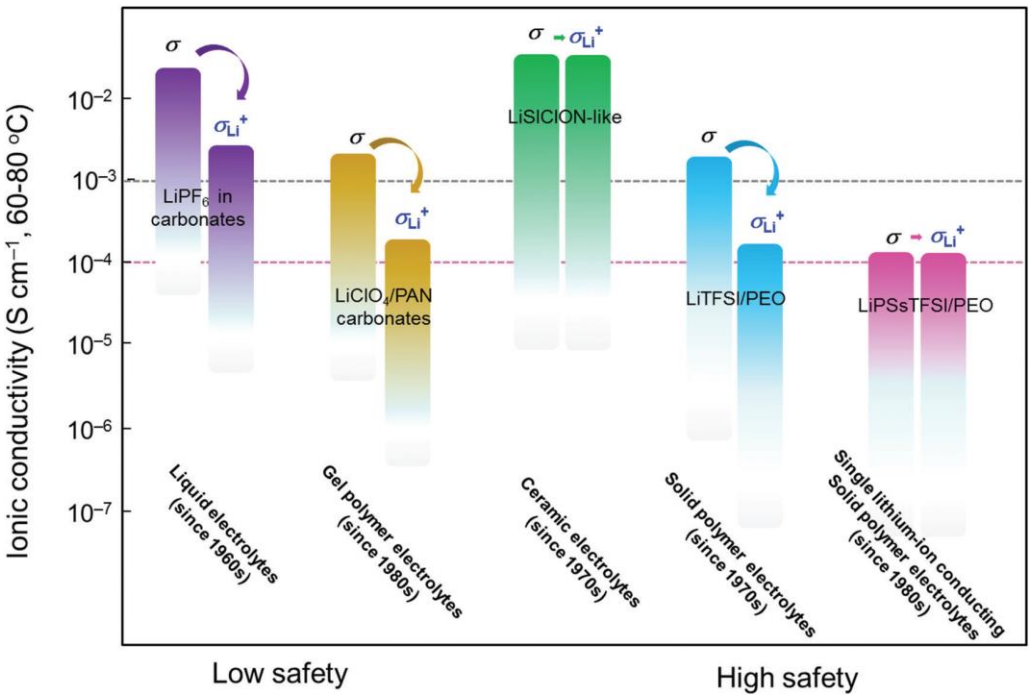

Figure 1.7. Roadmap of the development of lithium ion conducting polymer electrolytes, including liquid electrolytes, gel electrolytes, ceramic electrolytes, solid polymer electrolytes, and single lithium-ion conducting solid polymer electrolytes. Adapted from ref.[36]

also the ionic conductivity was enhanced (Figure 1.8).[37-38] Since then, substantial efforts have been devoted to develop new CPEs using a wide variety of high surface area nano-fillers: ZrO_2, TiO_2, Al_2O_3, ZnO, SiO_2, and carbon nanotubes were used to prepare polymer composites electrolytes.[39-45]

The size and surface area of the fillers play important role in improving the ionic conductivity. Greenbaum *et al.* reported a detailed study of how the size of Al_2O_3 affects the ionic conductivity (Figure 1.9).[46] To investigate the effect of surface groups. Dissanayake and coworkers studied effect of the acidic, weakly acidic, basic and neutral Al_2O_3 on the conductivity.[47] And these composites were able to enhance the ionic conductivities by suppressing the crystallinity of polymer matrix and creating interphase pathways for ion transport.[48-49] Giannelis *et al.* reported that the X-ray diffraction pattern of PEO/Na-montmorillonite hydride showed reduced crystallinity of PEO.[49] Chu *et al.* also found that hexagonal array of mesoporous structured MCM-41 was able to suppress the crystallinity of PEO and shift the melting point from 66 °C to 58 °C as shown in Figure 1.10. In addition, Table 1.1 lists ionic conductivity of several PEO based CPEs using different nano-fillers.[50]

Gel polymer electrolytes, on the other hand, consist of both liquid electrolytes, which enable the ion transport, electrochemical stability, and polymer skeleton, which enable structure integrity.[51] Because the polymer only serves to provide dimensional stability, the choice of polymer matrices has not been limited to have donor atom such as PEO. The most studied GPE systems were based on poly (ethylene oxide) (PEO),

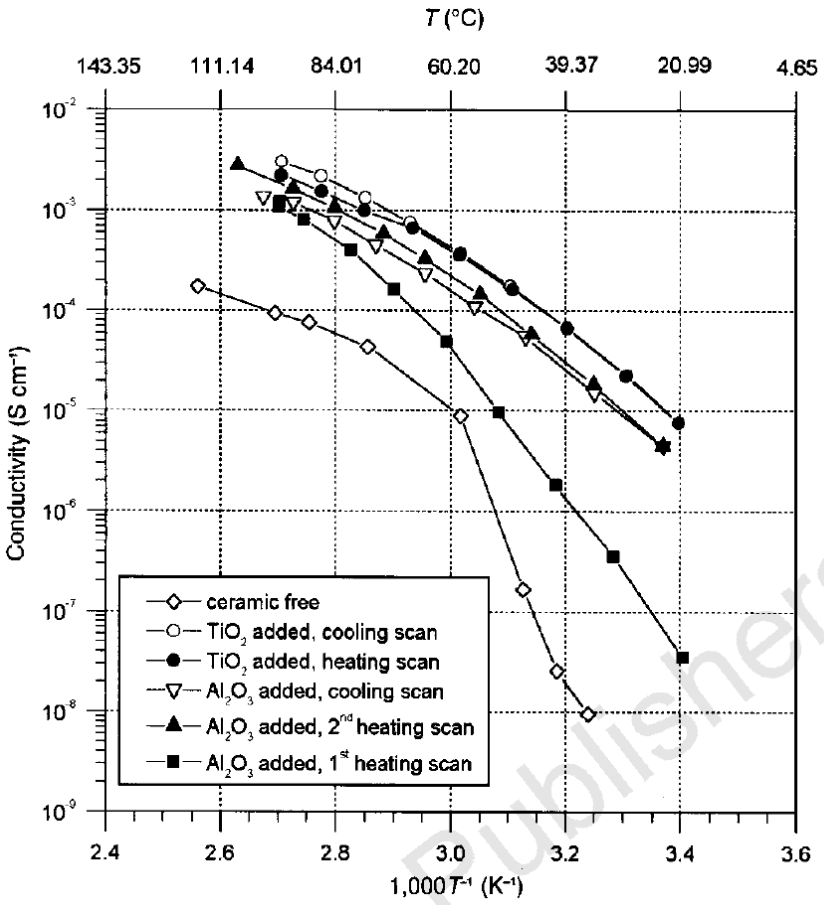

Figure 1.8. Arrhenius plots of the conductivity of ceramic-free PEO–$LiClO_4$ and of nanocomposite PEO–$LiClO_4$.10 wt% TiO2 and PEO–$LiClO_4$.10 wt% Al_2O_3 polymer electrolytes (PEO : $LiClO_4$ = 8 : 1 in all cases), reprinted from ref [52].

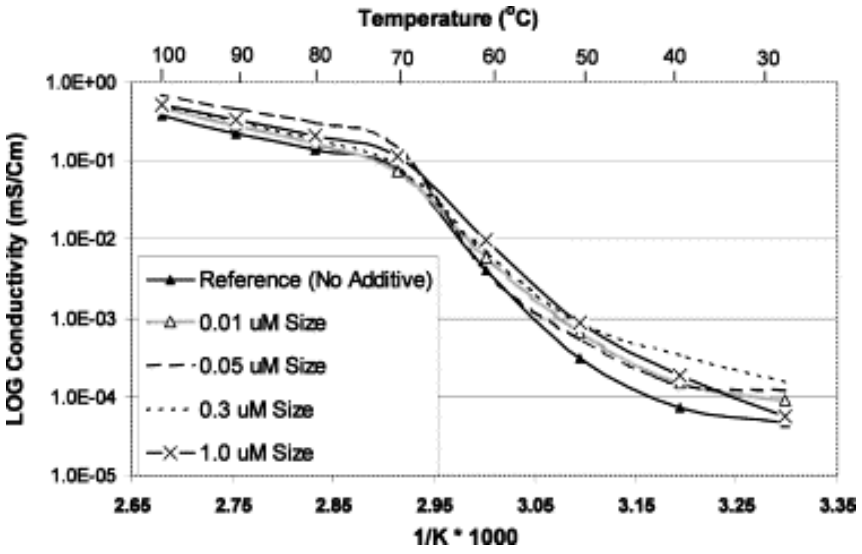

Figure 1.9. Specific conductivity as a function of temperature for a number of composite electrolytes prepared with PEO of MW 2×10^5 g/mol, where the particle size of Al_2O_3 was varied (0.01 μM, 0.05 μM, 0.30 μM, and 1.0 μM). Reprinted from ref.[46]

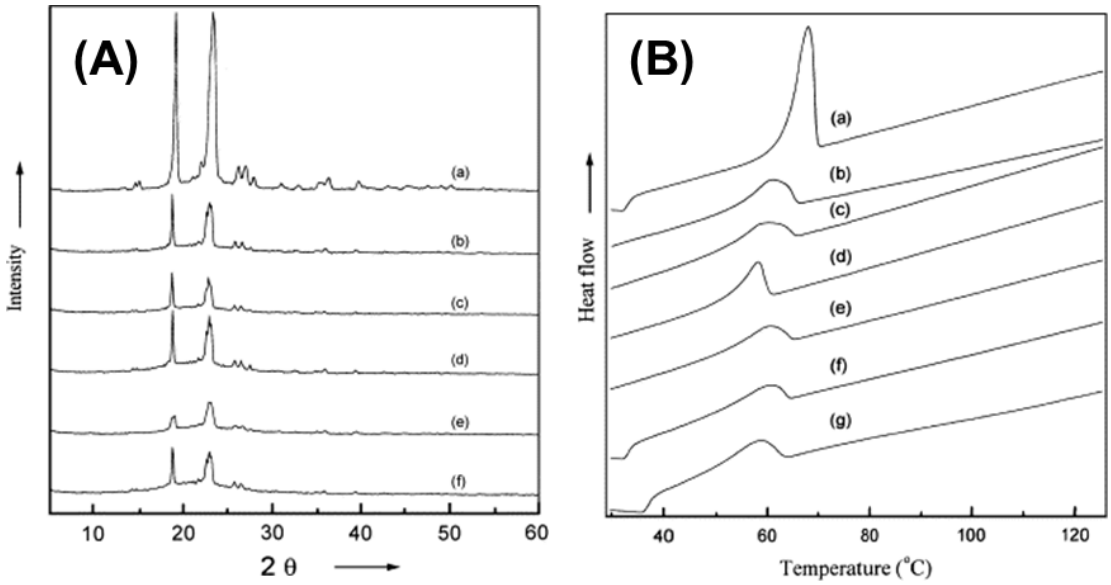

Figure 1.10. (A) X-ray diffraction patterns of (a) pure PEO, and PEO/LiClO4 (90:10) with MCM-41 of different weight ratios: (b) 0%, (c) 2%, (d) 5%, (e) 8% and (f) 10%. (B) The DSC traces of (a) pure PEO, and PEO/LiClO4 (90:10) with MCM-41 of different weight ratios: (b) 0%, (c) 2%, (d) 5%, (e) 8%, (f) 10% and (g) 15%. Reprinted from ref.[53]

Table 1.1. Properties of composite polymer electrolytes based on PEO.

Entry	Lithium salts	Nano-filler	Conductivity at 90 °C / S/cm	Lithium transferee number at 30°C	Ref
1	$LiClO_4$	TiO_2	1.8×10^{-3}	0.5-0.6	[54]
2	$LiClO_4$	SiO_2	2.01×10^{-4} (75 °C)	NA	[53]
3	$LiClO_4$	Al_2O_3	1.1×10^{-3}	0.31-0.33	[54]

poly(acrylonitrile) (PAN), poly(methyl methacrylate) (PMMA), and poly(vinylidene fluoride) (PVdF).

Numerous reports have discussed the fundamental aspects concerning the formation, morphological structure, and physical stability of GPE. Among them, PVdF-HFP copolymer has been demonstrated high performance, in which crystalline PVdF provides the dimensional stability and amorphous HFP supports the electrolytes. However, due to the semi-crystalline nature of this copolymer, swelling by liquid electrolyte could hardly achieve 100%.[55] Improvement has been reported by Wunder *et al.* They use PEO oligomer as a plasticizer to increase the pore size from nanoscale to microscale and achieved lithium ion conductivity 1.2×10^{-3} S/cm.[56] Moreover, doping with graphene oxide (GO) also showed significant improvement of ionic conductivity (Figure 1.11).[57]

It need to be pointed out that GPE based on PVdF-HFP copolymer has been licensed and utilized by major manufactures of lithium ion batteries up-to-date.[58-60] However, the conductivity is attributed to the use of flammable organic liquids. The electrochemical stability of these liquids is limited. The safety issue remains an obstacle when using GPEs. Moreover, there might be problems with the processing of crosslinked GPE networks since most of applications require the electrolytes materials in thin films.[61]

Unlike CPEs and GPEs, solid polymer electrolytes (SPEs) are a type of polymer electrolytes that only consist of polymer hosts and dissolved salt. SPEs offer several advantages compared to their liquid counterparts: (1) excellent processability and

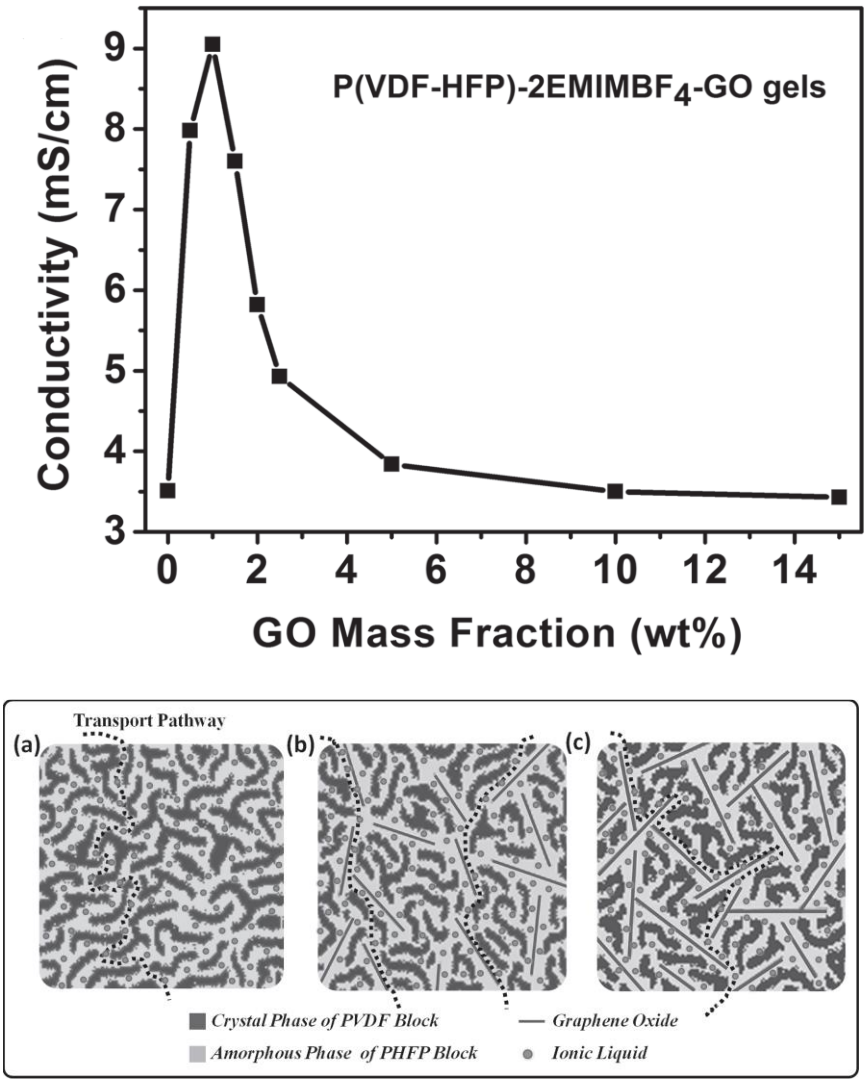

Figure 1.11. Top: ionic conductivity against the mass ratio of GO; bottom: proposed schematic structures of PVdF-HFP copolymer with different GO mass ratio. Reprinted from ref [57].

flexibility that could enable the fabrication of ultrathin lithium cells of various geometric shapes so that high energy and power density could be achieved for versatile applications, (2) higher safety due to the absence of flammable organic solvents and the much lower reactivity toward lithium, (3) the possible prevention of the growth of lithium dendrite crystals upon cycling, and (4) the high dimensional stability that could lead to the elimination of a separator, so further improvement in both energy density and manufacturing cost could be achieved due to the simplified cell configuration and enhanced packing efficiency.[62-65] Since the discovery of PEO/alkaline salt in 1973 by Wright *et al.*,[66] a large number of polymers hosts that can dissolve lithium salts have been synthesized and studied as discussed in the following sections.

1.2.2 Solid Polymer Electrolytes-The Effect of Polymer Matrix

Polyethylene oxide (PEO)/ lithium salt have been the most extensively studied system by far.[67-68] PEO has a repeating unit of ethylene oxide (Scheme 1.1) and it has different physical properties (e.g. viscosity, thermal properties, etc.) depending on molecular weights.[69] PEO with 90,000 g/mol has a T_g of -54 °C, T_m of 66 °C, and T_c of 48 °C.[70] PEO is employed as polymer host mainly due to it has good lithium salts solubility, in which the lithium ion can coordinate with the oxygen atom of the ether unit, and reasonably low T_g.[71-72]

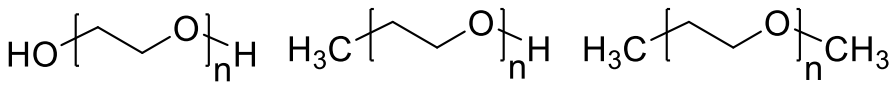

Scheme 1.1. Different structures of linear PEOs used in SPEs.

However, the maximum of conductivity was still lower 10^{-5} S/cm.[73] Although a few reports indicated that crystalline PEO can offer even greater ion conductivity than amorphous PEO,[74] crystallization is generally considered to be unfavorable to ion transport due to its slowed polymer chain relaxation. Numerous reports have studied to improve the performance of PEO based electrolytes such as the addition of a plasticizer,[75] polymer blends,[76-77] grafting short PEO oligomers onto polymer backbones or cross-linking PEO based polymers.[49, 51, 78-79] The results are summarized in Table 1.2.

Hyperbranched PEO derivatives have also received much attention owing to their unique molecular structures.[80] Because hyperbranched polymers can suppress the crystallization of polymer chains leading to increase of the amorphous phase, as compared with their linear counterparts. Hawker *et al.* synthesized hyperbranched PEO derivatives containing linear PEO units and 3,5-dioxybenzoate branching units by using the AB_2 macromonomer (Figure 1.12A). The ionic conductivity of the electrolyte with the $LiClO_4$ salt complex was at 7×10^{-5} S/cm at 60 °C.[81] Niitani *et al.* synthesized a hyperbranched copolymer based on a hard PS core and PPOEM shell via the combination of living anionic polymerization (LAP) of styrene and ATRP of POEM (Figure 1.12B). The obtained SPEs exhibited ionic conductivities of 10^{-4} S/cm at 30 °C.[82]

Table 1.2. The summary of lithium ion conductivity of representative solid polymer electrolytes.

Entry	Polymer host	Lithium salt[a]	Plasticizer	Conductivity at 25°C / S/cm	Ref.
1	PEO	CF_3SO_3Li	NA	7×10^{-8}	83
2	PEO	LiTFSI	NA	7×10^{-5}	83
3	PEO	LiTFSI	EC	9×10^{-4} 60°C	84
4	PEO	LiTFSI	PEO oligomer	7×10^{-5}	85
5	PEG	LiTFSI	EC/PC	1.2×10^{-4}	86
6	PEO	$LiPF_6$	$MMPIPF_6$	1.13×10^{-3}	87
7	PEO/P2VP	$LiClO_4$	NA	1.0×10^{-5}	88
8	PEO/PDMS	$LiPF_6$	NA	5.6×10^{-5} (30°C)	89
9	PEO/PEI	$LiClO_4$	NA	1.1×10^{-4}	90
10	PTMC	LiTFSI	NA	1×10^{-9}	91
11	PAN-PEO	$LiClO_4$	NA	6.79×10^{-4}	92
12	PDMS-PEO	LiTFSI	NA	1.33×10^{-4}	93
13	PVDF/PDMS	LiTFSI	NA	5.7×10^{-5}	94

[a]$MMPIPF_6$: 1-npropyl-2,3-dimethylimidazolium hexafluorophosphate.

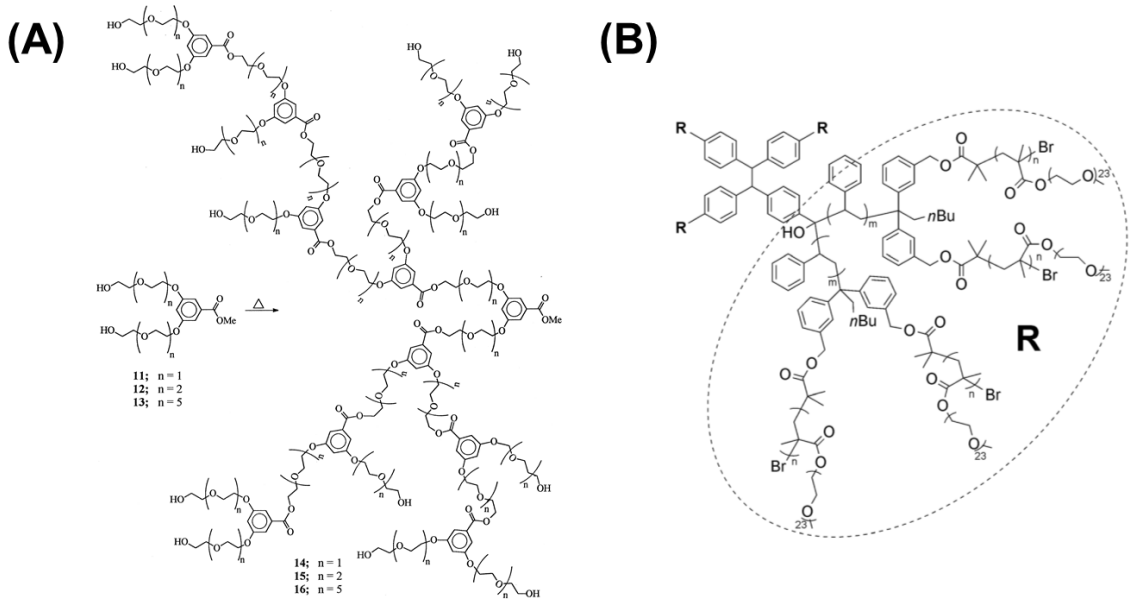

Figure 1.12. (A) Hyperbranched PEO. (B) (PS-block-PPEGMA2)$_8$star-shaped copolymer (only one arm is shown here due to the space limits).

On the other hand, Acosta *et al.* blended PEO with polypropylene oxide to improve the Li^+ transport.[95] Wang *et al.* employed low molecular weight polypropylene glycol (PPG) as an alternative system for polymer electrolytes since PPG does not have crystallinity. However, because of the relatively low salt solubility in PPG, it was revealed that microphase separation was observed due to the ion rich and ion-depleted domains depending on the lithium salts concentration.[96] Coats *et al.* prepared SPEs based on crosslinked polyethylene (PE)/PEO. The lithium dendrite growth was significantly suppressed and showed high conductivity (>10^{-4} S/cm at 25°C).[97] Alternatively, Tanaka and coworkers achieved ionic conductivity of 1.1×10^{-4} S/cm, 3 orders of magnitude higher than that of PEO/$LiClO_4$, using a polymer blending of PEO/PEI (8:2).[90] They reported that both compositions, PEO and PEI, are able to provide ion transport pathways.

Furthermore, PEI was able to erase the crystallization of PEO. Wang also reported using PAN-PEO copolymers to inhibit the lithium dendrite growth during the charging circle of LIB. The electrochemical window were found up to 4.8v vs Li^+/Li with a conductivity of 6.79×10^{-4} S/cm at room temperature.[92]

Very recently, block copolymers have drawn substantial attention for providing good ionic conductivity and mechanical strength. Mayes' team reported that diblock copolymer electrolytes based on poly(lauryl methacrylate)-*b*-poly[oligo(oxyethylene) methacrylate] complexed with $LiCF_3SO_3$ showed dimensional stability and exhibit conductivities around 10^{-5} S/cm at room temperature. Both blocks have Tg far below room temperature resulting into enhanced conductivity comparing with glassy-rubbery block

copolymer counterparts. The dimensional stability was also verified using rheological measurements.[98] Microphase separation of solid polymer electrolyte (polystyrene-*b*-poly[polyethyleneglycol methylether methacrylate-*b*-polystyrene](PS-*b*-PEGMA-*b*-PS) containing $LiClO_4$ was also reported having high ionic conductivity as high as 10^{-4} S/cm at room temperature.[99] They assumed that the PS block provided the mechanical strength and the PEO allowed for ion conduction in the polymer electrolyte as illustrated in Figure 1.13. To further increase the lithium ion conductivity, the lithium ion must be effectively dissociated from its counterion. In this scenario, polymers with cyclic carbonate has been developed.

Polycarbonate has alternating cyclic carbonate unit along the polymer backbone. Shriver *et al.* first reported Li conducting electrolyte using PVC, which can be readily synthesized by radical polymerization of vinylene carbonate (Scheme 1.2).

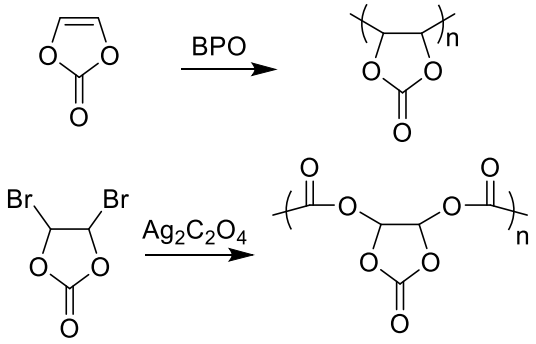

Scheme 1.2. Synthesis of polyvinylene carbonate.

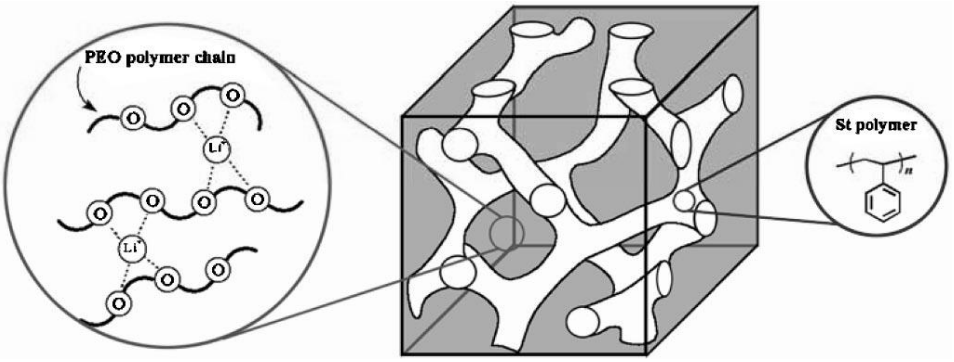

Figure 1.13. Schematic illustration of self-assembled nano structure of PS-*b*-PPEGMA-*b*-PS.

Although it is a very rigid polymer, having a T_g of 315 °C, it provides not only good mechanical stability but also several coordinating sites per repeating unit for better lithium solvating capability. Furthermore, these polar repeating unit facilitates to reduce the activation energy of lithium hopping, which results into a conductivity up to 10^{-4} S/cm at room temperature.[100] Inspired by this work, trimethylene carbonate has been polymerized and employed for study as a SPE. The mechanical properties were improved and good electrochemical stability up to 5V vs Li^+/Li electrode.

Polysiloxanes are well-known inorganic polymers with high chain flexibility (low T_g= -123°C for polydimethylsiloxane), chemical and thermal stability, and low toxicity. More importantly, various functionalities could be attached to the silicon in the backbone (Scheme 1.3).

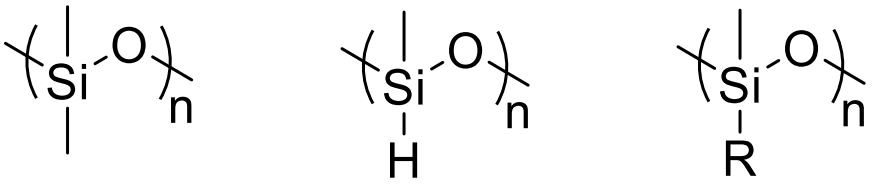

Scheme 1.3. Structures of polysiloxanes.

For example, PDMS-co-PEO has been prepared through the condensation reaction between dimethyldichlorosilane and monoethylene glycol and used as lithium conducting matrix. The ionic conductivity was found as high as 1.1×10^{-4} S/cm at room temperature with 5% wt. $LiClO_4$.[101] Nevertheless, its application was still limited due to the poor

mechanical strength. Several groups have synthesized cross-linked PDMS based SPEs to enhance the dimensional integrity. For instance, Oh *et al.* obtained a high Li conductivity of 10^{-4} S/cm at room temperature and very high thermal stability up to 500°C using comb poly(siloxane-*g*-ethylene oxide) (Figure 1.14).[102]

Lyon and coworkers prepared cross-linked PDMS using hydrosilylation reaction (Figure 1.15). The resulting SPEs not only showed improved mechanical properties, but also exhibited comparable conductivity (1.33×10^{-4} S/ cm at 25 °C) with a doping level EO/Li^+ of 20:1and an activation energy of 4.5 kJ/mol.[93]

Lin *et al.* has reported impressive results using new types of SPEs using mixture of PDMS, PVDF and LiTFSI. The membranes were prepared using solution cast method. The batteries assembled from the $LiFePO_4$ cathode, the electrolyte (20 wt% LiTFSI) and the Li anode display a discharge capacity of 115 mAh/g at 1 C even after 100 cycles at room temperature as shown in Figure 1.16.

1.2.3 Ionic Liquids and Polymerized Ionic Liquids

Ionic liquids (ILs) are room temperature molten salts. These salts usually contain a large cation and a charge-delocalized anion, which have weak columbic interactions. This results in a low tendency to crystallize. There are mainly two methods to prepare ionic liquids: acid-base neutralization and metathesis. For example, the preparation of imidazolium based IL was realized via the reaction between 1-methyl imidazole and bromobutane. On the other hand, 1-ethyl-3-methylimidazolium tetrafluoroborate ($EmiBF_4$) was synthesized via metathesis reaction between 1-ethyl-3-methylimidazolium chloride

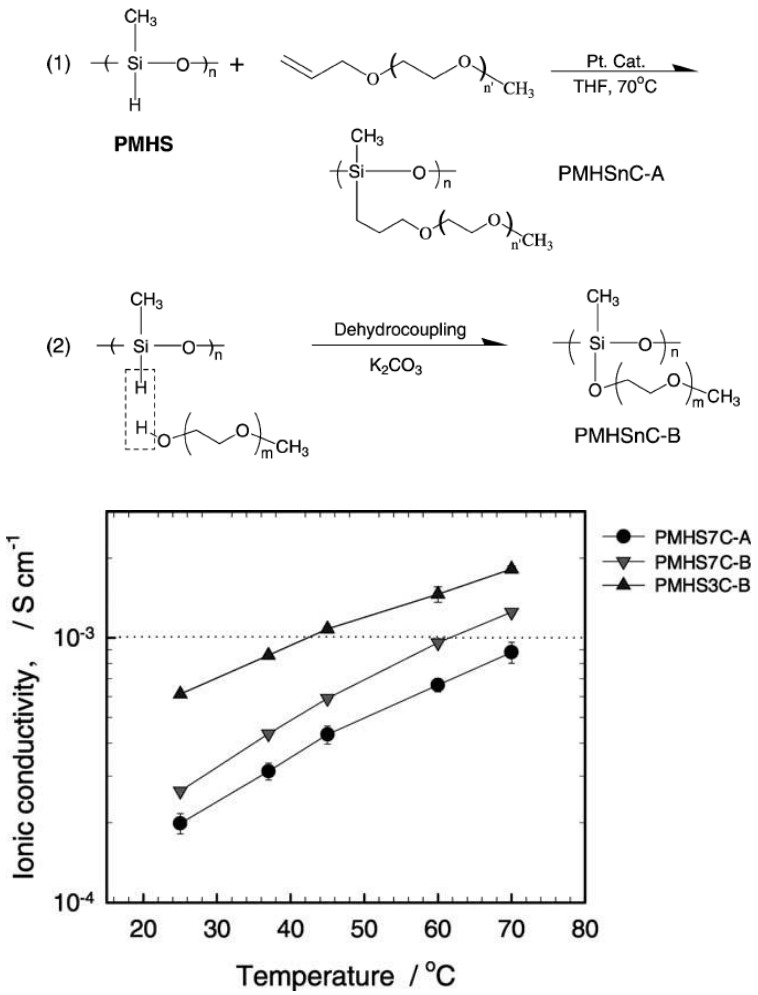

Figure 1.14. (A) Synthetic scheme of comb poly (siloxane-*g*-ethylene oxide). (B) ionic conductivity of comb PDMS-*g*-EO as a function of temperature.

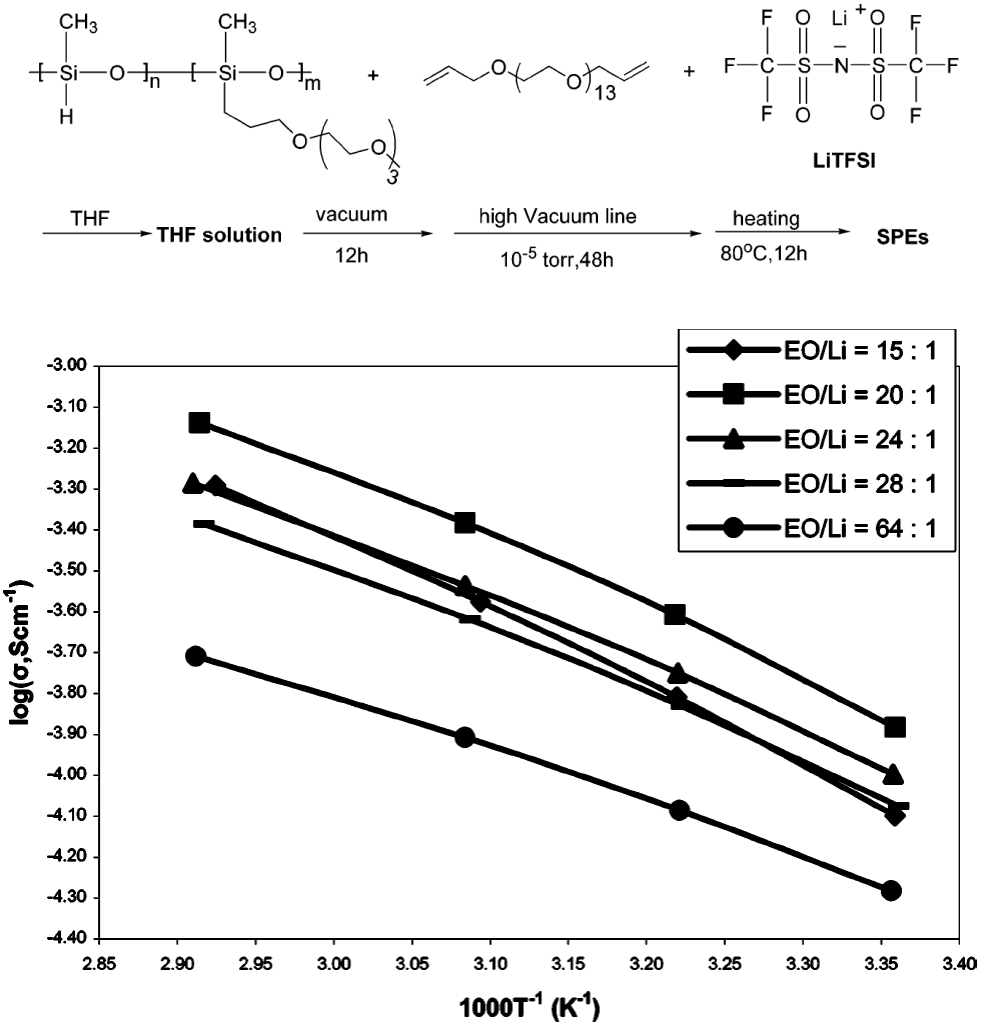

Figure 1.15. (a) synthetic procedure for crosslinked PDMS film. (b) ionic conductivity of crosslinked PDMS as a function of temperature. Reprinted from ref [93].

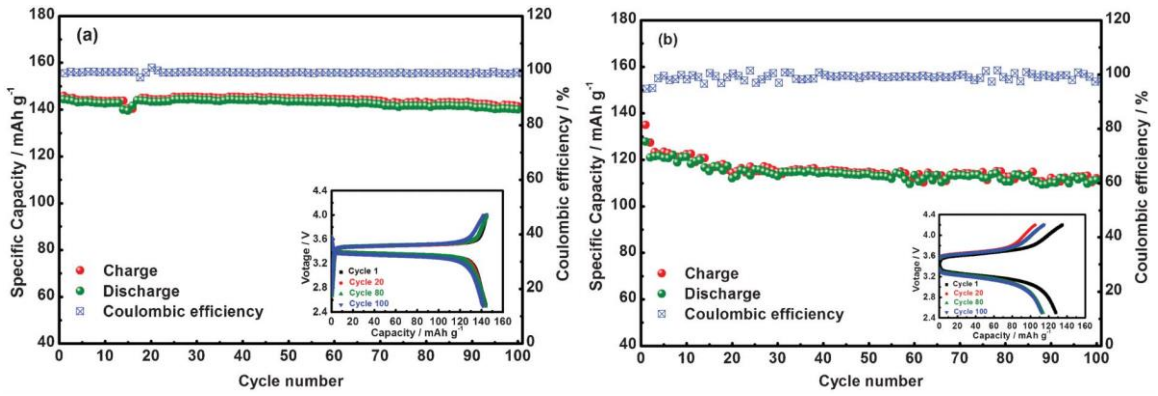

Figure 1.16. The room temperature cycling performance of the $LiFePO_4$/SPE/Li cell at (a) 0.2 C and (b) 1 C. Reprinted from ref [94].

and ammonium tetrafluoroborate in acetone.[103] These two examples were illustrated in Scheme 1.4.

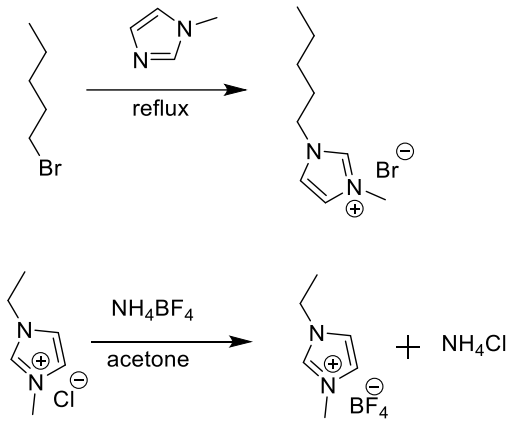

Scheme 1.4. Representative synthesis scheme for ILs through neutralization and metathesis.

ILs are basically having unlimited structural variations because of the accessibility of a large variety of their components. Therefore, various kinds of ILs can be tailored with desired properties. The archetype of ILs is formed by the combination of a 1-ethyl-3-methylimidazolium (EMI) cation and an bis(trifluoromethane)sulfonylimide (TFSI) anion (Scheme 1.5). This combination gives an ion conductivity comparable to many organic electrolyte solutions and rather high thermal stability up to ~300- 400 °C.

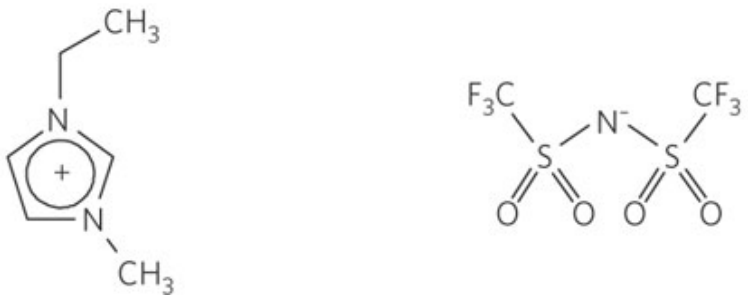

Scheme 1.5. Structure of 1-ethyl-3-methylimidazolium (EMI) cation and an bis(trifluoromethanesulfonyl)imide (TFSI) anion.

Other combinations such as imidazolium, pyrrolidinium and quaternary ammonium salts as cations and bis(trifluoromethanesulfonyl)imide, bis(fluorosulfonyl)imide and hexafluorophosphate as anions, are also extensively studied.[104-105]

Because ILs are non-flammable, low vapor pressure, and good electrodes compatibility,[106] they are soon becoming promising candidates for applications such as the polymer-electrolyte-membrane fuel cells, lithium batteries and supercapacitors (Figure 1.17).[107-110] The Li_xSi ($0 < x < 4.4$) alloying electrode with capacity reaching 2,000 mAh/g behaves quite well in contact with ionic liquids. The TFSI based electrolytes have been shown to cycle well with Li metal electrode, providing a significant enhancement in energy densities.[111] Furthermore, the chemical modification of the cation and of the anion allows the fine-tuning of the interactions at the interface and passivating-layer formation.[112]

However, the organic ionic-liquid cations suffer from electrochemical stability issues at the extremely negative potentials of alkali-metal deposition; in other words, the average electro negativity of an ion based on carbon, hydrogen or nitrogen cannot be as

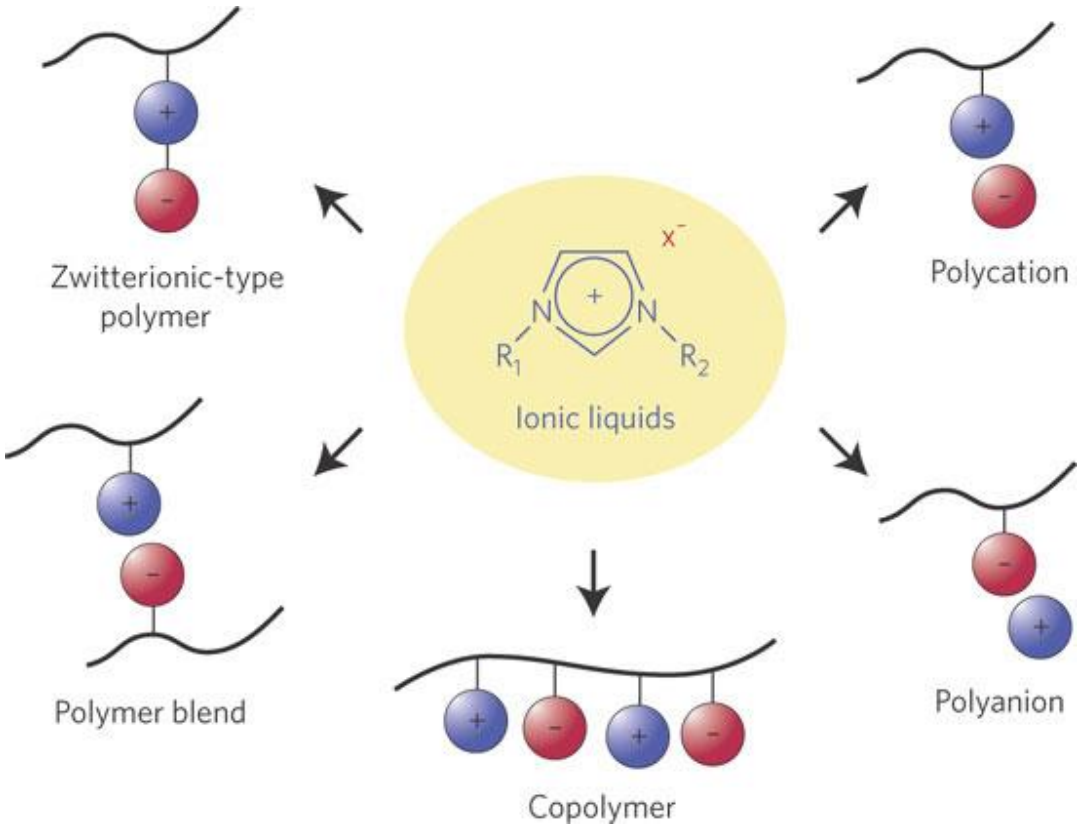

Figure 1.17. Types of polymerized ionic liquids.

low that of Li^+ or K^+. Because ILs liquids are only metastable at the potential of lithium reduction; the cations are sensitive to electron injection, with the subsequent formation of a radical, or proton elimination.[113] For instance, the archetypal ionic-liquid cation, ethyl methylimidazolium (Emi) possesses an acidic C2 proton that limits its stability below 1.3 V relative to Li^+/Li (-1.7 V vs standard H electrode). Although the electrochemical stability of ILs when using lithium metal as anode is poor, there have been a lot of research studies concerning ionic liquids that use imidazolium-based cations.[114] Seiko *et al.* examined the battery characteristics of lithium metal secondary batteries using an imidazolium based ionic liquid as electrolyte as illustrated in Figure 1.18. To improve the electrochemical stability, they introduced an electron-donating substituent at the second position of the imidazolium cation and a long alkyl chain at the third position to promote charge delocalization in the imidazolium (Figure 1.19).[110]

In conventional ambipolar SPEs, both Li^+ and counter ion could move during the charge/discharge circle. Due to the difference in diffusion rate of Li^+ and anion, anions tend to accumulate on the anode, causing cell voltage decrease, increased internal impedance and eventually cell failure. One of the best solutions is to prepare electrolyte with lithium transference number (t_{Li^+}) approaching to unity. According to simulation results by Monroe and Newman, no concentration gradient observed in the solution phase of electrolyte and lithium dendrite growth could be eliminated if the t_{Li^+} approaches to unity.[115-116] It also has been reported that the performance of an electrolyte with t_{Li^+} =1 is comparable to an ambipolar electrolyte even with a tenfold reduction in conductivity.[117]

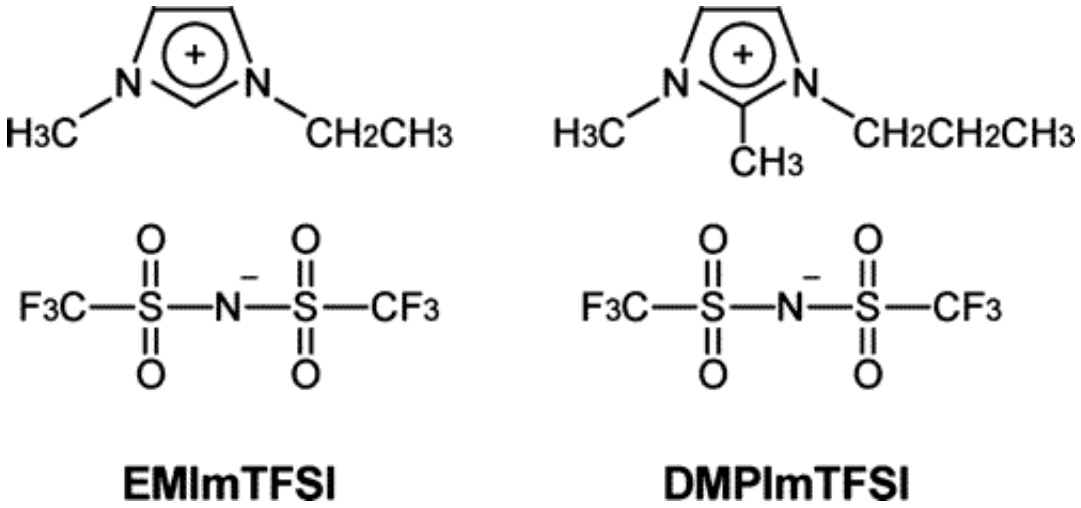

Figure 1.18. Chemical structures of imidazolium based ILs, EMImTFSI and DMPImTFSI.

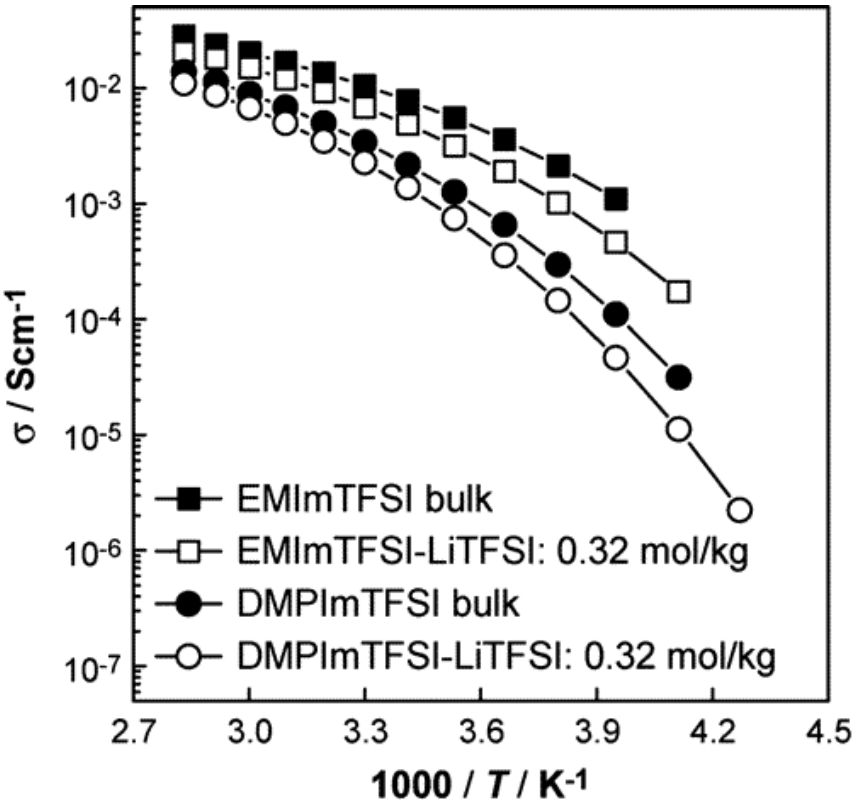

Figure 1.19. Arrhenius plots of ionic conductivity for the EMImTFSI, DMPImTFSI, EMImTFSI−LiTFSI mixture electrolyte, and DMPImTFSI−LiTFSI mixture electrolyte.

To realize t_{Li}^{+} =1, there are mainly two solutions to control the movement of anions during charging/discharging circles, by synthesizing polymers with anions covalently bonded to the polymer backbone and by incorporating the neutral anion acceptors that exclusively interacts with anions of the lithium salts. However, the main problem with neutral anion acceptors is its poor selectivity, self-coagulation, and relatively low transference number.[118-121] Therefore, single lithium ion conducting polymer electrolytes(SLICPEs) with anions are covalently bonded to the polymer backbone are of interest.

The synthetic strategy to prepare SLICPEs mainly focuses on the effect of anions. The anions that have been proposed are mainly carboxylate (CO_2^-), sulfonate (SO_3^-) and sulfonylimide (SO_2-N^--SO_2). SLICPEs with carboxylate as anion have been studied decades ago. Tsuchida *et al.* prepared lithium salts of poly [(ω-carboxy)oligo(oxyethylene) methacrylate] with a T_g of -44 °C and 3.2×10^{-9} S/cm at 30 °C.[122] Bannister and co-workers introduced fluorinated carboxylate to reduce the degree of ion-pairing and achieved approximately $1\times10^{-6.5}$ S/cm at 60 °C.[123] By grafting carboxylate to PDMS, the electrolytes showed increased conductivity of 5×10^{-6} S/cm at room temperature due to the increased chain flexibility.[124]

Compared with CO_2^-, sulfonate (SO_3^-) has a higher degree of negative charge delocalization. Several types of lithium electrolytes were prepared based on sulfonate or modified sulfonate as anion. Zhang *et al.* prepared PMMA-based lithium conducting polymer electrolyte with a T_g of 265 °C. When mixing with PEO, the ionic conductivity

achieved 1.8×10^{-7}S/cm at room temperature and further increased to 1.1×10^{-6} S/cm by replacing the semi-crystalline PEO with amorphous copolymer.[125] In 1997, Ohno *et al.* modified PEO oligomer (MW~ 350 g/mol) by attaching benzenesulfonate groups to its chain ends and obtained rather high conductivity of 4.45×10^{-6} S/cm at 30 °C and ts t_{Li}^{+} =0.75 at 20 °C.[126] However, the mechanical strength is too low. Several attempts were made to improve the mechanical properties by using rigid polymer backbones. For example, Kim *et al.* synthesized poly(lithium 4-styrenesulfonate) (PLSS) and blended with PEO. Nevertheless, it was found that ionic conductivity only passes a maximum value (3.0×10^{-8} S/cm) at [EO]/[Li] = 8.0.[127] Recently, Granados-Focil *et al.* prepared lithium conducting polymer electrolytes by blending linear poly(ethyleneimine)-graft-poly(ethylene glycol) with linear poly(ethyleneimine) bearing lithium N-propylsulfonate groups as the lithium source.[128] Ionic conductivity up to 4.0×10^{-4} S/cm at room temperature was achieved. Furthermore, copolymers with more flexible EO unit were also prepared. Kerr's group synthesized lithium sulfonate based on polyethylene glycol monomethyl ether acrylate and they reported highest conductivity of 2.0×10^{-7} S/cm at 25°C.[129] Comb electrolytes based on polysiloxane backbone with tetraglyme and lithiumsulfonate terminated perfluoroether side chains have been synthesized by Shriver and coworkers.[130] Cation conductivities for the systems here have been measured to reach a maximum of 2.5×10^{-6} S/cm at room temperature. The results are summarized in Table 1.3.

Table 1.3. The performance summary of representative single lithium ion conducting polymer electrolytes with carboxylate, sulfonate, and sulfonate imide as anion.

Entry	Polymer hosts	Type of anion	T_g	σ	t_{Li}^+	Ref.
			°C	S/cm		
1	PMMA	CO_2^-	-44	3.2×10^{-9}	NA	[122]
2	PMMA/PEO	$CF_2CO_2^-$	NA	$1\times10^{-6.5}$ (60°C)	NA	[123]
3	PDMS	CO_2^-	NA	5×10^{-6}	0.91	[124]
4	PMMA	SO_3^-	254	1.8×10^{-7}	NA	[125]
5	PEO	SO_3^-	-52.8	4.45×10^{-6}	0.75 (20°C)	[126]
6	PS	SO_3^-	NA	3.0×10^{-8}	0.85	[127]
7	PEI	SO_3^-	NA	4.0×10^{-4}	NA	[128]
8	PMA	SO_3^-	-58.9	2.0×10^{-7}	NA	[129]
9	PDMS	$C_nF_{2n}SO_3^-$	-70	2.5×10^{-6}	NA	[130]
10	TFSI	$COCF_2SO_2N^-$	67	10^{-6} (100°C)	NA	[131]
11	PEO	SO_2-N^--SO_2-CF_3	-38	2.7×10^{-6}	NA	[132]
12	PS-co-PMPEGA	SO_2-N^--SO_2-CF_3	-47	7.65×10^{-6}	0.93 (60°C)	[133]
13	PS-*b*-PEO-*b*-PS	SO_2-N^--SO_2-CF_3	NA	1.3×10^{-5} (60 °C)	>0.85	[134]

Table 1.3 (continued). The performance summary of representative single lithium ion conducting polymer electrolytes with carboxylate, sulfonate, and sulfonate imide as anion.

Entry	Polymer hosts	Type of anion	T_g °C	σ S/cm	t_{Li}^+	Ref.
14	PEO-*b*-PS	SO_2-N^--SO_2-CF_3	-10 to -19	6×10^{-8}	0.87-0.99	[135]
15	PDMS	$(C_6F_4)(C_6F_5)_3B^-$	-16	1.3×10^{-7}	NA	[136]

The above results suggested that SO_3^- as anion enhances the ion dissociation compared with CO_2^-. This effect was further amplified via fluorination. However, H^+ conductivity cannot be excluded in some protonated systems as the hydrogen atom in the Li-ion source moiety of $-CHFCF_2SO_3Li$ is acidic due to the strong electron-withdrawing effect of fluorine atoms.[36] The structures of these polymer electrolytes are shown in Figure 1.20.

Followed by the logic line described above, sulfonylimide (SO_2-N^--SO_2), which has even higher negative charge delocalization, has attracted attention for the next-generation single lithium ion conducting polymer electrolytes. Among them lithium bis(trifluoromethanesulfonyl)imide (LiTFSI) is the most popular lithium conducting salt because of its extremely high charge delocalization and high electrochemical stability due to the presence of the strongly electron-withdrawing group, $-CF_3$.[137] Since then, Watanabe et al. prepared novel lithium poly(2-oxo-1-difluoroethylenesulfonylimide)[131] and lithium poly (5-oxo-3-oxy-4-trifluoromethyl-1,2,4-pentafluoropentylene sulfonylimide)[138] in polyether. Unlike the polymer electrolytes mentioned previously, these electrolytes have polyanions as backbone rather than grafted as a dangled moiety. The t_{Li^+} was found to be one, however, the ionic conductivity was only in the order of 10^{-6} S/cm even at 100°C primarily due to the rigid structure of the polyanion. Followed this work, Desmarteau *et al.* reported various polymer electrolytes based on PEO oligomers and sulfonylimide as anion, which showed maximum conductivity of 2.7×10^{-6} S/cm at ambient temperature.[132]

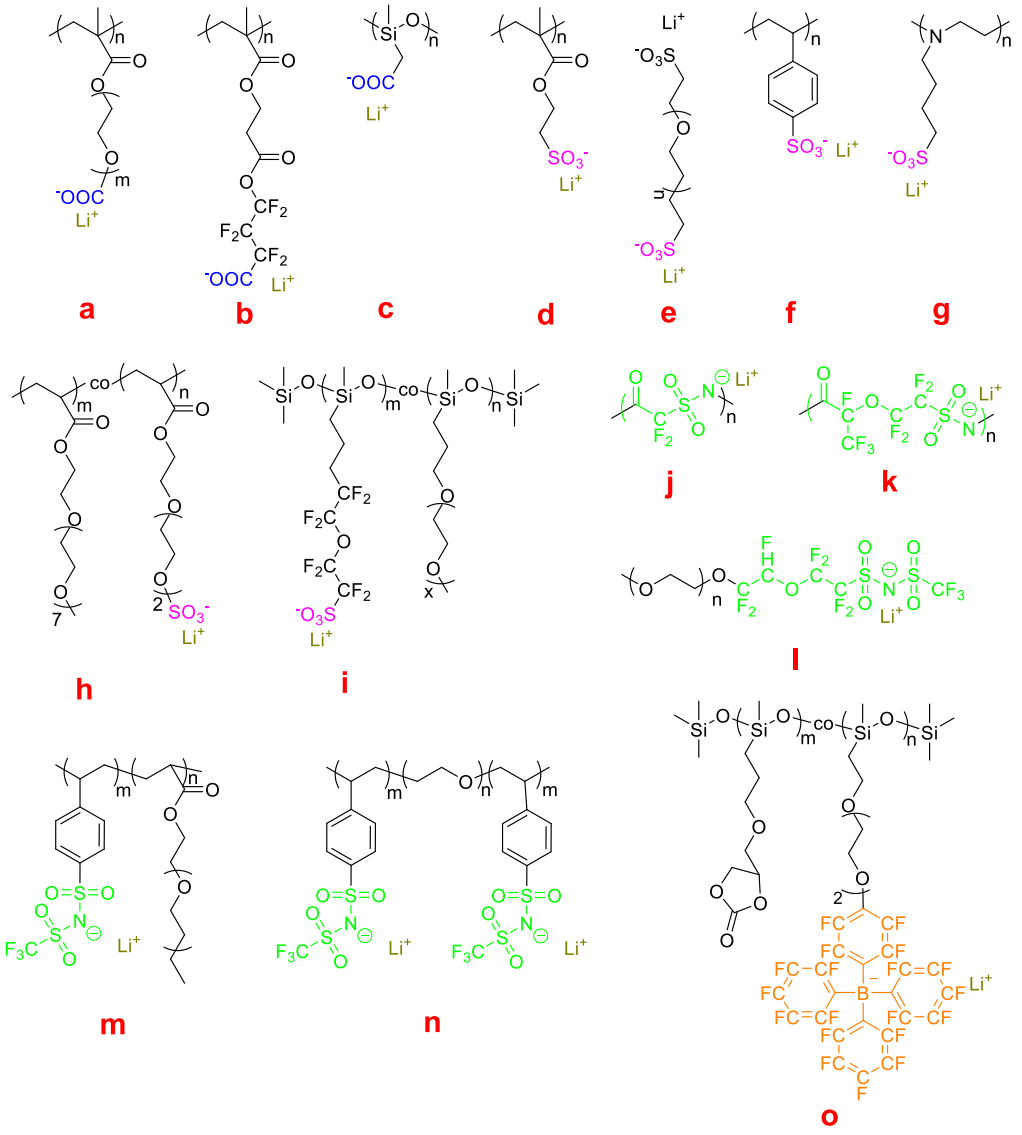

Figure 1.20. The structures of single lithium ion conducting polymer electrolytes with carboxylate, sulfonate, and sulfonylimide as anions.

It is clear that the incorporation of sulfonylimide group significantly improves the lithium ion conductivity. Zhou *et al.* successfully attached trifluorosulfonylimide to the para position of styrene monomer. Homopolymers and copolymers with methoxy polyethylene glycol acrylate were prepared as well. By tuning the content ratio of EO/Li^+, the maximum conductivity of 7.6×10^{-6} S/cm at 25 °C with a very high lithium transferee number of 0.93 at 60°C.[133] Block copolymers with the same anion center were also synthesized. Bouchet *et al.* reported a P(STFSILi)-PEO-P(STFSILi) as a polymer electrolyte exhibiting rather high ionic conductivity in dry state (1.3×10^{-5} S/cm at 60 °C), transport number (>0.85), improved mechanical strength compared with the neutral PS-PEO-PS triblock copolymer (10 MPa at 40 °C), and enlarged electrochemical stability window compared with PEO (up to 5 V versus Li^+/Li).[134] Ionic conductivity and morphology study of diblock copolymers, poly(ethylene oxide)-*b*-lithium poly[(4-styrenesulfonyl)(trifluoromethanesulfonyl)imide] (PEO-*b*-LiPSTFSI), suggested that ion transport in PEO-*b*-PSLiTFSI copolymers depends on a complex interplay between the volume fraction of the PEO block that provides ion pathways and that of the PSLiTFSI block where the ions are stored.[135] Below the PEO melting temperature, a lamellar morphology with ion clusters were found for PEO-PSLiTFSI(5-2), (5-3), and (5-4). These polymers exhibited an order-to-disorder transition coincident with the melting of the PEO crystals, and the conductivity increased abruptly by as much as 5 orders of magnitude (Figure 1.21).

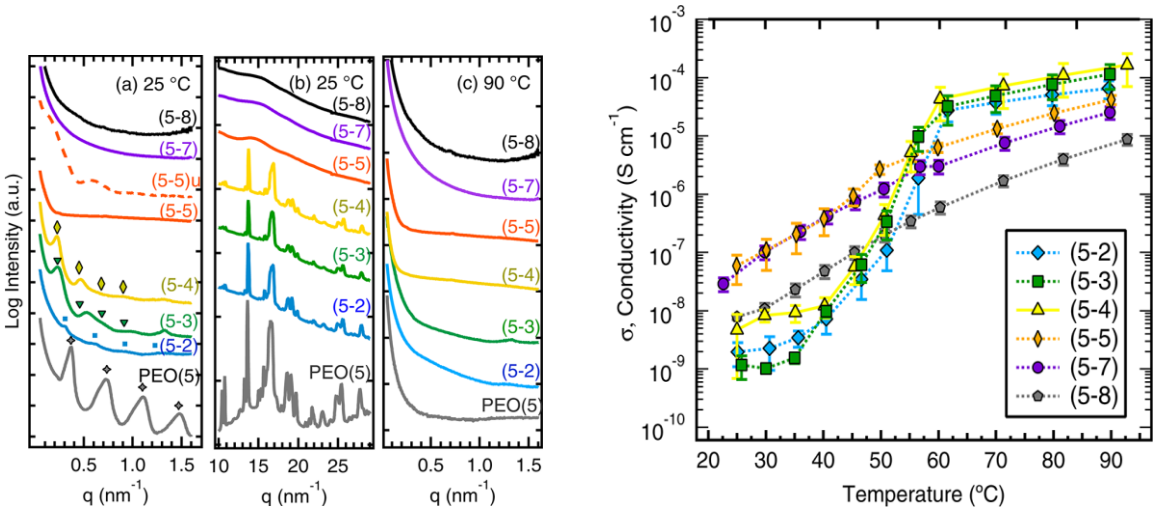

Figure 1.21. left: (a) SAXS intensity versus the magnitude of the scattering vector, q, at 25°C. (b) WAXS intensity versus the magnitude scattering vector, q, at 25 °C of PEO-*b*-PSLiTFSI copolymers. (c) SAXS intensity versus magnitude of the scattering vector, q, at 90 °C of PEO-*b*-PSLiTFSI copolymers. Right: ionic conductivity, σ, versus temperature of PEO-*b*-PSLiTFSI copolymers.

Other anions such as borate were also employed. Colby *et al.* prepared PDMS based SPEs with borate as anion. The perfluoronated phenyl rings showed much lower dissociation energy than nonfluorinated counterpart, resulting a three times higher conductivity at room temperature (1.3×10^{-7} S/cm). Nevertheless, the conductivity is still low because grafted phenyl rings hindered the segmental chain motion and the T_g of polymer electrolytes is only -16 °C.[136]

In summary, the types of anions affect the ionic conductivity significantly as well as the glass transition temperature of the polymer electrolytes. The anions with higher negative delocalization could enable the higher conductivity.

1.2.4 Lithium Ion Transport Mechanism

The challenging issue of SPEs in real world application is the electrode-electrolyte interfacial interaction, electrochemical stability window and the rather low lithium conductivity impedes the real-world applications of these types of polymer electrolytes.[139] It is generally accepted that the ionic conductivity is related to glass transition temperature, the dielectric constant and the solubility of lithium salt.[140]

The ionic conductivity can be expressed by the following equation:

$$\sigma = ne\mu$$

Where n, e and μ are the effective number of mobile ions, the elementary charge, and the ion mobility, respectively.

In a polymeric system, the diffusion of ions is coupled with the segmental relaxation of the polymer. The ionic conductivity in polymer electrolytes can therefore be described by the Nernst-Einstein relationship:

$$\sigma = \frac{pq^2D}{k_BT}$$

k_B is the Boltzmann constant and T is the absolute temperature.

The temperature dependence on conductivity of polymer electrolytes follows the Vogel-Tammann-Fulcher (VTF) equation,

$$\sigma = AT^{\frac{1}{2}}e^{\frac{E}{T-T_0}}$$

Where T_0 is the glass transition temperature of polymer electrolyte, E is the activation energy, A is the pre-exponential factor and T is the temperature of measurement.

In a typical PEO system, the generally accepted mechanism for lithium transporting is depicted in Figure 1.22. In this system, lithium ion is coordinated with oxygen atom and its transport is realized through breaking/forming Li-O bond. This process is believed coupled with the local chain relaxation. This relaxation decreases with decreasing temperature and increasing crystallinity. To achieve high ionic conductivity in SPEs requires a better understanding of the fundamentals of ion dissociation and transport.[141] Nevertheless, a principal goal has been to search new polymer hosts, which form a eutectic composition with PEO that melts at the lowest possible temperature and has minimum crystallinity. For example, attaching the side chain of the solvating group to the polymer increases the degrees of freedom. This improves the ionic conductivity, but compromises the mechanical properties.

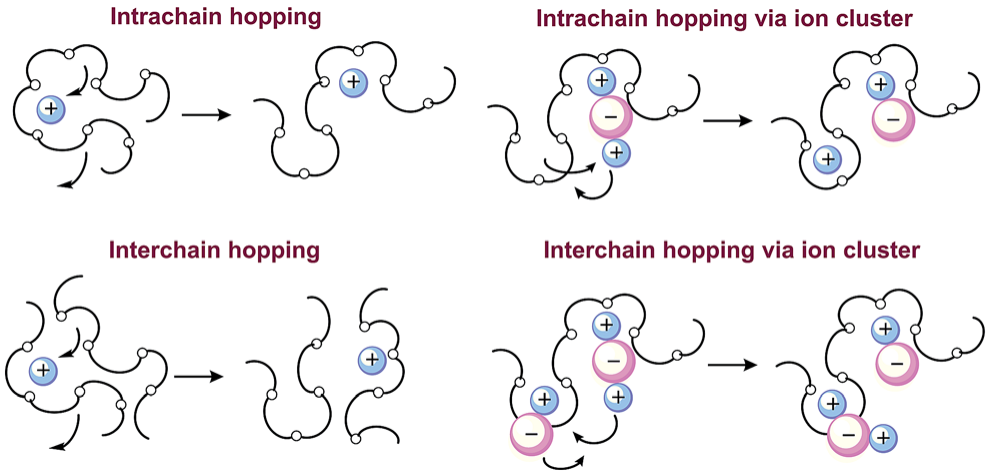

Figure 1.22. The mechanism of lithium ion transport in PEO matrix.

For the last few decades, much progress has been made on ionic conductive polymer based on poly (ethylene oxide). The primary focus was to improve the ionic conductivity by increasing the segmental mobility of the solvating polymer. Two most common strategies employed were the use of copolymers and the addition of side chains to reduce glass transition temperature. However, in most cases, the complexation of ions by the polymer reduces the segmental mobility of the polymer.

Another strategy is the development of single-ion conductor. The most widely used lithium salts are $LiClO_4$, $LiBF_4$, $LiPF_6$, $LiAsF_6$, $LiCF_3SO_3$, $LiN(CF_3SO_2)_2$, *etc*. The mobility of the ions and their dissociation constants are in the following order:

Mobility of ions: $LiBF_4$ > $LiClO_4$ > $LiPF_6$ > $LiAsF_6$ > $LiCF_3SO_3$ > LiTFSI. Dissociation constants: LiTFSI > $LiAsF_6$ > $LiPF_6$ > $LiClO_4$ > $LiBF_4$ > $LiCF_3SO_3$.

Progress has been made over the last 20 years in increasing the level of ionic conductivity.[142]Both the nature of the polymer-salt interaction and the precise structure of highly concentrated electrolyte solutions have always resisted rationalization.[143] Nevertheless, to facilitate the dissociation of inorganic salts in polymer hosts and to obtain high ionic conductivity, the following features should be satisfied to have high ionic conductivity: the lattice energy of the salt should be relatively low, the dielectric constant of the host polymer should be relatively high. Undoubtedly, the polymer architecture also play a key role independently of dissociation. Bruce *et al.*[144] proposed a structural view that stresses the importance of aligning the polymer chains in order to enhance the ionic conductivity.

On the contrary to the conventional view of ion transport in polymer matrix, rigid polymer backbones have been found that the ionic conductivity could be decoupled with their segmental relaxation.[100, 145] Sokolov *et al.* employed polymers backbone with different degrees of rigidity and PEO as side chain to increase salt solvation capability. They demonstrated that on the contrary to the conventional view of ion transport mechanism, ion diffusion and conductivity can be strongly decoupled from the segmental chain relaxation and the degree of decoupling correlates with the steepness of the temperature dependence of the segmental dynamics but not with T_g.[146] Wang *et al.* compared the relation between ionic transport and structural relaxation in polymers and small-molecule liquid electrolytes (Figure 1.23).[147] They reported that in small-molecule electrolytes, motion of ions is usually coupled to structural relaxation and high ionic conductivity is possible due to very short structural relaxation time. The ionic transport in polymer electrolytes can be strongly decoupled from structural relaxation, especially in polymers with relatively rigid structures.[148] Ions may utilize the loose local packing structure of long chains and diffuse through the polymer matrix even when segmental dynamics are slow or frozen (Figure 1.24).[149-150]

In summary, achieving high ionic conductivity in Li-based polymer electrolytes requires a better understanding of the fundamentals of ion dissociation and transport.[151]

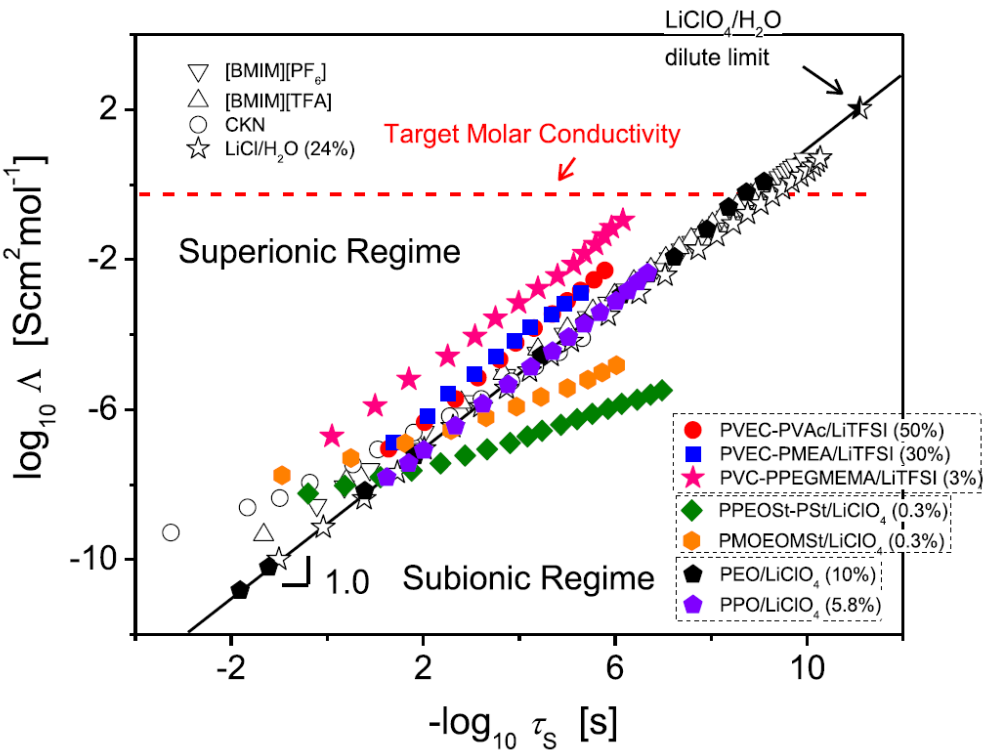

Figure 1.23. Relationship of apparent molar conductivity (Λ) to structural relaxation rate, adapted from ref. [147]

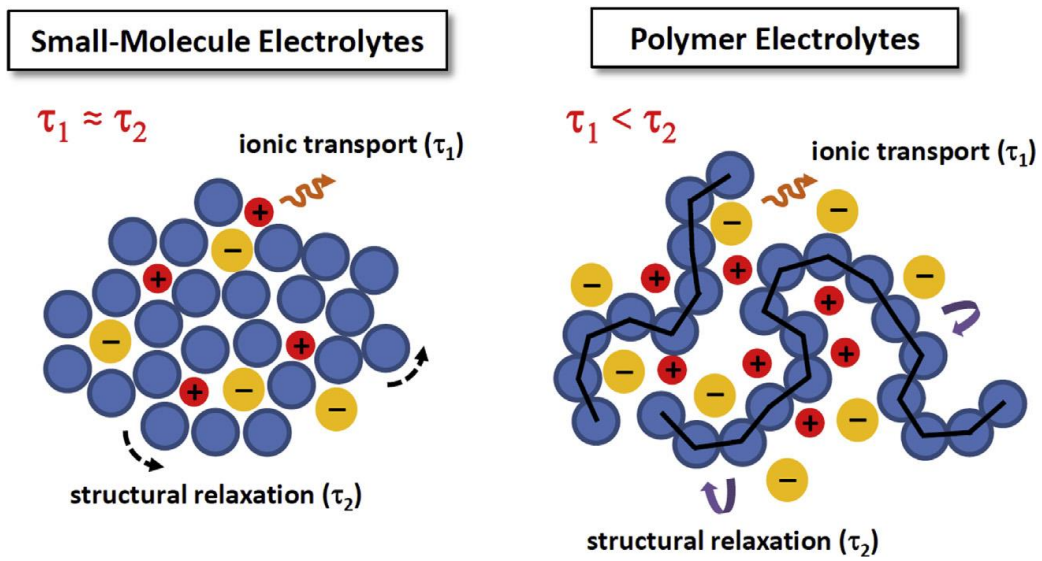

Figure 1.24. The schematic illustration of between the ion transport mechanisms in small molecules and polymers. Adapted from ref. [147]

Ionic conductivity in crystalline polymer

The view that ion transport in polymer hosts is coupled with polymer segmental chain motion has been established for decades. It has driven researchers to develop low T_g polymers, which has high chain motion at room temperature. However, it is worth mentioning that attempts also have been made to develop crystalline polymer for ionic conductivity,[152] even though it is beyond the scope of this thesis. Bruce *et al* prepared crystalline PEO_6:$LiSbF_6$ and PEO_6:$LiPF_6$ (six ether units per lithium ion).[153] Using *ab initio* from x-ray diffraction result suggested that PEO chains fold to form cylindrical tunnels and lithium ion can migrate within the tunnel (Figure 1.25A). The ionic conductivity in the crystalline domain was found higher than the amorphous state (Figure 1.25B).

1.3 CO_2/N_2 Gas Separation

There are many options for CO_2/N_2 separation including absorption, adsorption cryogenic condensation, and membrane separation.[27, 154] Among these technologies, amine absorption process has been used in natural gas industry for over 60 years and has been most extensively studied system.[155]

Mono-ethanolamine (MEA) is the most widely used type of amine for CO_2 capture by far. CO_2 recovery of 98% and product purity in excess of 99% can be achieved (Figure 1.26).[156] However, the rate of degradation in the oxidizing environment of flue gases, and the amount of energy required for regeneration remains a big issue.[157] Numerous reports have also focused on the modification of amines.[158] For example, Xu *et al.* studied a novel

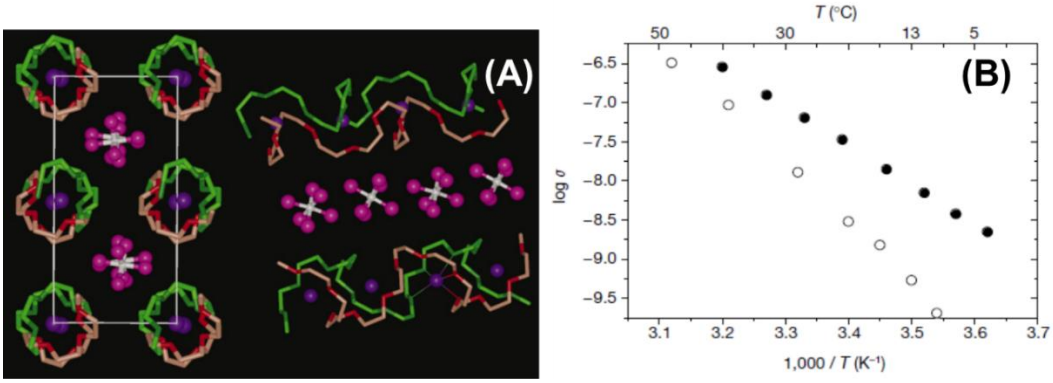

Figure 1.25. (A) Computation results of the crystalline structure of PEO_6:$LiAsF_6$. (B) lithium conductivity of amorphous and crystalline PEO_6:$LiSbF_6$ as a function of 1000/T. Adapted from ref. [153]

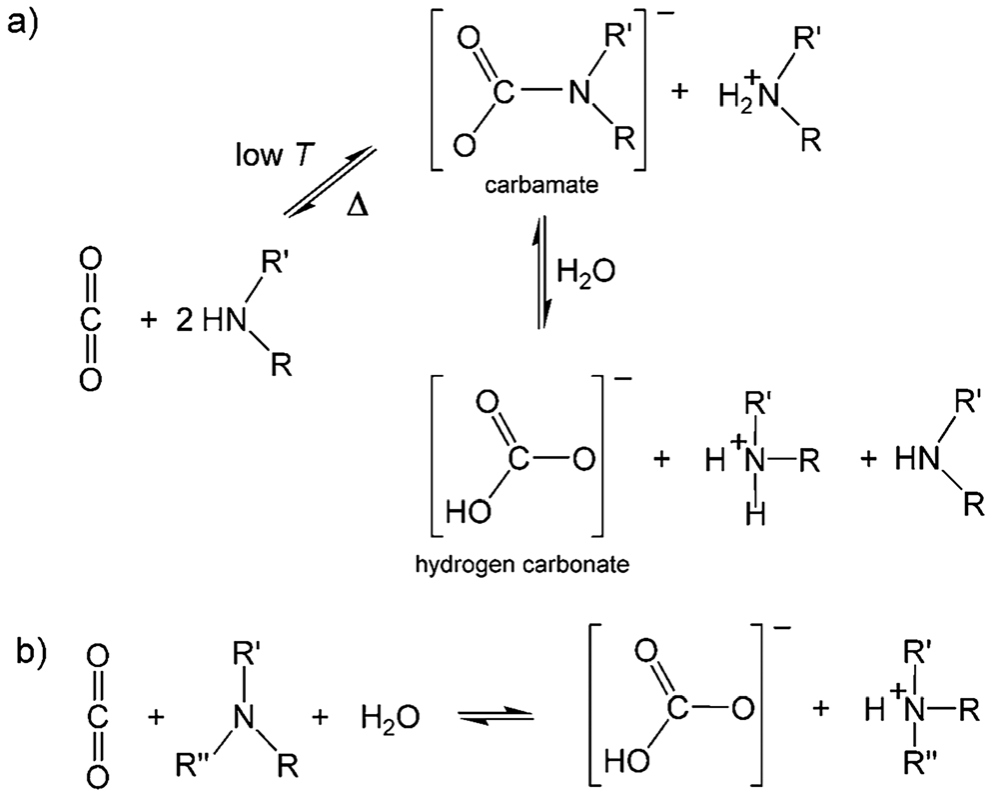

Figure 1.26. Reaction schemes for CO_2 absorption by amines.

CO_2 "molecular basket" adsorbent using a mesoporous molecular sieve of MCM-41 blended with polyethyleneimine (PEI). At 50 wt.% of PEI loading, the highest CO_2 adsorption capacity of 246 mg/g PEI was obtained, which is about 23 times that of the pure PEI (Figure 1.27).[159] Materials with high surface areas and open pore structures, such as activated carbon, silica aerogels, zeolites, and new porous materials like amine-based sorbents and MOFs, can also be utilized in the adsorption process to separate CO_2 from gas mixtures.[160]

The adsorption capacity and selectivity of CO_2 can be significantly affected by the pore structure, surface area, pressure, and temperature. Many reviews were published recently that discussed the CO_2 capture with MOFs (Figure 1.28).[161-162] Those reviews have discussed the CO_2 adsorption properties of MOFs based membranes for separations, and breakthrough analysis of multi-component gas mixtures, etc. MOF-210 has the highest CO_2 storage with up to 2400 mg/g under 50 bar at room temperature.

On the other hand, CO_2 can also be separated from other gases by condensation due to their distinct boiling temperatures. In fact, cryogenic separation is already used commercially for gases that only have high CO_2 concentrations (typically >90%).[163] This method can be operated at high pressure conditions compared with membrane separations. Nevertheless, one of the major disadvantages is that it requires enormous amount of energy for the refrigeration.[155] Moreover, NO_x and SO_x need to be removed before condensation.

Membranes have been widely used in various industrial separations for the last two decades due to their passive nature, which render polymeric membrane separation

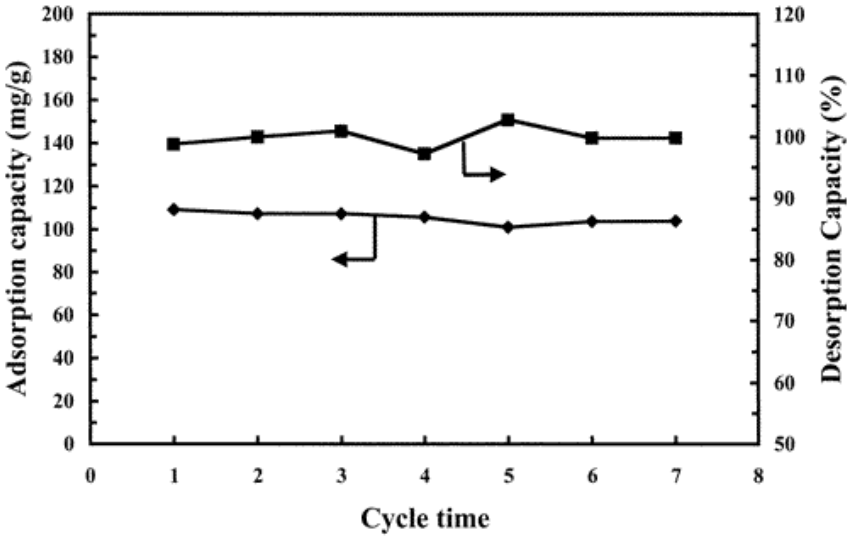

Figure 1.27. Adsorption capacity of MCM-41/PEI blend. Reprinted from ref.[159]

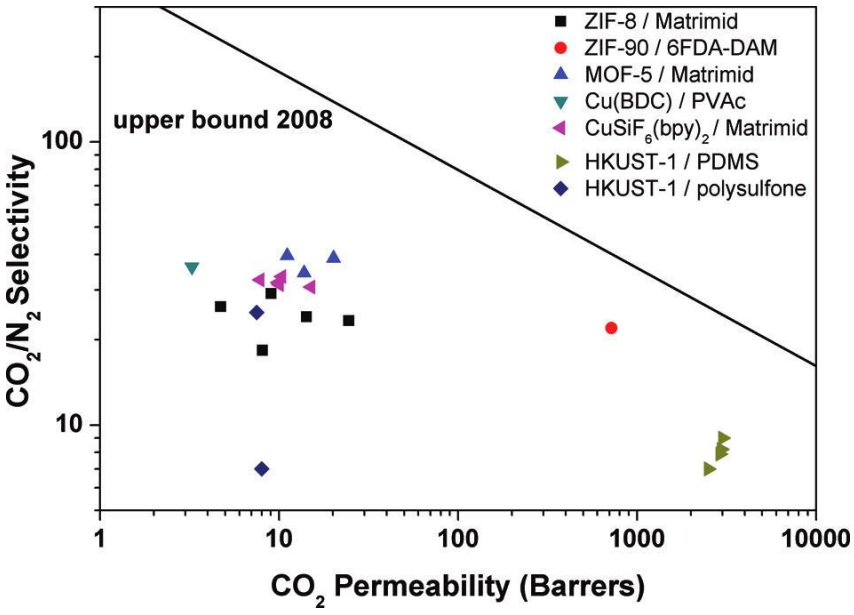

Figure 1.28. CO_2/N_2 separation performance of MOFs-based on membranes. The solid line represents the 2008 Robeson upper bond. Reprinted from ref.[162]

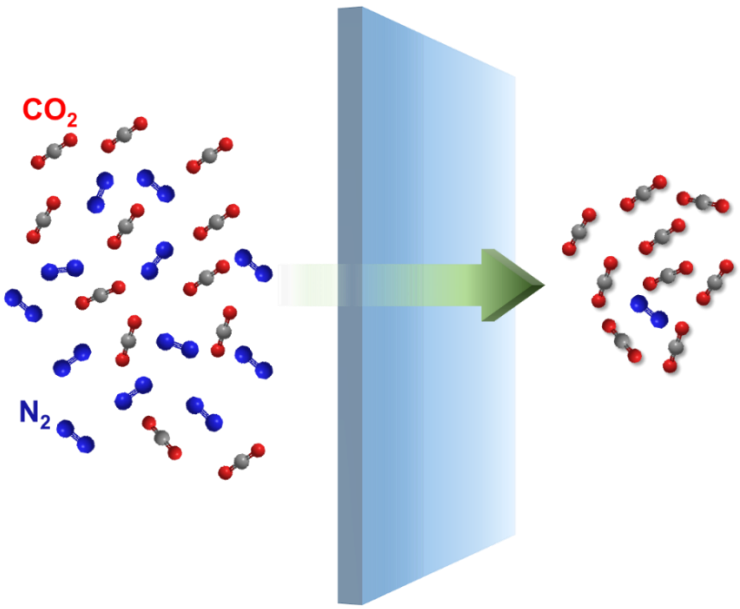

Figure 1.29. Illustration of CO_2/N_2 separation through a membrane.

processes more energy efficient than conventional CO_2 separation.[164] Gas separation membranes allow one gas species to pass through faster than the others (Figure 1.29).The candidate membranes should have the following features in order to be useful for CO_2 capture: (1) cost effective, high permeability to CO_2, (2) high selectivity toward CO_2, (3) and high dimensional stability at high temperatures and pressures.[165] Generally, gas molecules transport through a polymeric membrane by a solution-diffusion mechanism. The terms permeability and selectivity are often used to evaluate the performance of a gas separation membrane: the gas permeability (P_A), which is determined by the product of the gas solubility (S_A) and diffusivity (D_A) ($P_A = S_A \times D_A$); and the gas selectivity (α_{AB}) which is defined as the ratio of the permeability of any two gases ($\alpha_{AB} = \frac{P_A}{P_B}$).

Furthermore, selectivity can also be separated into solubility selectivity and diffusivity selectivity by the following equation: $\alpha_{AB} = \frac{P_A}{P_B} = \frac{S_A}{S_B} \times \frac{D_A}{D_B}$.

There appears to be a trade-off between selectivity and permeability, which has been illustrated by Robeson et al (Figure 1.30).[166]

Gas molecules move through free volumes within between polymeric structures. Because of the movement of the polymer chains, a channel between gaps can be formed allowing gas molecules to move from one gap to another and thus gas molecules can effectively diffuse through the membrane structure. However, the diffusion coefficients for this two-gas pair are close (Figure 1.31). They also have similar kinetic diameter (N_2 (kinetic diameter = 3.64 Å), CO_2 (kinetic diameter = 3.30 Å)).

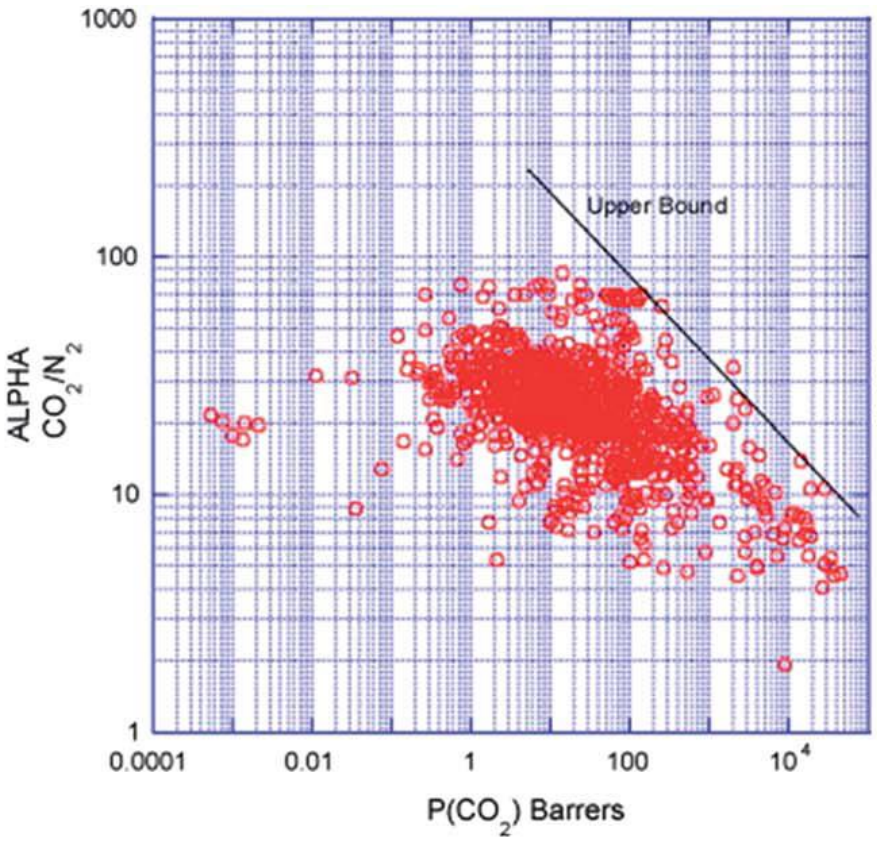

Figure 1.30. Robeson "upper bound" for CO_2/N_2. Reprinted from ref.[166]

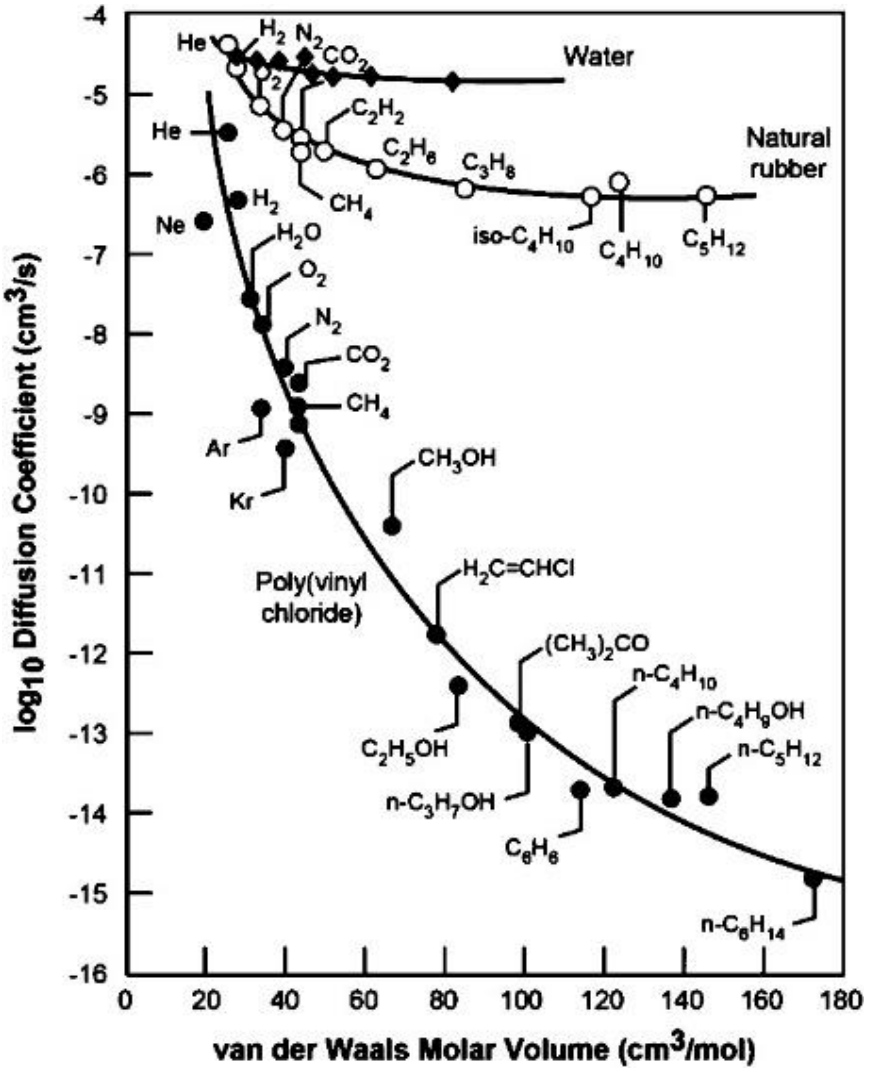

Figure 1.31. Diffusion coefficient as a function of molar volume for a variety of gas permeants in water, natural rubber, and a glassy polymer.

Therefore, the synthesis of the polymeric membranes located above the "upper bound" limit is challenging. The key is to prepare polymers with good CO_2/N_2 selectivity and the high CO_2 permeability. Rubbery polymers containing ethylene oxide blocks have strong CO_2-philicity. However, pure and linear PEOs tends to crystallize leading to low gas permeability and poor film-forming properties.[167]

Fortunately, crystallization of PEO can be reduced by using block copolymers containing glassy hard segments and rubbery soft segments. Poly(ethylene oxide)-*b*-(butylene terephthalate), known as Polyactive, has an intrinsic CO_2 permeability of 150 barrer.[168] Blending PEG-oligomers into Polyactive can also be used to increase CO_2 permeability.[169] The resulting blends exhibit CO_2 permeability of 150−750 barrer and CO_2/N_2 selectivity of 36−50. Other rubbery polymer materials such as poly(dimethylsiloxane), ethylene oxide/propylene oxide amide copolymers) and glassy polymers (e.g., cellulose acetate, polyperfluorodioxoles, polycarbonates, polyimides, polynorbornene and polysulfone) have also been studied (Table 1.4).[170]

Very recently, new materials such as PIMs, polymers with intrinsic microporosity, have attracted massive attention due to their adaptability and controllable free volume.[171] Take PIM-1 as example (Scheme 1.6). It can be prepared via condensation reaction between 5,5,6,6-tetrahydroxy-3,3,3,3-tetramethylspiro-bisindane with tetrafluorophthalonitrile. Many PIMs have the selectivity in the range of 20–30, and permeability from 200 to 11000 barrers.[172] Poly(1-trimethylsilyl-1-propyne) (PTMSP) is another type of polyacetylenes. Since the first report of synthesis of Poly(1-trimethylsilyl-

Table 1.4. CO_2/N_2 separation performance of several representative polymers.

Entry	Polymer	Permeability	Selectivity	Ref.
		$m^3/m^2Pa\ s$	$\alpha_{CO2/N2}$	
1	Polyimide	735	43	[167]
2	polyethersulfone	665	24.7	[172]
3	Polysulfone	450	31	[169]
4	PAN/PEO	91	27.9	[173]

1-propyne) (PTMSP)) in 1983, it has drawn significant attention because of its orders higher gas permeability than other known polymers.

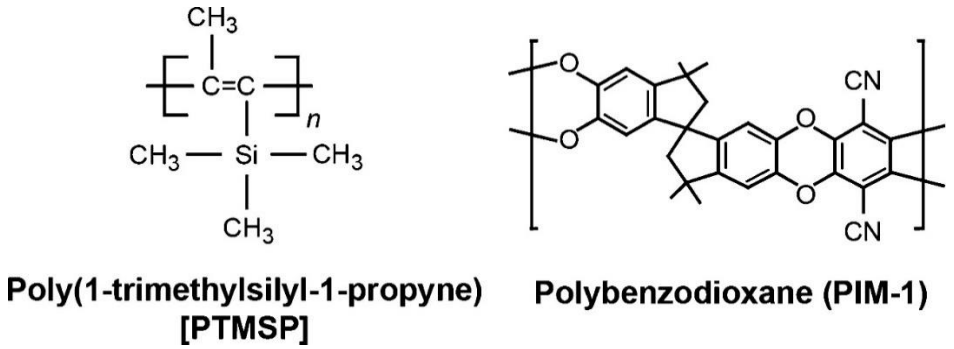

Scheme 1.6. Structures of PTMSP and PIM-1.

Polymerization of 1-(trimethylsilyl)-1-propyne is initiated by $TaCl_5$ and $NbCl_5$. A detailed study of polymerization of TMSP was reported elsewhere.[174] Its exceptionally high fractional free volume is attributed to a rigid, low cohesive energy density backbone composed of alternating double bonds and bulky methyl and trimethylsilyl substituents.[175] From the practical point of view, membranes having high permeability are favored for flue gas separations due to the enormous volumes of flue gas emissions from coal-fired power plants that produce a limited pressure differential.[176] Soon after PTMSP was made, it was found that permeation of the polymer were not stable. Membrane permeability was initially exceptionally high but declined overtime. The decrease is probably the combination of physical aging, chemical aging and contamination.[177] Another major drawback that limited

the real world application of PTMSP is its rather low selectivity.[178-179] This research focused on the modification of PTMSP to enhance CO_2/N_2 selectivity.

1.4 References

1. Agency, I. E. World Energy Outlook 2011. http://www.worldenergyoutlook.org (International Energy Agency, 2011).

2. Huntingford, C.; Zelazowski, P.; Galbraith, D.; Mercado, L. M.; Sitch, S.; Fisher, R.; Lomas, M.; Walker, A. P.; Jones, C. D.; Booth, B. B., *Nat. Geosci.* **2013,** *6*, 268-273.

3. Munday, P. L.; Cheal, A. J.; Dixson, D. L.; Rummer, J. L.; Fabricius, K. E., *Nat. Clim. Change* **2014,** *4*, 487-492.

4. Peters, G. P.; Andrew, R. M.; Canadell, J. G.; Fuss, S.; Jackson, R. B.; Korsbakken, Jan I.; Le Quéré, C.; Nakicenovic, N., *Nat. Clim. Change* **2017,** *7*, 118-122.

5. O'Neill, B. C.; Oppenheimer, M.; Warren, R.; Hallegatte, S.; Kopp, R. E.; Pörtner, H. O.; Scholes, R.; Birkmann, J.; Foden, W.; Licker, R.; Mach, K. J.; Marbaix, P.; Mastrandrea, M. D.; Price, J.; Takahashi, K.; van Ypersele, J.-P.; Yohe, G., *Nat. Clim. Change* **2017,** *7*, 28-37.

6. Solomon, S.; Plattner, G. K.; Knutti, R.; Friedlingstein, P., *Proc Natl Acad Sci U S A* **2009,** *106*, 1704-9.

7. Hoegh-Guldberg, O.; Mumby, P. J.; Hooten, A. J.; Steneck, R. S.; Greenfield, P.; Gomez, E.; Harvell, C. D.; Sale, P. F.; Edwards, A. J.; Caldeira, K.; Knowlton, N.; Eakin, C. M.; Iglesias-Prieto, R.; Muthiga, N.; Bradbury, R. H.; Dubi, A.; Hatziolos, M. E., *Science* **2007,** *318*, 1737-42.

8. Change, I. P. o. C., *Climate Change 2014–Impacts, Adaptation and Vulnerability: Regional Aspects*. Cambridge University Press: 2014.

9. Lewis, N. S., *MRS Bull.* **2007,** *32*, 808-820.

10. Larcher, D.; Tarascon, J.-M., *Nat. Chem* **2015,** *7*, 19-29.

11. Tarascon, J.-M.; Armand, M., *Nature* **2001,** *414*, 359-367.

12. Haszeldine, R. S., *Science* **2009,** *325*, 1647-52.

13. Erickson, L. E.; Jennings, M., *Aims Public Health* **2017,** *4*, 47-61.

14. Tarascon, J. M.; Armand, M., *Nature* **2001,** *414*, 359-367.

15. Jow, T. R.; Xu, K.; Borodin, O.; Makoto, U., *Electrolytes for lithium and lithium-ion batteries*. Springer: 2014; Vol. 58.

16. Goodenough, J. B.; Park, K. S., *J. Am. Chem. Soc.* **2013,** *135*, 1167-76.

17. Xue, Z.; He, D.; Xie, X., *J. Mater. Chem. A* **2015,** *3*, 19218-19253.

18. Whittingham, M. S., *Science* **1976,** *192*, 1126-1127.

19. Whittingham, M. S., *Chem. Rev.* **2004,** *104*, 4271-4302.

20. Whittingham, M. S., Chalcogenide battery. Google Patents: 1977.

21. Lu, L.; Han, X.; Li, J.; Hua, J.; Ouyang, M., *J. Power Sources* **2013,** *226*, 272-288.

22. Eisler, M. N. The History of Lithium Ion Batteries Is Explosive. http://www.slate.com/articles/technology/future_tense/2016/09/the_explosive_history_of_lithium_ion_batteries.html.

23. Jacoby, M., *Chem. Eng. News* **2013,** *91*, 33-37.

24. Arico, A. S.; Bruce, P.; Scrosati, B.; Tarascon, J. M.; van Schalkwijk, W., *Nat Mater* **2005,** *4*, 366-77.

25. Sides, C. R.; Li, N.; Patrissi, C. J.; Scrosati, B.; Martin, C. R., *MRS Bull.* **2011,** *27*, 604-607.

26. Yang, H.; Xu, Z.; Fan, M.; Gupta, R.; Slimane, R. B.; Bland, A. E.; Wright, I., *J Environ Sci (China)* **2008,** *20*, 14-27.

27. Nugent, P.; Belmabkhout, Y.; Burd, S. D.; Cairns, A. J.; Luebke, R.; Forrest, K.; Pham, T.; Ma, S.; Space, B.; Wojtas, L., *Nature* **2013,** *495*, 80-84.

28. Haszeldine, R. S., *Science* **2009,** *325*, 1647-1652.

29. D'Alessandro, D. M.; Smit, B.; Long, J. R., *Angew. Chem. Int. Ed.* **2010,** *49*, 6058-6082.

30. Wang, M.; Lawal, A.; Stephenson, P.; Sidders, J.; Ramshaw, C., *Chem. Eng. Res. Des.* **2011,** *89*, 1609-1624.

31. Thiruvenkatachari, R.; Su, S.; An, H.; Yu, X. X., *Prog. Energy Combust. Sci.* **2009,** *35*, 438-455.

32. Romeo, L. M.; Abanades, J. C.; Escosa, J. M.; Paño, J.; Giménez, A.; Sánchez-Biezma, A.; Ballesteros, J. C., *Energy Convers. Manage.* **2008,** *49*, 2809-2814.

33. Rubin, E. S.; Mantripragada, H.; Marks, A.; Versteeg, P.; Kitchin, J., *Prog. Energy Combust. Sci.* **2012,** *38*, 630-671.

34. Weston, J.; Steele, B., *Solid State Ionics* **1982,** *7*, 75-79.

35. Figueroa, J. D.; Fout, T.; Plasynski, S.; McIlvried, H.; Srivastava, R. D., *Int. J. Greenhouse Gas Control* **2008,** *2*, 9-20.

36. Zhang, H.; Li, C.; Piszcz, M.; Coya, E.; Rojo, T.; Rodriguez-Martinez, L. M.; Armand, M.; Zhou, Z., *Chem. Soc. Rev.* **2017**.

37. Li, Q.; Itoh, T.; Imanishi, N.; Hirano, A.; Takeda, Y.; Yamamoto, O., *Solid State Ionics* **2003,** *159*, 97-109.

38. Quartarone, E.; Mustarelli, P.; Magistris, A., *Solid State Ionics* **1998,** *110*, 1-14.

39. Peled, E.; Golodnitsky, D.; Ardel, G.; Eshkenazy, V., *Electrochim. Acta* **1995,** *40*, 2197-2204.

40. Capuano, F., *J. Electrochem. Soc.* **1991,** *138*, 1918.

41. Panero, S.; Scrosati, B.; Sumathipala, H.; Wieczorek, W., *J. Power Sources* **2007,** *167*, 510-514.

42. Croce, F.; Appetecchi, G.; Persi, L.; Scrosati, B., *Nature* **1998,** *394*, 456-458.

43. Xiong, H. M.; Wang, Z. D.; Liu, D. P.; Chen, J. S.; Wang, Y. G.; Xia, Y. Y., *Adv. Funct. Mater.* **2005,** *15*, 1751-1756.

44. Wetjen, M.; Navarra, M. A.; Panero, S.; Passerini, S.; Scrosati, B.; Hassoun, J., *ChemSusChem* **2013,** *6*, 1037-1043.

45. Ibrahim, S.; Johan, M. R., *Int J Electrochem Sci* **2012,** *7*, 2596-2615.

46. Cheung, I.; Chin, K.; Greene, E.; Smart, M.; Abbrent, S.; Greenbaum, S.; Prakash, G.; Surampudi, S., *Electrochim. Acta* **2003,** *48*, 2149-2156.

47. Dissanayake, M.; Jayathilaka, P.; Bokalawala, R.; Albinsson, I.; Mellander, B., *S0378-7753 (03)* **2003**, 00262-3.

48. Nan, C. W.; Fan, L.; Lin, Y.; Cai, Q., *Phys. Rev. Lett.* **2003,** *91*, 266104.

49. Vaia, R. A.; Vasudevan, S.; Krawiec, W.; Scanlon, L. G.; Giannelis, E. P., *Adv. Mater*. **1995,** *7*, 154-156.

50. Stephan, A. M.; Nahm, K., *Polymer* **2006,** *47*, 5952-5964.

51. Song, J.; Wang, Y.; Wan, C., *J. Power Sources* **1999,** *77*, 183-197.

52. Scrosati, B.; Croce, F.; Appetecchi, G. B.; Persi, L., *Nature* **1998,** *394*, 456-458.

53. Chu, P. P.; Reddy, M. J.; Kao, H., *Solid State Ionics* **2003,** *156*, 141-153.

54. Croce, F.; Persi, L.; Ronci, F.; Scrosati, B., *Solid State Ionics* **2000,** *135*, 47-52.

55. Sakuda, A.; Hayashi, A.; Tatsumisago, M., *Sci. Rep.* **2013,** *3*, 2261.

56. Wang, H.; Huang, H.; Wunder, S. L., *J. Electrochem. Soc.* **2000,** *147*, 2853-2861.

57. Yang, X.; Zhang, F.; Zhang, L.; Zhang, T.; Huang, Y.; Chen, Y., *Adv. Funct. Mater.* **2013,** *23*, 3353-3360.

58. Oh, B.-K.; Kim, Y.-R.; Kim, D.-w.; Baek, C.-W. Gel polymer electrolyte of vinyl acetate. U.S. 6,268,088, 2001.

59. Gozdz, A. S.; Schmutz, C. N.; Tarascon, J.-M. Rechargeable lithium intercalation battery with hybrid polymeric electrolyte. U.S. 5,296,318, 1994.

60. Oliver, M.; Gies, P. J.; Pendalwar, S. L.; Coalson, C. E.; Eschbach, F. O. Polymer gel electrolyte. U.S. 5,639,573, 1997.

61. Meyer, W. H., *Adv. Mater.* **1998,** *10*, 439-48.

62. Abraham, K.; Alamgir, M., *J. Electrochem. Soc.* **1990,** *137*, 1657-1658.

63. MacCallum, J. R.; Vincent, C. A., *Polymer electrolyte reviews*. Springer Science & Business Media: 1989; Vol. 2.

64. Fergus, J. W., *J. Power Sources* **2010,** *195*, 4554-4569.

65. Quartarone, E.; Mustarelli, P., *Chem. Soc. Rev.* **2011,** *40*, 2525-2540.

66. Fenton, D. E.; Parker, J. M.; Wright, P. V., *Polymer* **1973,** *14*, 589-589.

67. Scrosati, B.; Vincent, C. A., *MRS Bull.* **2000,** *25*, 28-30.

68. Evans, J.; Vincent, C. A.; Bruce, P. G., *Polymer* **1987,** *28*, 2324-2328.

69. Wang, H.; Keum, J. K.; Hiltner, A.; Baer, E.; Freeman, B.; Rozanski, A.; Galeski, A., *Science* **2009,** *323*, 757-760.

70. Pielichowski, K.; Flejtuch, K., *Polym. Adv. Technol.* **2002,** *13*, 690-696.

71. Bujdák, J.; Hackett, E.; Giannelis, E. P., *Chem. Mater.* **2000,** *12*, 2168-2174.

72. Abraham, K.; Jiang, Z.; Carroll, B., *Chem. Mater.* **1997,** *9*, 1978-1988.

73. Tominaga, Y., *Polym. J.* **2016,** *49*, 291-299.

74. Fullerton-Shirey, S. K.; Maranas, J. K., *Macromolecules* **2009,** *42*, 2142-2156.

75. Nicotera, I.; Ranieri, G. A.; Terenzi, M.; Chadwick, A. V.; Webster, M. I., *Solid State Ionics* **2002,** *146*, 143-150.

76. Aoki, T.; Konno, A.; Fujinami, T., *Electrochim. Acta* **2004,** *50*, 301-304.

77. Brandell, D.; Kasemägi, H.; Tamm, T.; Aabloo, A., *Solid State Ionics* **2014,** *262*, 769-773.

78. Sun, H.; Takeda, Y.; Imanishi, N.; Yamamoto, O.; Sohn, H. J., *J. Electrochem. Soc.* **2000,** *147*, 2462-2467.

79. Kelly, I.; Owen, J.; Steele, B., *J. Power Sources* **1985,** *14*, 13-21.

80. Scrosati, B.; Croce, F.; Persi, L., *J. Electrochem. Soc.* **2000,** *147*, 1718-1721.

81. Hawker, C. J.; Chu, F.; Pomery, P. J.; Hill, D. J., *Macromolecules* **1996,** *29*, 3831-3838.

82. Niitani, T.; Amaike, M.; Nakano, H.; Dokko, K.; Kanamura, K., *J. Electrochem. Soc.* **2009,** *156*, A577-A583.

83. Nagasubramanian, G.; Shen, D. H.; Surampudi, S.; Wang, Q.; Prakash, G. K. S., *Electrochim. Acta* **1995,** *40*, 2277-2280.

84. Bandara, L.; Dissanayake, M.; Mellander, B.-E., *Electrochim. Acta* **1998,** *43*, 1447-1451.

85. Niedzicki, L.; Kasprzyk, M.; Kuziak, K.; Żukowska, G.; Armand, M.; Bukowska, M.; Marcinek, M.; Szczeciński, P.; Wieczorek, W., *J. Power Sources* **2009,** *192*, 612-617.

86. Pitawala, H.; Dissanayake, M.; Seneviratne, V.; Mellander, B.-E.; Albinson, I., *J. Solid State Electrochem.* **2008,** *12*, 783-789.

87. Sutto, T. E., *J. Electrochem. Soc.* **2007,** *154*, P101-P107.

88. Li, J.; Khan, I. M., *Macromolecules* **1993,** *26*, 4544-4550.

89. Das, A.; Thakur, A. K.; Kumar, K., *Ionics* **2013,** *19*, 1811-1823.

90. Tanaka, R.; Sakurai, M.; Sekiguchi, H.; Mori, H.; Murayama, T.; Ooyama, T., *Electrochim. Acta* **2001,** *46*, 1709-1715.

91. Sun, B.; Mindemark, J.; Edström, K.; Brandell, D., *Solid State Ionics* **2014,** *262*, 738-742.

92. Yuan, F.; Chen, H.-Z.; Yang, H.-Y.; Li, H.-Y.; Wang, M., *Mater. Chem. Phys.* **2005,** *89*, 390-394.

93. Zhang, Z.; Sherlock, D.; West, R.; West, R.; Amine, K.; Lyons, L. J., *Macromolecules* **2003,** *36*, 9176-9180.

94. Lin, Y.; Li, J.; Lai, Y.; Yuan, C.; Cheng, Y.; Liu, J., *RSC Adv.* **2013,** *3*, 10722.

95. Acosta, J.; Morales, E., *Solid State Ionics* **1996,** *85*, 85-90.

96. Fan, F.; Wang, Y.; Sokolov, A. P., *Macromolecules* **2013,** *46*, 9380-9389.

97. Khurana, R.; Schaefer, J. L.; Archer, L. A.; Coates, G. W., *J. Am. Chem. Soc.* **2014,** *136*, 7395-7402.

98. Soo, P. P., *J. Electrochem. Soc.* **1999,** *146*, 32-37.

99. Niitani, T.; Shimada, M.; Kawamura, K.; Dokko, K.; Rho, Y.-H.; Kanamura, K., *Electrochem. Solid-State Lett.* **2005,** *8*, A385.

100. Wei, X.; Shriver, D. F., *Chem. Mater.* **1998,** *10*, 2307-2308.

101. Fonseca, C. P.; Neves, S., *J. Power Sources* **2002,** *104*, 85-89.

102. Oh, B.; Vissers, D.; Zhang, Z.; West, R.; Tsukamoto, H.; Amine, K., *J. Power Sources* **2003,** *119-121*, 442-447.

103. Fuller, J., *J. Electrochem. Soc.* **1997,** *144*, 3881.

104. Welton, T., *Chem. Rev.* **1999,** *99*, 2071-2084.

105. Gido, S. P.; Lee, C.; Pochan, D. J.; Pispas, S.; Mays, J. W.; Hadjichristidis, N., *Macromolecules* **1996,** *29*, 7022-7028.

106. Fernicola, A.; Croce, F.; Scrosati, B.; Watanabe, T.; Ohno, H., *J. Power Sources* **2007,** *174*, 342-348.

107. Garcia, B.; Lavallée, S.; Perron, G.; Michot, C.; Armand, M., *Electrochim. Acta* **2004,** *49*, 4583-4588.

108. Matsumoto, H.; Sakaebe, H.; Tatsumi, K.; Kikuta, M.; Ishiko, E.; Kono, M., *J. Power Sources* **2006,** *160*, 1308-1313.

109. Scrosati, B.; Hassoun, J.; Sun, Y. K., *Energ Environ Sci* **2011,** *4*, 3287-3295.

110. Seki, S.; Kobayashi, Y.; Miyashiro, H.; Ohno, Y.; Usami, A.; Mita, Y.; Kihira, N.; Watanabe, M.; Terada, N., *J. Phys. Chem. B* **2006,** *110*, 10228-10230.

111. Howlett, P. C.; MacFarlane, D. R.; Hollenkamp, A. F., *Electrochem. Solid-State Lett.* **2004,** *7*, A97-A101.

112. Shin, J.-H.; Henderson, W. A.; Passerini, S., *Electrochem. Commun.* **2003,** *5*, 1016-1020.

113. Buzzeo, M. C.; Evans, R. G.; Compton, R. G., *ChemPhysChem* **2004,** *5*, 1106-1120.

114. Fuller, J.; Carlin, R. T.; Osteryoung, R. A., *J. Electrochem. Soc.* **1997,** *144*, 3881-3886.

115. Thomas, K. E.; Sloop, S. E.; Kerr, J. B.; Newman, J., *J. Power Sources* **2000,** *89*, 132-138.

116. Rosso, M.; Brissot, C.; Teyssot, A.; Dollé, M.; Sannier, L.; Tarascon, J.-M.; Bouchet, R.; Lascaud, S., *Electrochim. Acta* **2006,** *51*, 5334-5340.

117. Doyle, M.; Fuller, T. F.; Newman, J., *Electrochim. Acta* **1994,** *39*, 2073-2081.

118. Hekselman; Kalita, M.; Plewa-Marczewska, A.; Żukowska, G. Z.; Sasim, E.; Wieczorek, W.; Siekierski, M., *Electrochim. Acta* **2010,** *55*, 1298-1307.

119. Mathews, K. L.; Budgin, A. M.; Beeram, S.; Joenathan, A. T.; Stein, B. D.; Werner-Zwanziger, U.; Pink, M.; Baker, L. A.; Mahmoud, W. E.; Carini, J. P.; Bronstein, L. M., *J. Mater. Chem. A* **2013,** *1*, 1108-1116.

120. Stephan, A. M.; Prem Kumar, T.; Angulakshmi, N.; Salini, P. S.; Sabarinathan, R.; Srinivasan, A.; Thomas, S., *J. Appl. Polym. Sci.* **2011,** *120*, 2215-2221.

121. Blazejczyk, A.; Szczupak, M.; Wieczorek, W.; Cmoch, P.; Appetecchi, G. B.; Scrosati, B.; Kovarsky, R.; Golodnitsky, D.; Peled, E., *Chem. Mater.* **2005,** *17*, 1535-1547.

122. Tsuchida, E.; Ohno, H.; Kobayashi, N.; Ishizaka, H., *Macromolecules* **1989,** *22*, 1771-1775.

123. Bannister, D. J.; Davies, G. R.; Ward, I. M.; McIntyre, J. E., *Polymer* **1984,** *25*, 1291-1296.

124. Huang, X., *Solid State Ionics* **1992,** *51*, 69-73.

125. Zhang, S.; Deng, Z.; Wan, G., *Polym. J.* **1991,** *23*, 73-78.

126. Ito, K.; Nishina, N.; Ohno, H., *J. Mater. Chem.* **1997,** *7*, 1357-1362.

127. Park, C. H.; Sun, Y.-K.; Kim, D.-W., *Electrochim. Acta* **2004,** *50*, 375-378.

128. Doyle, R. P.; Chen, X.; Macrae, M.; Srungavarapu, A.; Smith, L. J.; Gopinadhan, M.; Osuji, C. O.; Granados-Focil, S., *Macromolecules* **2014,** *47*, 3401-3408.

129. Sun, X.-G.; Hou, J.; Kerr, J. B., *Electrochim. Acta* **2005,** *50*, 1139-1147.

130. Snyder, J. F.; Hutchison, J. C.; Ratner, M. A.; Shriver, D. F., *Chem. Mater.* **2003,** *15*, 4223-4230.

131. Watanabe, M.; Suzuki, Y.; Nishimoto, A., *Electrochim. Acta* **2000,** *45*, 1187-1192.

132. Herath, M. B.; Creager, S. E.; Rajagopal, R. V.; Geiculescu, O. E.; DesMarteau, D. D., *Electrochim. Acta* **2009,** *54*, 5877-5883.

133. Feng, S.; Shi, D.; Liu, F.; Zheng, L.; Nie, J.; Feng, W.; Huang, X.; Armand, M.; Zhou, Z., *Electrochim. Acta* **2013,** *93*, 254-263.

134. Bouchet, R.; Maria, S.; Meziane, R.; Aboulaich, A.; Lienafa, L.; Bonnet, J. P.; Phan, T. N. T.; Bertin, D.; Gigmes, D.; Devaux, D.; Denoyel, R.; Armand, M., *Nat. Mater.* **2013,** *12*, 452-457.

135. Rojas, A. A.; Inceoglu, S.; Mackay, N. G.; Thelen, J. L.; Devaux, D.; Stone, G. M.; Balsara, N. P., *Macromolecules* **2015,** *48*, 6589-6595.

136. Liang, S.; Choi, U. H.; Liu, W.; Runt, J.; Colby, R. H., *Chem. Mater.* **2012,** *24*, 2316-2323.

137. Armand, M. B., *Annu. Rev. Mater. Sci.* **1986,** *16*, 245-261.

138. Tokuda, H.; Muto, S.; Hoshi, N.; Minakata, T.; Ikeda, M.; Yamamoto, F.; Watanabe, M., *Macromolecules* **2002,** *35*, 1403-1411.

139. Wang, Y.; Sokolov, A. P., *Curr. Opin. Chem. Eng.* **2015,** *7*, 113-119.

140. Ghosh, A.; Wang, C.; Kofinas, P., *J. Electrochem. Soc.* **2010,** *157*, A846-A849.

141. Doyle, M.; Fuller, T. F.; Newman, J., *J. Electrochem. Soc.* **1993,** *140*, 1526-1533.

142. Bruce, P. G., *Electrochim Acta* **1995,** *40*, 2077-2085.

143. Ngai, K. S.; Ramesh, S.; Ramesh, K.; Juan, J. C., *Ionics* **2016,** *22*, 1259-1279.

144. MacGlashan, G. S.; Andreev, Y. G.; Bruce, P. G., *Nature* **1999,** *398*, 792-794.

145. Agapov, A. L.; Sokolov, A. P., *Macromolecules* **2011,** *44*, 4410-4414.

146. Wang, Y.; Agapov, A. L.; Fan, F.; Hong, K.; Yu, X.; Mays, J.; Sokolov, A. P., *Phys. Rev. Lett.* **2012,** *108*, 088303.

147. Wang, Y.; Fan, F.; Agapov, A. L.; Saito, T.; Yang, J.; Yu, X.; Hong, K.; Mays, J.; Sokolov, A. P., *Polymer* **2014,** *55*, 4067-4076.

148. Fan, F.; Wang, W.; Holt, A. P.; Feng, H.; Uhrig, D.; Lu, X.; Hong, T.; Wang, Y.; Kang, N.-G.; Mays, J.; Sokolov, A. P., *Macromolecules* **2016,** *49*, 4557-4570.

149. Kumar, R.; Goswami, M.; Sumpter, B. G.; Novikov, V. N.; Sokolov, A. P., *PCCP* **2013,** *15*, 4604-4609.

150. Wang, Y.; Fan, F.; Agapov, A. L.; Yu, X.; Hong, K.; Mays, J.; Sokolov, A. P., *Solid State Ionics* **2014,** *262*, 782-784.

151. Holt, A. P.; Sangoro, J. R.; Wang, Y.; Agapov, A. L.; Sokolov, A. P., *Macromolecules* **2013,** *46*, 4168-4173.

152. Andreev, Y. G.; Seneviratne, V.; Khan, M.; Henderson, W. A.; Frech, R. E.; Bruce, P. G., *Chem. Mater.* **2005,** *17*, 767-772.

153. Gadjourova, Z.; Andreev, Y. G.; Tunstall, D. P.; Bruce, P. G., *Nature* **2001,** *412*, 520-523.

154. Yang, R. T., *Gas separation by adsorption processes*. Butterworth-Heinemann: 2013.

155. Pires, J.; Martins, F.; Alvim-Ferraz, M.; Simões, M., *Chem. Eng. Res. Des.* **2011,** *89*, 1446-1460.

156. Robeson, L. M., *J. Membr. Sci.* **1991,** *62*, 165-185.

157. Powell, C. E.; Qiao, G. G., *J. Membr. Sci.* **2006,** *279*, 1-49.

158. Kentish, S. E.; Scholes, C. A.; Stevens, G. W., *Recent Pat. Chem. Eng.* **2008,** *1*, 52-66.

159. Xu, X.; Song, C.; Andresen, J. M.; Miller, B. G.; Scaroni, A. W., *Energy Fuels* **2002,** *16*, 1463-1469.

160. Zhang, Z.; Zhao, Y.; Gong, Q.; Li, Z.; Li, J., *Chem. Commun.* **2013,** *49*, 653-661.

161. Lau, C. H.; Babarao, R.; Hill, M. R., *Chem. Commun.* **2013,** *49*, 3634-3636.

162. Sumida, K.; Rogow, D. L.; Mason, J. A.; McDonald, T. M.; Bloch, E. D.; Herm, Z. R.; Bae, T.-H.; Long, J. R., *Chem. Rev.* **2011,** *112*, 724-781.

163. Pfaff, I.; Kather, A., *Energy Procedia* **2009,** *1*, 495-502.

164. Yu, C.-H.; Huang, C.-H.; Tan, C.-S., *Aerosol Air Qual. Res* **2012,** *12*, 745-769.

165. Bara, J. E.; Gabriel, C. J.; Lessmann, S.; Carlisle, T. K.; Finotello, A.; Gin, D. L.; Noble, R. D., *Ind. Eng. Chem. Res.* **2007,** *46*, 5380-5386.

166. Robeson, L. M., *J. Membr. Sci.* **2008,** *320*, 390-400.

167. Leung, D. Y.; Caramanna, G.; Maroto-Valer, M. M., *Renewable Sustainable Energy Rev.* **2014,** *39*, 426-443.

168. Car, A.; Stropnik, C.; Yave, W.; Peinemann, K. V., *Adv. Funct. Mater.* **2008,** *18*, 2815-2823.

169. Yave, W.; Car, A.; Funari, S. S.; Nunes, S. P.; Peinemann, K.-V., *Macromolecules* **2009,** *43*, 326-333.

170. Gmernicki, K. R.; Hong, E.; Maroon, C. R.; Mahurin, S. M.; Sokolov, A. P.; Saito, T.; Long, B. K., *ACS Macro Letters* **2016,** *5*, 879-883.

171. McKeown, N. B.; Budd, P. M., *Chem. Soc. Rev.* **2006,** *35*, 675-683.

172. Zhang, L.; Xu, N.; Li, X.; Wang, S.; Huang, K.; Harris, W. H.; Chiu, W. K., *Energ Environ Sci* **2012,** *5*, 8310-8317.

173. Songolzadeh, M.; Soleimani, M.; Takht Ravanchi, M.; Songolzadeh, R., *Sci. World J.* **2014,** *2014*.

174. Masuda, T.; Isobe, E.; Higashimura, T., *Macromolecules* **1985,** *18*, 841-845.

175. Wang, X.-Y.; Willmore, F. T.; Raharjo, R. D.; Wang, X.; Freeman, B. D.; Hill, A. J.; Sanchez, I. C., *J. Phys. Chem. B* **2006,** *110*, 16685-16693.

176. Merkel, T. C.; Lin, H. Q.; Wei, X. T.; Baker, R., *J. Membr. Sci.* **2010,** *359*, 126-139.

177. Bartlett, M.; Bird, M.; Howell, J., *J. Membr. Sci.* **1995,** *105*, 147-157.

178. Robeson, L. M., *Curr. Opin. Solid State Mater. Sci.* **1999,** *4*, 549-552.

179. Du, N.; Park, H. B.; Robertson, G. P.; Dal-Cin, M. M.; Visser, T.; Scoles, L.; Guiver, M. D., *Nat. Mater.* **2011,** *10*, 372-375.

CHAPTER 2 Synthetic Methodology and Characterization

Abstract

Living/controlled polymerization techniques facilitate the preparation of well-defined/ controlled polymers with precisely controlled compositions and architectures. On the other hand, the combination of these techniques with post-polymerization functionalization helps polymer chemists to obtain a wide range of functional polymers. This chapter will briefly describe the experimental techniques employed in this dissertation including living anionic polymerization, living cationic ring opening polymerization and hydrosilylation. In addition, the most commonly used characterization techniques will be discussed.

2.1 Introduction

A wide variety of polymerization techniques facilitate the development of both polymer chemistry and polymer physics because they realize the preparation of well-defined polymers with precisely controlled molecular weight, defined molecular architectures and nanoscale morphologies.[1-5] These techniques, especially living anionic polymerization (LAP) have also been utilized in industry for mass production of several important commercial products.[6-7]

Post polymerization modification are usually performed using reactions that have high efficiency, facial experiment setup and high selectivity.[8] The combination of living/controlled polymerization techniques and post-polymerization modifications has helped chemists to develop a wide range of functional materials including: chain end and pendant-functional polymers; block copolymers and micelles; complex architectures such as star, brush, graft, hyperbranched, and dendritic polymers; gels and networks; and polymers conjugated to nanomaterials.[9-13] For instance, the hydrosilylation reaction is commonly used to modify polysiloxanes. There are other polymerization techniques and modification reactions. However, these are beyond the scope of this thesis.

This chapter described the polymerization methodology that was employed in this thesis including living anionic polymerization (LAP) and living cationic ring-opening polymerization (LCROP). High vacuum techniques and representative purification procedures for common monomer, initiators, solvents and terminators are also presented.

The corresponding polymerization mechanisms are briefly explained followed by the discussion of hydrosilylation.

2.2 Synthetic Methodology and Experimental Techniques

2.2.1 Living Anionic Polymerization and High Vacuum Techniques

The pioneering work on living anionic polymerization was reported by Szwarc in 1956.[14-15] The propagating species are anionic ion pairs and/or free ions depending on the reaction media.[16] It is a type of chain growth polymerization without termination or chain transfer. The reactivity of chain end carbanion is preserved and therefore it can initiate freshly added monomer. Over the last 60 years, it has been proved that LAP is the most appropriate method for the synthesis of polymers with predictable molecular weight and well-defined architectures.[17-18] These polymers have not only served as perfect templates for structure-property relationship studies but have also been employed as important commercial products.[19-22] For example, Mays *et al.* developed novel super thermoplastic elastomers using multi-grafted copolymers via the combination of LAP and emulsion polymerization.[23-24] Wang *et al.* reported a novel synthetic approach to polymerize benzofulvene in hydrocarbon solvent and successfully raised the upper service temperature of the resulting polybenzofulvene–polyisoprene–polybenzofulvene elastomer almost 50°C.

The initiator required to polymerize a monomer is largely dependent on the reactivity of the monomer toward the nucleophilic attack. Monomer reactivity increases

with increasing ability to stabilize carbanion.[16] For the polymerization of dienes, the most commonly used initiators are alkyllithiums. The molecular weight of obtained polymers can be precisely controlled by monomer/initiator ratio.

However, in the case of polar monomers, such as methyl methacrylate (MMA), acrylonitrile (AN), these polar moiety (ester, nitrile) are susceptible to nucleophilic attack during initiation or propagation, leading to termination and complicated side reactions. This results in uncontrollable molecular weight and difficulties in achieving living polymerization.[25] For example, in the polymerization of methyl methacrylate, MMA was converted into isopropenyl alkyl ketone. Nucleophilic substitution by intramolecular backbiting of a propagating carbanion on monomer, leading to the abstraction of α-hydrogen of acrylate monomers by initiator, also leads to serious side reactions.

The effort to minimize the side reactions includes control of temperature, solvent and the addition of ligands to achieve LAP with narrow PDI.[26] The main strategy to minimize side reactions is through addition of ligands. Efficient ligands include metal alkoxides, inorganic salts, alkyl aluminum and crown ethers. These ligands are capable of coordinating with propagating anion center and/or counter ion to minimize or even eliminate the side reactions during propagation. We will employ these strategies to achieve the living polymerization of 2-isopropenyl-2-oxazoline, which will be discussed in chapter 5.

Due to the high sensitivity to impurities, the purification of monomers, initiators, additives, and terminators is critical. There are mainly two techniques to perform LAP:

Schlenk techniques and high vacuum techniques. Schlenk techniques involve an inert gas, vacuum pump and a three-way valve. This technique is attractive to most researchers due to its convenience and acceptable performance for many applications. On the other hand, high vacuum techniques require highly-demanding experimental skills and glass-blowing. It is time-consuming, however, is the best method to prepare model macromolecules with complex architectures.[27-28] A typical high vacuum manifold assembly consists of a mechanical vacuum pump, an oil diffusion pump (mercury diffusion pump is also used, however, with the concern of highly toxic nature of mercury), a liquid nitrogen trap, an upper glass tube rig, and a lower glass tube rig (Figure 2.1). The mechanical pump reduces the system pressure down to 10^{-2}-10^{-3} mbar. The pressure can be further lowered to high vacuum level (10^{-5} to 10^{-7} mbar) when the oil in the connected diffusion pump starts to reflux. It is also mandatory to place a liquid nitrogen trap between diffusion pump and high vacuum manifold to condense any volatile chemicals and prevent damaging refluxing oil in the diffusion pump. The manifold contains upper and lower rigs with Teflon stopcocks so that different experimental procedures such as short-path distillation, degassing can be performed simultaneously. Although mastery of glassblowing and highly demanding experimental techniques are required, LAP achieved via high vacuum techniques are the most reliable experimental tools for preparing polymer samples with well-defined and complex macromolecular architectures.[29] The typical purification and polymerization procedures are described as follows.

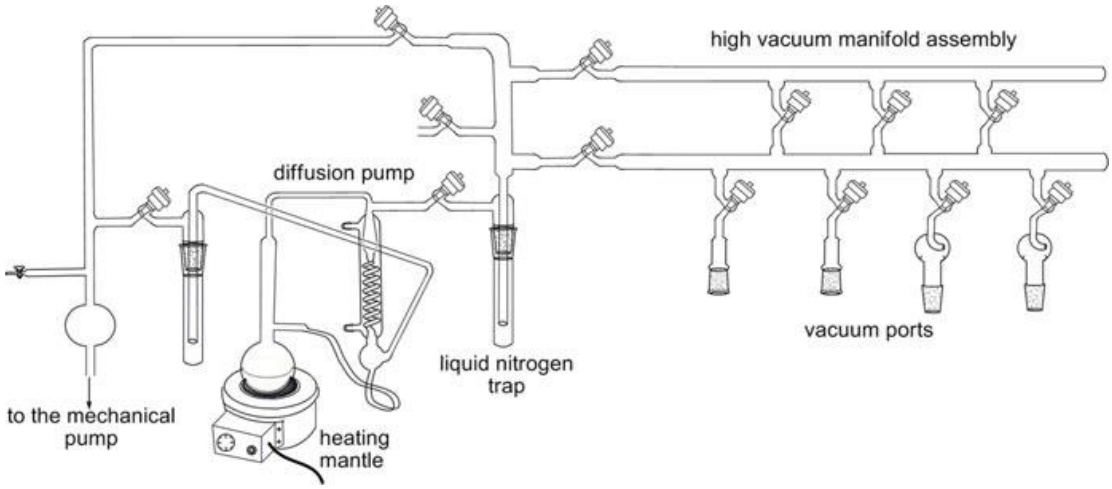

Figure 2.1. The scheme of high vacuum line. Reprinted from ref.[30].

THF is the most commonly used solvent for LAP of polar monomers. The purification procedure is described as follows. THF from a commercial source is first distilled over CaH_2 under high vacuum using the set-up as illustrated in Figure 2.2. The collected THF was then charged into a flask with Na/naphthalene. The flask was then attached to the high vacuum line, degassed. After stirring, the appearance of a dark green color indicates the THF is free of impurities (Figure 2.3).

For monomers, distillation over CaH_2 only usually does not provide high enough purity. Further purification over organometallic agent e.g. alkyl lithium, dibutyl magnesium or diethyl zinc is required. The apparatus is shown in Figure 2.4. Methanol is the most frequently used terminating agent for anionic polymerization. A typical purification method is described as follows. Methanol is added to an apparatus attached to the vacuum line and then stirred with CaH_2 over night. After degassing, the methanol was then distilled into ampoules with break-seals and stored in the freezer at -30°C. Depending on the selection of solvents, the shape of reactors also varies. For the polymerization in no polar solvent such as benzene, n-hexane, a typical round bottom reactor is commonly used as depicted in Figure 2.5A. On the other hand, a tubular reactor is preferred when polymerization in THF (Figure 2.5B).

2.2.2 Living Cationic Ring Opening Polymerization.

Heterocyclic monomers with sufficient strain such as cyclic ethers, cyclic esters (lactones), cyclic acetals, cyclic amides (lactams), cyclic iminoethers, cyclic sulfides and cyclic phosphazenes are capable of ring opening polymerization.[33-37] For rings without

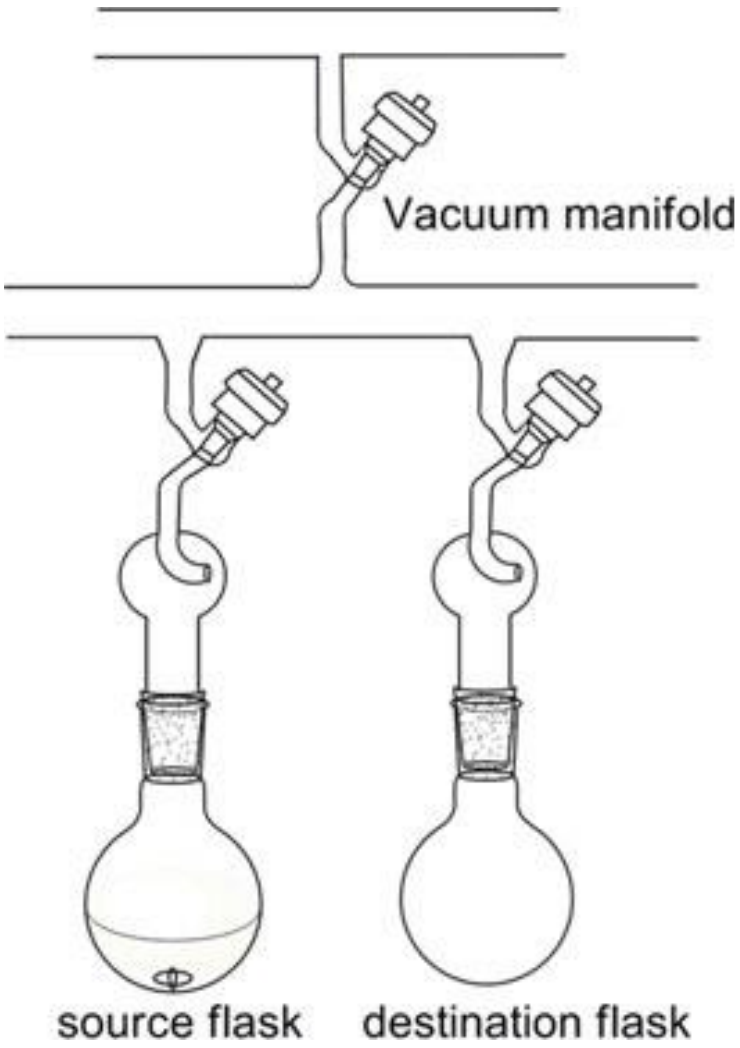

Figure 2.2. Distillation setup on a high vacuum line.

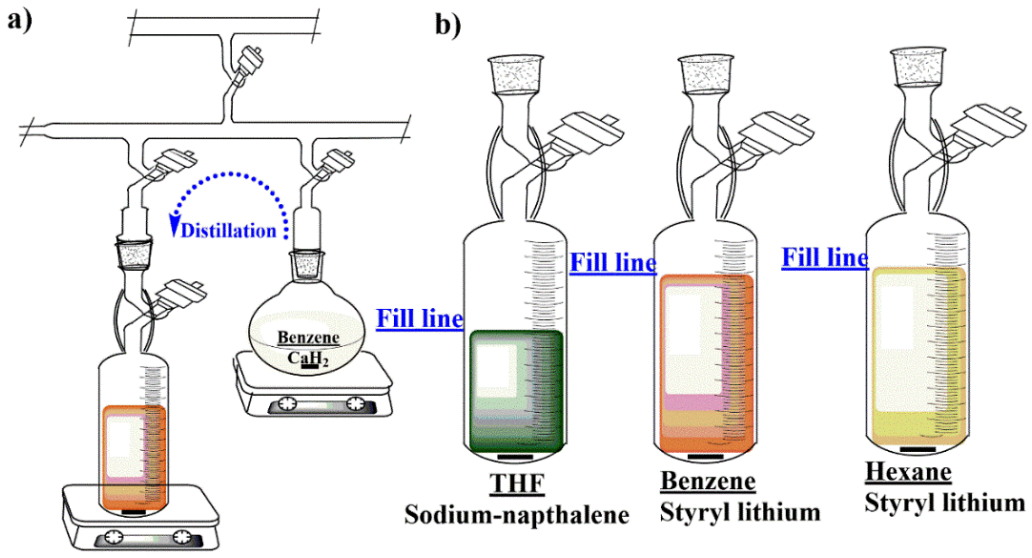

Figure 2.3. Purification of THF, benzene, and hexane. (The color of reservoir indicates the purity of the solvent). Reprinted from ref.[31]

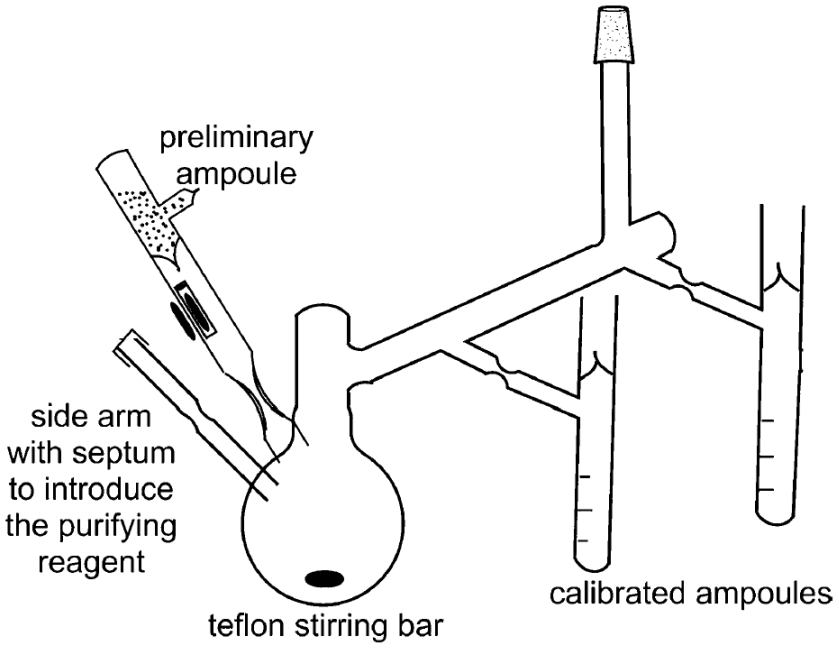

Figure 2.4. Short path distillation apparatus for further purification.

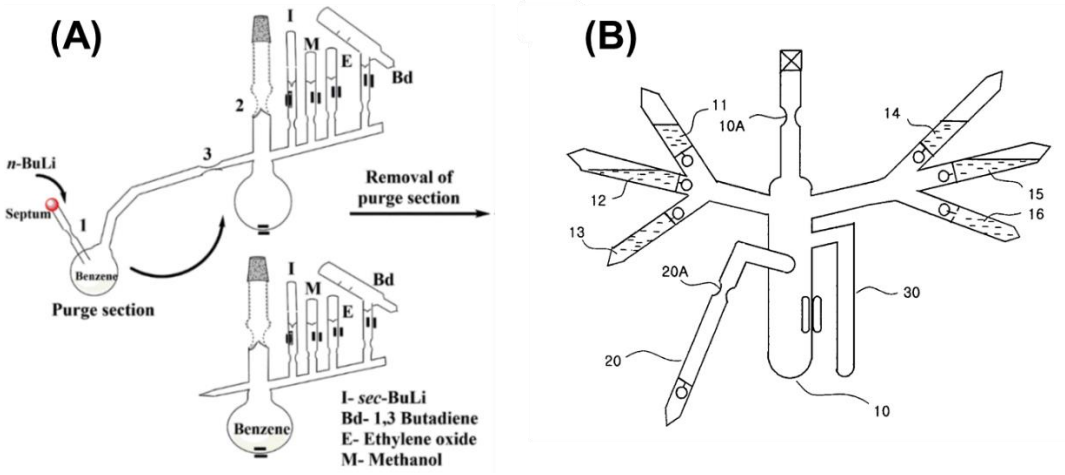

Figure 2.5. (A) Polymerization reactor in nonpolar solvent. (B) tubular reactor for polymerization in THF. Reprinted from ref.[31-32]

enough ring strain, polymerization could also occur driven by the increased entropy of linear chains.[38] Cationic ring opening polymerization is a powerful approach to prepare important industrial materials, e.g. polynorbornene, polyethylene oxide, polysiloxane and polyphosphazene.

And recently, polylactides are becoming an important bio-degradable packing material. CROP can be initiated by Brönsted acids, oniumions and carbenium ions. The propagating chain end usually contains a carbocation and acts as the reactive center for the incoming monomer.

2-Substituted-2-oxazoline is a well-known monomer that can undergo cationic ring opening polymerization (CROP) in a living manner to produce poly(N-acylethylenimines) (POxs). This type of polymers have been recognized as material of importance in surface chemistry and biomaterial sciences such as nonionic surfactants, protein modifiers, hydrogels and drug carriers.[17, 39] Moreover, several POxs have been approved by US Food and Drug Administration.[40] Among them poly(2-ethyl-2-oxazoline) exhibits improved biocompatibility comparable with conventional poly ethylene glycol.[39] It also should be noted that POx is the only route to prepare linear polyethyleneimine (PEI) via hydrolysis because the polymerization of ethyleneimine only yields highly branched and cyclic PEI.[41]

The propagation step involves the nucleophilic attack of the electron lone pairs from the nitrogen atom of the incoming monomer on C5 position of oxazolium ring of the living

chain end as shown in Scheme 2.1.

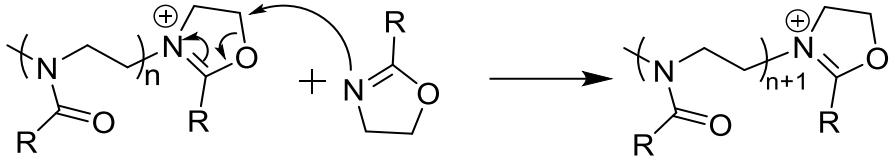

Scheme 2.1. Propagation step of cationic ring opening polymerization of 2-substituted-2-oxazoline.

The propagation rate varies depending on the R group, solvents and reaction temperatures. For example, polymerization of 2-ethyl-2-oxazoline could reach 100% in acetonitrile using methyl trifluoromethanesulfonate as initiator within 12 h.[40] However, it takes more than 20 days to polymerize 2-isopropyl-2-oxazoline.[42] Schubert *et al.* demonstrated that using microwave irradiation the polymerization time could be reduced significantly form 6 h (conventional heating at 82 °C) down to less than 1 min.[43]

Solvents that are suitable for cationic ring opening polymerization must be stable under polymerization conditions. Very recently, ionic liquids are also used under microwave irradiation. Polymerization of 2-ethyl-2-oxazoline in 1-butyl-3-methyl-imidazolium hexafluorophosphate (B3Imi-PF_6) showed a faster reaction rate. It was revealed that (B3Imi-PF_6) can lower the activation energy for CROP of EtOx relative to polymerization in acetonitrile.[44]

Polysiloxane, industrially known as silicone, is an important inorganic polymer. They have good thermal, chemical resistance and low toxicity making them applied in a

wide range of applications such as surfactants, adhesives, medicine and thermal insulation.[45-46] They can be prepared via either condensation polymerization or ring opening polymerization (Scheme 2.2). Compared with condensation polymerization, ring opening polymerization (ROP) of cyclic silicone monomers (hexamethylcyclotrisiloane (D3) and octamethylcyclotetrasiloxane (D4) are the most commonly used monomers to prepare polydimethylsiloxanes) can produce high molecular weight polysiloxanes.[47-48]

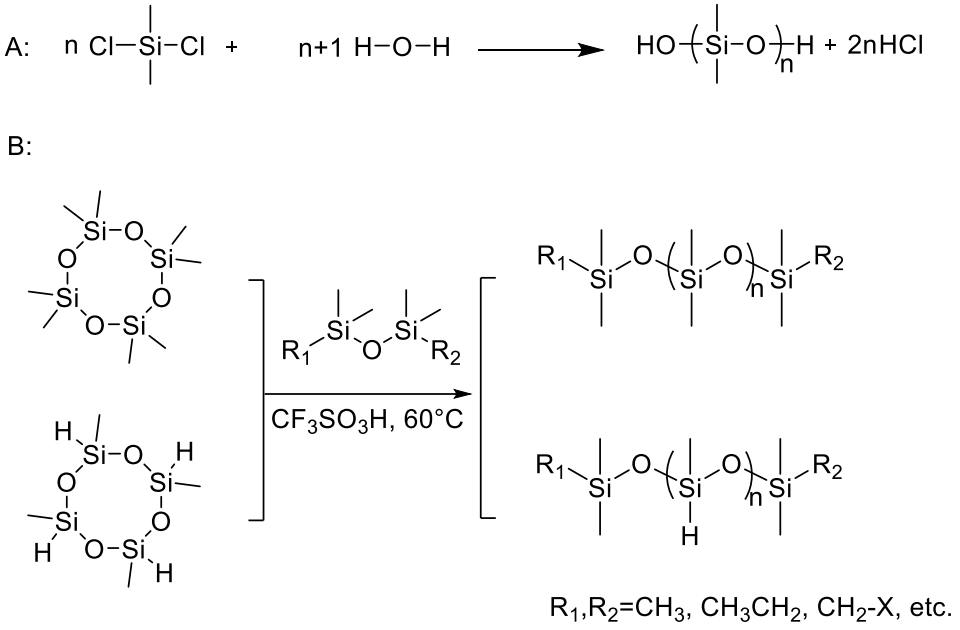

Scheme 2.2. The synthetic route for the preparation of polydimethylsiloxane via (A) condensation polymerization and (B) ring opening polymerization.

2.2.3 Hydrosilylation

Hydrosilylation is one of the most important reactions to modify polysiloxanes. It is the reaction of addition of silicon hydride (Si-H) across multiple bonds including carbon-carbon and carbon-heteroatom as well as heteroatom-heteroatom bonds. Hydrosilylation of C=C bonds is the most versatile approach for the formation of Si-C bond (Scheme 2.3).

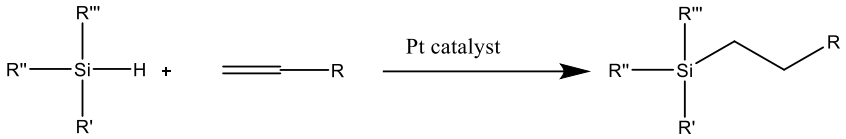

Scheme 2.3. General hydrosilylation reaction between Si-H and alkene.

It was first reported by Leo Sommer in 1947 through a radical initiator. Metal complexes based on platinum precursor ($H_2PtCl_6 \cdot H_2O$) has been the most studied catalyst in academia and industrial syntheses.[49-50] In the past few decades, many new Pt (0) and Pt(II) complexes with various ligands and activators such as dienes, norbornenes and cycloolefins have been prepared.[49, 51]

The most commonly used catalysts are: Speier's catalyst, which is the solution of $H_2PtCl_6 \cdot H_2O$ in isopropyl alcohol (1-10%); Karstedt's catalyst, which was obtained by treating Speier's catalyst with vinyl siloxane. Compared with Speier's catalyst, Karstedt's (Scheme 2.4) catalyst have been utilized in industry for decades to prepare functionalized silicone product due to their high selectivity, high activity and high stability to heat and oxygen.

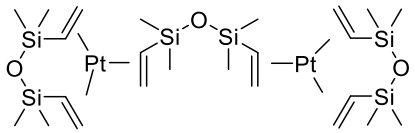

Scheme 2.4. Karstedt's catalyst.

Many reviews and literature papers have reported the mechanism of catalysis of hydrosilylation by Pt metal complexes. The generally accepted mechanism is shown in Scheme 2.5.

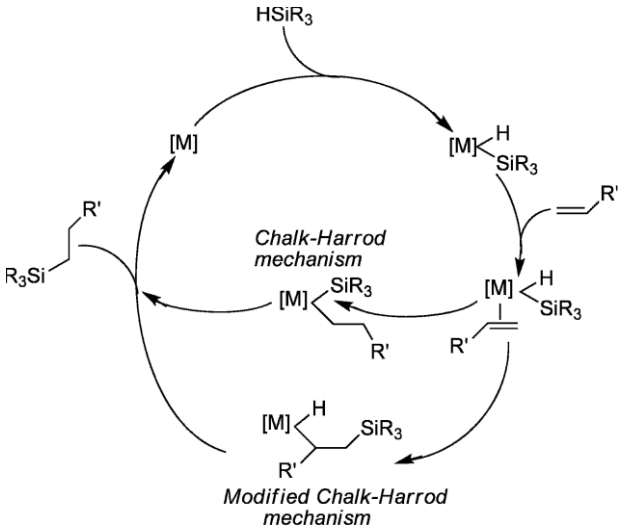

Scheme 2.5. The mechanism for catalysis of hydrosilylation of olefins proposed by Chalk-Harrod.[52]

Unfortunately, there are also several known disadvantages. One of them is that certain functionalities such as hydroxyl, amino groups will react with Si-H under the hydrosilylation conditions and therefore need to be protected before the reaction.[53] Amino

group also forms complex with the Pt catalyst and eventually inhibit the reaction. The formation of platinum during the reaction leads to the contamination of products. The residual platinum could also act as catalyst causing serious side reactions in some cases.[54] The reaction system must be kept anhydrous in order to prevent undesired crosslinking. It was also reported that addition of small amounts of anhydrous O_2 to the reaction mixture could reduce platinum aggregation.[55]

2.3 Characterization

2.3.1 Molecular Weight Characterization

Size exclusion chromatograph (SEC) is a method of separation based on the molecular size or hydrodynamic volume. This method first appeared in the late 1950s. One important breakthrough in SEC was the combination with online detectors, especially viscometers and light scattering detectors.[56-59] Since then, SEC has been one of the most powerful instruments in characterizing molecular weights (MWs) and molecular weight distributions (MWDs) of macromolecules. For a typical measurement, polymer sample is dissolved in an appropriate solvent, and then injected into the SEC column with defined pores sizes. As the polymer elutes through the column, polymers that are too large for the pore size tend to elute out early. As the polymer size approaches the column pore size, it will partition into the pores and retain more time, therefore elute out lately. Figure 2.6 depicts the cross section view of pores and macromolecules. The intrinsic viscosity [η] is

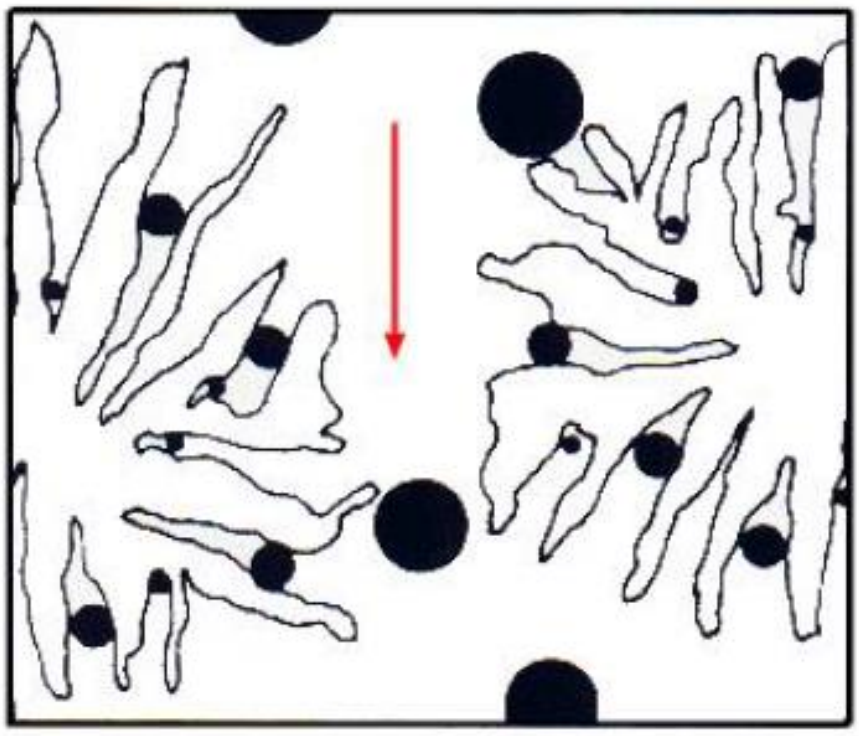

Figure 2.6. Illustration of partition behavior of a particle pass through column pores.

another fundamental property of polymers in dilute solution and has been widely used as a convenient means for determining the molecular weight, size, and topological structure of polymers in material, engineering, and biology.[60-61]

The first molecular theory of viscosity dates back to Einstein who calculated the viscosity of a dilute suspension of impermeable spheres.[62] The relationship between intrinsic viscosity of polymers and molecular weights can be elucidated by the empirical Mark−Houwink−Sakurada (MHS) equation,

$$[\eta] = KM^{\alpha}$$

where M is the molecular weight and K and α are constants for a given polymer−solvent pair. α in the MHS equation for linear polymers is a constant between 0.5 and 1,[60] while for some randomly hyper-branched polymers it is significantly less than 0.5 and varies with molecular weight.

Intrinsic viscosity can be deduced by measuring the flow time of a dilute polymer solution through a glass capillary. We can further use either the Huggins equation, which is derived from a virial expansion of the specific viscosity in powers of the intrinsic viscosity, or the Kraemer equation, which results from an expansion of the inherent viscosity, to determine the intrinsic viscosity.

In Huggins equation, the specific viscosity is related to the intrinsic viscosity by a power series of the form:

$$\eta_{sp} = k_0 [\eta]c + k_1 [\eta] c^2 + k_2 [\eta] c^3 + \ldots$$

Where k_0, k_1, K_2... are dimensionless coefficients, and $k_0 = 1$. Huggins equation can be formed by dividing concentration c, and keep the second term, Huggins equation was formed as

$$\frac{\eta_{sp}}{c} = [\eta] + k_H[\eta]^2 c$$

The Huggins constant k_H has values ranging from 0.3 in good solvents to 0.5 in poor solvents. Intrinsic viscosity can be obtained by extrapolating to zero concentration. In Kraemer equation, we have

$$\frac{\ln(\eta_r)}{c} = [\eta] - k_K[\eta]^2 c$$

Combining equation (2) and (3), the intrinsic viscosity is calculated using following equations:

$$[\eta] = \lim_{c\to 0} \frac{\ln \eta_r}{c} = \lim_{c\to 0} \frac{\eta_{sp}}{c}$$

Where $\eta_r = \frac{t}{t_0}$, $\eta_{sp} = \eta_r - 1$.

Dynamic light scattering (DLS) is one of the most popular techniques to characterize particle size and particle size distribution in emulsions, micelles, polymers and nanoparticles.[63] By measuring the time-dependent fluctuations of scattered light, a photo correlation function can be generated. Different mathematical approaches can be applied to determine the information in it. The simplest method is to use the correlation function as a single exponential decay as follows:

$$\Gamma = D_T q^2$$

$$q = \frac{4\pi}{\lambda} \sin\left(\frac{\theta}{2}\right), \lambda = \frac{\lambda_0}{n_0}$$

Where D_T is the translational diffusion coefficient of the analyte and q is the scattering vector. And hydrodynamic radius R_h can be calculated by

$$R_h = \frac{k_B T}{6\pi\eta_s D_T}$$

2.3.2 Thermal Properties Characterization

Differential scanning calorimetry (DSC) is a technique in which the difference in the amount of heat required or released to change the temperature of a sample at a constant rate is recorded. When the sample undergoes a thermal transition, different amounts of heat will be needed to flow to it comparing with the reference to maintain them both at the same temperature. DSC is able to measure the amount of heat absorbed or released during such transition. This technique was first developed by E.T. Watson and M.J. O'Neill in 1962.[64] There are mainly two types of DSC, power compensated DSC in which the power supply is kept constant and heat flux DSC in which the heat flux is constant. DSC is a common technique to examine the thermal transitions like glass transition temperatures, melting points and crystallinity of polymeric materials. A typical DSC profile of polyethylene terephthalate (PET) is shown in Figure 2.7.

Thermogravimetric analysis (TGA) is a method of thermal analysis used to determine characteristics of materials that exhibit either mass loss or gain due to decomposition, oxidation, or loss of volatiles as a function of increasing temperature, or as a function of time.[65] TGA has two major components, a precision balance with a pan loaded

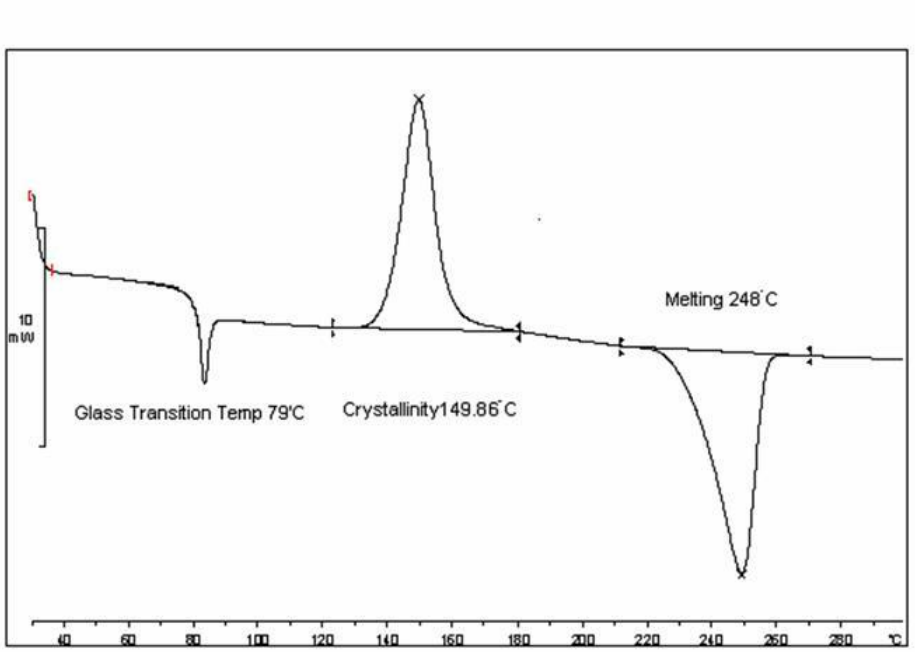

Figure 2.7. Representative DSC curve of semi-crystal PET.

and a programmable furnace, which can be programmed either for a constant heating rate, or for heating at a constant temperature.

It is an important technique in characterization of material decomposition, degradation mechanisms and reaction kinetics. For example, Baskaran *et al.* used TGA to analyze the quantity of the initiator attached to the surface of carbon nanotubes.[66]

2.4 References

1. Braunecker, W. A.; Matyjaszewski, K., *Prog. Polym. Sci.* **2007,** *32*, 93-146.

2. Gido, S. P.; Lee, C.; Pochan, D. J.; Pispas, S.; Mays, J. W.; Hadjichristidis, N., *Macromolecules* **1996,** *29*, 7022-7028.

3. Theodosopoulos, G. V.; Hurley, C. M.; Mays, J. W.; Sakellariou, G.; Baskaran, D., *Polym. Chem.* **2016,** *7*, 4090-4099.

4. Zhang, H.; Hong, K.; Mays, J. W., *Macromolecules* **2002,** *35*, 5738-5741.

5. Sikka, M.; Schneider Jr, J. W.; Tsao, Y.-H.; Tirrell, M.; Mays, J. W., *Macromolecules* **1995,** *28*, 3125-3134.

6. Morton, M., *Rubber technology*. Springer Science & Business Media: 2013.

7. Fink, J. K., *High performance polymers*. William Andrew: 2014.

8. Gauthier, M. A.; Gibson, M. I.; Klok, H. A., *Angew. Chem. Int. Ed. Engl.* **2009,** *48*, 48-58.

9. Golas, P. L.; Matyjaszewski, K., *Chem. Soc. Rev.* **2010,** *39*, 1338-54.

10. Pitsikalis, M.; Pispas, S.; Mays, J. W.; Hadjichristidis, N., Nonlinear block copolymer architectures. In *Blockcopolymers-Polyelectrolytes-Biodegradation*, Springer: 1998; pp 1-137.

11. Sakellariou, G.; Ji, H.; Mays, J. W.; Baskaran, D., *Chem. Mater.* **2008,** *20*, 6217-6230.

12. Bobade, S.; Wang, Y.; Mays, J.; Baskaran, D., *Macromolecules* **2014,** *47*, 5040-5050.

13. Pochan, D. J.; Gido, S. P.; Pispas, S.; Mays, J. W.; Ryan, A. J.; Fairclough, J. P. A.; Hamley, I. W.; Terrill, N. J., *Macromolecules* **1996,** *29*, 5091-5098.

14. Szwarc, M., *Nature* **1956,** *178*, 1168-1169.

15. Szwarc, M.; Levy, M.; Milkovich, R., *J. Am. Chem. Soc.* **1956,** *78*, 2656-2657.

16. Hadjichristidis, N.; Iatrou, H.; Pitsikalis, M.; Mays, J., *Prog. Polym. Sci.* **2006,** *31*, 1068-1132.

17. Feng, H.; Changez, M.; Hong, K.; Mays, J. W.; Kang, N.-G., *Macromolecules* **2017,** *50*, 54-62.

18. Wang, W.; Schlegel, R.; White, B. T.; Williams, K.; Voyloy, D.; Steren, C. A.; Goodwin, A.; Coughlin, E. B.; Gido, S.; Beiner, M., *Macromolecules* **2016,** *49*, 2646-2655.

19. Verduzco, R.; Botiz, I.; Pickel, D. L.; Kilbey, S. M.; Hong, K.; Dimasi, E.; Darling, S. B., *Macromolecules* **2011,** *44*, 530-539.

20. Zhu, Y.; Burgaz, E.; Gido, S. P.; Staudinger, U.; Weidisch, R.; Uhrig, D.; Mays, J. W., *Macromolecules* **2006,** *39*, 4428-4436.

21. Mays, J. W.; Uhrig, D.; Gido, S.; Zhu, Y.; Weidisch, R.; Iatrou, H.; Hadjichristidis, N.; Hong, K.; Beyer, F.; Lach, R. In *Synthesis and structure–property relationships for regular multigraft copolymers*, Macromolecular Symposia, Wiley Online Library: 2004; pp 111-126.

22. Youk, J. H.; Park, M.-K.; Locklin, J.; Advincula, R.; Yang, J.; Mays, J., *Langmuir* **2002,** *18*, 2455-2458.

23. Mays, J. W.; Gido, S. P.; Weidisch, R. Multigraft Copolymers as Superelastomers. U.S. 13/877,229, 2014.

24. Wang, W.; Wang, W.; Li, H.; Lu, X.; Chen, J.; Kang, N.-G.; Zhang, Q.; Mays, J., *Ind. Eng. Chem. Res.* **2015,** *54*, 1292-1300.

25. Efstratiadis, V.; Tselikas, G.; Hadjichristidis, N.; Li, J.; Yunan, W.; Mays, J. W., *Polym. Int.* **1994,** *33*, 171-179.

26. Baskaran, D., *Prog. Polym. Sci.* **2003,** *28*, 521-581.

27. Hong, K.; Uhrig, D.; Mays, J. W., *Curr. Opin. Solid State Mater. Sci.* **1999,** *4*, 531-538.

28. Uhrig, D.; Mays, J. W., *J. Polym. Sci., Part A: Polym. Chem.* **2005,** *43*, 6179-6222.

29. Uhrig, D.; Mays, J. W., *Macromolecules* **2002,** *35*, 7182-7190.

30. Ratkanthwar, K.; Hadjichristidis, N.; Mays, J., High vacuum techniques for anionic polymerization. In *Anionic Polymerization*, Springer: 2015; pp 19-59.

31. Bobade, S. L. Supramolecular Association of Hydrogen-bonded Polybutadienes Functionalized with Ureidopyrimidone. dissertation, University of Tennessee, 2014.

32. Lee, J.-S.; Rahman, S.; Samal, S.; Yoo, H.-S. Amphiphilic triblock copolymers comprising poly (2-vinylpyridine) block and poly (alkyl isocyanate) block, and the preparation method thereof. US7425593, 2008.

33. Ariga, T.; Takata, T.; Endo, T., *Macromolecules* **1997,** *30*, 737-744.

34. Nakatsubo, F.; Kamitakahara, H.; Hori, M., *J. Am. Chem. Soc.* **1996,** *118*, 1677-1681.

35. Kobayashi, S.; Uyama, H.; Narita, Y., *Macromolecules* **1990,** *23*, 353-354.

36. Aida, T.; Kawaguchi, K.; Inoue, S., *Macromolecules* **1990,** *23*, 3887-3892.

37. Kricheldorf, H. R.; Jonté, J. M.; Dunsing, R., *Macromol. Chem. Phys.* **1986,** *187*, 771-785.

38. Nuyken, O.; Pask, S. D., *Polymers* **2013,** *5*, 361-403.

39. Aoi, K.; Okada, M., *Prog. Polym. Sci.* **1996,** *21*, 151-208.

40. Weber, C.; Remzi Becer, C.; Guenther, W.; Hoogenboom, R.; Schubert, U. S., *Macromolecules* **2009,** *43*, 160-167.

41. Hoogenboom, R., *Angew. Chem. Int. Ed.* **2009,** *48*, 7978-7994.

42. Park, J. S.; Akiyama, Y.; Winnik, F. M.; Kataoka, K., *Macromolecules* **2004,** *37*, 6786-6792.

43. Wiesbrock, F.; Hoogenboom, R.; Leenen, M. A. M.; Meier, M. A. R.; Schubert, U. S., *Macromolecules* **2005,** *38*, 5025-5034.

44. Guerrero-Sanchez, C.; Hoogenboom, R.; Schubert, U. S., *Chem. Commun.* **2006**, 3797-3799.

45. Abbasi, F.; Mirzadeh, H.; Katbab, A. A., *Polym. Int.* **2001,** *50*, 1279-1287.

46. McCarthy, D.; Mark, J.; Schaefer, D., *J. Polym. Sci. Part B Polym. Phys.* **1998,** *36*, 1167-1190.

47. Isaacman, M. J.; Barron, K. A.; Theogarajan, L. S., *J Polym Sci A Polym Chem* **2012,** *50*, 2319-2329.

48. Chojnowski, J.; Cypryk, M., Synthesis of linear polysiloxanes. In *Silicon-Containing Polymers*, Springer: 2000; pp 3-41.

49. Steffanut, P.; Osborn, J. A.; DeCian, A.; Fisher, J., *Chem. - Eur. J.* **1998,** *4*, 2008-2017.

50. Hsiao, Y.-L.; Waymouth, R. M., *J. Am. Chem. Soc.* **1994,** *116*, 9779-9780.

51. Marciniec, B., *Hydrosilylation*. Springer: 2009.

52. Chalk, A. J.; Harrod, J. F., *J. Am. Chem. Soc.* **1965,** *87*, 16-21.

53. Buslov, I.; Keller, S. C.; Hu, X., *Org. Lett.* **2016,** *18*, 1928-1931.

54. Marciniec, B., *Comprehensive handbook on hydrosilylation*. Elsevier: 2013.

55. MacMillan, S. N.; Harman, W. H.; Peters, J. C., *Chem. Sci.* **2014,** *5*, 590-597.

56. Jordan, R. C., *J. Liq. Chromatogr.* **1980,** *3*, 439-463.

57. Haney, M. A., *J. Appl. Polym. Sci.* **1985,** *30*, 3037-3049.

58. Barth, H. G.; Mays, J. W., *Modern methods of polymer characterization*. John Wiley & Sons: 1991; Vol. 113.

59. Jackson, C.; Chen, Y. J.; Mays, J. W., *J. Appl. Polym. Sci.* **1996,** *61*, 865-874.

60. Theillet, F.-X.; Binolfi, A.; Frembgen-Kesner, T.; Hingorani, K.; Sarkar, M.; Kyne, C.; Li, C.; Crowley, P. B.; Gierasch, L.; Pielak, G. J.; Elcock, A. H.; Gershenson, A.; Selenko, P., *Chem. Rev.* **2014,** *114*, 6661-6714.

61. Rai, G. J.; Kumar, A.; Biswas, P., *J. Chem. Phys.* **2015,** *142*, 174906.

62. Perez-Baena, I.; Moreno, A. J.; Colmenero, J.; Pomposo, J. A., *Soft Matter* **2014,** *10*, 9454-9459.

63. Chu, B., *Laser light scattering*. Elsevier: 1974.

64. J, O. M.; S, W. E., Differential microcalorimeter. Google Patents: 1966.

65. Coats, A.; Redfern, J., *Analyst* **1963,** *88*, 906-924.

66. Baskaran, D.; Mays, J. W.; Bratcher, M. S., *Angew. Chem. Int. Ed.* **2004,** *43*, 2138-2142.

CHAPTER 3 PDMS-Based Ambipolar Polymer Electrolytes:

Preparation and Characterization

Abstract

Since the discovery of polymer electrolytes based on poly(ethylene oxide) in the 1970s, the rational understanding to improve ion transport remains a mystery. Solid polymer electrolytes containing lithium ions are ideal candidates for electrochemical devices and energy storage applications. Understanding their ionic transport mechanism is the key for designing of highly conductive polymer matrices. In this chapter, we focus on synthesis of polymer electrolytes based on polysiloxane backbone due to its low T_g. By incorporating cyclic sulfonate, carbonate, and tri-arm ethylene oxide unit to the soft polysiloxane backbone, we achieved high ionic conductivity of 9.5×10^{-6} S/cm at ambient temperature. The lithium ion transport mechanism is discussed based on dielectric spectroscopy and differential scanning calorimetry results.

3.1 Introduction

The lithium ion battery (LIBs) technology has drawn significant attention in industry and academia because it offers exceptionally high energy density, minimal memory effect, and low self-discharge rates, and fast charging rate.[1-2] Since the first commercialized LIB was introduced by SONY in early 1990s, LIBs have rapidly dominated the electronic devices such as laptops, smartphones.[3] Moreover, they have shown great potential to be utilized in electric vehicles, aviation and energy storage instruments, *etc*.[4-6] A LIB cell consists of two electrodes and electrolyte, which separates two electrodes and only allow lithium ions to transport during charge/discharge cycles. The conventional liquid electrolytes employed organic small molecules such as ethylene carbonate and propylene carbonate and offers high ionic conductivity.[2] However, the LIBs using these types of electrolytes usually suffer from safety issues due to the volatile and highly flammable electrolytes.[7-10]

Substituting a solid polymer-based electrolyte for the organic counterpart is crucial because it offers several advantages such as enhanced resistance to variations in the volume of the electrodes during the charge/discharge process, improved safety features, excellent flexibility and processability.[6, 11] Since the first polymer electrolytes were reported by Wright *et al*. using polyethylene oxide and alkaline salts in the 1970s,[12] substantial research efforts toward new polymer electrolytes and theoretical modeling of their ion transfer mechanism, the physical and chemical properties of the electrolyte/electrode interface, has been carried out.[13-15] A generally accepted view of lithium ion transport is that the ion

conductivity is coupled with the segmental chain relaxation. The lithium ion could transport between polymer chains or hop from one chain to another.[16] However, the inherently poor conductivity of dry polymer electrolytes at ambient temperature remains the fundamental obstacle to their widespread application (the lithium ionic conductivity should exceed 10^{-3} S/cm).[15]

In order to raise the ionic conductivity, we turned to poly(dimethylsiloxane) (PDMS) with its T_g of -123 °C, substantially lower than that of any other known polymer.[17] It has extremely large free volume and fast chain segmental dynamics[18-19], which makes it a promising polymer host for lithium ion transport. However, PDMS is hydrophobic and has rather low lithium salts solubility. Thus, we attached high dielectric moieties, cyclic carbonate, sulfone, and tri-arm ethylene oxide to the polymer backbone to increase the lithium salt solubility and to enhance ion dissociation. In addition, the lithium ion transport mechanism was illustrated using dielectric spectroscopy.

3.2 Experimental Section

Materials. Vinyl ethylene carbonate (VEC, Aldrich), tetrathiolphene-1,1-dioxide (SUL, Aldrich), platinum (0)-1,3-divinyl-1,1,3,3-tetramethyldisiloxane complex solution in xylene, Pt ~2% (Pt[dvs], Aldrich) and n-butyllithium (*n*-BuLi in hexane, 2.5M, Aldrich) were used as received. Octamethylcyclotetrasiloxane (D4, 98%, Acros Organics), tetramethylcyclotetrasiloxane (D4H, 98%, Acros Organics), hexamethyldisiloxane (HDS, 99%, Acros Organics) and allyl bromide (AB, 98%, Aldrich) were distilled over CaH_2 before use. Toluene was refluxed over sodium overnight before use. Lithium

bis(trifluoromethanesulfonyl)imide (LiTFSI, 99.99%, Aldrich), trifluoromethanesulfonic acid (TFA, 99%, Aldrich) was used as received.

Instrumentation. NMR spectra were recorded on a liquid state Varian VNMRS 500 MHz spectrometer at 25 °C. The internal standard was $CDCl_3$ at 7.26 ppm. Attenuated Total Reflection-IR (ATR-IR) spectra were obtained using a Nicolet iS50 FT-IR spectrometer equipped with a deuterated triglycine sulfate (DTGS) detector. Broadband dielectric measurements were performed using a Novocontrol Concept 80 system in the frequency range of 10^{-2}-10^{7} Hz, which includes an Alpha- A impedance analyzer, a ZGS active sample cell interface, and a Quatro Cryosystem temperature control unit. Samples were placed between two gold-plated electrodes separated by a Teflon spacer. Before measurements, each sample was loaded within the spacer on the bottom electrode and dried under vacuum at 353 K to remove bubbles. The experiments proceeded from high to low temperatures. The samples were equilibrated at the highest temperature (353 K) for at least 3 h until the measurement results were reproducible, indicating that the samples did not degrade and there was no residual solvent. The samples were equilibrated at each temperature for 20 min before the dielectric measurements.

Details of SPE Preparation. The polymer electrolyte samples were prepared inside the glove box in a nitrogen atmosphere. The polymer was premixed inside a known concentration of acetonitrile solution. Each of the Li-salts, $LiPF_6$ and LiTFSi, was mixed into acetonitrile solvent with to a known concentration. The Li-salts were added in a certain weight concentration to the polymer. Before drying, each sample was left under stirring

for at least 48 hours for sufficient dispersion of lithium salts in polymer matrix. Once the samples were mixed, each sample was placed inside the small dielectric cell and placed inside the vacuum oven for a slow-solvent evaporation before any measurements.

DSC Measurements. The glass transition temperatures T_g were investigated using the TA instrument Q1000. The polymerized electrolytes samples were hermetically sealed in aluminum pans while using an empty pan for reference. These samples were initially equilibrated at 383 K for forty-five minutes, then cooled down to 130 K and heated up to 453 K. The heating and cooling cycle was performed with a rate of 10K/min and repeated three times to make certain of reproducibility of the results. The cooling cycle was used to analyze the glass transition.

3.2.1 Synthesis of Polyhydromethylsiloxane (PHMS).

D4H (6.0 g, 24.9 mmol) and HDS (0.41 g, 2.5 mmol) were charged to a flame-dried round bottom flask equipped with a stir bard through rubber septum. TFA (30 μL) was then carefully added into the mixture via a gas-tight syringe. The mixture was stirred for 20 min at room temperature and then heated to 65 °C and stirred for 3days. The mixture was then cooled to room temperature and diluted with ether and followed by the neutralization with K_2CO_3 aqueous solution. After extraction with petroleum ether (100 mL×3), the organic layer was collected and dried over $MgSO_4$. The solvent was then removed under reduced pressure and cyclic oligomers were distilled off at 130 °C under high vacuum. A clear viscous liquid was collected. Yield=4.9 g, 66.7%. ^{1}H-NMR ($CDCl_3$, 500 MHz), δ (ppm): 4.72 (Si-H), 0.06 (Si-CH_3).

3.2.2 Synthesis of 2-Allyltetrahydrothiophene 1,1-Dioxide (ACS).

To a solution of 24 g SUL in 250 ml THF in a three-neck round bottom flask pre-cooled to -30 °C was added 80 ml n-BuLi in hexane (2.5 M) dropwise under a super dry N_2 atmosphere. Then the mixture was stirred for one additional hour. AB (0.2 mol in 250 mL of THF) was added dropwise over 45 min. After stirring for three additional hours. The mixture was acidified with 300 mL ammonium chloride solution. The organic phase was dried over $NaSO_4$ overnight. The solvent was removed in vacuo evaporated leaving a viscous residue. The residue was then chromatographed (hexanes/ethyl acetate=5/5 (v/v), R_f=0.55) and obtained a light-yellow oil. Yield=44%. ^{1}H-NMR (500 MHz, $CDCl_3$): δ (ppm) 5.13-5.09 (2H, HC=CH), 5.77 (1H, HC=CH), 3.13-2.98 (3H, CH(sulfolane)),2.64 (1H, CH), 2.30-2.12 (3H, CH(sulfolane)), 2.18 (1H, CH(sulfolane)), 2.05 (1H, CH).

3.2.3 Synthesis of Polyhydromethylsiloxane Based Polymer Electrolytes.

Synthesis of polyhydromethylsiloxane-*g*-2-allyltetrahydrothiophene 1,1-dioxide (PHMS-*g*-ACS). PHMS (1.2 g) was charged into a pre-dried three-neck round bottom flask equipped with a condenser and a magnetic stirrer. The flask was then attached to a vacuum line and degassed overnight. 2.5 g of ACS and 40 mL of acetonitrile was then added to the flask via a gas-tight syringe followed by the addition of 30 µL of Pt[dvs]. The reaction mixture was stirred at 65 °C for 24 h. The reaction progress was monitored using ^{1}H-NMR spectroscopy (by the disappearance of Si-H at 4.72 ppm). Upon the completion of reaction, the mixture was concentrated and precipitated into excess methanol three times. The ^{1}H-NMR spectra of these polymers are shown in the Discussion section.

Synthesis of polyhydromethylsiloxane-*g*-vinyl ethylene carbonate (PHMS-*g*-VEC). PHMS (2.4 g) was charged into a pre-dried three-neck round bottom flask equipped with a condenser and a magnetic stirrer. The flask was then attached to a vacuum line and degassed overnight. 3.56 g of ACS and 40 mL of acetonitrile were then added to the flask via a gas-tight syringe followed by the addition of 30 µL of Pt[dvs]. The reaction mixture was stirred at 65 °C. The reaction progress was monitored using ^{1}H-NMR spectroscopy (by the disappearance of Si-H at 4.72 ppm). Upon the completion of reaction, the mixture was concentrated and precipitated into excess methanol three times.

Synthesis of polyhydromethylsiloxane-*g*-tris(2-methoxyethoxy)vinylsilane (PMHS-*g*-TES). PMHS-*g*-TES was synthesized via hydrosilylation of TES. PMHS (2.0 g) and TMS (2.4 g) were dissolved in toluene followed by the addition of Pt[dvs] (30 µL). The reaction was purged with Ar and then stirred at 60 °C. The reaction progress was monitored by ^{1}H-NMR. Upon the completion of reaction, the solvent was removed and yielded brown oil. Yield=4.4g, 100%.

3.3 Results and Discussion

3.3.1 Synthesis of Polyhydromethylsiloxane (PHMS).

PDMS could be synthesized via ring opening polymerization of cyclic monomer D3 or D4. The molecular weight could be controlled through the ratio of monomer/end-blocker.[20] To attach the high dielectric moiety to the PDMS backbone, PHMS was used as parent polymer. The preparation of designed polymer electrolytes could be realized through

hydrosilylation. Because Si-H bond is susceptible to nucleophilic attack by the basic initiator, the synthesis of PHMS was therefore carried out via cationic ring opening polymerization initiated using TFA. The synthetic strategy is shown in Scheme 3.1

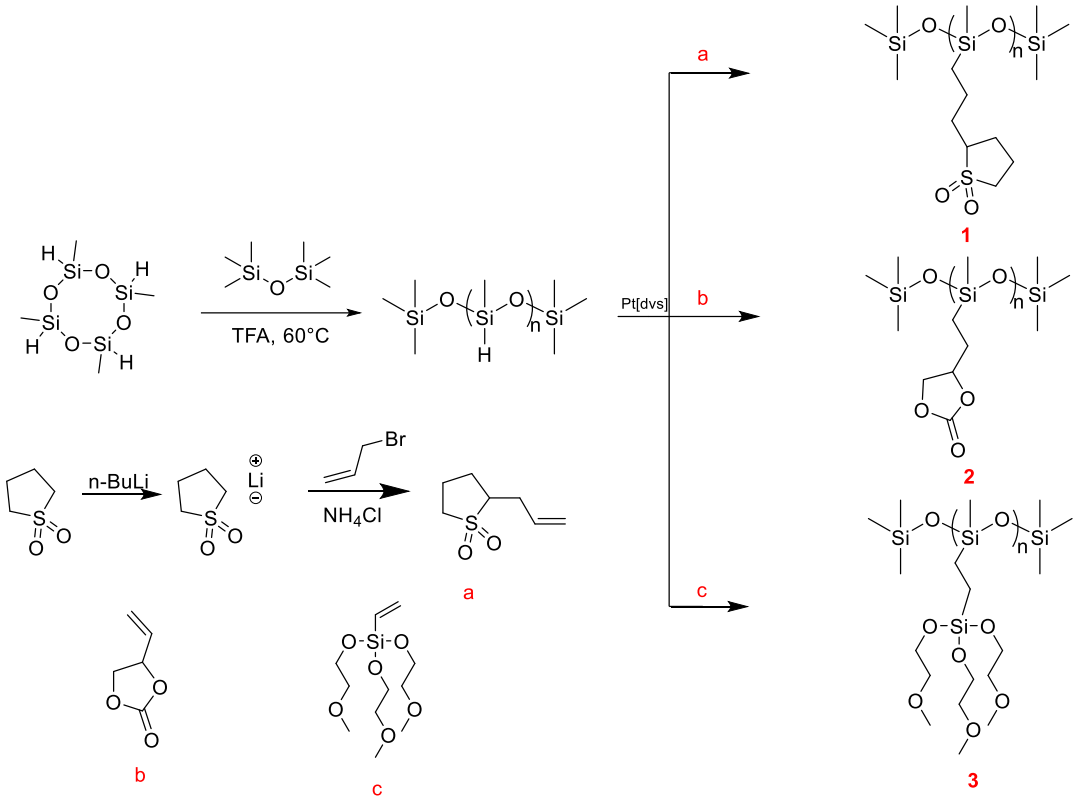

Scheme 3.1. The synthetic routine for polymer electrolytes.

The molecular weight of PMHS could be controlled by the ratio of monomer/ end-blocker (D4H: HDS). The molecular weight was determined by end-group analysis through ^{1}H-NMR (Figure 3.1). The calculate DP=38.14, M_n=~2,450 g/mol.

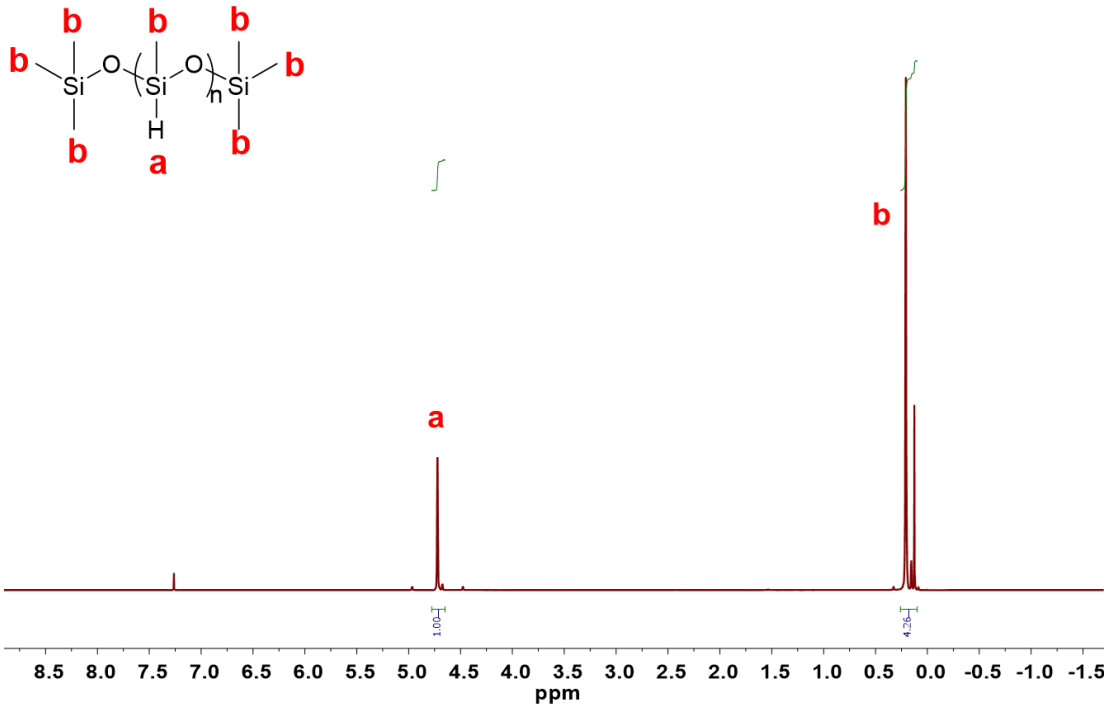

Figure 3.1. ^{1}H-NMR spectrum of PHMS.

3.3.2 Synthesis of 2-Allyltetrahydrothiophene 1,1-Dioxide (ACS).

The α-hydrogens of tetrahydrothiophene 1,1- dioxide (THTD) are acidic due to the resonance and inductive effect of the sulfonyl oxygens. Therefore, they can undergo nucleophilic reactions with strong bases, such as *n*-BuLi. The attachment of vinyl moiety was then performed through the coupling reaction between carbanion and allyl bromide. Since the two α-hydrogens have same reactivity, chromatography was then carried out to isolate the mono-allyl sulfone. The desired product was then characterized using ^{1}H-NMR spectroscopy (Figure 3.2).

3.3.3 Synthesis of PDMS-Based Polymer Electrolytes

Hydrosilylation using Karstedt's catalyst is one of the most convenient methods to attach vinyl moiety to PHMS backbone.[21-22] Following this protocol, PHMS-*g*-ACS, PHMS-*g*-VEC and PHMS-TES were prepared and characterized using ^{1}H-NMR spectroscopy (Figure 3.3). The absence of Si-H (4.70 ppm) and new peak corresponding to Si-CH_2-CH_2- emerged at 0.57 ppm (Figure 3.3A) indicates that the hydrosilylation was quantitative.

3.3.4 Ionic Conductivity and Ion Transport Mechanism

In the case of polymer electrolytes, ion transport depends on the local segmental dynamics, while the motion of the entire chain controls viscosity. These electrolytes were mixed with different portions of LiTFSI. The results are summarized in Table 3.1.

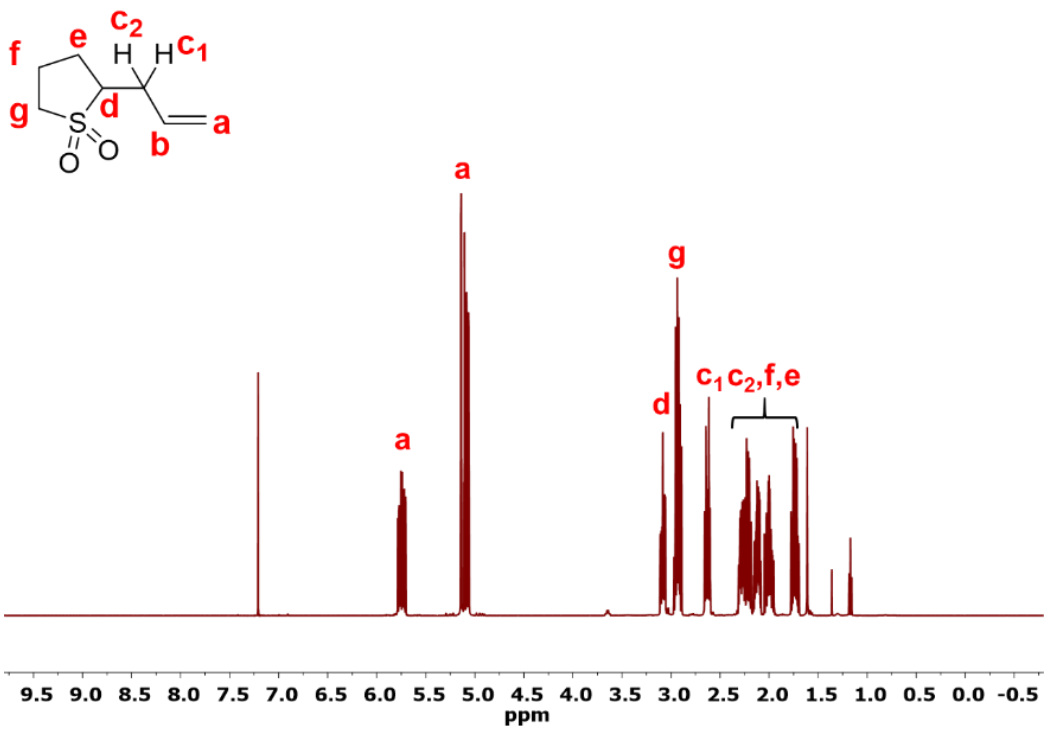

Figure 3.2. The ^{1}H-NMR spectrum of mono-allyl sulfone in $CDCl_3$.

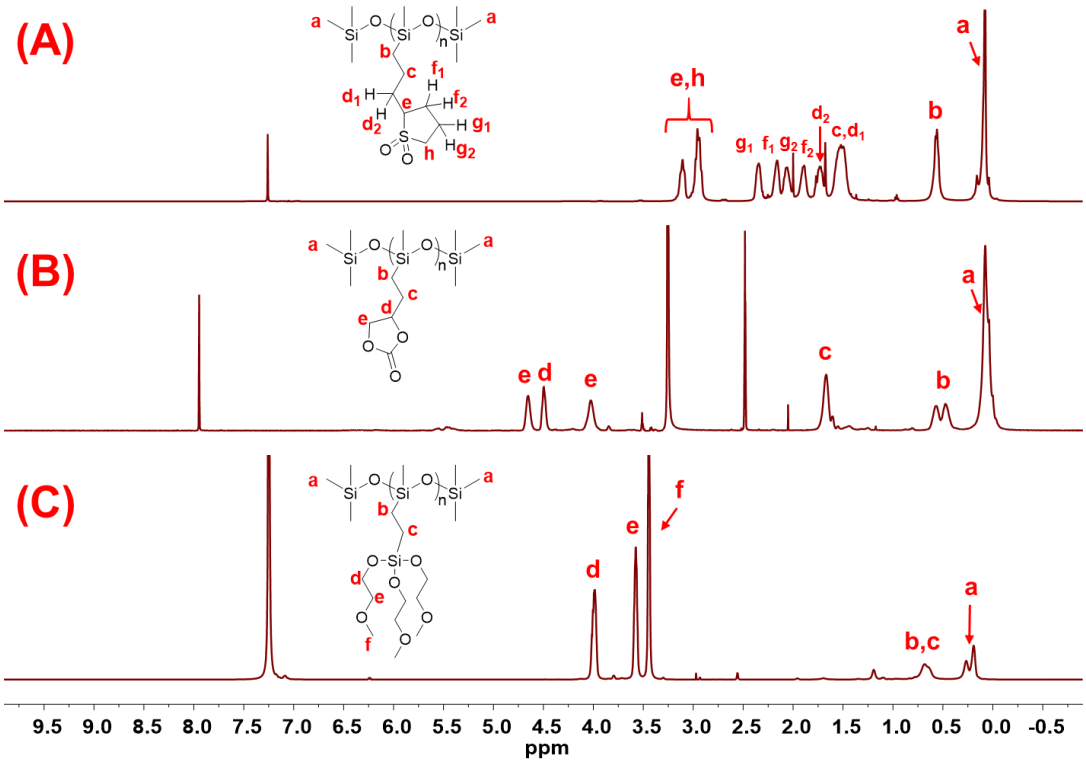

Figure 3.3. The ^{1}H-NMR spectra of (A) PHMS-*g*-ACS in $CDCl_3$, (B) PHMS-VEC in DMSO, and (C) PHMS-*g*-TEO in $CDCl_3$.

Table 3.1. Summary of ionic conductivity, glass transition of PHMS based polymer electrolytes.

Sample	Salt	T_g	Ionic conductivity at room temperature
		°C	S/cm
PHMS-VEC	NA	-36.5	4.68×10^{-9}
PHMS-VEC	LiTFSI-3%	-36.1	4.67×10^{-7}
PHMS-VEC	LiTFSI-10%	-39.1	1.82×10^{-6}
PHMS-VEC	LiTFSI-30%	-43.2	9.58×10^{-6}
PHMS-VEC	LiTFSI-50%	-44.7	3.42×10^{-6}
PHMS-ACS	NA	-21.3	4.68×10^{-9}
PHMS-ACS	LiTFSI-3%	-21.5	6.41×10^{-8}
PHMS-ACS	LiTFSI-10%	-24.5	1.49×10^{-7}
PHMS-ACS	LiTFSI-30%	-27.9	4.74×10^{-7}

When VEC was grafted on the PDMS backbone, the ionic conductivity increased with the increased loading of LiTFSI. This is because cyclic carbonate which has a high dielectric constant can promote ion-pair dissociation of LiTFSI salt.[23] On the other hand, T_g decreased as the concentration of LiTFSI increased. The fast chain motion was attributed not only to the soft backbone but also to the plasticizer effect of TFSI. This leads to an ionic conductivity as high as 9.58×10^{-6} S/cm at room temperature.

When using ACS as pendant group, only up to 30 wt% of LiTFSI is able to be dissolved. Nevertheless, dielectric spectra also showed a similar trend, lithium conductivity increases as the loading of LiTFSI increases (Figure 3.4). The dielectric spectra of these two systems exhibits that lithium transport was coupled with the polymer chain relaxation, as proved by the VTF behavior. The highest performance of PHMS-g-ACS (up to 4.74×10^{-7} S/cm) was achieved with 30% of LiTFSI. However, this is still two orders of magnitude lower than PEO/$LiClO_4$ system, which could be attributed to reduced chain segmental dynamics.

In the case of PHMS-g-TES, we tried to investigate the effect of lithium salts on the ionic conductivity by using LiTFSI and $LiPF_6$. The neat polymer has one of the lowest T_gs among known polymers.[24] Its low glass transition temperature would help to achieve desired conductivity at room temperature. The heat flow curves from DSC measurements are illustrated in Figure 3.5.

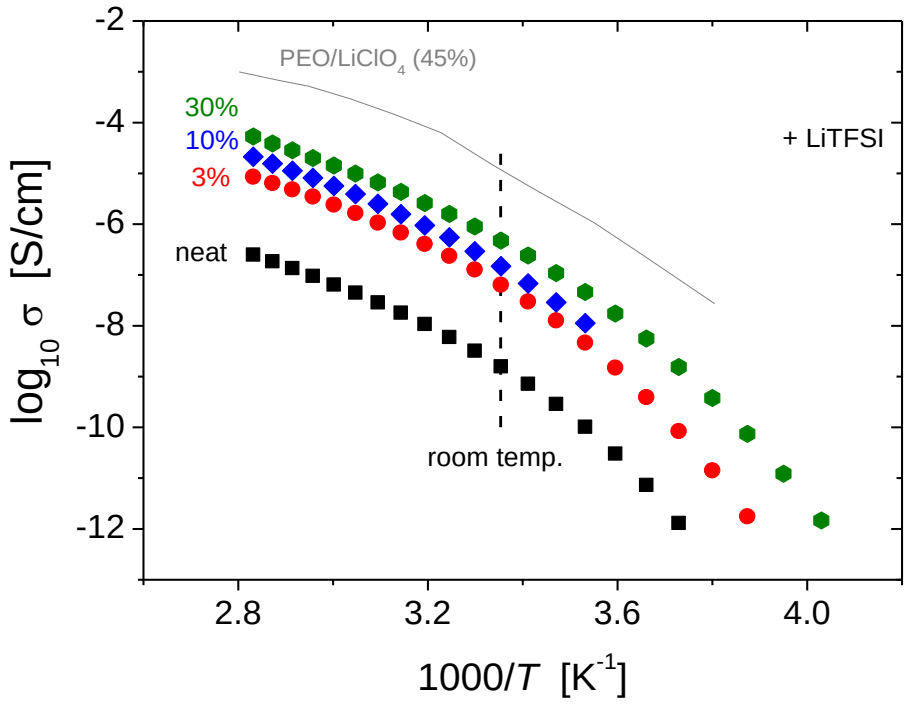

Figure 3.4. Conductivity of PHMS-*g*-ACS as a function of 1000/T.

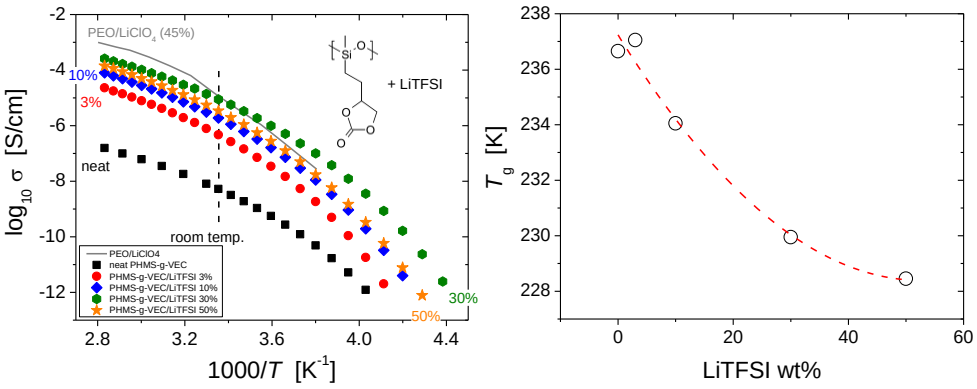

Figure 3.5. Conductivity of PHMS-*g*-VEC as a functional of 1000/T. and summary of T_g as a function of LiTFSI concentration.

There was no crystallization observed with any of the following samples. All the samples exhibited one glass transition (T_g) process that was clearly seen for each of the heat flow curves (Figure 3.6). It is worth noting that when increasing the salt concentration of each sample the T_g increase compared to the neat sample. LiTFSi samples have a lower glass transition temperature compared to $LiPF_6$. This difference could be attributed to the coulombic interaction of the salts inside the polymer matrix.

The d.c. and a.c. conductivities are shown in Figure 3.7c. The relaxation process is clearly observed at the maximum peak in the M" representative. The conductivity relaxation time is obtained from the M" maximum peak by taking the frequency, f_σ, and by using the $\tau_\sigma = {}^{1}/_{2\pi f_\sigma}$.

Detailed analysis shows that an ionic conductivity of 5.5×10^{-6} S/cm was reached with 30 wt% of $LiPF_6$. The polymer electrolyte also shows a clear crossover from VFT-like temperature to Arrhenius behavior of conductivity at T_g is known for many materials with high ionic conductivity (Figure 3.8). The crossover temperature marks the T_g and the values obtained from DSC are comparable to each other.

3.4 Conclusion

Polysiloxane based electrolytes were prepared and characterized using NMR, dielectric spectroscopy. Three different pendant groups: cyclic carbonate, sulfone, and tri-arm ethylene oxide were studied. When doped with LiTFSI, PHMS-*g*-VEC showed a room

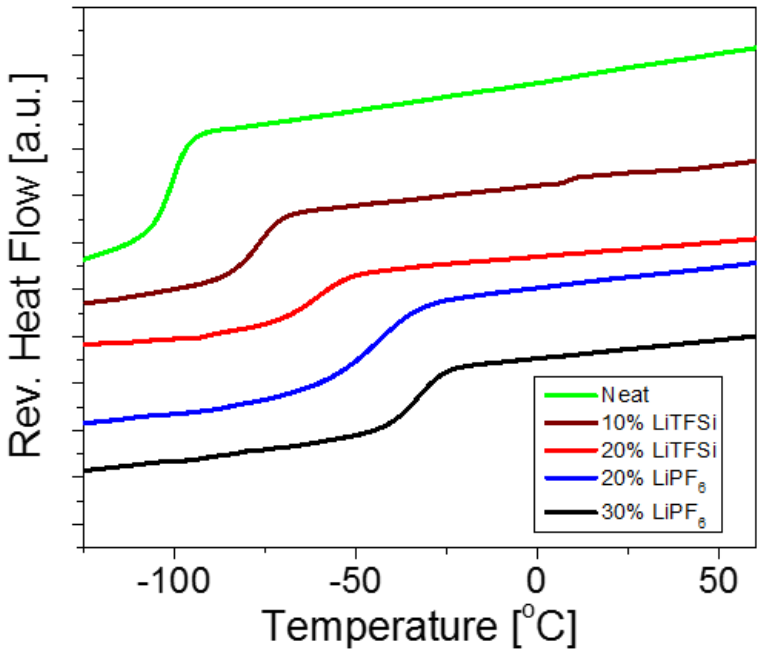

Figure 3.6. Heat flow from the DSC curves showing the glass transition for all the samples. The presented data was recorded on cooling. Worth noting for increase of salt concentration, the glass transition temperature increased, respective to that of the neat sample.

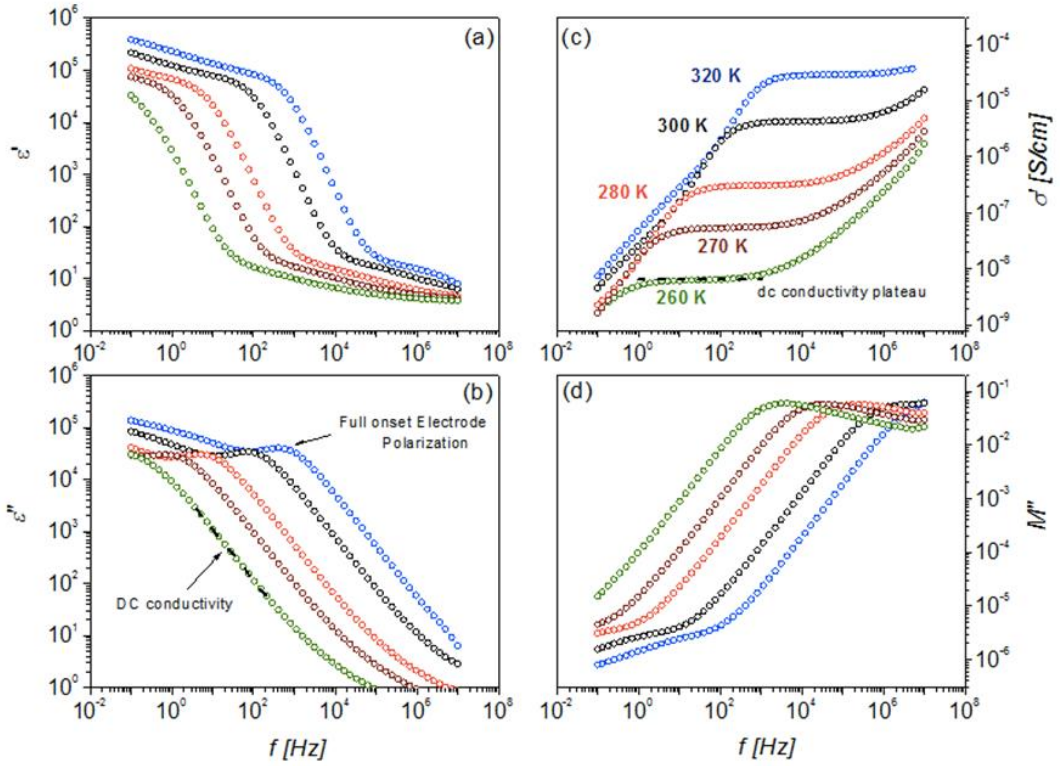

Figure 3.7. The dielectric spectra *vs* frequency at different temperatures for polymer electrolyte (30% wt. $LiPF_6$) at few selected temperatures. (a) real part permittivity, (b) imaginary part permittivity, (c) real part conductivity, and (d) electric loss modulus *M".* In (b) and (c) the solid dash line presents the dc conductivity from the dielectric spectra.

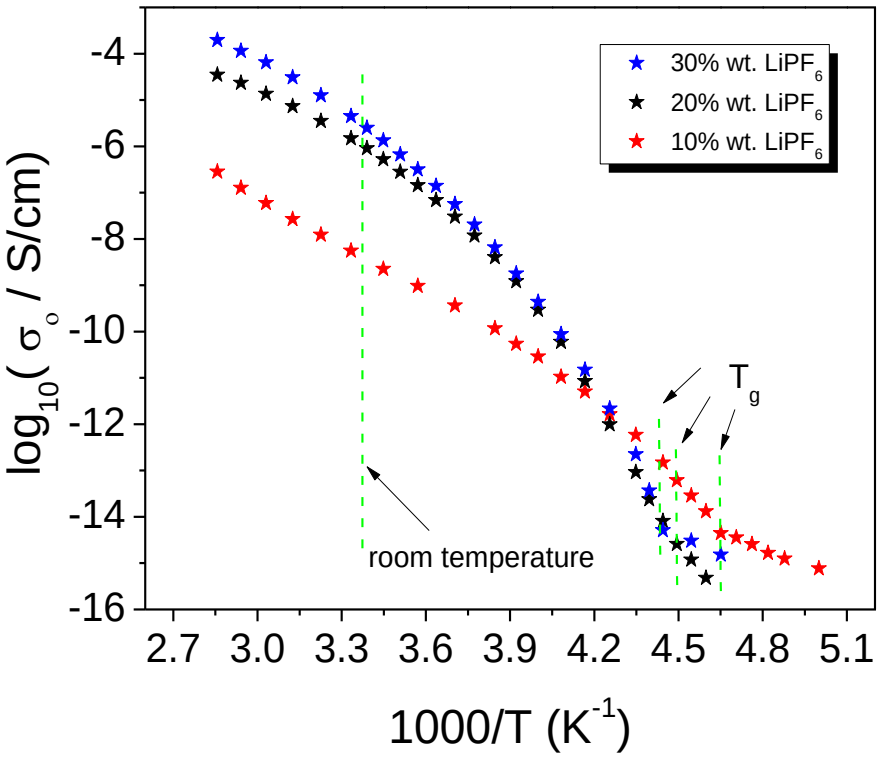

Figure 3.8. Conductivity of PHMS-*g*-TEO using $LiPF_6$ as a function of 1000/T.

temperature of 9.58×10^{-6} S/cm. on the other hand, PHMS-*g*-ACS showed conductivity almost two orders of magnitude lower. When tri-arm ethylene oxide unit was investigated, It has been suggested that siloxane-based polymer has an ideal structural relaxation rate that would promote ion conduction.

3.5 References

1. Tarascon, J. M.; Armand, M., *Nature* **2001,** *414*, 359-367.

2. Long, L.; Wang, S.; Xiao, M.; Meng, Y., *J. Mater. Chem. A* **2016,** *4*, 10038-10069.

3. Arico, A. S.; Bruce, P.; Scrosati, B.; Tarascon, J. M.; van Schalkwijk, W., *Nat Mater* **2005,** *4*, 366-77.

4. Quartarone, E.; Mustarelli, P., *Chem. Soc. Rev.* **2011,** *40*, 2525-2540.

5. Scrosati, B.; Croce, F.; Appetecchi, G. B.; Persi, L., *Nature* **1998,** *394*, 456-458.

6. Kamaya, N.; Homma, K.; Yamakawa, Y.; Hirayama, M.; Kanno, R.; Yonemura, M.; Kamiyama, T.; Kato, Y.; Hama, S.; Kawamoto, K.; Mitsui, A., *Nat Mater* **2011,** *10*, 682-6.

7. Jow, T. R.; Xu, K.; Borodin, O.; Makoto, U., *Electrolytes for lithium and lithium-ion batteries*. Springer: 2014; Vol. 58.

8. Gainaru, C.; Stacy, E. W.; Bocharova, V.; Gobet, M.; Holt, A. P.; Saito, T.; Greenbaum, S.; Sokolov, A. P., *J. Phys. Chem. B* **2016,** *120*, 11074-11083.

9. Kelly, I.; Owen, J.; Steele, B., *J. Power Sources* **1985,** *14*, 13-21.

10. Soo, P. P., *J. Electrochem. Soc.* **1999,** *146*, 32-37.

11. Wei, X.; Shriver, D. F., *Chem. Mater.* **1998,** *10*, 2307-2308.

12. Fenton, D. E.; Parker, J. M.; Wright, P. V., *Polymer* **1973,** *14*, 589.

13. Bruce, P. G.; Scrosati, B.; Tarascon, J. M., *Angew. Chem. Int. Ed. Engl.* **2008,** *47*, 2930-46.

14. Wang, Y.; Fan, F.; Agapov, A. L.; Yu, X.; Hong, K.; Mays, J.; Sokolov, A. P., *Solid State Ionics* **2014,** *262*, 782-784.

15. Fan, F.; Wang, W.; Holt, A. P.; Feng, H.; Uhrig, D.; Lu, X.; Hong, T.; Wang, Y.; Kang, N.-G.; Mays, J.; Sokolov, A. P., *Macromolecules* **2016,** *49*, 4557-4570.

16. Ratner, M. A.; Shriver, D. F., *Chem. Rev.* **1988,** *88*, 109-124.

17. Zhang, Z.; Jin, J.; Bautista, F.; Lyons, L.; Shariatzadeh, N.; Sherlock, D.; Amine, K.; West, R., *Solid State Ionics* **2004,** *170*, 233-238.

18. Jones, R. G.; Ando, W.; Chojnowski, J., *Silicon-containing polymers: the science and technology of their synthesis and applications*. Springer Science & Business Media: 2013.

19. McCarthy, D.; Mark, J.; Schaefer, D., *J. Polym. Sci. Part B Polym. Phys.* **1998,** *36*, 1167-1190.

20. Chakraborty, R.; Soucek, M. D., *Macromol. Chem. Phys.* **2008,** *209*, 604-614.

21. Marciniec, B., *Comprehensive handbook on hydrosilylation*. Elsevier: 2013.

22. Steffanut, P.; Osborn, J. A.; DeCian, A.; Fisher, J., *Chem. - Eur. J.* **1998,** *4*, 2008-2017.

23. Li, J.; Lin, Y.; Yao, H.; Yuan, C.; Liu, J., *ChemSusChem* **2014,** *7*, 1901-1908.

24. Jo, B.-H.; Van Lerberghe, L. M.; Motsegood, K. M.; Beebe, D. J., *J. Microelectromech. Syst.* **2000,** *9*, 76-81.

CHAPTER 4 Polymerized Ionic Liquid based on PDMS Backbone: ionic transport under pressure

Abstract

Polymerized ionic liquids (PILs), composed mostly of organic ions covalently bonded to the polymer backbone and free counterions, are considered ideal electrolytes for various electrochemical devices, including fuel cells, supercapacitors and batteries. In this chapter, we report the synthesis of polysiloxane based ionic liquid. The structure was characterized using NMR and IR. In addition, dielectric spectroscopy revealed that a rather high conductivity of 3.3×10^{-5} S/cm at room temperature was achieved. High pressure conductivity studies help to identify the charge transport mechanism in this PIL.

4.1 Introduction

Ever increasing energy demand has become one of the greatest challenges of our time.[1-4] This in turn creates a growing demand for various types of energy storage devices in households and in industry.[4-7] Therefore, a significant research effort during the past decade has been focused on the development of new functional materials for energy storage.[8-12] Since the discovery of polyethylene oxide based electrolytes in 1970s, this new type of electrolytes has attracted massive attention.[13-17] Unfortunately, over the past decades, rare examples have been shown to have ionic conductivity exceeding 10^{-3} S/cm at room temperature, which is a minimum requirement for practical applications.[1, 18]

The family of polymerized ionic liquids (PILs), combining unique futures of ionic liquids with the outstanding mechanical properties of polymers, might offer an ideal solution for these purposes.[19] PILs are non-flammable, have low vapor pressure, and good electrode compatibility.[19] They are fast becoming promising candidates for applications such as the polymer-electrolyte-membrane fuel cells, lithium batteries and supercapacitors.[20-23] For example, the TFSI based electrolytes have been shown to cycle well with Li metal electrode, providing a significant enhancement in energy densities.[24] Furthermore, there are almost unlimited combinations of cations, anions and polymer chains.[25] Numerous researcher reported the synthesis of ILs and PILs. However, few of them barely achieve room temperature conductivity larger than 10^{-4} S/cm.[26-28]

Poly(dimethylsiloxane) (PDMS) is a well-known inorganic polymer with a large variety of industrial applications.[29-32] Its unique features, such as extremely low glass

transition temperature, optical transparency, elasticity, high thermal and chemical stability of PDMS make it a promising candidate for use as the polymer hosts for PILs.[32] However, due to its hydrophobic nature, PDMS is immiscible with many ILs.[33]

Herein we describe a facile method to overcome the immiscibility between PDMS and ILs by grafting IL precursor to the PDMS backbone through facile hydrosilylation. Followed by neutralization reaction and metathesis reaction, PDMS based PILs could be synthesized with high grafting density and highly tunable properties. In this work, we employ high pressure conductivity measurements to reveal the charge transport mechanism in PILs.

4.2 Experimental Section

Materials. Platinum(0)-1,3-divinyl-1,1,3,3-tetramethyldisiloxane complex solution in xylene, Pt ~2% (Pt[dvs], Aldrich) and lithium bis(trifluoromethane) sulfonimide (LiTFSI, 99.95%, Aldrich) were used as received. 5-Bromo-1-pentene (B5B, 99%, Acros Organics), 1-methylimidazole (Imi, 99%, Acros Organics) was distilled over CaH_2 before use. Toluene was refluxed over sodium overnight before use. All the reactions were carried out under inert atmosphere.

Instrumentation. ^{1}H-NMR were measured using Varian Mercury 500. Attenuated total reflectance infrared spectroscopy (ATR-IR) were conducted using a Nicolet iS50 FT-IR spectrometer equipped with a deuterated triglycine sulfate (DTGS) detector. Electronspray ionization mass spectrometry (ESI-MS) was measured using Applied Biosystems QStar Elite system**.** Dielectric measurements. Isobaric dielectric measurements

at ambient pressure from 10^{-1} to 10^{7} Hz were carried out using a Novocontrol GMBH Alpha dielectric spectrometer. For the isobaric measurements, the sample was placed between two stainless steel electrodes of the capacitor with a gap of 0.1 mm. The dielectric spectra of PILs were collected over a wide temperature. The temperature was controlled by the Novocontrol Quattro system, with the use of a nitrogen gas cryostat.

4.2.1 Synthesis of Polyhydromethylsiloxane (PHMS).

D4H (6.0 g, 24.9 mmol) and HDS (0.41 g, 2.5 mmol) were charged to a flame-dried round bottom flask equipped with a stir bard through rubber septum. TFA (30 μL) was then carefully added into the mixture via a gas-tight syringe. The mixture was stirred for 20 min at room temperature and then heated to 65 °C and stirred for 3 days. The mixture was then cooled to room temperature and diluted with ether and followed by the neutralization with K_2CO_3 aqueous solution. After extraction with petroleum ether (100 mL×3), organic layer was collected and dried over $MgSO_4$. The solvent was then removed under reduced pressure and cyclic oligomers were distilled off at 130 °C under high vacuum. A clear viscous liquid was collected. Yield=4.9 g, 66.7%. ^{1}H-NMR ($CDCl_3$, 500 MHz), δ (ppm): 4.72 (Si-H), 0.06 (Si-CH_3).

4.2.2 Synthesis of 3-Methyl-1-(pent-4-en-1-yl)-1h-imidazol-3-ium Bromide (Imi-Br).

The synthesis was modified based on previously reported work.[34] To a pre-dried two neck round bottom flask equipped with a condenser and a magnetic stirrer was charged B5B (3.0 g, 20.1 mmol, 1.1eq) and Imi (1.50 g, 18.3 mmol, 1eq). The reaction mixture was then stirred at 70 °C for 24 h. The deep orange viscous oil was washed with ethyl acetate three times and dried in vacuum oven at 40°C. Yield: 4.2 g, 99%. ^{1}H-NMR δ ($CDCl_3$, 500 MHz): 10.18 (1H, NCHN); 7.60 (1H, $CH_3NCHCHN$); 7.48 (1H, $CH_3NCHCHN$ imidazolium); 5.66 (1H, CH_2=CH-); 4.94 (2H, CH_2=CH-); 4.27 (2H, $NCH_2CH_2CH_2$-); 4.04 (3H, N-CH_3); 2.12-1.88 (4H, -CH_2-CH_2-). Mass (ESI+) m/z: 151.12 (Imi), (ESI-) m/z: 78.92 (Br).

Synthesis of 3-methyl-1-(pent-4-en-1-yl)-1H-imidazol-3-ium bis (trifluoromethane) sulfonamide (Imi-TFSI). The anion exchange was carried out with LiTFSI using the similar process as reported earlier.[34] LiTFSI (2.44 g, 13.0 mmol) was added to a solution of Imi-Br (2.0 g, 8.65 mmol) in dichloromethane (50 mL, DCM) and stirred for 24 h. The reaction mixture was then filtered and the filtrate was washed with DI-H_2O until no precipitation occurred in the aqueous phase on the addition of $AgNO_3$ solution. DCM layer was concentrated to yield a light orange oil. Yield: 2.7 g, 95%. ^{1}H-NMR δ (acetone-d_6, 500 MHz): 9.06 (1H, NCHN); 7.79 (1H, $CH_3NCHCHN$); 7.72 (1H, $CH_3NCHCHN$); 5.81 (1H, CH_2=CH-); 5.02 (2H, CH_2=CH-); 4.38 (2H, $NCH_2CH_2CH_2$-);

4.07 (3H, N-CH_3); 2.19-2.01 (4H, -CH_2-CH_2-). Mass (ESI+) m/z: 151.12 (Imi), (ESI-) m/z: 279.91 (TFSI).

4.2.3 Synthesis of Polymethylhydrosiloxane-graft-5-imidazolium-1-pentene bis (trifluoromethane) sulfonamide (PMHS-Imi-TFSI).

To a pre-dried two neck round bottom flask equipped with a condenser, a rubber septum and a magnetic stirrer was added PMHS (2.0 g, 0.84 mmol) and B5B (5.0 g, 33.6 mmol, 40 eq) The reactor was purged with Ar for 20 min followed by the addition of Pt[dvs] (30 μL). The reaction mixture was then stirred at 60 °C. The reaction progress was monitored using ^{1}H-NMR spectroscopy. Upon the completion of reaction, the solvent was removed and precipitated into excess methanol to obtain brown oil. Yield: 5.9 g, 98%. ^{1}H-NMR δ ($CDCl_3$, 500MHz): 3.41 (-C<u>H</u>$_2$-Br); 1.86 (-C<u>H</u>$_2$CH_2-Br); 1.28-1.53 (-C<u>H</u>$_2$C<u>H</u>$_2$-); 0.53 (Si-C<u>H</u>$_2$); 0.07 (Si-C<u>H</u>$_3$).

Synthesis of polymethylhydrosiloxane-graft-5-imidazolium-1-pentene bromide (PMHS-Imi-Br). To a two-neck round bottom flask equipped with a condenser and a magnetic stirrer was added the solution of PMHS-B5B (2.4 g, 0.36 mmol) in DCM (30 mL) and 1-methylimidazole (1.03 g, 12.5 mmol, 35 eq). The reaction was stirred at 70 °C for 72 h. Upon the completion of the reaction, the solvent was removed under reduced pressure and the product was recovered by washing with DCM three times and drying in vacuum oven at 40 °C. Yield: 3.2 g, 98%. ^{1}H-NMR δ (D_2O, 500 MHz): 8.95 (NCHN); 7.56 (CH_3NCHCHN); 4.26 (NCH_2-); 3.95 (N-CH_3); 2.14-1.27 (4H, -CH_2-CH_2-); 0.58(Si-CH_2); 0.10 (Si-CH_3). Mass (ESI-) m/z: 78.92 (Br).

Synthesis of polymethylhydrosiloxane-graft-5-imidazolium-1-pentene bis (trifluoromethane) sulfonamide (PMHS-Imi-TFSI). To a one neck round bottom flask equipped with a magnetic stirrer was added the solution of PMHS-Imi-Br (1.0 g, 0.11 mmol) in deionized water DI-H_2O (20 mL) followed by the addition of LiTFSI (1.3 g, 6.9 mmol, 64 eq). The mixture was stirred at room temperature for 7 days. The precipitation was further washed with DI-H_2O 3 times and dried in vacuum oven at 40 °C. Yield: 1.5 g, 99%. ^{1}H-NMR δ (acetone, 500 MHz): 8.87 (NCHN); 7.66 (CH_3NCHCHN); 4.30 (NCH_2-); 4.02 (N-CH_3); 2.03-1.30 (4H, -CH_2-CH_2-); 0.61 (Si-CH_2); 0.13 (Si-CH_3). Mass (ESI-) m/z: 279.91 (TFSI).

4.3 Results and Discussion

4.3.1 Synthesis of PHMS Based Ionic Liquids.

The synthetic procedure is shown in Scheme 4.1. PMHS-B5B was synthesized via hydrosilylation reaction between PMHS and B5B using Karstedt's catalyst. Upon the completion of the reaction, vinyl protons disappeared in the ^{1}H-NMR spectra while the new protons corresponding to Si-CH_2-CH_2 appear (0.54 ppm and 1.39 ppm). On the other hand, the absence of the peak corresponding to Si-H (δ=4.70 ppm) indicates the hydrosilylation reaction was 100% as shown in Figure 4.1A.

Quaternization of PMHS-B5B was then carried out with 1-methylimidazole (Imi) to obtain PMHS-Imi-Br. A slight excess amount of 1-methylimidazole was added to the solution of PMHS-B5B in dichloromethane (DCM). Precipitate formed as the reaction

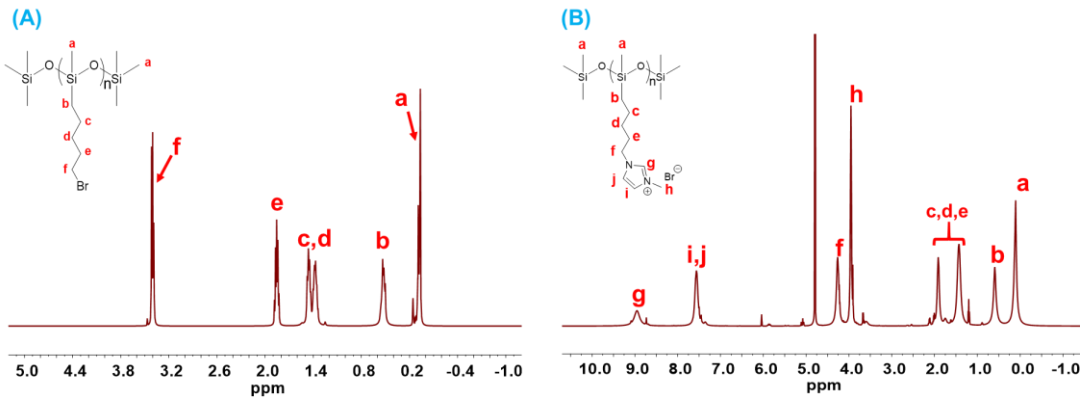

Figure 4.1. ^{1}H-NMR spectrum of (A) polymethylhydrosiloxane-graft-5-bromo-1-pentene (PMHS-B5B) in $CDCl_3$ and (B) polymethylhydrosiloxane-graft-5-imidazolium-1-pentene bromide (PMHS-Imi-Br) in D_2O.

proceeded. After the reaction was completed, the product was isolated, dried and further characterized using ^{1}H-NMR and ATR-IR. From its ^{1}H-NMR spectrum, new peaks corresponding to imidazolium emerged at 7.56 and 8.96 ppm after quaternization.

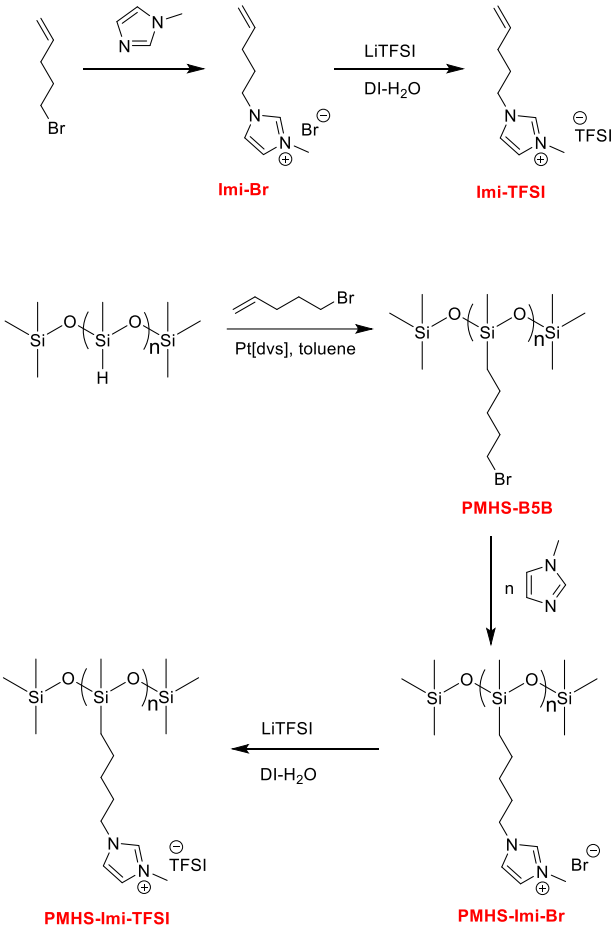

Scheme 4.1. Synthetic routine of Imi-Br, Imi-TFSI, PMHS-Imi-Br and PMHS-Imi-TFSI.

The chemical shift of CH_2 next to Br was altered from 3.41 ppm to 4.10 ppm, which could be attributed to the presence of positively charged imidazolium moiety as shown in Figure 4.1B.

Furthermore, PMHS-Imi-TFSI was prepared through metathesis with LiTFSI in DI-H_2O. Because the product is insoluble in H_2O, it could be purified by washing with DI-H_2O multiple times. After washing, the clear upper layer was mixed with $AgNO_3$ solution, no precipitation was observed indicating the absence of bromide ion. ESI-MS analysis also showed that absence of Br^- peak, while peak 279.91 corresponding to $TFSI^-$ was present. Therefore, complete anion exchange was achieved and further characterized by ATR-IR.

On the other hand, the quaternization of 1-methyl-2-imidazole using brobutane were also carried out. The 1H-NMR spectrum showed characteristic peak of imidazolium protons at 10.18, 7.61, and 7.47 ppm, respectively (Figure 4.2). In addition, the IR spectrum of Imi-TFSI showed characteristic absorption peaks of asymmetric, symmetric vibration of O=S=O, and S-N-S at 1342 cm^{-1}, 1128 cm^{-1} and 1045 cm^{-1}, respectively (Figure 4.3). These peaks were also observed in PMHS-Imi-TFSI. Furthermore, ESI-MS results showed that there was no mass speak corresponding to Br^- (78.92) as shown in Figure 4.4.

These results suggested that the anion exchange was successful. Nevertheless, it should be noted that IR absorption of O-H stretch (~ 3415 cm^{-1}) was observed in Imi-Br (Figure 4.3A(a)) and PMHS-Imi-Br (Figure 4.3 B(c)). It was attributed to the moisture absorbed by these hygroscopic ionic liquids/polymerized ionic liquids.

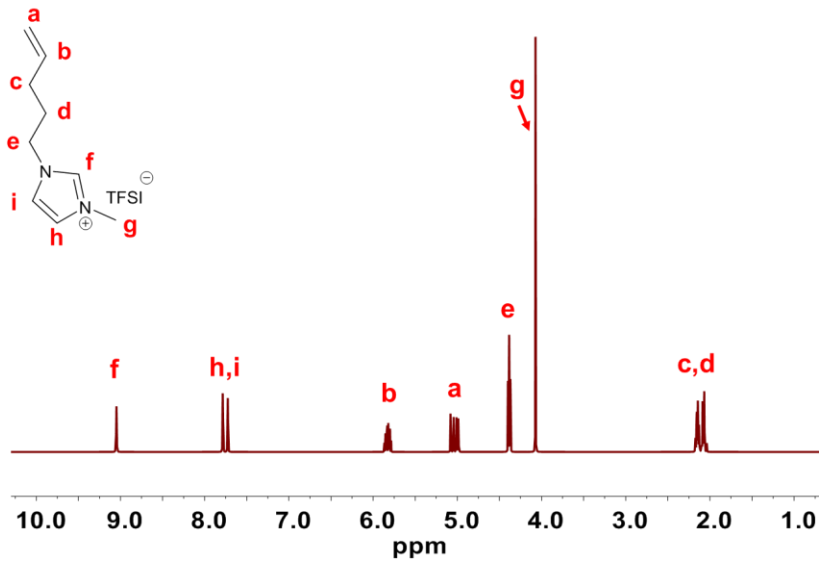

Figure 4.2. The ^{1}H-NMR spectrum of 3-methyl-1-(pent-4-en-1-yl)-1H-imidazol-3-ium bis(trifluoromethane) sulfonamide (Imi-TFSI).

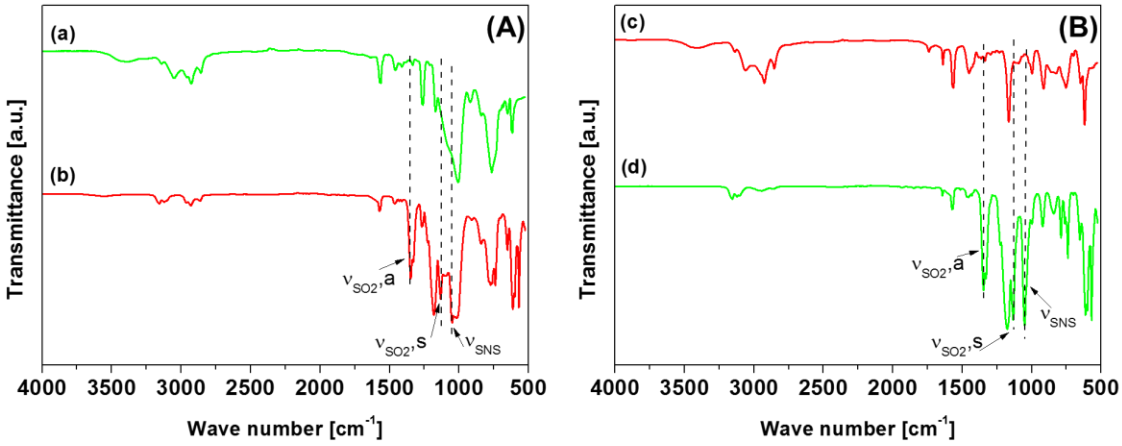

Figure 4.3. (A): ATR-IR spectra of (a) Imi-Br and (b) Imi-TFSI. (B): ATR-IR spectra of (c) PMHS-Imi-Br and (d) PMHS-Imi-TFSI. The dotted lines are guided to eyes.

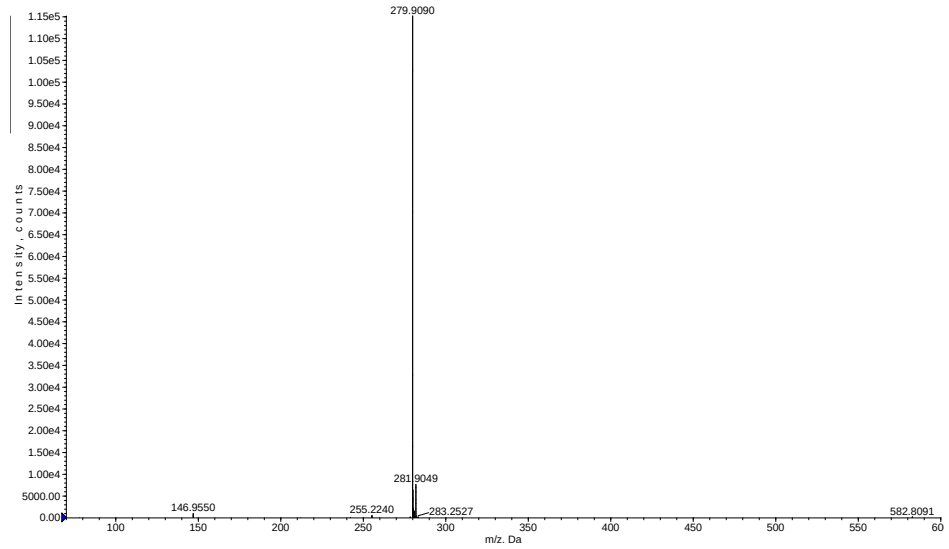

Figure 4.4. ESI-mass spectrum of PHMS-Imi-TFSI.

Moreover, due to the difference in hydrophobicity of anions in PMHS-Imi-Br and PMHS-Imi-TFSI, their solubility behavior was also investigated and the results are summarized in Table 4.1.

4.3.2 Ionic conductivity

In this PIL, TFSI anions are able to move freely while imidazolium cations are immobilized. Dielectric loss and conductivity vs frequency spectra of PHMS-Imi-TFSI are shown in Figure 4.5. Two clearly visible regions characterize the real part of the complex conductivity spectra: the power law behavior observed at higher frequencies and frequency-independent plateau that corresponds to the dc-conductivity σ_{dc}.

Figure 4.6 reveals that the movement of TFSI was coupled with the polymer segmental relaxation, perfectly fit to VFT behavior. Because of the flexible PDMS as backbone and the plasticizer effect of TFSI,[35] the room temperature ionic conductivity reached 3.3×10^{-5} S/cm. The ion transport shifted from Vogel-Fulcher-Tamman (VFT) behavior to Arrhenius behavior (green line in Figure 4.6) as the temperature dropped below T_g (T_g= -46.2 °C), which is a typical behavior observed in ionic systems. This is because the chain motion freezes below T_g, and the motion of ions were controlled by the diffusion.

Moreover, to provide microscopic details of the charge transport mechanism in examined PIL we also carried out high pressure dielectric measurements. As the pressure increased, the PIL was squeezed and the free volume decreased Figure 4.7 indicates that isothermal compression has basically the same effect on ion dynamics as isobaric cooling.

Table 4.1. The solubility of PMHS, PMHS-Imi-Br and PMHS-Imi-TFSI in several common solvents.

Sample name	Toluene	$CHCl_3$	Acetone	THF	MeOH	H_2O
PMHS	+	+	+	+	-	-
PMHS-Imi-Br	-	-	-	-	+	+
PMHS-Imi-TFSI	-	-	+	-	-	-

Denote: + is soluble; - is insoluble.

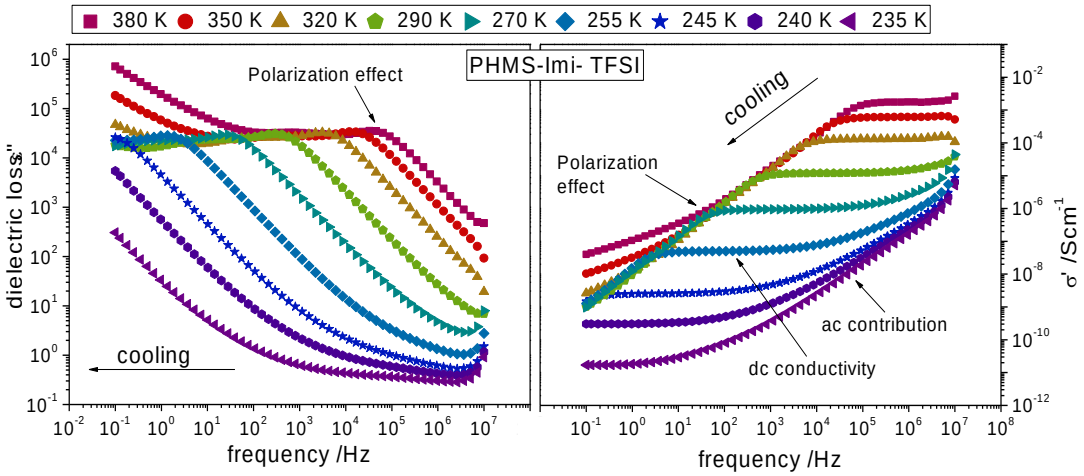

Figure 4.5. Dielectric loss and conductivity vs frequency spectra of PHMS-Imi-TFSI.

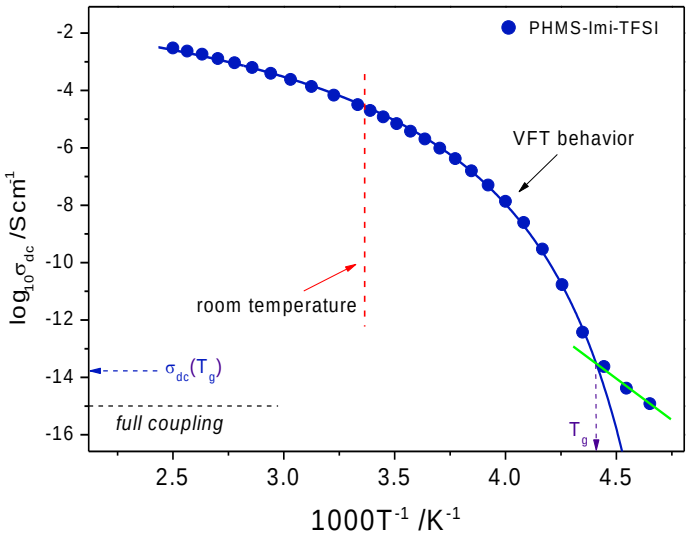

Figure 4.6. The ionic conductivity of PIL as a functional of 1000/T.

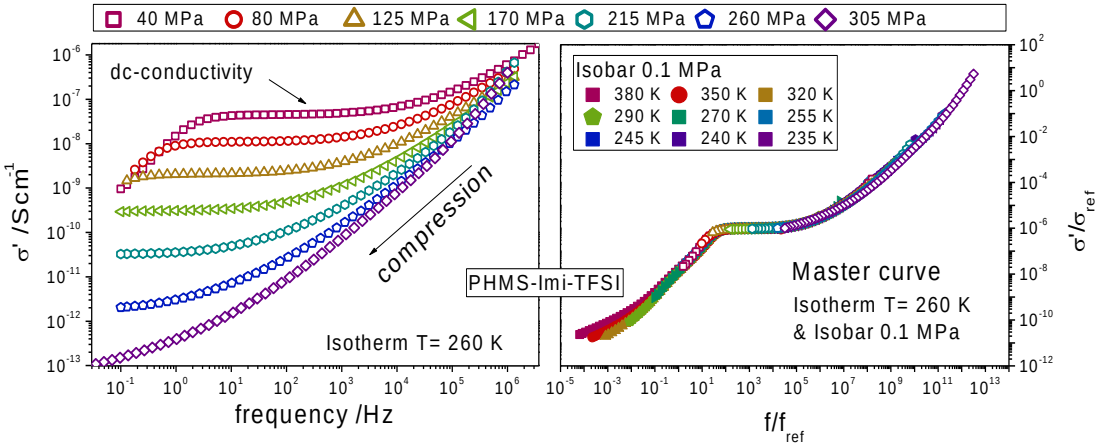

Figure 4.7. Ionic conductivity of PHMS-Imi-TFSI under different pressures.

At extremely high pressure the time scales of charge transport and segmental dynamics of PHMS-Imi-TFSI was found to be almost the same. In this PIL, only TFSI anion is freely moving through free volume associated with frustration in polymer chains packing. Therefore, any reduction of free volume, including compression-induced, should result in slowing down of charge transport at the same segmental relaxation time. PHMS-Imi-TFSI with the same TFSI counterion exhibits the smallest decoupling, consistent with the expectation that the most flexible chain should reveal better packing and lower free volume.

4.4 Conclusion

In this chapter, we introduced an efficient synthetic approach for PDMS based ionic liquids. Through hydrosilylation, quaternization and metathesis reaction, the desired PIL was synthesized successfully and further characterized using NMR and IR. By changing the anion, PIL showed varied solubility behavior. In addition, dielectric spectroscopy data showed a room temperature ionic conductivity of 3.3×10^{-5} S/cm. Under high pressure condition, the ionic conductivity dropped drastically due to the loss of free volume.

4.5 References

1. Scrosati, B.; Vincent, C. A., *MRS Bull.* **2000,** *25*, 28-30.

2. Fan, F.; Wang, Y.; Hong, T.; Heres, M. F.; Saito, T.; Sokolov, A. P., *Macromolecules* **2015,** *48*, 4461-4470.

3. Peters, G. P.; Andrew, R. M.; Canadell, J. G.; Fuss, S.; Jackson, R. B.; Korsbakken, Jan I.; Le Quéré, C.; Nakicenovic, N., *Nat. Clim. Change* **2017,** *7*, 118-122.

4. Wang, Y.; Sokolov, A. P., *Curr. Opin. Chem. Eng.* **2015,** *7*, 113-119.

5. Aoki, T.; Konno, A.; Fujinami, T., *Electrochim. Acta* **2004,** *50*, 301-304.

6. Fullerton-Shirey, S. K.; Maranas, J. K., *Macromolecules* **2009,** *42*, 2142-2156.

7. Xue, Z.; He, D.; Xie, X., *J. Mater. Chem. A* **2015,** *3*, 19218-19253.

8. Kelly, I.; Owen, J.; Steele, B., *J. Power Sources* **1985,** *14*, 13-21.

9. Fergus, J. W., *J. Power Sources* **2010,** *195*, 4554-4569.

10. Long, L.; Wang, S.; Xiao, M.; Meng, Y., *J. Mater. Chem. A* **2016,** *4*, 10038-10069.

11. Kamaya, N.; Homma, K.; Yamakawa, Y.; Hirayama, M.; Kanno, R.; Yonemura, M.; Kamiyama, T.; Kato, Y.; Hama, S.; Kawamoto, K.; Mitsui, A., *Nat Mater* **2011,** *10*, 682-6.

12. Wei, X.; Shriver, D. F., *Chem. Mater.* **1998,** *10*, 2307-2308.

13. Ngai, K. S.; Ramesh, S.; Ramesh, K.; Juan, J. C., *Ionics* **2016,** *22*, 1259-1279.

14. Mathews, K. L.; Budgin, A. M.; Beeram, S.; Joenathan, A. T.; Stein, B. D.; Werner-Zwanziger, U.; Pink, M.; Baker, L. A.; Mahmoud, W. E.; Carini, J. P.; Bronstein, L. M., *J. Mater. Chem. A* **2013,** *1*, 1108-1116.

15. Niedzicki, L.; Kasprzyk, M.; Kuziak, K.; Żukowska, G.; Armand, M.; Bukowska, M.; Marcinek, M.; Szczeciński, P.; Wieczorek, W., *J. Power Sources* **2009,** *192*, 612-617.

16. Yuan, F.; Chen, H.-Z.; Yang, H.-Y.; Li, H.-Y.; Wang, M., *Mater. Chem. Phys.* **2005,** *89*, 390-394.

17. Zhang, Z.; Sherlock, D.; West, R.; West, R.; Amine, K.; Lyons, L. J., *Macromolecules* **2003,** *36*, 9176-9180.

18. Gadjourova, Z.; Andreev, Y. G.; Tunstall, D. P.; Bruce, P. G., *Nature* **2001,** *412*, 520-523.

19. Fernicola, A.; Croce, F.; Scrosati, B.; Watanabe, T.; Ohno, H., *J. Power Sources* **2007,** *174*, 342-348.

20. Garcia, B.; Lavallée, S.; Perron, G.; Michot, C.; Armand, M., *Electrochim. Acta* **2004,** *49*, 4583-4588.

21. Matsumoto, H.; Sakaebe, H.; Tatsumi, K.; Kikuta, M.; Ishiko, E.; Kono, M., *J. Power Sources* **2006,** *160*, 1308-1313.

22. Scrosati, B.; Hassoun, J.; Sun, Y. K., *Energ Environ Sci* **2011,** *4*, 3287-3295.

23. Seki, S.; Kobayashi, Y.; Miyashiro, H.; Ohno, Y.; Usami, A.; Mita, Y.; Kihira, N.; Watanabe, M.; Terada, N., *J. Phys. Chem. B* **2006,** *110*, 10228-10230.

24. Howlett, P. C.; MacFarlane, D. R.; Hollenkamp, A. F., *Electrochem. Solid-State Lett.* **2004,** *7*, A97-A101.

25. Shin, J.-H.; Henderson, W. A.; Passerini, S., *Electrochem. Commun.* **2003,** *5*, 1016-1020.

26. Blazejczyk, A.; Szczupak, M.; Wieczorek, W.; Cmoch, P.; Appetecchi, G. B.; Scrosati, B.; Kovarsky, R.; Golodnitsky, D.; Peled, E., *Chem. Mater.* **2005,** *17*, 1535-1547.

27. Shin, J., *Electrochem. Commun.* **2003,** *5*, 1016-1020.

28. Bandara, L.; Dissanayake, M.; Mellander, B.-E., *Electrochim. Acta* **1998,** *43*, 1447-1451.

29. Horowitz, A. I.; Panzer, M. J., *Angew. Chem. Int. Ed.* **2014,** *53*, 9780-9783.

30. Chakraborty, R.; Soucek, M. D., *Macromol. Chem. Phys.* **2008,** *209*, 604-614.

31. Chojnowski, J.; Cypryk, M., Synthesis of linear polysiloxanes. In *Silicon-Containing Polymers*, Springer: 2000; pp 3-41.

32. Lötters, J.; Olthuis, W.; Veltink, P.; Bergveld, P., *J. Micromech. Microeng.* **1997,** *7*, 145.

33. Izák, P.; Ruth, W.; Fei, Z.; Dyson, P. J.; Kragl, U., *Chem. Eng. J.* **2008,** *139*, 318-321.

34. Fan, F.; Wang, W.; Holt, A. P.; Feng, H.; Uhrig, D.; Lu, X.; Hong, T.; Wang, Y.; Kang, N.-G.; Mays, J.; Sokolov, A. P., *Macromolecules* **2016,** *49*, 4557-4570.

35. Yoshizawa, M.; Ohno, H., *Electrochim. Acta* **2001,** *46*, 1723-1728.

CHAPTER 5 Synthesis of Well-Defined Poly(2-Isopropenyl-2-Oxazoline): Homopolymer And Block Copolymer via Living Anionic Polymerization

A version of this chapter was originally published by Hongbo Feng, Mohammad Changez, Kunlun Hong, Jimmy W. Mays and Nam-Goo Kang, 2-Isopropenyl-2-oxazoline: Well-Defined Homopolymers and Block Copolymers via Living Anionic Polymerization, *Macromolecules* **2017**, 50(1), 54-62.

Abstract

Poly(2-isopropenyl-2-oxazoline) (PIPOx) has drawn significant attention for numerous applications. However, the successful living anionic polymerization of 2-isopropenyl-2-oxazoline has not been reported previously. Herein, we describe how well-defined PIPOx with quantitative yields, controlled molecular weights from 6,800 to over 100,000 g/mol, and low polydispersity indices (PDI = 1.17) were synthesized successfully via living anionic polymerization using diphenyl methyl potassium/diethyl zinc (DPM-K/Et_2Zn) in tetrahydrofuran (THF) at 0 °C. In particular, we report the precise synthesis of well-defined PIPOx with the highest molecular weight ever reported (over 100,000 g/mol) and low PDI of 1.17. The resulting polymers were characterized by 1H- and 13C-nuclear magnetic resonance spectroscopy (NMR), along with size exclusion chromatography (SEC). Additionally, the reactivity of living PIPOx was investigated by crossover block copolymerization with styrene (St), 2-vinyl pyridine (2VP), and methyl methacrylate (MMA). It was found that the nucleophilicity of living PIPOx is of this order: living PS > living P2VP > living PMMA > living PIPOx. The self-assembly behavior in bulk of PIPOx-*b*-PS-*b*-PIPOx triblock copolymers having different block ratios of 10:80:10 and 25:50:25 was studied using transmission electron microscopy (TEM). The formation of spherical and lamellar nanostructures, respectively, was observed.

5.1 Introduction

Functional polymers containing heterocyclic units have received a great deal of attention and played critical roles in material science and polymer chemistry[1] because they demonstrate potentially exploitable properties such as optical, catalytic, electrochemical, sensory, photochemical, magnetic, and mechanical behavior.[2-3] Among heterocycle-containing monomers, 2-isopropenyl-2-oxazoline (IPOx) is quite versatile because 2-isopropenyl-2-oxazoline (IPOx), as a dual-functional monomer, can undergo living cationic ring-opening polymerization via the oxazoline moiety resulting in poly(2-oxazoline)s, which have found multiple pharmaceutical and medical applications.[4] In addition, IPOx can be polymerized through the vinyl moiety leading to poly(2-isopropenyl-2-oxazoline) (PIPOx). PIPOxs are water-soluble, showing specific reactivity in quaternization and addition reactions with a variety of nucleophiles,[5] and they can serve as an electron transporting medium in organic electronic divices.[6] Moreover, PIPOx-containing copolymers and block copolymers have shown the ability to form self-assembled nanostructures, such as micelles and vesicles, which show great potential for drug and gene delivery.[7-10]

For the preparation of these interesting oxazole-containing polymers, several research groups have demonstrated free radical, anionic, and RAFT (reversible addition fragmentation chain transfer) polymerization via the α-carbon, and cationic ring opening polymerization (CROP) through the β-carbon.[11] In this regard, Jordan *et al.* produced cylindrical molecular brushes on a modified silicon substrate via surface-initiated radical

polymerization and CROP of oxazoline units in PIPOx and thus studied their protein and cell adhesion behavior,[12] and Schubert *et al.* employed RAFT polymerization to synthesize PIPOx homopolymers and copolymers of IPOx with MMA and NiPAM (N-*iso*-propylacrylamide). The polydispersity indices (PDIs) of the resulting polymers were reduced significantly as compared with products of conventional free radical polymerization.[13] Atom-transfer radical polymerization (ATRP) of IPOx was also attempted, but it was not successful due to strong coordination of the Cu catalyst with the oxazoline moiety.[14]

Rieger *et al.* reported successful synthesis of well-controlled PIPOx materials (*M*W= 21,000 g/mol) with very low PDI and a yield of 95 % via rare earth metal-mediated group transfer polymerization (REM-GTP).[14] Recently, Kelland *et al.* studied the performance of a kinetic hydrate inhibitor using well-defined PIPOx synthesized anionically using the *n*-butyllithium (*n*-BuLi)/lithium chloride (LiCl) initiator system and obtained a maximum molecular weight (*M*W) of approximately 29,000 g/mol with PDI of 1.23.[15] To the best of our knowledge, none of these approaches have produced well-defined PIPOx with a combination of quantitative yield, very low PDI (≤ 1.15), and high *M*W (> 30,000 g/mol). Consequently, superior synthetic methods for the preparation of well-defined PIPOx and block copolymers containing PIPOx segments are required for specific applications and for creation of various nanostructures by self-assembly of amphiphilic homopolymers.[16-18]

Living anionic polymerizations has proven itself over the past 60 years to be the most powerful method for the synthesis of homopolymers and block copolymers with various tailored architectures and very low PDIs.[19-20] In this study, we developed novel synthetic methods to produce well-defined PIPOx with controlled molecular weight and narrow polydispersity via anionic polymerization in tetrahydrofuran (THF) using different initiators based on alkyllithiums and aryl potassium, with additives including 1,1-diphenylethylene (DPE), LiCl, and Et_2Zn at -78, -41, 0, and 25 °C. Well-defined PIPOx homopolymers with MW up to 100,000 g/mol were synthesized. To understand the living nature and reactivity of PIPOx, crossover sequential block copolymerizations of IPOx with styrene, 2-vinyl pyridine, and methyl methacrylate were carried out. The microphase self-assembly of PIPOx-*b*-PS-*b*-PIPOx block copolymers in bulk was also examined.

5.2 Experimental Section

Materials. The monomers 2-isopropenyl-2-oxazoline (IPOx, 99%, Aldrich), 2-vinyl pyridine (2VP, 99% Aldrich), styrene (St, 99%, Aldrich) and methyl methacrylate (MMA, 99%, Aldrich) were passed through basic alumina columns, dried over CaH_2 and twice distilled under reduced pressures of 10^{-1} and 10^{-6} mm Hg. These monomers were diluted and transferred to pre-calibrated ampoules equipped with break-seals under high vacuum conditions and stored at -30 °C. THF (Fisher scientific, HPLC grade) was distilled over potassium naphthalenide solution under reduced pressure (10^{-6} mm Hg) on a high vacuum line.

Initiators. *n*-Butyllithium (*n*-BuLi) solution (1.6 M in hexanes, Aldrich) and *sec*-butyllithium (*sec*-BuLi) solution (1.4 M in cyclohexane, Aldrich) were diluted and ampoulized on a high vacuum line. Lithium chloride (99.999%, LiCl, Aldrich) was dried at 130 °C for 2 days and then diluted to the target concentration in THF and ampoulized under a reduced pressure of 10^{-6} mm Hg. Sodium (Na-Naph) and potassium naphthalenide (K-Naph) were prepared by the reaction of the corresponding metal with naphthalene in THF at room temperature for 48 h. Diphenyl methyl potassium (DPM-K) was prepared by the reaction of K-Naph with diphenylmethane in THF under high vacuum conditions at room temperature for 72 h.[21-22] (3-Methyl-1,1-diphenylpentyl)lithium was prepared by adding *s*-BuLi solution dropwise to 1,1-diphenylethylene (DPE). Triphenylmethyl potassium (TPM-K) was prepared by the reaction of triphenylmethane (TPM, Aldrich, 99%) and potassium in THF at room temperature for 2 days, and the excess K metal was removed by passing the solution through a glass filter under high vacuum conditions.[23] Concentrations of DPM-K and TPM-K were determined by titration using octyl alcohol and used for anionic polymerization. All initiators were sealed off under high vacuum into ampoules with break seals and stored at -30 °C.

Instrumentation. NMR spectra were recorded on a liquid state Varian VNMRS 500 MHz spectrometer at 25 °C. The internal standard was $CDCl_3$ at 7.26 ppm. Attenuated Total Reflection-IR (ATR-IR) spectra were obtained using a Nicolet iS50 FT-IR spectrometer equipped with a deuterated triglycine sulfate (DTGS) detector. Size exclusion chromatography (SEC) was performed on a modular (Waters pump Model 515 HPLC,

Knauer RI detector, Mini-DAWN multi-angle light scattering detector) using PSS columns as the stationary phase and *N, N*-dimethylformamide (DMF, T = 25 °C, 1 mL/min) as the mobile phase. The calculation of the weight-average molecular weight (M_w) and number-average molecular weight (M_n) was based on PS standards and, in some cases, light scattering. Before each SEC measurement, a solution of the polymer sample in DMF was prepared at a concentration of 2.0 mg/ml and filtered through a 0.2 μm pore size PTFE filter. The specific refractive index increment (dn/dc = 0.01048 mL/g) was determined using the Wyatt Optilab Rex in DMF at 25 °C with a laser, λ = 658.0 nm. Transmission electron microscopy (TEM) images were acquired using a ZEISS LIBRA 200 instrument. The TEM samples were first annealed at 180 °C under high vacuum for 4 days, trimmed and microtomed into ~40 nm thick slices. The thin slices were then loaded onto carbon coated TEM grids and stained with iodine vapor for 30 min before use. Differential scanning calorimetry (DSC) was performed on a TA Q2000 instrument with a scanning rate of 5 °C/min under N_2 atmosphere. In order to eliminate the effect of thermal history, the second heating cycle was selected for use in measuring the glass transition. Thermal gravimetric analysis (TGA) was performed on a TA Q50 instrument with a heating rate of 10 °C/min under N_2 flow.

5.2.1 Synthesis of IPOx Homopolymers via Anionic Polymerization.

Anionic polymerization of IPOx with *n*-BuLi. The anionic polymerization of IPOx was performed in glassware equipped with break seals under high vacuum (10^{-6} mm Hg) for 120 min. *n*-BuLi (0.054 mmol) in heptane (2.50 mL) was transferred into the

reaction flask and thermally equilibrated at -78 °C. Chilled solution of IPOx (5.01mmol) in THF (6.40 mL) was then added to the initiator solution. The polymerization mixture was kept at this temperature for 120 min and terminated with degassed methanol (1.00 mL). Then the reaction mixture was concentrated and dissolved in chloroform, precipitated from diethyl ether twice and dried in a vacuum oven at 40 °C.

Anionic polymerization of IPOx with DPM-K. The procedure of anionic polymerization and purification was followed as described above, except using DPM-K as an initiator instead of *n*-BuLi at -78 and 0 °C.

Anionic polymerization of IPOx with s-BuLi and DPE. DPE (0.15 mmol) in THF (1.53 mL) was added to *s*-BuLi (0.058 mmol) solution in heptane at -78 °C. The color turned from colorless to yellow indicating (3-methyl-1,1-diphenylpentyl)lithium was formed. The chilled solution of IPOx (5.18 mmol) in THF (6.60 mL) was then added to the initiator mixture after 30 min. Polymerization was terminated with degassed methanol. The purification procedure was performed as described above.

Anionic polymerization of IPOx with DPM-K and Et_2Zn. A typical polymerization procedure is described as follows. The solution of DPM-K (0.093 mmol) in THF (4 mL) was transferred to main reactor at -78 °C and the solution of Et_2Zn (1.76 mmol) in THF (2 mL) was added to DPM-K solution at -78 °C. The solution of IPOx monomer (7.28 mmol) in THF (9.30 mL) was then added to the initiator mixture and the solution was maintained at -78 °C for 30 min to allow for complete initiation. The propagation in anionic polymerization was performed for 10 to 24 h at -78, -41, 0, and 25

°C. The polymerizations were terminated with degassed methanol. The purification of the polymer was performed as described above. The resulting polymer was characterized by SEC, DSC, TGA, ^{1}H- and ^{13}C-NMR, and FT-IR. ^{1}H-NMR spectra (500 MHz, $CDCl_3$), δ (ppm) = 4.08 - 4.25 (2H, CH_2 of the pendant oxazoline), 3.65 - 3.85 (2H, CH_2 of the pendant oxazoline), 1.70 - 2.00 (2H, CH_2 of the polymer backbone), 1.01 - 1.56 (3H, α-CH_3). ^{13}C-NMR spectra (75 MHz, $CDCl_3$), δ (ppm) = 172.97 (C, N=C-O of the pendant oxazoline), 66.95 and 54.27 (CH_2-CH_2 of the pendant oxazoline), 40.11 (CH_2 of the polymer backbone), 20.00 and 18.00 (α-CH_3, heterotactic and syndiotactic). FT-TR (cm^{-1}): 2928 (C-H stretch, m), 1652 (C=N, stretch, s), 1125 (C-O (unconjugated), stretch, s), 991, 960, 928 (oxazoline ring skeleton vibration).

Anionic polymerization of IPOx with K-NaPh, Na-NaPh, and TPM-K. The solution of K-Naph, Na-Naph, and TPM-K in THF, respectively, was transferred into the reaction flask and then the solution was thermally equilibrated at -78 °C. The chilled solution of IPOx in THF was added to the initiator solution and polymerization was carried out at -78 °C for 10 and 12 h. After terminating with degassed methanol, the polymers were obtained as described above.

5.2.2 Synthesis of IPOx Block Copolymers via Anionic Polymerization.

Block copolymerization of 2VP with IPOx using DPM-K and Et_2Zn. Living poly(2-vinylpyridine) was prepared via living anionic polymerization using DPM-K at -78 °C for 30 min in an all-glass apparatus under reduced pressure of 10^{-6} mm Hg, as reported previously.[24-25] A small portion of living poly(2-vinyl pyridine) (P2VP) solution was

transferred to an attached receiver and then characterized by SEC to determine M_n of first block P2VP. The solution of Et_2Zn in THF was then added to the remainder of the living P2VP solution, followed by addition of IPOx monomer. The monomer IPOx was initiated at -78 °C for 5 min and then the anionic polymerization was kept at 0 °C for 12 h. The polymers were obtained as described earlier. The resulting block copolymer was characterized by SEC, ^{1}H-NMR. ^{1}H-NMR spectra (500 MHz, $CDCl_3$), δ (ppm) = 8.51-8.08(pyridine), 7.51-6.98 (pyridine), 6.96-6.64 (pyridine), 6.55-6.10 (pyridine). 4.31-3.91 (CH_2 of the pendent oxazoline), 3.91-3.44 (CH_2 of the pendent oxazoline), 2.05-1.52 (CH_2 of the polymer backbone), 1.42-0.89 (α-CH_3).

Block copolymerization of MMA with IPOx. The solution of DPM-K and Et_2Zn in THF was added to the glass apparatus and thermally equilibrated at -78 °C. The solution of MMA in THF was then added. After 30 min, a small portion of the living PMMA solution was transferred to an attached receiver, and the polymer was characterized by SEC to obtain M_n of first block, PMMA. The chilled solution of IPOx in THF was then added at -78 °C with vigorous shaking. After 5 min, the polymeric mixture was warmed to 0 °C, kept at 0 °C for 12 h, and terminated with degassed methanol. The polymers were obtained as described earlier. The resulting block copolymer was characterized by SEC and ^{1}H-NMR. ^{1}H-NMR spectra (500 MHz, $CDCl_3$), δ (ppm) = 4.31-4.07 (CH_2 of the pendent oxazoline), 3.88-3.68 (CH_2 of the pendent oxazoline), 3.62-3.53 (-O-CH_3, ester), 2.10-1.56 (CH_2 of the polymer backbone), 1.31-0.74 (α-CH_3).

Block copolymerization of Styrene with IPOx. The synthesis of PIPOx-*b*-PS-*b*-PIPOx (f_{PIPOx}=0.5) is described as follows. The solution of K-Naph (0.087 mmol) in THF (4.10 mL) was added to an all-glass apparatus at -78 °C and the chilled solution of St (14.10 mmol) in THF (19.80 mL) was then added. The polymerization was kept at -78 °C for 40 min. A portion of the living PS solution was transferred to an attached receiver and the polymer was characterized by SEC to obtain M_n of the first block, PS. The solution of DPE (0.23 mmol) in THF (2.40 mL) was then added to the living PS solution, followed by Et_2Zn (1.04 mmol in 4 mL THF). The reaction mixture maintained at -78 °C for 30 min. The chilled solution of IPOx (14.67 mmol) in THF was then added with vigorous shaking for complete initiation. After 5 min, the solution was warmed to 0 °C, kept at this temperature for 12 h, and terminated with degassed methanol. The polymer purification procedure was performed as described earlier. The resulting block copolymer was characterized by SEC, DSC and ^{1}H-NMR. ^{1}H-NMR spectra (500 MHz, $CDCl_3$), δ (ppm) = 7.17-6.38 (phenyl), 4.21-4.03 (CH_2 of the pendent oxazoline), 3.86-3.61 (CH_2 of the pendent oxazoline), 2.05-1.33 (CH_2 of the polymer backbone), 1.31-0.97 (α-CH_3).

5.3 Results and Discussion

5.3.1 Homopolymerization of IPOx with Different Initiation Systems.

All of the polymerizations in this work were carried out using high-vacuum and glass blowing techniques.[26] The conditions and results for homopolymerization using different initiators, additives, reaction time, and temperatures are summarized in Table 5.1**.**

Table 5.1. Synthesis of poly(2-isopropenyl-2-oxazoline) with different initiation systems in THF.

Run	IPOx	Initiator	Additive	Time	Temp	Yield[a]	M_n ($\times 10^{-3}$ g/mol)		PDI[c]
	mmol	mmol	mmol	h	°C	%	calcd[b]	obsd[c]	
1	5.01	*n*-BuLi, 0.054	None	2	-78	57.8	10.3	8.8	2.38
2	5.74	DPM-K, 0.065	None	2	-78	40.3	9.8	24.6	1.40
3	4.95	DPM-K, 0.071	None	2	0[d]	70.0	7.8	22.3	1.52
4	5.18	s-BuLi/DPE, 0.058/0.150	LiCl, 0.45	2	-78	40.0	7.7	6.80	1.13
5	6.72	s-BuLi/DPE, 0.073/0.293	LiCl, 0.49	10	-78	64.1	10.2	6.2	1.48
6	8.57	DPM-K, 0.076	Et_2Zn, 1.00	10	-78	73.0	12.7	9.6	1.12
7	9.23	DPM-K, 0.102	Et_2Zn, 1.00	24	-78	68.0	10.1	8.0	1.13
8	8.27	DPM-K, 0.087	Et_2Zn, 1.00	10	-45	60.4	10.6	7.8	1.15
9	7.28	DPM-K, 0.093	Et_2Zn, 1.76	10	0	100	6.9	6.8	1.10
10	10.20	DPM-K, 0.090	Et_2Zn, 1.35	12	25[e]	100	12.6	12.3	1.15
11	11.64	DPM-K, 0.023	Et_2Zn, 0.31	20	25	84.3	55.7	36.3	1.25
12	21.53	DPM-K, 0.031	Et_2Zn, 0.47	36	25	94.3	77.2	45.7	1.57
13	13.20	K-Naph, 0.189	None	12	0	100	15.5	14.0	1.30
14	9.10	Na-Naph, 0.180	None	10	0	100	11.2	16.0	1.50
15	8.85	TPM-K, 0.066	None	10	0	99.9	14.9	49.1	1.31

[a]Yield was calculated by the ^{1}H-NMR integration of corresponding peaks. [b]M_n(calcd)=(MW of IPOx) × [IPOx]/[initiator]× f × yield of polymer (%); f = 1 or 2, corresponding to functionality of the initiators. [c]M_n(obsd) and PDI were determined by SEC against narrow polystyrene standard in DMF at 25 °C. [d]0: polymerization was initiated at -78 °C for 5 min and then temperature was increased to 0°C. [e]25: the polymerization was initiated at -78 °C for 5 min and then the temperature was increased to 25 °C.

Initially, the effect of various initiation systems (initiators and combinations of initiator/additive) on homopolymerization of IPOx were investigated. The initiation systems include *n*-BuLi, DPM-K, TPM-K, *s*-BuLi/DPE/LiCl, and DPM-K/Et_2Zn. The homopolymerization of IPOx, which has the strong electron withdrawing oxazoline unit (N=C-O), using *n*-BuLi at -78 °C resulted in low yield (57.8%) and very high PDI (2.38) due to side reactions (Run 1 in Table 5.1). These size reactions could occur through the possible mechanisms of the termination and/or chain transfer of the propagating species via H^+ abstraction during the polymerization, as shown in Scheme 1.[6, 11, 27] To circumvent such nucleophilic attack, DPM-K, a weaker nucleophile, was used to initiate the anionic polymerization of IPOx. However, this polymerization also showed low yield (40.3%) and rather high PDI (1.40) at -78 °C. The conversion was improved to 70% by increasing the reaction temperature from -78 °C to 0 °C (Run 2 in Table 5.1). The polymerization initiated by the even bulkier initiator of TPM-K exhibited quantitative yield. However, the observed M_n is almost three times higher than calculated M_n and the PDI was high (1.31, Run 15 in Table 5.1). It was thus concluded that the TPM-K is not sufficiently nucleophilic to completely initiate the polymerization of IPOx and that possible side reactions still occurred.

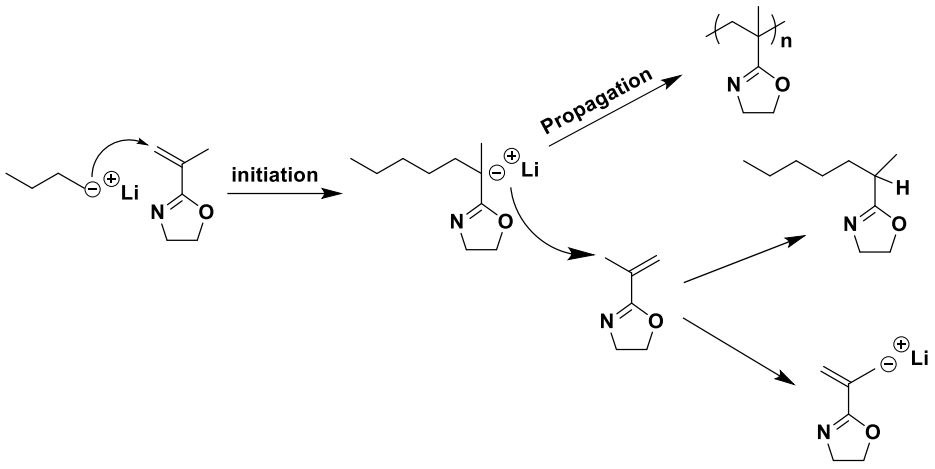

Scheme 5.1. The mechanism of possible side reactions via termination and chain transfer by H^+ abstraction in the polymerization of IPOx using *n*-BuLi as initiator.[6, 11, 27]

To further suppress the side reactions during the polymerization, additives such as DPE, LiCl, and Et_2Zn were employed as coordinating ligands along with *s*-BuLi and DPM-K. The *s*-BuLi/DPE system with ~15 eq of LiCl (*s*-BuLi/DPE/LiCl), regarded as an efficient initiation system for the synthesis of living PMMA,[28-29] was used for the polymerization of IPOx. The polymerizations at -78 ^oC were controlled with rather low PDI (1.13) but the yield was only 40% after 2 h (Run 4 in Table 5.1). In order to obtain quantitative conversion, the reaction time was increased to 10 h. Unfortunately, a low yield (64.1%) was still obtained and the PDI turned out to be even higher (Run 5 in Table 5.1). On the other hand, polymerization initiated by DPM-K/Et_2Zn at -78°C was well-controlled even with increased polymerization times (Run 6 and 7 in Table 5.1). This could be attributed to the polarizability of the carbanion/K^+ ion pair being higher than that of the carbanion/Li^+ and carbanion/Na^+ ion pairs during propagation, caused by the different radii

of the counter ions ($K^+ > Na^+ > Li^+$).[29] Reaction time was further increased to 24 h but the yield was only 68% (Run 7 in Table 5.1). It should be noted that the polymeric mixture became turbid during propagation. This heterogeneous solution of the polymeric mixture caused by the low solubility of PIPOx in THF at -78 °C limited the synthesis of polymer having molecular weight over 9,600 g/mol. We speculate that the propagating chains were trapped in the aggregates so that it was difficult for the chain end carbanion to attack the incoming monomer, leading to low conversion.

Additionally, to investigate the effect of polymerization temperature, the polymerizations were carried out at -45, 0, and 25 ^{o}C, respectively (Runs 8, 9, & 10 in Table 5.1). Surprisingly, the low PDI (1.10) and quantitative yield (100%) could be achieved via anionic polymerization even at 0 °C (Run 9 in Table 5.1). The polymerization using 20 eq of Et_2Zn at 25 ^{o}C also produced polymer with low PDI and in quantitative yield within 10 h (Run 10 in Table 5.1). It thus appears that Et_2Zn is an effective ligand to suppress side reactions during anionic polymerization of these monomers. However, as the polymerization time was increased to over 12 h at 25 °C, side reactions turned to be substantial as indicated by large PDIs (Runs 11 and 12 in Table 5.1**)**. The polymerization mixture was hazy in appearance with a gel-like substance present. It is thus concluded that temperature should not be above 0 °C in order to produce well-defined PIPOx.

Furthermore, to demonstrate the unique merit of our anionic polymerization method, PIPOx was also synthesized via RAFT polymerization. In contrast to RAFT polymerization in toluene at 70 °C (Figure 5.1 blue line), RAFT polymerization reported

elsewhere,[13, 15] and anionic polymerization initiated by *n*-BuLi (Run 1 in Table 5.1**,** Figure 5.1c red line), our synthetic approach produced well-defined polymers as shown in Figure 5.1a (black line). In particular, anionic polymerization using DPM-K/Et_2Zn in THF at 0 °C showed quantitative yield.

In ^{13}C-NMR spectra of PIPOx homopolymer (Figure 5.2A), the 121.52 ppm and 132.65 ppm peaks of vinyl groups disappeared completely after living anionic polymerization and 40.27, 19.96, and 17.80 ppm peaks of main chain of PIPOx polymer were generated. FT-IR spectra also verified that the ring skeleton vibration (991, 958 and 930 cm^{-1}) was intact after polymerization as shown in Figure 5.2B. The resulting homopolymers of PIPOx were characterized by ^{1}H-NMR (Figure 5.3). The ^{1}H-NMR spectra of PIPOx demonstrated the successful anionic polymerization. The vinyl proton signals at 5.76 and 5.39 ppm disappeared completely and new peaks at 1.76-2.13 ppm emerged from protons of methylene on the polymer backbone. On the other hand, the signals corresponding to protons of the oxazoline ring shift slightly from 3.92 and 4.26 ppm to 3.76 and 4.16 ppm, respectively. Moreover, detailed analysis of α-methyl protons reveals that the tacticity ratio of isotactic (i): heterotactic (h): syndiotactic (s) = 13.6: 39.7: 46.7.

Two characteristic absorption peaks of monomer at 1606 cm^{-1} (C=C, stretch) and 1281 cm^{-1} (C=O (conjugated), stretch) were disappeared after polymerization indicating the isopropenyl group was reacted completely. Thus, it was confirmed that well-defined

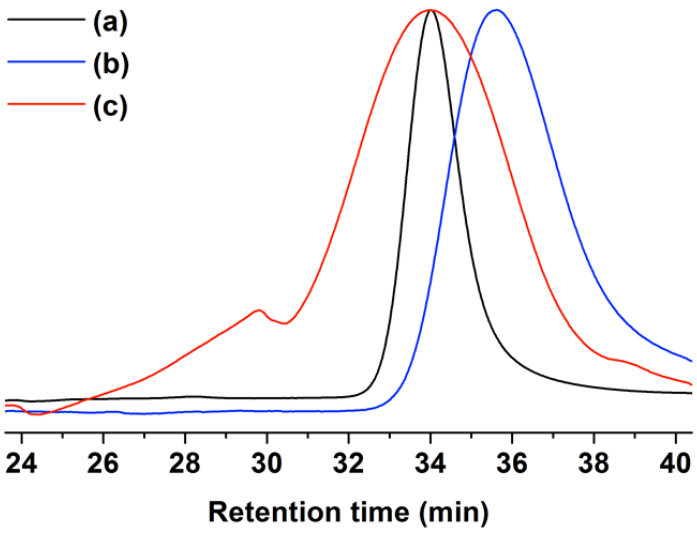

Figure 5.1. SEC curves of PIPOx synthesized by (a) anionic polymerization using DPM-K/Et_2Zn in THF at 0 °C (Mn = 6,800 g/mol and PDI = 1.10), (b) RAFT in toluene at 70 °C (M_n = 1,900 g/mol and PDI = 1.23) and (c) anionic polymerization using *n*-BuLi in THF at -78 °C.

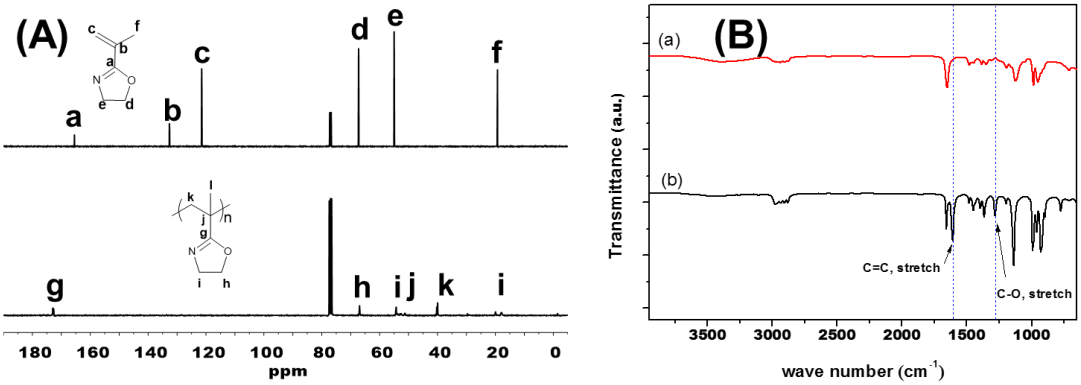

Figure 5.2. (A) 13C-NMR spectra of IPOx and PIPOx. (B) ATR-IR spectra of (a) PIPOx and (b) IPOx.

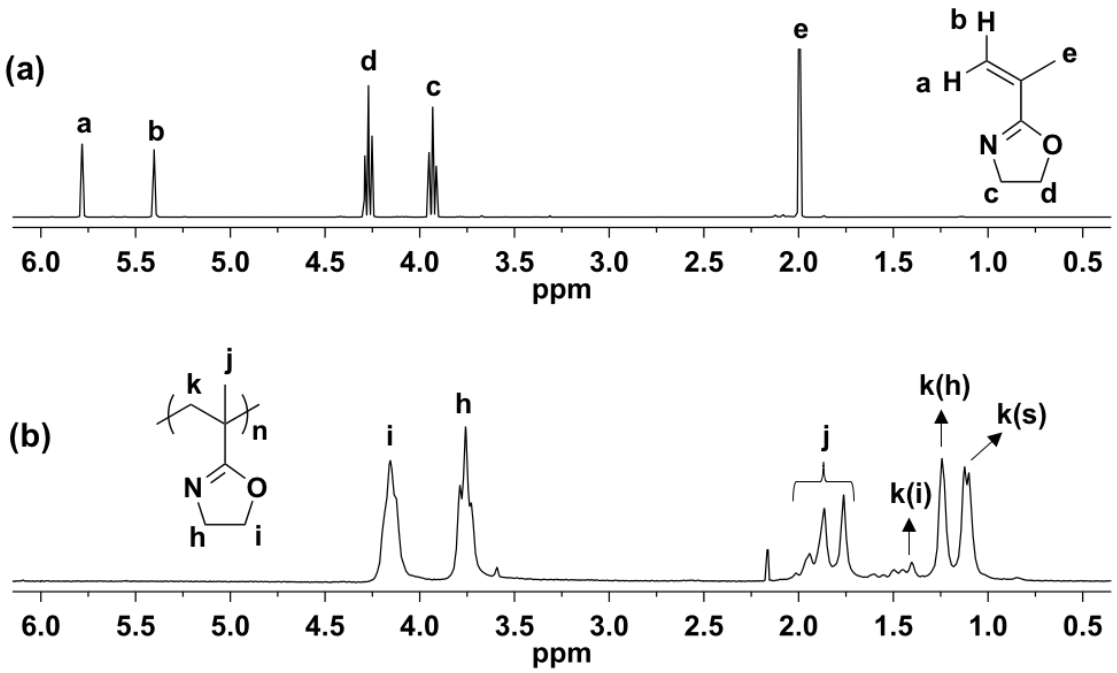

Figure 5.3. ^{1}H-NMR spectra of (a) IPOx and (b) PIPOx. Denote: (i) isotactic, (h) heterotactic, and (s) syndiotactic.

PIPOx was synthesized by living anionic polymerization with DPM-K/Et_2Zn as the initiation system.

Several anionic polymerizations targeting different *M*Ws were carried out using the optimized reaction condition as shown in Table 5.2 and Scheme 5.2.

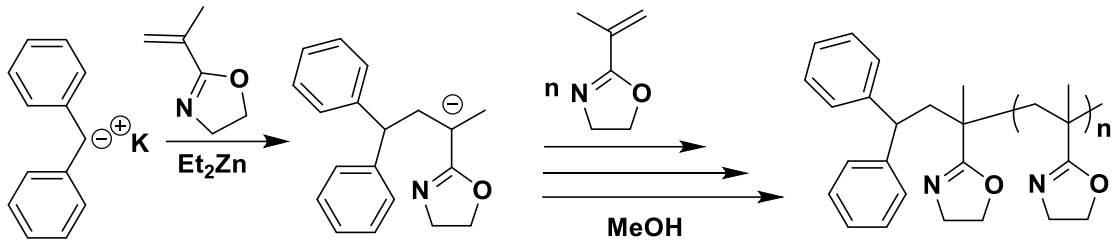

Scheme 5.2. Synthesis of PIPOx using DPM-K/Et_2Zn initiation system in THF at 0 °C.

Well-defined polymers with molecular weights from 6,800 to 104,400 g/mol and low PDIs from 1.12 to 1.17 were synthesized successfully by controlling the molar ratios of the IPOx to DPM-K/Et_2Zn, and their SEC profiles are shown in Figure 5.4. The synthesis of PIPOx with very high molecular weight (M_n > 100,000 g/mol) is reported for the first time to the best of our knowledge. The theoretical molecular weights (calcd M_n) are in good agreement with values from SEC, and a linear relationship between M_n and the feed ratio of monomer to initiation system is observed as shown in Figure 5.4.

Table 5.2. Living anionic polymerization of IPOx in THF at 0 °C using DPM-K in the presence of Et_2Zn.

run	IPOx	DPM-K[d]	Et_2Zn	Time	Yield[e]	M_n ($\times 10^{-3}$ g/mol)			PDI[b]
	mmol	mmol	mmol	h	%	calcd[a]	obsd[b]	obsd[c]	
1	8.57	0.0928	1.00	10	100	10.3	9.6	13.7	1.09
2	11.53	0.0756	1.32	10	100	18.7	16.2	20.9	1.13
3	11.54	0.0419	0.63	10	100	28.2	24.6	28.5	1.15
4	12.50	0.0323	0.47	15	100	43.0	38.0	50.3	1.15
5	15.83	0.0230	0.30	21	100	76.5	76.2	105.1	1.12
6	18.56	0.0190	0.30	24	100	108.6	104.4	133.2	1.17

[a]M_n(calcd)=(MW of IPOx)×[IPOx]×yield/[initiator]. [b]M_n(obsd) and PDI were determined by SEC with calibration using narrow polystyrene standard in DMF as eluent at 25°C. [c]M_n(obsd) was determined using light scattering detection in DMF at 25°C. The value of dn/dc is 0.01048 mL/g. [d]DPM-K: diphenylmethyl potassium. [e]Yield was calculated from the ^{1}H-NMR integration of corresponding peaks.

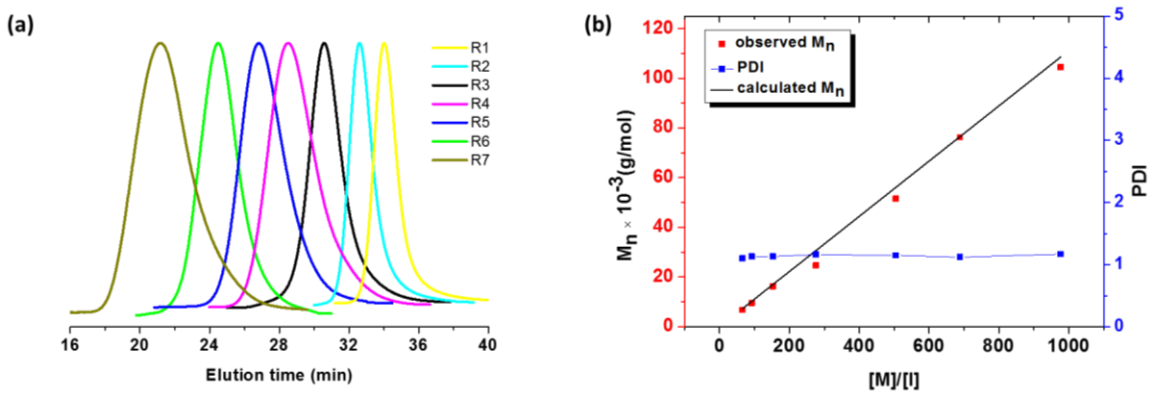

Figure 5.4. (a) SEC curves of homopolymer PIPOx. (R1: 6,800 g/mol (Run9 in Table 5.1), R2: 9,600 g/mol, R3: 16,200 g/mol, R4: 24,600 g/mol, R5: 38,000 g/mol, R6: 76,200 g/mol and R7: 104,000 g/mol in Table 5.2). (b) Plot of molecular weight (M_n) and PDI vs feed ratio of IPOx monomer to DPM-K initiator.

The glass transition temperatures (T_g) of PIPOx homopolymers were characterized using DSC. Figure 5.5a shows DSC curves of six samples of PIPOx homopolymer with M_n ranging from 6,800 to 104,400 g/mol. The plot of T_g vs M_n plot (Figure 5.5b) shows that at high M_n (> 24,600 g/mol) there is no dependence of the T_g on M_n. However, as M_n decreases (< 24,600 g/mol), there is a sharp drop of from 173.1°C to 165.5 °C at M_n of 6,800 g/mol. As compared with other nitrogen-containing polymers, the T_g of PIPOx is much higher than the T_g of poly(*N*-isopropylacrylamide) (PNiPAM) (110 to 150 °C)[30], similar to the T_g of poly(*N*-methacryloylazetidine) (PNMAA) (168 °C)[31], and lower than that of poly(2-isopropenylbenzoxazole) (PIPBOz) (195 °C)[6].

5.3.2 Block copolymerization of IPOx with 2VP, MMA and St.

A key advantage of sequential living anionic polymerization is the facile preparation of various precisely tailored block copolymers. Block copolymerizations of IPOx with 2VP and MMA were thus conducted using the optimized initiation system of DPM-K/Et_2Zn in THF at 0 °C. The sequential block copolymerization of IPOx as the first monomer with 2VP and MMA as the second monomer only afforded homopolymers of PIPOx (Runs 2 and 4 in Table 5.3). This indicates that the nucleophilicity of living PIPOx is not strong enough to initiate 2VP and MMA, and therefore reactivity of the carbanions is in the order of living PIPOx < living PMMA < living P2VP.

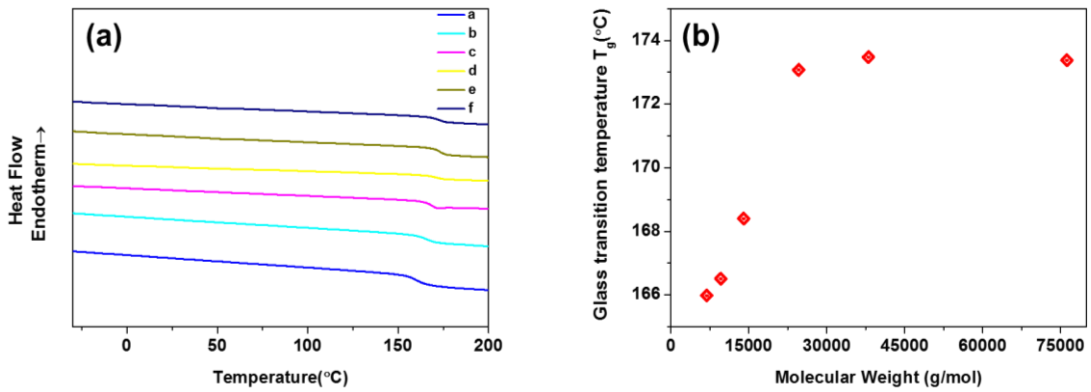

Figure 5.5. (a) DSC curves of PIPOx homopolymer with a) 6,800 g/mol (T_g=165.9 °C), b) 9,600 g/mol (T_g=166.5 °C), c) 16,200 (T_g=168.4 °C), d) with 24,600 (T_g=173.1 °C), e) 38,000 g/mol (T_g=173.5 °C), and f) 76,200 g/mol (T_g=173.4 °C) and (b) relationship between molecular weight and glass transition temperature.

Table 5.3. Cross-over block copolymerization of IPOx with 2VP and MMA using DPM-K in the presence of Et_2Zn in THF.

run	Monomer1		Monomer2		DPM-K/Et_2Zn[c]	time	Temp.	M_n($\times10^{-3}$ g/mol)		
	mmol		mmol		mmol/mmol	h	°C	calcd[a]	obsd[b]	PDI[c]
1	2VP[c]	3.21	IPOx	9.50	0.115/1.81	2/11	-78/0[d]	12.1(2.9)	12.5(3.0)	1.16
2	IPOx	7.65	2VP	3.60	0.104/1.85	11/2	0/-78	11.8(8.1)	8.1(8.1)	1.12
3	MMA[c]	5.00	IPOx	19.6	0.123/1.85	1/10	-78/0	21.8(4.1)	22.5(4.9)	1.13
4	IPOx	12.25	MMA	5.00	0.112/2.01	10/1	0/-78	16.6(12.2)	9.5(9.5)	1.10

[a]M_n(calcd) = (MW of Monomer1) × [Monomer1]/[initiator] + (MW of Monomer2) × [Monomer2]/[initiator] × yield. [b]M_n(obsd) of the block copolymer and PDI of block copolymer were determined by SEC with calibration using narrow polystyrene standards in *N, N*-dimethylformamide (DMF) as eluent at 25 °C. [c]2VP: 2-vinylpyridine, MMA: methylmethacrylate, DPM-K: diphenylmethyl potassium, and Et_2Zn: diethylzinc. [d]Polymerization was initiated at -78 °C for 5 min and the temperature was then increased to 0 °C.

Sequential block copolymerization with IPOx as the second monomer thus yielded well-defined diblock copolymers of P2VP-*b*-PIPOx and PMMA-*b*-PIPOx (Runs 1 and 3 in Table 5.3), as shown in Scheme 5.3a and b.

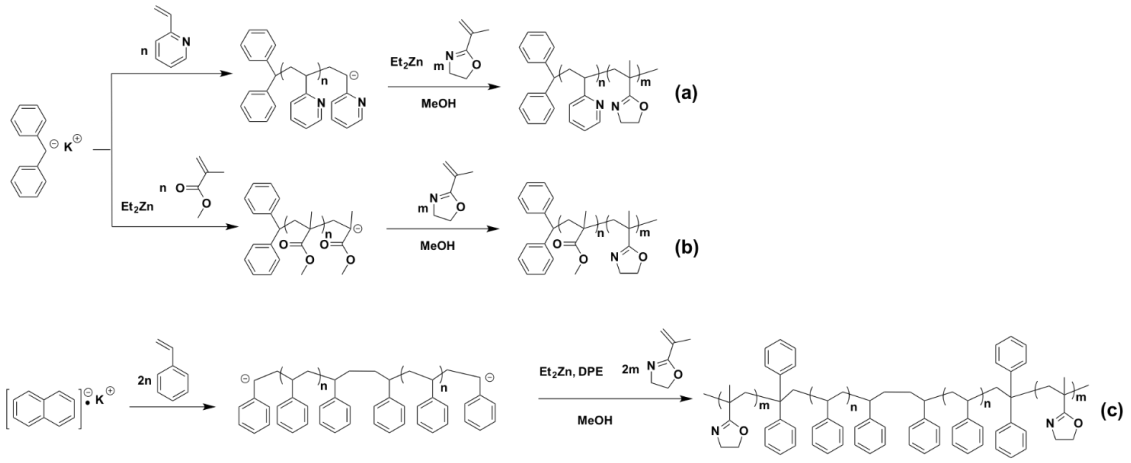

Scheme 5.3. The synthetic routine of (a) P2VP-*b*-PIPOx, (b) PMMA-*b*-PIPOx and (c) PIPOx-*b*-PS-*b*-PIPOx.

In addition, amphiphilic triblock copolymers of PIPOx-*b*-PS-*b*-PIPOx with different block compositions (PIPOx: PS: PIPOx = 25:50:25, 10:80:10 and 40:20:40) were synthesized via sequential living anionic polymerization using the bi-directional initiator of K-Naph with DPE in the presence of Et_2Zn as shown in Scheme 5.3c. The results of triblock copolymerizations are summarized in Table 5.4.

Table 5.4. Synthesis of PIPOx-*b*-PS-*b*-PIPOx triblock copolymers with different block ratios.

Run	St[d]	IPOx	K-Naph[d]	DPE/Et_2Zn[d]	M_n($\times10^{-3}$g/mol)				Block ratio
	mmol	mmol	mmol	Mmol	calcd[a]	obsd[b]	obsd[c]	PDI[b]	
1	14.40	14.67	0.087	0.230/1.040	61.9	63.2	74.6	1.14	25:50:25
2	11.47	2.84	0.055	0.155/0.750	54.9	76.7	60.9	1.17	10:80:10
3	3.84	15.28	0.065	0.222/0.910	64.6	76.3	66.4	1.12	40:20:40

[a]M_n(calcd) = (MW of Monomer1) × [Monomer1]/[initiator] + (MW of Monomer2) × [Monomer2]/[initiator]. [b]M_n(obsd) and [b]PDI of block copolymer were determined by SEC with calibration using narrow polystyrene standards in DMF at 25 °C. M_n(obsd)[c] was determined by light scattering. dn/dc of PS=0.16 ml/g [d]St: styrene, K-Naph: Potassium naphthalenide, DPE: 1,1-diphenylethylene, and Et_2Zn: diethylzinc. [e]Polymerization was initiated at -78 °C for 5 min and then the temperature was increased to 0 °C.

The successful sequential block copolymerization was proven by the shift of the SEC profile from homopolymer PS of 11,900 g/mol and PDI = 1.06 to PIPOx-*b*-PS-*b*-PIPOx of 76,300 g/mol and PDI = 1.12 (Run 3 in Table 5.4), as shown in Figure 5.6a. Moreover, the block ratio was determined by ^{1}H-NMR (Figure 5.6b). The successful synthesis of these block copolymers based on IPOx are the first reported via living anionic polymerization. Upon introducing the polystyrene block, the DSC profile of PIPOx-*b*-PS-*b*-PIPOx (f_{IPOx} = 0.5) showed two T_gs, 106.5 °C and 171.3 °C, corresponding to the T_g of PS and T_g of PIPOx, respectively, as shown in Figure 5.7.

5.3.3 Microphase Separation of PIPOx-b-PS-b-PIPOx Triblock Copolymers.

Block copolymers consisting of thermodynamically incompatible components usually show microphase separation behavior, with the particular morphology controlled by the properties of the polymers such as chemical composition and molecular weight, as well as by the solvent used for film casting, annealing temperature, *etc*.[32] The microphase separation behavior of the amphiphilic triblock copolymers PIPOx-*b*-PS-*b*-PIPOx (f_{IPOx} = 0.2) and PIPOx-*b*-PS-*b*-PIPOx (f_{IPOx} = 0.5) were studied in the bulk. TEM images of PIPOx-*b*-PS-*b*-PIPOx (f_{IPOx} = 0.2) and PIPOx-*b*-PS-*b*-PIPOx (f_{IPOx} = 0.5) exhibited spherical (Figure 5.8a) and lamellar structure with long-range order (Figure 5.8b), respectively. In TEM images of Figure 5.8a and b, the dark domains represent iodine stained PIPOx block and the gray domains are PS blocks in the resulting block copolymer nanostructures. From molecular length consideration, the effective length of one vinyl unit

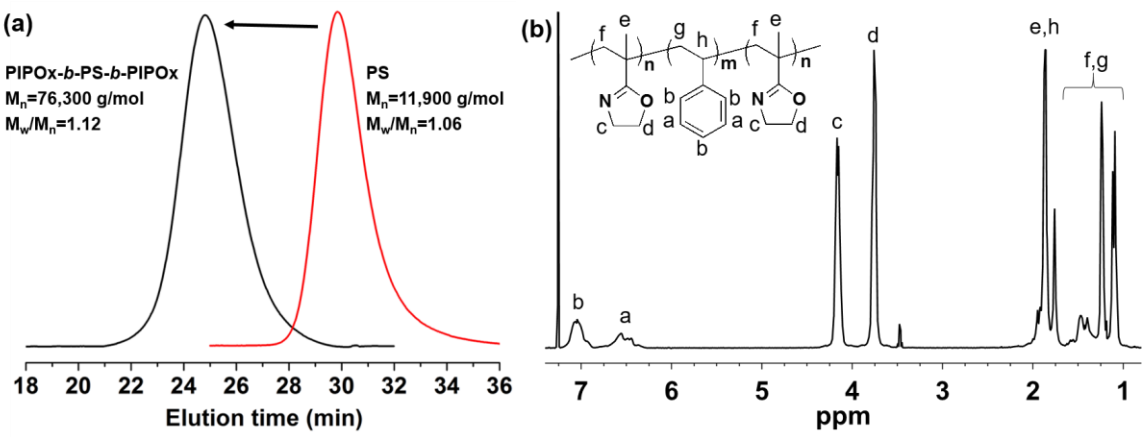

Figure 5.6. (a) SEC profile of PS homopolymer (red curve) and PIPOx-*b*-PS-*b*-PIPOx (f_{IPOx} = 0.8) (black curve) (Run 7 in Table 5.3) and b) ^{1}H-NMR spectrum of corresponding PIPOx-*b*-PS-*b*-PIPOx (f_{IPOx} = 0.8).

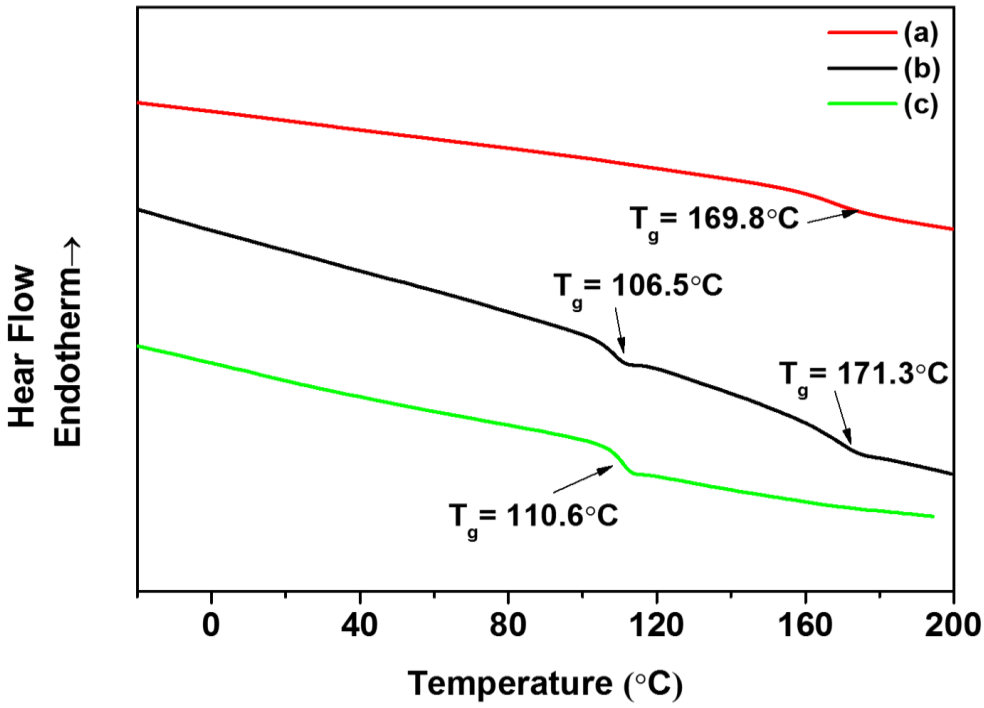

Figure 5.7. DSC profiles of (a) PIPOx-*b*-PS-*b*-PIPOx (f_{IPOx} = 0.8), (b) PIPOx-*b*-PS-*b*-PIPOx (f_{IPOx} = 0.5) and (c) PIPOx-*b*-PS-*b*-PIPOx (f_{IPOx} = 0.2).

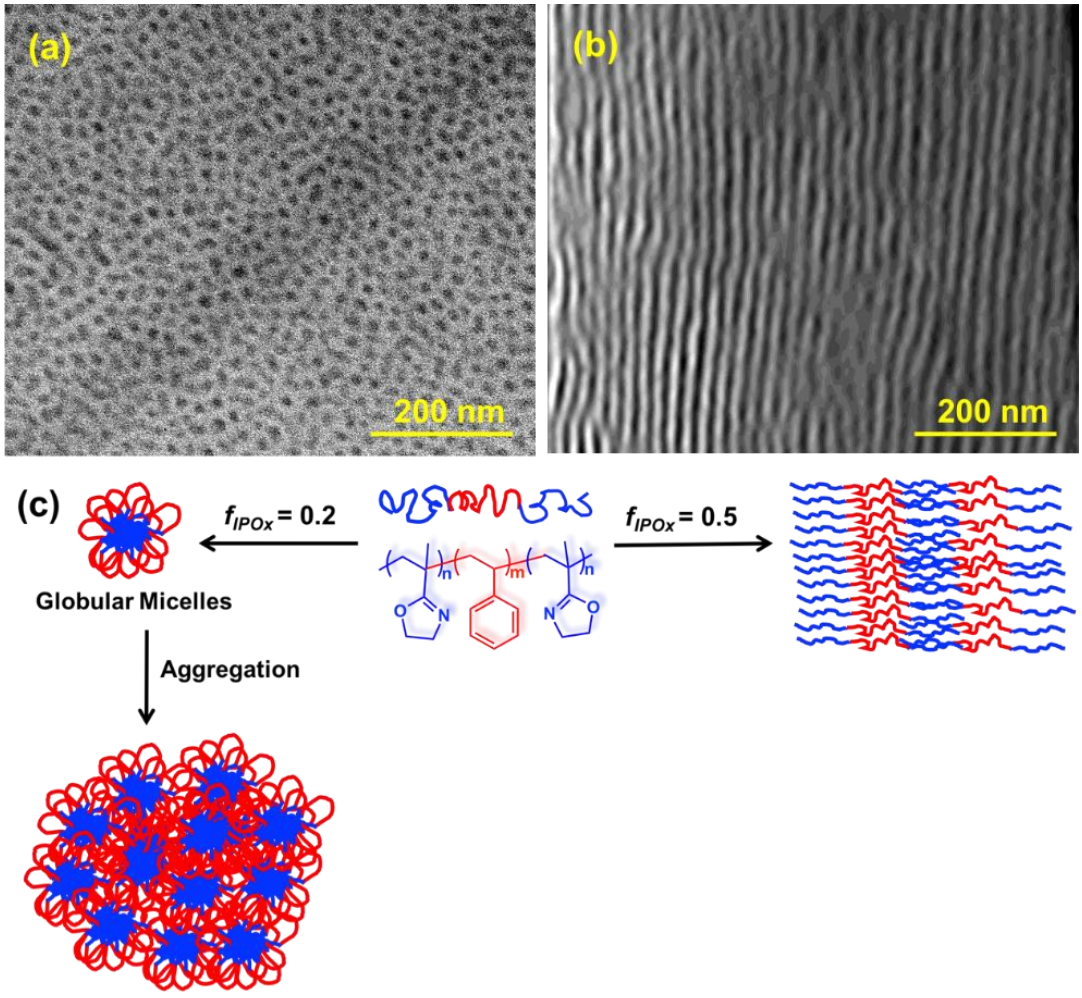

Figure 5.8. TEM images of PIPOx-*b*-PS-*b*-PIPOx triblock copolymers: (a) f_{IPOx} = 0.2 and (b) f_{IPOx} = 0.5. The dark regions represent IPOx domain stained with iodine vapor and the PIPOx domain size is 18.9 ± 2.0 nm, and (c) model for self-assembly into spherical and lamella nanostructures.

is roughly 0.2 nm. The fully extended length of PIPOx unit in PIPOx-*b*-PS-*b*-PIPOx (f_{IPOx} = 0.2) is close to 22 nm and for the PS block the fully extended length is roughly 122 nm.

TEM analysis using Gatan software[33] shows that the dark zone is not regular in shape, the average size is in range of 17 ± 2 nm and it is surrounded by 22 ± 1.5 nm gray zone of PS block, which is 18 percent of fully extended length of PS block. This indicates that the PS segments are bent due to their flexible coil nature to accommodate intrachain interactions among PIPOx chain (Figure 5.8c). Owing to the short chain length of PIPOx, it not able the balance to long chain hydrophobic interaction of the PS blocks and makes first globular micelles and later these micelles aggregate due to high concentration and ultimately form networks as shown in Figure 5.8c. However, as the chain length of PIPOx in PIPOx-*b*-PS-*b*-PIPOx (f_{IPOx} = 0.5) is increased, a long-range lamellar structure is observed due to balance in interactions between PIPOx and PS blocks. Furthermore, detailed analysis of Figure 5.8b, the average domain size of PIPOx and PS is in range of 18.9 ± 2.0 for both blocks, which is roughly equal to 30 percent length of the fully extended chain lengths of the blocks as shown in Figure 5.8c. The fully extended length of the three blocks in PIPOx-*b*-PS-*b*-PIPOx (f_{IPOx} = 0.5) is roughly 60 nm.

5.4 Conclusion

We report a superior and effective synthetic method to prepare well-defined poly(2-isopropenyl-2-oxazoline) via living anionic polymerization through the use of high vacuum and glass blowing techniques. The optimized initiator system for living anionic

homopolymerization of IPOx was found: DPM-K/Et_2Zn ([Et_2Zn]/[DPM-K] = 20), temperature: 0 °C, and time: 10 h. Well-defined PIPOx with MW as high as 100,000 g/mol and PDI of 1.15 was synthesized for the first time. The linear relationship between molecular weight and [monomer]/[initiator] ratio verified the living nature of these polymerizations. The living nature of this polymerization was further confirmed by block copolymer synthesis. The anionic polymerization reactivity order of IPOx < MMA < 2VP < St, attributed to the stability of carbanions, was established via block copolymerizations using IPOx as the first or second monomer. It was observed that films of amphiphilic triblock copolymers PIPOx-*b*-PS-*b*-PIPOx with f_{IPOx} = 0.2 formed a spherical morphology while a lamellar structure was formed by PIPOx-*b*-PS-*b*-PIPOx with f_{IPOx} = 0.5. Both systems exhibit good long-range order.

5.5 References

1. Darbre, T.; Reymond, J.-L., *Acc. Chem. Res.* **2006,** *39*, 925-934.

2. Koh, H.-D.; Kang, N.-G.; Lee, J.-S., *Langmuir* **2007,** *23*, 12817-12820.

3. Koh, H.-D.; Kang, N.-G.; Lee, J.-S., *Langmuir* **2007,** *23*, 11425-11429.

4. Viegas, T. X.; Bentley, M. D.; Harris, J. M.; Fang, Z.; Yoon, K.; Dizman, B.; Weimer, R.; Mero, A.; Pasut, G.; Veronese, F. M., *Bioconjugate Chem.* **2011,** *22*, 976-86.

5. Culbertson, B. M., *Prog. Polym. Sci.* **2002,** *27*, 579-626.

6. Ishizone, T.; Oka, N.; Hirao, A.; Nakahama, S., *Macromolecules* **1996,** *29*, 528-534.

7. Pack, D. W.; Hoffman, A. S.; Pun, S.; Stayton, P. S., *Nat. Rev. Drug Discovery* **2005,** *4*, 581-593.

8. Kwon, G. S.; Forrest, M. L., *Drug Dev. Res.* **2006,** *67*, 15-22.

9. Adams, M. L.; Lavasanifar, A.; Kwon, G. S., *J. Pharm. Sci.* **2003,** *92*, 1343-1355.

10. Hoogenboom, R., *Angewandte Chemie International Edition* **2009,** *48*, 7978-7994.

11. Tomalia, D.; Thill, B.; Fazio, M., *Polym. J.* **1980,** *12*, 661-675.

12. Zhang, N.; Pompe, T.; Amin, I.; Luxenhofer, R.; Werner, C.; Jordan, R., *Macromol. Biosci.* **2012,** *12*, 926-936.

13. Weber, C.; Neuwirth, T.; Kempe, K.; Ozkahraman, B.; Tamahkar, E.; Mert, H.; Becer, C. R.; Schubert, U. S., *Macromolecules* **2012,** *45*, 20-27.

14. Zhang, N.; Salzinger, S.; Soller, B. S.; Rieger, B., *J. Am. Chem. Soc.* **2013,** *135*, 8810-3.

15. Reyes, F. T.; Malins, E. L.; Becer, C. R.; Kelland, M. A., *Energy Fuels* **2013,** *27*, 3154-3160.

16. Zhang, J.; Liu, K.; Müllen, K.; Yin, M., *Chem. Commun.* **2015,** *51*, 11541-11555.

17. Changez, M.; Kang, N. G.; Lee, C. H.; Lee, J. S., *Small* **2010,** *6*, 63-68.

18. Changez, M.; Kang, N. G.; Lee, J. S., *Small* **2012,** *8*, 1173-1179.

19. Hong, K.; Uhrig, D.; Mays, J. W., *Curr. Opin. Solid State Mater. Sci.* **1999,** *4*, 531-538.

20. Wang, W.; Schlegel, R.; White, B. T.; Williams, K.; Voyloy, D.; Steren, C. A.; Goodwin, A.; Coughlin, E. B.; Gido, S.; Beiner, M., *Macromolecules* **2016,** *49*, 2646-2655.

21. Candau, F.; Afchar-Taromi, F.; Rempp, P., *Polymer* **1977,** *18*, 1253-1257.

22. Ishizone, T.; Yanase, E.; Matsushita, T.; Nakahama, S., *Macromolecules* **2001,** *34*, 6551-6553.

23. Ji, H.; Farmer, B. S.; Nonidez, W. K.; Advincula, R. C.; Smith, G. D.; Kilbey, S. M.; Dadmun, M. D.; Mays, J. W., *Macromol. Chem. Phys.* **2007,** *208*, 807-814.

24. Kang, N.-G.; Changez, M.; Kim, M.-J.; Lee, J.-S., *Macromolecules* **2014,** *47*, 6706-6714.

25. Kang, N.-G.; Changez, M.; Lee, J.-S., *Macromolecules* **2007,** *40*, 8553-8559.

26. Uhrig, D.; Mays, J. W., *J. Polym. Sci., Part A: Polym. Chem.* **2005,** *43*, 6179-6222.

27. Whitney, S. E.; Rickborn, B., *J. Org. Chem.* **1991,** *56*, 3058-3063.

28. Varshney, S. K.; Hautekeer, J.; Fayt, R.; Jérôme, R.; Teyssié, P., *Macromolecules* **1990,** *23*, 2618-2622.

29. Baskaran, D., *Prog. Polym. Sci.* **2003,** *28*, 521-581.

30. Hirano, T.; Okumura, Y.; Kitajima, H.; Seno, M.; Sato, T., *J. Polym. Sci., Part A: Polym. Chem.* **2006,** *44*, 4450-4460.

31. Fuchise, K.; Sakai, R.; Satoh, T.; Sato, S.-i.; Narumi, A.; Kawaguchi, S.; Kakuchi, T., *Macromolecules* **2010,** *43*, 5589-5594.

32. Bates, F. S., *Science* **1991,** *251*, 898-905.

33. Liu, Z.; Suenaga, K.; Harris, P. J.; Iijima, S., *Phys. Rev. Lett.* **2009,** *102*, 015501.

CHAPTER 6 Template Synthesis of Gold Nanoparticles using PIPOx Homopolymer

Abstract

Gold nanoparticles has been one of the most investigated areas in science, its renaissance now leads to an exponentially increasing number of publications, especially in the context of emerging nanoscience and nanotechnology. In this chapter, we present a template synthesis of AuNPs using PIPOx homopolymer. By changing the loading ratio of gold precursor/repeating unit in the template, surface plasma resonance showed varied maximum absorption wavelength. Moreover, when the loading is 1%, the AuNPs showed a photoluminescence at an emission wavelength at 685 nm. In addition, the interaction of Au and PIPOx was studied using XPS.

6.1 Introduction

It is well-known that diverse self-assembled nanostructures such as micelles, vesicles, and cylinders are generated dominantly by a suitable hydrophilic-hydrophobic balance in amphiphilic block copolymers (BCPs) among numerous factors.[1-4] In recent years, macromolecular self-assemblies induced by amphiphilic homopolymers (AHs) as an alternative have appeared impressively. For the preparation of AHs-based self-assemblies, two main routes of "monomer-induced" and "hydrophobic-group-induced" were suggested.[5] The former approach has been utilized widely and rapidly since Thayumanavan *et al.* reported the micelles-, inverse micelles-, and vesicle-type assembly by AHs containing a series of styrene-based and glycine-based repeating unit.[6-7] In addition, Lee *et al.* described formation of several unique micelle behaviors such as reversible and pH-sensitive bilayer vesicles, stable hollow micelles, and micelles[8-10] by self-assemblies of 2-, 3-, and 4-(4-vinylphenyl)pyridine, respectively, synthesized via living anionic polymerization.[11] These pyridine-containing polymers are the AHs with simplest chemical compositions and structures among numerous AHs reported previously.[6-7, 12-14]

The dominant factors for monomer-induced approach to form AHs self-assemblies are chemical compositions, controlled MW, and narrow MWD of AHs containing hydrophilic and hydrophobic moieties in same monomer. In particular, to form homogeneous size and shape of nanostructures by self-assembly such as micelles and vesicles, controlled MW and MWD of AHs should be controlled precisely. Correspondingly, LAP is one of best candidates for controlled polymerization. Until now,

it has been discussed in chapter 5 that anionic polymerization of well-defined PIPOx with controlled molecular weight and MWD is achievable under optimized conditions.[15-16] Moreover, the control of nanostructures by self-assembly is considered to be a key aspect for numerous applications.[17-18]

Gold nanoparticles (AuNPs) are the most stable metal nanoparticles, and they present fascinating aspects such as their assembly of multiple types involving materials science, the behavior of the individual particles, size-related electronic, magnetic and optical properties (quantum size effect), and their applications to catalysis and biology.[19-20] AuNPs are usually synthesized using a reduction of Au (III) precursors, $HAuCl_4$.[21] Alkane thiols are the most commonly used stabilizing ligand in the synthesis of AuNPs, which is attributed to the soft character of Au and S.[22] In fact, ligands contain lone pairs could be used as ligand.[23] These include phosphine, phosphine oxide, amine and carboxylate.[24-26] In this work, we tried to use PIPOx homopolymer as a template to synthesize gold nanoparticles. The characteristics of the obtained AuNPs were studied using TEM and AFM. The interaction between AuNPs and polymer template was analyzed using XPS.

6.2 Experimental section

Materials. The monomer 2-isopropyl-2-oxazoline (IPOx, 99%, Aldrich) was passed through neutral alumina column, dried over CaH_2 and distilled under reduced pressure. The monomer was further purified, diluted and transferred to pre-calibrated ampoules equipped with break-seals under high vacuum and stored at -30°C.

Tetrahydrofuran (THF, Fisher scientific, HPLC grade) was distilled from potassium naphthalenide solution on high vacuum line. All other agents were used as received.

Instrumentation. NMR spectra were recorded on a liquid state Varian VNMRS 500MHz spectrometer at 25.00°C. The internal standard was $CDCl_3$ at 7.26 ppm. Attenuated Total Reflection- FT-IR spectra were obtained using a Perkin Elmer Spotlight 400 FT-IR Imaging System with scanning wavenumber range from 4000cm^{-1} to 400cm^{-1}. Size exclusion chromatography (SEC) was performed using a Waters GPC system consisting of a Waters model 510 pump and a Knauer Smartline model 2300 RI detector. The column set is four PSS (Polymer Standards Service) GRAM; 8x300 mm; 10µm; 100, 1000, and 3000 Å along with an 8×50, 10µm guard. DMF was used as eluent solvent at 1.00mL/min at 55°C. Before each measurement, the polymer sample was dissolved in DMF and filtered through 0.45 µm PTFE filter. Transmission electron microscopy (TEM) images were acquired by ZEISS LIBRA 200 HT FE MC. The solution samples were loaded on a carbon coated copper grid and air dried before TEM measurement. X-ray photoelectron spectroscopy (XPS) was performed using a Thermo Scientific Model KAlpha XPS instrument. Analyses are conducted with a 400 µm X-ray spot size for maximum signal and to obtain an average surface composition over the largest possible area. Wide energy range survey spectra (0-1350 eV) are acquired for qualitative and quantitative analysis using an analyzer pass energy of 200 eV. For assessing the chemical bonding of identified elements, narrow energy range core level spectra were acquired with an analyzer pass energy of 50 eV.

6.2.1 Synthesis of Well-Defined Poly (2-isopropenyl-2-oxazoline) PIPOx.

The detailed synthetic procedure refers to chapter 5. A typical polymerization procedure is described as follows. The solution of DPM-K (0.093 mmol) in THF (4 mL) was transferred to main reactor at -78 °C and the solution of Et_2Zn (1.76 mmol) in THF (2 mL) was added to DPM-K solution at -78 °C. The solution of IPOx monomer (7.28 mmol) in THF (9.30 mL) was then added to the initiator mixture and the solution was maintained at -78 °C for 30 min to allow for complete initiation. The propagation in anionic polymerization was performed for 10 to 24 h at -78, -41, 0, and 25 °C. The polymerizations were terminated with degassed methanol. The desired polymer was recovered by repeatedly precipitation into excess cold ether.

6.2.2 In situ Synthesis of AuNPs using PIPOx as Template.

A typical preparation procedure is presented as follows. To a clean vial was added a solution of 500 mg of PIPOx, 12.0 mg of $HAuCl_4$ and 10 mL of DI-H_2O. After stirring overnight at room temperature, 2.0 mg of anhydrous N_2H_4 was then added to the reaction mixture. The color changed from light yellow to light pink upon the addition. The solution was then stirred for another 12 h. The resulting solution was used for UV, PL analysis without any further treatment.

6.3 Results and Discussion

6.3.1 Synthesis of PIPOx homopolymer

As discussed in chapter 5, we prepared PIPOx homopolymer using living anionic polymerization. The structure of obtained polymer was characterized using NMR and ATR-IR as illustrated in Figure 6.1

The resulting homopolymers of PIPOx were characterized by ^{1}H-NMR (Figure 6.1A). The ^{1}H-NMR spectra of PIPOx demonstrated the successful anionic polymerization. The vinyl proton signals disappeared completely and new peaks at 1.76-2.13 ppm emerged from protons of methylene on the polymer backbone. On the other hand, the signals corresponding to protons of the oxazoline ring emerged at 3.76 and 4.16 ppm, respectively. ATR-IR spectra also verified that the ring skeleton vibration (991, 958 and 930 cm^{-1}) was intact after polymerization as shown in Figure 6.1B. Two characteristic absorption peaks of monomer at 1606 cm^{-1} (C=C, stretch) and 1281 cm^{-1} (C=O (conjugated), stretch) were disappeared after polymerization indicating the isopropenyl group was reacted completely. Molecular weight was analyzed using SEC (Figure 6.2). The results are summarized in Table 6.1.

6.3.2 Synthesis of AuNPs and Characterizations

The AuNPs were synthesized using a reduction of $HAuCl_4$ in H_2O. The reducing agent used is N_2H_4. $HAuCl_4$ was first mixed with PIPOx (16k) thoroughly. 2eq N_2H_4 was then added. The solution was stirred at ambient conditions. The color of the solution

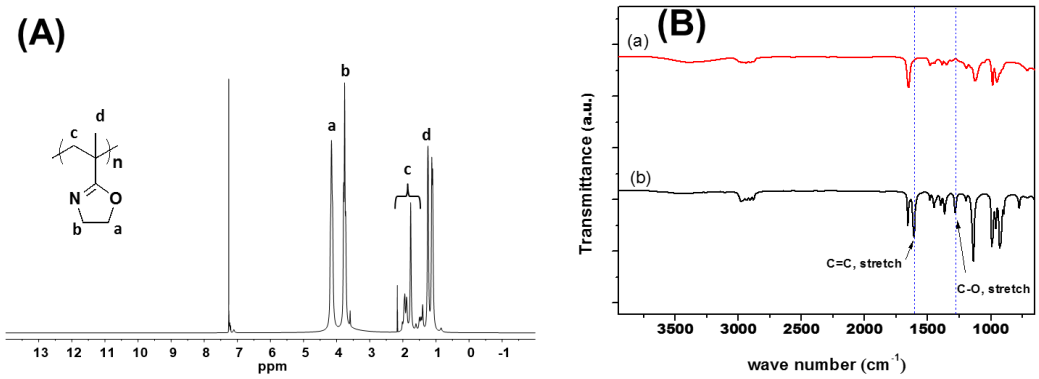

Figure 6.1. (A) 1H-NMR spectrum of PIPOx. (B) ATR-IR spectra of IPOx (red curve) and PIPOx (black curve).

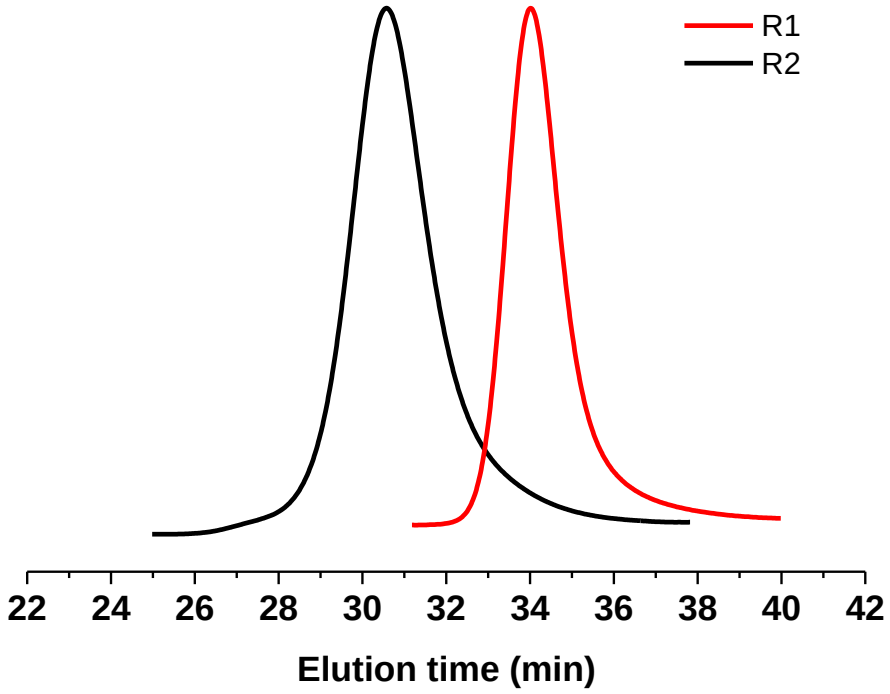

Figure 6.2. The SEC profiles of PIPOx homopolymer.

Table 6.1. Synthesis of PIPOx homopolymer

run	IPOx	DPM-K[d]	Et_2Zn	M_n ($\times 10^{-3}$ g/mol)			PDI[b]
	mmol	mmol	mmol	calcd[a]	obsd[b]	obsd[c]	
1	8.57	0.0928	1.00	10.3	9.6	13.7	1.09
2	11.53	0.0756	1.32	18.7	16.2	20.9	1.13

gradually transformed from light yellow to pink, indicating the reduction was occurring. Different loading ratios of $HAuCl_4$/Oxazoline were employed (Table 6.2).

We further studied aggregate formation capacity of homopolymer in aqueous media. Furthermore, the resulting aggregates were used for formation of ultra-thin gold nanoparticles.

The gold precursor was first mixed with PIPOx in H_2O solution. The mixture was stirred overnight. Hydrazine was selected as reducing agent. Upton mixing, the color was changed from light yellow to blush purple immediately. Furthermore, we found the Au nanoparticles were rather stable and no precipitation was observed even after 3 months of storage time at room temperature. The morphologies of self-assembly was studied by transmission electron microscope (TEM) and atomic force microscope (AFM), as seen in Figure 6.3. The micrograph (Figure 6.3A) clearly shows a bilayer vascular structure in which reduced gold atoms or cluster are decorated at vesicles membrane. A detailed analysis shows the AuNPs in the dark region have a size of 3.8±1 nm.

The self-assembly behavior of amphiphilic homopolymer is rarely reported, as compared to well-established amphiphilic block copolymers. The PIPOx has two main chemical constituents (a) hydrophobic and flexible isopropyl back bone and (b) hydrophilic oxazoline pendent group. As expected, oxazoline is more favorable with water media and try to protect hydrophobic flexible isopropyl backbone from water, which is present outside and inside of the aggregates. Dark contrast at the vesicles membrane provides strong evidence for the orientation of oxazoline groups in vesicular structures at the membrane.

Table 6.2. Sample code and Au loading ratios of the samples studied in this chapter.

Sample code	M_n of PIPOx template (g/mol)	$HAuCl_4$ Loading ratio*
PIPOx	16200	na
PIPOx-Au-0.1%	16200	0.1%
PIPOx-Au-1.0%	16200	1.0%
PIPOx-Au-5.0%	16200	5.0%
PIPOx-Au-15%	16200	15%
PIPOx-Au-25%	16200	25%

*The loading ratios was determined as the moles of $HAuCl_4$/moles of repeating unit in the polymer template.

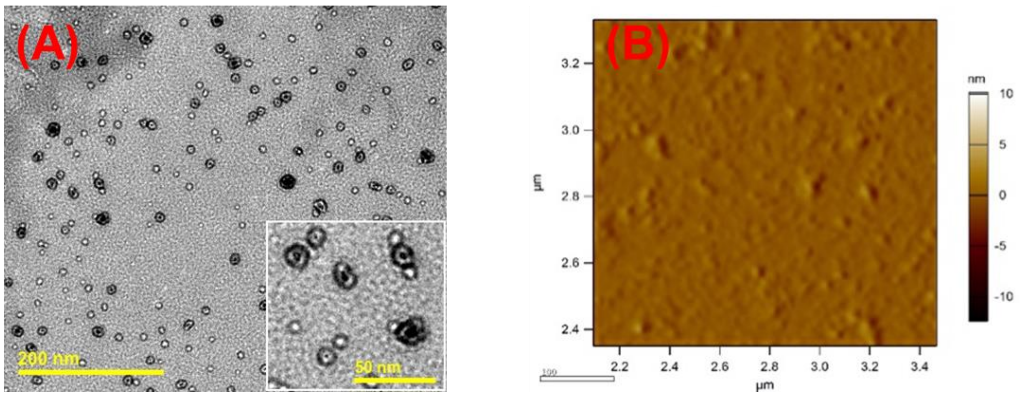

Figure 6.3. (A) TEM image of PIPOx-Au-1.0%. (B) AFM image of PIPOx-Au-1.0%.

Furthermore, this also indicated that molecular rotation of the sigma bond between isopropyl and oxazoline pendent group probably freezes. Size of gold nanoparticles depends upon the interaction among mainly three forces (a) interaction among reduced Au atoms, (b) interaction between reduced Au particles and solvent molecules and most importantly force between reduced Au atom and stabilizing agent (oxazoline group here in this case). During the synthesis process, we observed that as the Au^{o} precursor concentration decreases, the Au NPs plasma band shifted to blue which is indicative of a decrease in Au particle size (Figure 6.4A). A relation between plasma absorption wavelength and size of AuNPs has been reported elsewhere.[27] It is well known that Au nanoparticles with more than 100 atoms do not give PL spectra.[28] The origin of the luminescence spectra may be due to the inter-band transitions between the filled $5d^{10}$ band and $6(sp)^{1}$ conduction band of Au or Au^{+}.[29] The presence of PL spectra (maxima at 685nm) (Figure 6.4B) clearly indicates the presence of Au cluster at PIPOx host. This also suggests that PIPOx is capable of not only stabilizing AuNPs but also preventing small AuNPs from aggregating into large particles.

Moreover, to study the interaction of Au and oxazoline moiety, XPS analysis was performed. The optical image on the left shows the region mapped by the red box. The image to the right shows the Au distribution (Figure 6.5 red) and the Si distribution (Figure 6.5 blue). XPS full spectra of these series of samples is shown in Figure 6.6. Since both nitrogen and oxygen have electron lone pairs, core level spectra of XPS data of O (1s) and N (1s) (Figure 6.7) were used to analyze the interaction of oxazoline moiety and AuNPs.

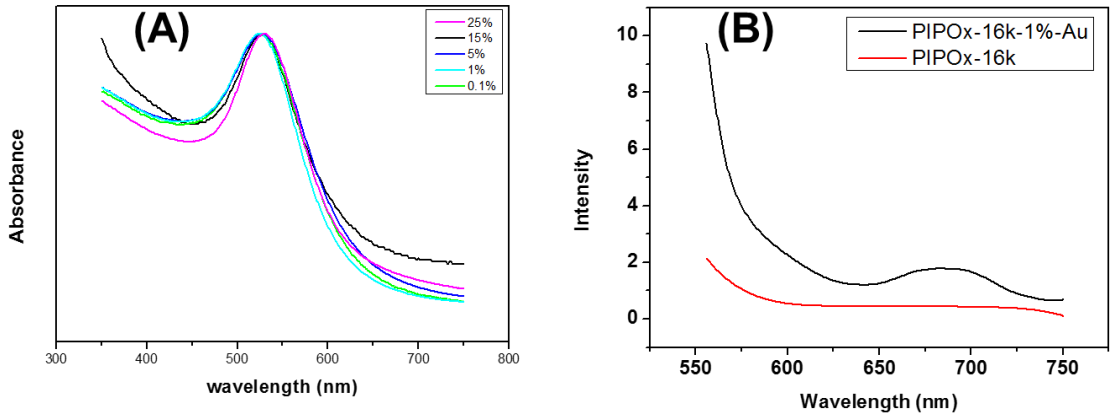

Figure 6.4. (A) UV spectra of PIPOx homopolymer with different loading ratios of $HAuCl_4$. (B) photoluminescence spectra of PIPOx homopolymer and PIPOx with 1% loading ratio using a excited wavelength at 530 nm.

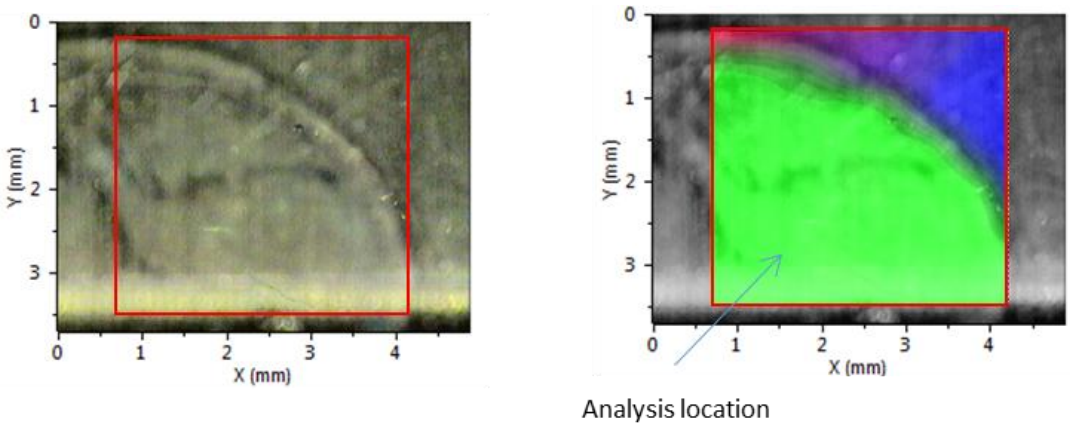

Figure 6.5. The optical image of PIPOx-Au samples subjected to XPS analysis.

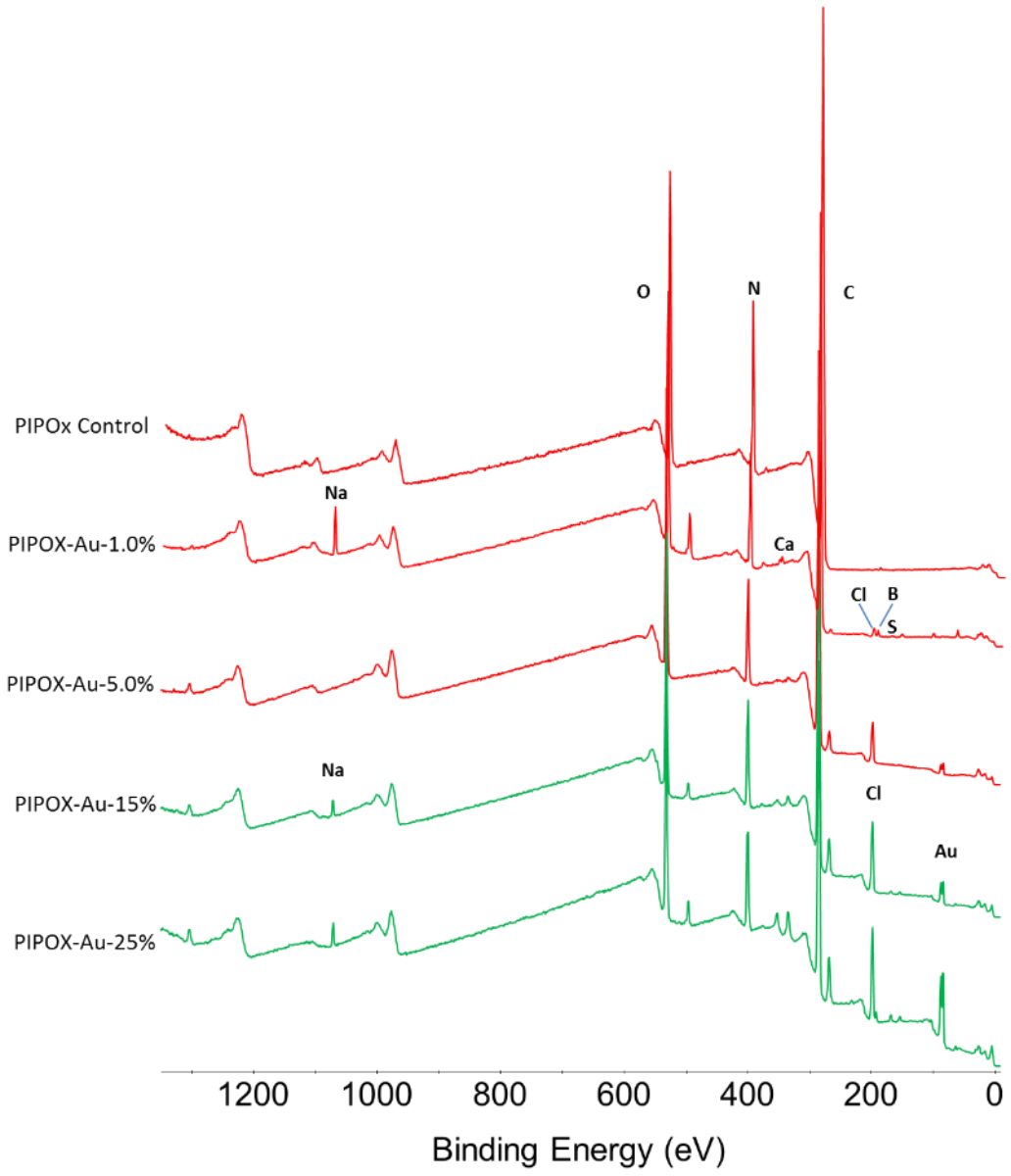

Figure 6.6. XPS spectra of PIPOx homopolymer and PIPOx with different Au loading ratios.

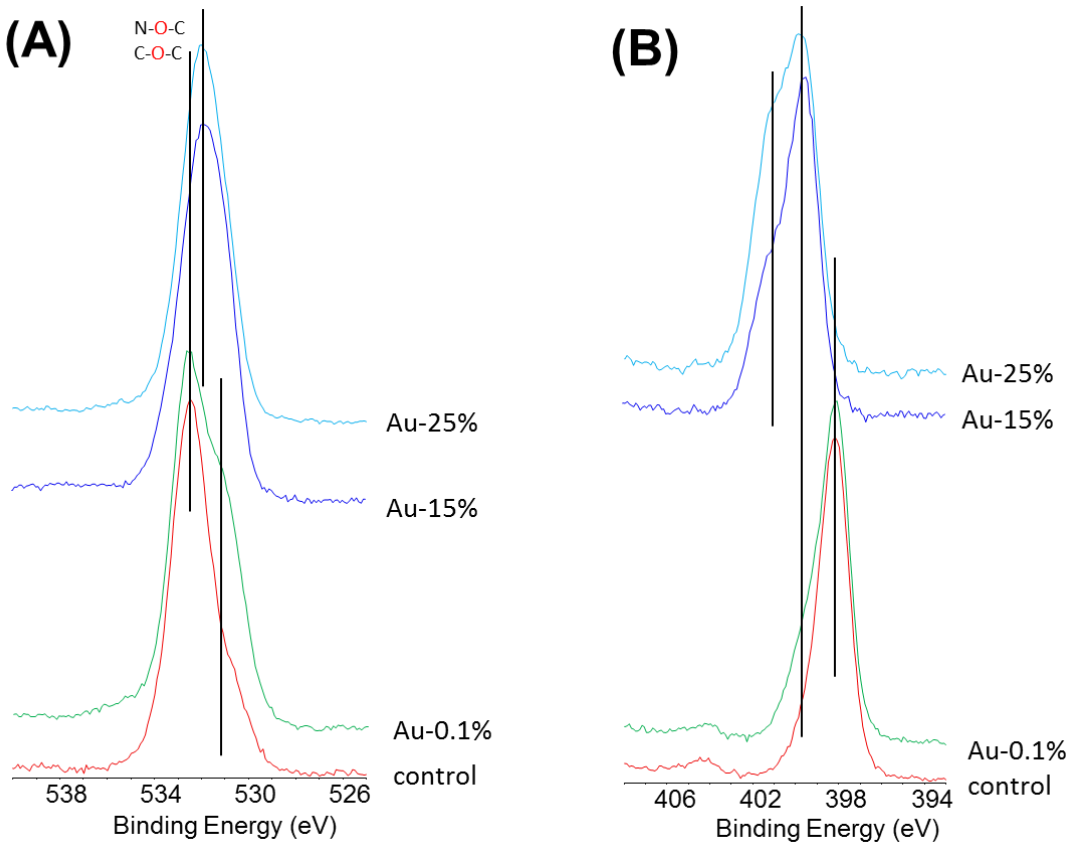

Figure 6.7. Core level XPS analysis of (A) O (1s) and (B) N (1s).

As with the O data, the spectra for the control and Au-0.1% samples are similar and both show a prominent peak at ~398 eV and a smaller shoulder at ~399.5 eV. The N 1s spectra for the Au-containing sample also show two peaks: one at ~399.5 eV, which is the biggest, and another one at ~401 eV. This is clear indication that the Au is likely binding at the N site on the polymer.

6.4 Conclusion

We prepared PIPOx homopolymer using living anionic polymerization. Well-defined PIPOx with molecular weight 16,200g/mol was employed to synthesis gold nanoparticles. By varying the loading ratio of $HAuCl_4$/oxazoline moiety, the synthesized AuNPs showed a size range 3.8±1.0 nm, which was proved by TEM and AFM analysis. For 1% loading ratio, weak photoluminescence was also observed, indicating the presence of ultra-thin Au clusters. Core level XPS analysis showed that the N in the oxazoline moiety is responsible for the AuNPs stabilization.

6.5 References

1. Kang, N.-G.; Kang, B.-G.; Koh, H.-D.; Changez, M.; Lee, J.-S., *React. Funct. Polym.* **2009,** *69*, 470-479.

2. Israelachvili, J. N.; Mitchell, D. J.; Ninham, B. W., *Biochimica et Biophysica Acta (BBA)-Biomembranes* **1977,** *470*, 185-201.

3. Hayward, R. C.; Pochan, D. J., *Macromolecules* **2010,** *43*, 3577-3584.

4. Cui, H.; Chen, Z.; Zhong, S.; Wooley, K. L.; Pochan, D. J., *Science* **2007,** *317*, 647-650.

5. Zhang, J.; Liu, K.; Müllen, K.; Yin, M., *Chem. Commun.* **2015,** *51*, 11541-11555.

6. Basu, S.; Vutukuri, D. R.; Shyamroy, S.; Sandanaraj, B. S.; Thayumanavan, S., *J. Am. Chem. Soc.* **2004,** *126*, 9890-9891.

7. Savariar, E. N.; Aathimanikandan, S. V.; Thayumanavan, S., *J. Am. Chem. Soc.* **2006,** *128*, 16224-16230.

8. Changez, M.; Kang, N. G.; Lee, J. S., *Small* **2012,** *8*, 1173-1179.

9. Hur, Y. H.; Kang, N. G.; Kang, B. G.; Yu, Y. G.; Changez, M.; Lee, J. S., *J. Polym. Sci., Part A: Polym. Chem.* **2013,** *51*, 3458-3469.

10. Changez, M.; Kang, N. G.; Lee, C. H.; Lee, J. S., *Small* **2010,** *6*, 63-68.

11. Kang, N.-G.; Changez, M.; Lee, J.-S., *Macromolecules* **2007,** *40*, 8553-8559.

12. Luo, C.; Liu, Y.; Li, Z., *Macromolecules* **2010,** *43*, 8101-8108.

13. Feng, C.; Lu, G.; Li, Y.; Huang, X., *Langmuir* **2013,** *29*, 10922-10931.

14. Wang, Y.; Alb, A. M.; He, J.; Grayson, S. M., *Polym. Chem.* **2014,** *5*, 622-629.

15. Zhang, N.; Salzinger, S.; Soller, B. S.; Rieger, B., *J. Am. Chem. Soc.* **2013,** *135*, 8810-3.

16. Feng, H.; Changez, M.; Hong, K.; Mays, J. W.; Kang, N.-G., *Macromolecules* **2017,** *50*, 54-62.

17. Linic, S.; Aslam, U.; Boerigter, C.; Morabito, M., *Nat. Mater.* **2015,** *14*, 567-576.

18. Gupta, S.; Tripathi, M., *Chin. Sci. Bull.* **2011,** *56*, 1639-1657.

19. Nie, Z.; Petukhova, A.; Kumacheva, E., *Nat. Nanotechnol.* **2010,** *5*, 15-25.

20. Ding, Y.; Jiang, Z.; Saha, K.; Kim, C. S.; Kim, S. T.; Landis, R. F.; Rotello, V. M., *Mol. Ther.* **2014,** *22*, 1075-1083.

21. Majewski, P.; Thierry, B., *Crit. Rev. Solid State Mater. Sci.* **2007,** *32*, 203-215.

22. Austin, L. A.; Kang, B.; El-Sayed, M. A., *Nano Today* **2015,** *10*, 542-558.

23. Tenne, R., *Nat. Nanotechnol.* **2006,** *1*, 103-111.

24. Gomez, S.; Philippot, K.; Collière, V.; Chaudret, B.; Senocq, F.; Lecante, P., *Chem. Commun.* **2000**, 1945-1946.

25. Selvakannan, P.; Mandal, S.; Phadtare, S.; Pasricha, R.; Sastry, M., *Langmuir* **2003,** *19*, 3545-3549.

26. Cheng, W.; Dong, S.; Wang, E., *Angew. Chem. Int. Ed.* **2003,** *42*, 449-452.

27. Zhou, M.; Zeng, C.; Chen, Y.; Zhao, S.; Sfeir, M. Y.; Zhu, M.; Jin, R., *Nat Commun* **2016,** *7*, 13240.

28. Ghosh, P.; Han, G.; De, M.; Kim, C. K.; Rotello, V. M., *Adv. Drug Delivery Rev.* **2008,** *60*, 1307-1315.

29. Alex, S.; Tiwari, A., *J. Nanosci. Nanotechnol.* **2015,** *15*, 1869-1894.

CHAPTER 7 Gas Separation Mechanism of CO_2 Selective Amidoxime-Poly(1-Trimethylsilyl-1-Propyne) Membranes

A version of this chapter was originally submitted by Hongbo Feng, Tao Hong, Shannon M. Mahurin, Konstantinos D. Vogiatzis, Kevin R. Gmernicki, Brian K. Long, Jimmy W. Mays, Alexei P. Sokolov, Nam-Goo Kang and Tomonori Saito to *Polymer Chemistry*, revision submitted.

Abstract

Polymeric membranes for CO_2 separation have drawn significant attention in academia and industry. In this work, we prepared amidoxime-functionalized poly(1-trimethylsilyl-1-propyne) (AO-PTMSP) membranes through hydrosilylation and post-polymerization modification. Compared to neat PTMSP membranes, the AO-PTMSP membranes showed significant enhancements in CO_2/N_2 gas separation performance (CO_2 permeability ~ 6000 Barrier; CO_2/N_2 selectivity ~17). This systematic study provides clear guidelines on how to tune the CO2-philicity within PTMSP matrices and the effects on gas selectivity. Key parameters for elucidating the gas transport mechanism were discussed based on CO_2 sorption measurements and fractional free volume estimates. The effect of the AO content on CO_2/N_2 selectivity was further examined by means of density functional theory (DFT) calculations. Both experimental and theoretical data provide consistent results that conclusively show that CO_2/N_2 separation performance is enhanced by increased CO_2-polymer interactions.

7.1 Introduction

The steady growth of carbon dioxide (CO_2) emissions, mostly from power plant flue gas, is believed to be the main cause of global warming and undesirable climate changes.[1-2] To mitigate CO_2 emissions, a variety of CO_2 capture and separation technologies have been developed. Among them, membrane-based separations are considered one of the most promising approaches for flue gas treatment. This is because such membrane technology could offer a significant reduction in costs as well as its sustainability due to its passive nature.[3] Therefore, the development of high-performance CO_2 separation membranes and deepening understanding of their separation mechanisms have been a research priority in this field.

The performance of polymeric, gas separation membranes is typically evaluated through investigation of two major parameters: the gas permeability (P_A), which is determined by the product of the gas solubility (S_A) and diffusivity (D_A) ($P_A = S_A \times D_A$); and the gas selectivity (α_{AB}) which is defined as the ratio of the permeability of any two gases ($\alpha_{AB} = \frac{P_A}{P_B}$). Furthermore, selectivity can also be separated into solubility selectivity and diffusivity selectivity by the following equation: $\alpha_{AB} = \frac{P_A}{P_B} = \frac{S_A}{S_B} \times \frac{D_A}{D_B}$. Membranes that exhibit high permeability are typically less selective and vice versa. This trade-off relationship between permeability and selectivity was illustrated by Robeson and Freeman.[4-6] From the practical point of view, membranes having high permeability are favored for flue gas separations due to the enormous volumes of flue gas emissions from coal-fired power plants that produce a limited pressure differential.[7]

Since the first successful synthesis reported in 1983,[8] poly(1-trimethylsilyl-1-propyne) (PTMSP) has gained significant attention in gas separation because it has orders of magnitude higher permeability than other polymers, which could be attributed to the exceptionally large free volume and large intersegmental gaps in the polymer matrix.[9] However, the rather low CO_2/N_2 selectivity is one of the major drawbacks that limits its deployment in various applications.

There are two approaches to improve gas selectivity: either improving diffusivity or solubility. Many recent studies have investigated improving diffusivity selectivity by tailoring pore size and concentration. Though this approach works well for gas pairs with distinct kinetic sizes, CO_2/N_2 separations have proven far more challenging due to the similar kinetic diameters of CO_2 (~3.30 Å) and N_2 (~ 3.64 Å), thereby rendering enhancements in diffusivity selectivity is insufficient.[6] Alternatively, modifying the CO_2/N_2 solubility selectivity of polymer membranes by introducing CO_2-philic functionalities has been proposed to enhance the CO_2 separation performance. It is known that basic or polar components, e.g. polyethylene oxide (PEO) or amine-containing groups, can enhance polymer-CO_2 interactions and contribute to improved CO_2 solubilities.[10-22] For example, amorphous PEO was reported to exhibit CO_2/N_2 selectivity around 50[10] while tetrazole-containing polymers also demonstrated significant enhancement in CO_2/N_2 selectivity.[14-15] Thus, considering the great potential for improving solubility selectivity, our research focused on the incorporation of CO_2-philic groups into the PTMSP matrix.

To accomplish this, we chose to incorporate amidoxime (AO) groups into our polymer matrix due to its strong calculated binding energy (BE) with CO_2 (~20 KJ/mol),[23] and based upon previous studies that have shown that AO functionalities improve CO_2/N_2 selectivity[19-20, 24-26]. In this study, we report an efficient method to prepare novel amidoxime- functionalized PTMSP (AO-PTMSP) membranes for CO_2 separation, targeting the enhancement of solubility selectivity. By careful control of the AO grafting ratio, the synthesized AO-PTMSP membranes showed a systematic change in CO_2/N_2 selectivity and improved overall performance in CO_2/N_2 separation. Compared with unmodified PTMSP, the overall CO_2/N_2 selectivity was improved by a factor of five in the highest performing membrane and achieved a performance very close to the Robeson upper bound. Key parameters for tuning the gas transport properties are discussed based on CO_2 sorption measurements and fractional free volume estimations. The effect of the AO content on the noncovalent interactions between the gas molecules and the AO functional groups was further examined by means of density functional theory (DFT) calculations.

7.2 Experimental section

Materials. Poly(1-trimethylsilyl-1-propyne) (PTMSP) was purchased from Gelest and used as received. Chloro(dimethyl)vinylsilane (97%), hydroxylamine solution (50 wt.% in H_2O), platinum(0)-1,3-divinyl-1,1,3,3-tetramethyldisiloxane complex solution (in xylene, Pt ~2 %, Pt [dvs]) and n-butyllithium solution (*n*-BuLi, 2.5 M in hexanes) were purchased from Sigma-Aldrich and used as received. Nitrogen (N_2) and carbon dioxide (CO_2) (99.99% purity) were obtained from Air Liquide. Tetrahydrofuran (THF) and

toluene were distilled over sodium naphthalide and sodium, respectively. All the reactions were carried out under Argon (Ar) atmosphere.

Instrumentation. ^{1}H-NMR (Varian Mercury 500) were measured using $CDCl_3$ as the deuterated solvent and spectra were referenced to the residual non-deuterated solvent signal. Size exclusion chromatography (SEC) was carried out at 40 ^{o}C using a Polymer Labs GPC-120 equipped with a differential refractometer. The column set was Polymer Labs PLgel; 7.5× 300 mm; 10 μm; 500, 10^3, 10^5, and 10^6 Å. The calibration range was 600 to 7,500,000 g/mol using narrow molecular weight distribution polystyrene standards (PSS). The mobile phase was THF at a flow rate of 1.0 mL/min. Fourier transform infrared spectroscopy (FT-IR) was conducted using a Nicolet iS50 FT-IR spectrometer equipped with a deuterated triglycine sulfate (DTGS) detector. Thermal properties were characterized using thermogravimetric analysis (TGA, TA instrument-Q50) at a heating rate of 10 °C /min under N_2 flow.

7.2.1 Synthesis of Amidoxime Functionalized PTMSP.

Synthesis of 4-(chlorodimethylsilyl) butanenitrile (CN-S). To a flame-dried two-neck round bottom flask was charged allyl cyanide (1.34 g, 20 mmol) and Pt [dvs] (20 μL) under argon. The reaction mixture was cooled to 0 °C followed by addition of chlorodimethylsilane (20 mmol). The mixture was then heated to 40 °C. The reaction progress was monitored by ^{1}H-NMR spectroscopy, and upon completion of the reaction, the product was obtained by fractional distillation. Yield: 94%. ^{1}H-NMR ($CDCl_3$, 500 MHz), δ (ppm): 2.40 (t, 2H), 1.78 (m, 2H), 0.96 (m, 2H), 0.42 (s, 6H).

Synthesis of cyano-functionalized PTMSP (CN-PTMSP). To a flame-dried round bottom flask was added the solution of PTMSP (1.0 g, 8.9 mmol (repeating unit)) in THF (200 mL). The flask was purged with Ar for 30 min and then placed in an ice/water bath followed by the dropwise addition of n-BuLi solution (1.6 M, 8.9 mmol). The mixture was stirred for 1.5 h at this temperature. The desired amount of functionalized precursor was added to the mixture dropwise via a gas-tight syringe and stirred overnight. Upon completion of the reaction, the majority of the solvent was removed under reduced pressure and the concentrated residue was precipitated into excess methanol. The polymer (CN-PTMSP) was obtained after filtration and drying in vacuum oven at 40 °C overnight.

Synthesis of Amidoxime-functionalized PTMSP (AO-PTMSP). To a flame-dried round bottom flask was added the solution of CN-PTMSP (0.5 g) in toluene (100 mL) and methanol (40 mL). After purging with Argon for 20 min, NH_2-OH solution (10 mL) was added dropwise to the flask. The homogeneous solution was stirred for 48 h at 70 °C. The polymer (AO-PTMSP) was then recovered by precipitation into methanol.

7.2.2 Membrane Preparation and Characterization

Membrane preparation. Membranes were prepared using solution casting. In a typical example, a solution of AO-PTMSP (0.2 g) was prepared in toluene (15 mL) at a concentration of 1.5 wt% and was dispersed onto a PTFE dish (with a diameter of 6 cm) after filtration using a 0.45 μm PTFE filter. The homogeneous and clear membrane was formed by slow evaporation of the solvent in an isolating container at ambient temperature after two days. All the resulting membranes had thicknesses of 70-90 μm and were soaked

in methanol to remove residual solvent and prevent the aging effect. Each membrane was removed from the methanol solvent and dried in air for 24 h prior to any measurements.

Density measurement and fractional free volume (FFV) estimation. The density of AO-PTMSP membranes were measured in methanol using Archimedes Principle,[27] and calculated as follows:

$$\rho = \frac{M_A}{M_A - M_L}\rho_0 \quad (1)$$

where M_A is the film weight in air, and M_L is the film weight in the auxiliary liquid (methanol), and ρ_0 is the density of methanol at the temperature where the measurement was performed.

The FFV of the membranes was estimated using the following group contribution method,

$$FFV = \frac{V - V_0}{V} \quad (2)$$

where V is the specific volume of the AO-PTMSP polymer obtained from density measurements at the temperature of interest; V_0 is the specific occupied volume at 0 K, which was estimated as 1.3 times the van der Waals volume estimated using Bondi's group contribution method.[28-29]

Gas permeability measurement. Membrane gas permeability was measured using a custom constant volume-variable pressure test chamber. The membrane sample was

mounted on a 47 mm non-porous aluminum tape with a hole (typically 5 mm in diameter) cut in the center. The edges of the film were sealed with epoxy (Devcon) and then loaded into the chamber. The membrane sample was carefully placed on a highly porous stainless steel support to provide mechanical support and negligible resistance to gas flux, and the entire assembly was installed into the test chamber. The chamber was evacuated with a mechanical pump to a base pressure of 20 mTorr and allowed to remain in the test chamber for 2 h to degas any solvent residue before the gas permeability measurement.

Gas sorption measurement. Low-pressure CO_2 solubility measurements were acquired using an Intelligent Gravimetric Analyzer (Hiden Analytical Limited, UK).[30] In a typical experiment, approximately 50 mg of a particular membrane sample was loaded into a quartz container and evacuated to 0.003 bar for 6 h at 150 ˚C to degas and dry the sample. All measurements were performed at room temperature. The mass uptake (corrected for buoyancy) was then measured as a function of pressure up to a final pressure of 1 atm to obtain the absorption isotherm. Desorption isotherms were subsequently acquired by measuring the mass as a function of decreasing pressure to ensure that the solubility behavior was reversible and to test for the hysteresis effects. The sorption of glassy polymer is analyzed by a dual-mode model[31]:

$$C = k_D p + \frac{C'_H bp}{1 + bp} \tag{3}$$

where C is the equilibrium penetrant concentration in the polymer at pressure p, k_D is the Henry's law solubility parameter describing penetrant dissolution into the

equilibrium densified polymer matrix, and C'_H is the Langmuir capacity parameter, which describes the sorption capacity of the nonequilibrium excess free volume characteristic of the glassy state. The Langmuir affinity parameter, *b*, is an equilibrium constant describing the affinity of a penetrant for a Langmuir site. In terms of the dual-mode model, the solubility coefficient, *S*, may be expressed as:

$$S = \frac{C}{p} = k_D + \frac{C'_H b}{1 + bp} \tag{4}$$

Quantum Chemical calculations. The PBE0 functional[32] with the D3 dispersion correction[33], the Becke-Johnson (BJ) dumping function[34] and the def2-TZVPP basis set[35] were applied in all DFT calculations. The choice of the PBE0-D3/def2-TZVPP level of theory was based on recent benchmark studies of noncovalent interactions between CO_2 and CO_2-philic functional groups.[36-37] A scaling factor of 0.950 was applied for all vibrational frequencies discussed in this work.[38] All DFT calculations were performed with the *Gaussian09* program package, revision D.01.[39]

7.3 Results and discussion

7.3.1 Functionalization of PTMSP

To prepare new polymeric membranes with high CO_2 selectivity and permeability, AO functionality was introduced to the PTMSP matrix. The synthetic strategy is shown in Scheme 7.1.

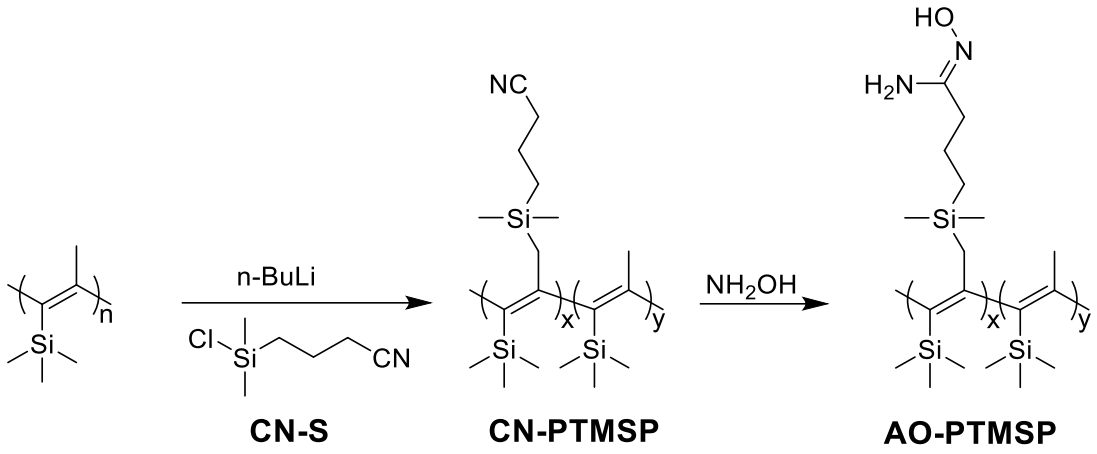

Scheme 7.1. The synthetic scheme of AO-PTMSP.

The precursor (CN-S) was synthesized via hydrosilylation of allyl cyanide using chlorodimethylsilane and Karstedt's catalyst. Allyl cyanide, instead of acrylonitrile, was used because relatively few catalysts lead to exclusively β-addition to the double bond in acrylonitrile[40] and the hydrosilylation of acrylonitrile using Karstedt's catalyst gives low yield.[41] The reaction using allyl cyanide was carried out with 95% yield (purity>98%) as shown by the ^{1}H-NMR spectrum (Figure 7.1). The peaks of vinyl protons in the allyl cyanide and of Si-H in the chlorosilane disappeared completely, while the new peaks corresponding to -Si-CH_2-CH_2– (Figure 7.1, b, c) emerged. On the other hand, the methyl groups in the chlorosilane have a slightly higher chemical shift of 0.42 ppm (Figure 7.1, d) due to the presence of the strong electron-withdrawing group, Si-Cl.

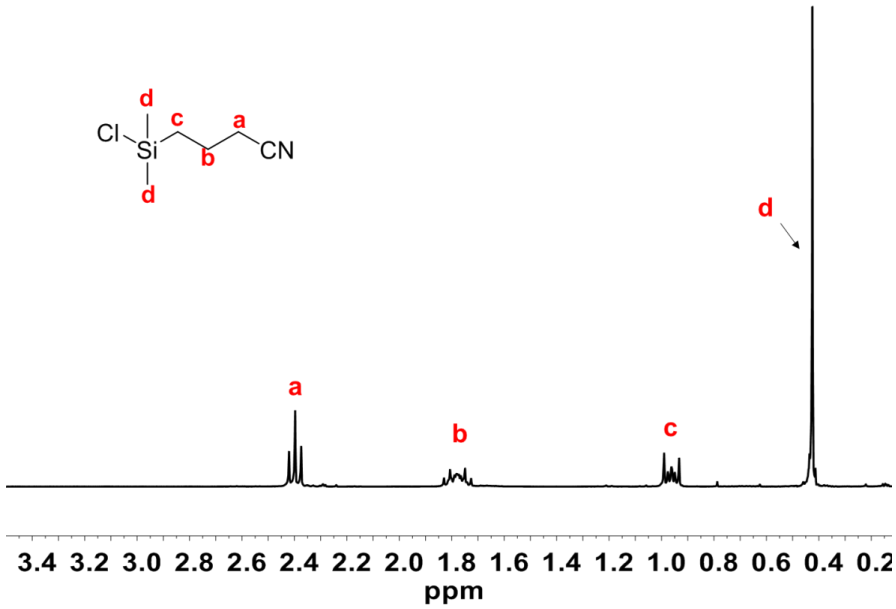

Figure 7.1. ^{1}H-NMR spectrum of 4-(chlorodimethylsilyl) butanenitrile.

The protons of the alpha carbon on the alternating C=C backbone in PTMSP have are weakly acidic in nature, and carbanions (C^-) can be readily generated by deprotonation with using a strong base, e.g. *n*-BuLi, and thus post-polymerization functionalization was readily performed through nucleophilic substitution of the silyl chloride (CN-S). PTMSP was first dissolved in anhydrous and degassed THF and formed a light yellow homogeneous solution. The reaction was carried out at 0 °C to diminish undesired side reactions. The color of the solution turned from yellow gradually to dark purple upon addition of *n*-BuLi, indicating that living carbanions were generated. Upon the addition of CN-S, the color turns to yellow immediately. The color change indicates that the coupling reaction between living carbanions and chlorosilane occurred. After the completion of the reaction, the excess chlorosilane precursor was removed by precipitating the product mixture repeatedly into excess methanol and the desired product, CN-PTMSP, was isolated from the mixture.

CN-PTMSP was further characterized by ^{1}H-NMR and SEC. On the ^{1}H-NMR spectra (Figure 7.2b), broad peaks at 0.20 and 1.81 ppm with intensity ratio close to 3:1 are assigned to the methyl protons of the PTMSP backbone. Peaks at 2.41, 0.90 and 0.78 ppm are assigned to the methylene protons of the $\underline{CH_2}$-Si$(CH_3)_2$-$\underline{CH_2}$-CH_2-$\underline{CH_2}$-CN. Protons assigned to Si-CH_2-$\underline{CH_2}$-CH_2-CN were overlapped by the methyl protons of the backbone. The grafting ratio was estimated by comparing the intensity ratio of the peak at 2.41 ppm and the peak at 1.81 ppm. Amidoxime–bearing PTMSP (AO-PTMSP) was synthesized by amidoximation using hydroxylamine (NH_2OH). Amidoximation of nitrile in a polar

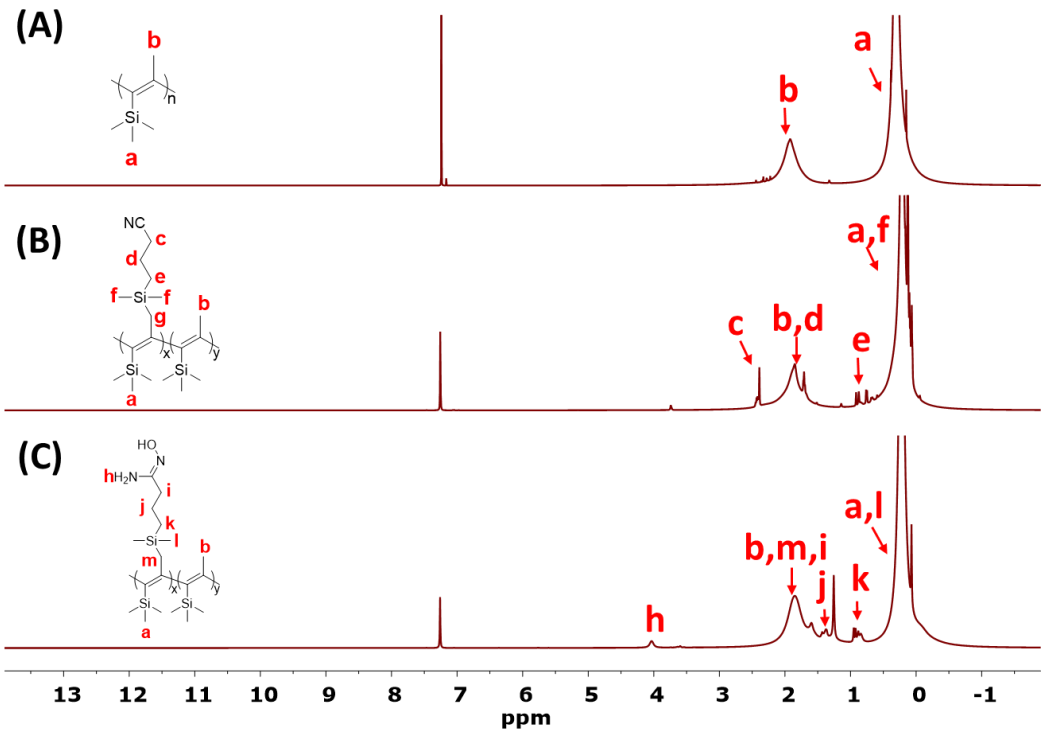

Figure 7.2. The ^{1}H-NMR spectrum of (A) neat PTMSP, (B) CN-PTMSP, and (C) AO-PTMSP.

solvent is a well utilized process for the preparation of amidoximes.[42] However, due to the rather low solubility of CN-PTMSP in methanol, the reaction was carried out in the mixed solvent of toluene and methanol at 70 ^{o}C for 48 h. The excess NH_2OH could be easily removed by precipitating the product repeatedly into excess methanol. The extent of amidoximation was determined by ^{1}H-NMR. The peak at 2.41 ppm disappeared after the reaction, suggesting that the -CN groups were transformed completely. The retention time shift in SEC profiles (Table 7.1) of neat PTMSP and cyano-functionalized PTMSP (CN-PTMSP) also verified that the grafting reaction was successful.

FTIR analysis of neat PTMSP and AO-PTMSP samples was performed and representative data are shown in Figure 7.3. For all samples, the C=C peaks at 1560 cm^{-1}, the Si-C-H peaks at 1240 cm^{-1} and Si-C peaks at 1360 cm^{-1}, 840 cm^{-1}, 750 cm^{-1} are observed. The peak corresponding to -C ≡ N (2250 cm^{-1}) of the starting material disappeared completely after the amidoximation reaction, indicating the complete conversion of polymers.[43-44] The conversion of the amidoximation reaction was also confirmed by the emergence of the new peaks of -C=N at 1635 cm^{-1} and a broad peak at 3400 cm^{-1} of OH and NH_2, respectively **(**Figure 7.3**)**.

7.3.2 Relationship of The Feeding Ratio of n-BuLi and Grafting ratio

After the confirmation of AO functionalization in the PTMSP matrix, the grafting ratio of AO moieties in the PTMSP matrix was plotted against *n*-BuLi/monomer feed ratio. Within a certain *n*-BuLi/monomer feed ratio range (< 3), the AO grafting content increased monotonically with the increase of feed ratio. However, the grafting ratio (> 31.5%).

Table 7.1. Results of SEC measurement of neat PTMSP and modified PTMSP intermediate (CN-PTMSP).

Sample code	M_w	M_n	PDI	dn/dc
	kg/mol	kg/mol		
PTMSP	170.1	115.1	1.48	0.1018
CN-8-PTMSP	227.6	147.8	1.54	0.0887
CN-20-PTMSP	252.4	156.2	1.62	0.0880
CN-30.5-PTMSP	261.4	172.6	1.52	0.0830

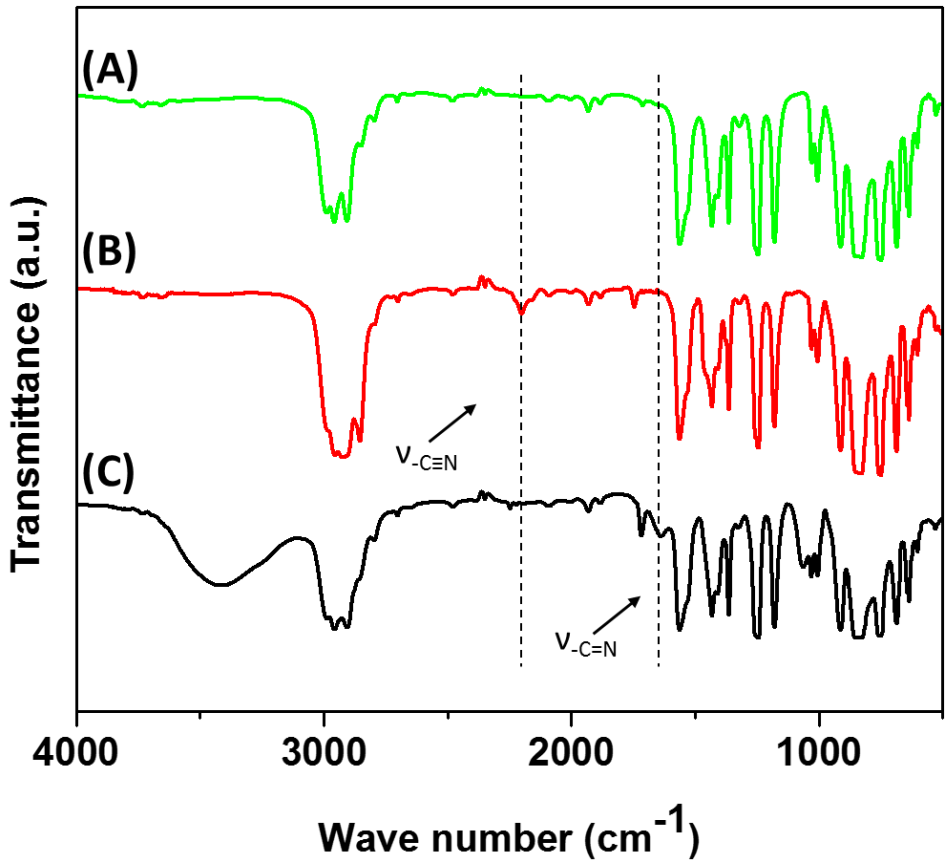

Figure 7.3. FT-IR spectra of (A) neat PTMSP, (B) CN-PTMSP, and (C) AO-PTMSP.

plateaued with further increases in feed ratio, probably due to the reduced efficiency of nucleophilic reaction at high grafting ratios (Figure 7.4).

The thermal stability of the modified membranes and the grafting ratio were also determined by TGA (Figure 7.5) and the results are summarized in Table 7.2. The modified membranes show good thermal stability.

Neat PTMSP showed a single-step decomposition at 341 $^{\circ}C$, while a two-step decomposition is observed in AO-PTMSP. The initial weight loss within 200-320 $^{\circ}C$ for AO-PTMSP was assigned to the loss of amidoxime functionality.[42] These results are consist with the one determined by ^{1}H-NMR.

7.3.3 Gas Transport Properties of AO-PTMSP Membranes.

The effect of AO grafting on gas permeation properties was investigated by evaluating the membrane permeability using the constant-volume variable-pressure gas flux method. The AO-PTMSP membrane showed much higher CO_2 permeability than that of N_2. The results for gas permeability and CO_2/N_2 selectivity values are summarized in Table 7.3 and Figure 7.6.

Generally, the reported CO_2/N_2 separation performance of PTMSP membranes ranges from a CO_2 permeability from 20000-35000 Barrer and CO_2/N_2 selectivity from 3.5-11, due to different testing conditions and the aging effect of samples.[5, 45-48] Our measured gas permeability of neat PTMSP (CO_2 permeability 30600 Barrer and CO_2/N_2 selectivity 3.5) is comparable to those previously reported data. With the higher incorporation of AO moiety, the permeability of both CO_2 and N_2 show a monotonic

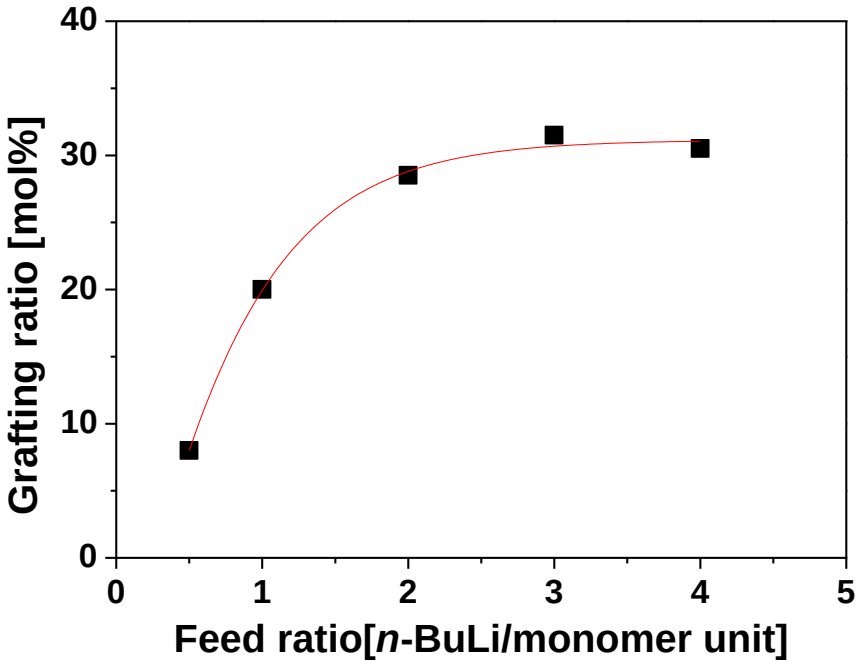

Figure 7.4. Relationship of the feed ratio of n-BuLi and Grafting ratio. The line is present to guide the eye.

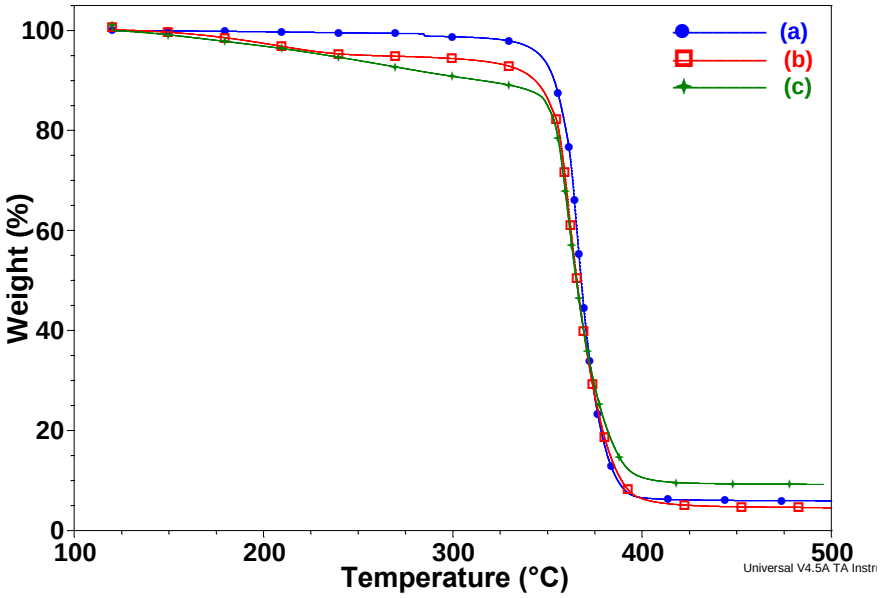

Figure 7.5. Representative TGA curves of (a) neat PTMSP, (b) CN-8-PTMSP and (c) AO-8-PTMSP.

Table 7.2. General characterization of AO-PTMSP.

Sample Code	Grafting yield (%)		AO functionality (mmol/g)	T_d (°C)*
	NMR	TGA		
PTMSP	-	-	-	341
AO-8-PTMSP	7.9	11.3	0.71	218
AO-20-PTMSP	20.0	20.5	1.43	206
AO-31-PTMSP	31.5	30.9	2.67	200

*Reported as the temperature at ~5% weight loss.

Table 7.3. Summary of density, FFV and gas transport properties for AO-PTMSP membranes.

Sample code	Density (g/cm^3)[a]	FFV[b]	Permeability (Barrer)		α (CO_2/N_2)
			CO_2	N_2	
PTMSP	0.79	0.25	30000	8600	3.5
AO-8-PTMSP	0.84	0.21	20000	3300	6.1
AO-20-PTMSP	0.90	0.16	6500	480	13.5
AO-31-PTMSP	0.96	0.11	6000	350	17.2

[a]Determined using Archimedes Principle in MeOH at 22 °C. [b]Estimated using Bondi's group contribution method.

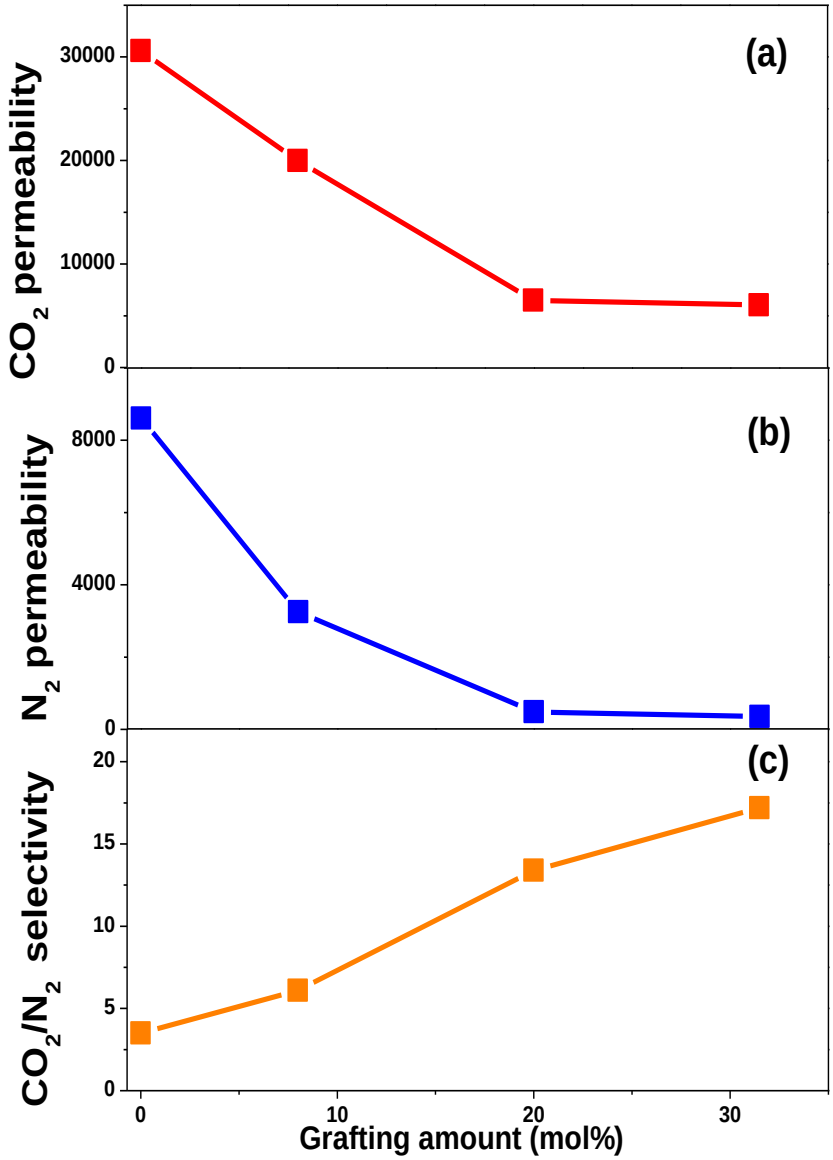

Figure 7.6. a) CO_2 permeability, b) N_2 permeability and c) CO_2/N_2 selectivity versus grafting ratio (mol%) for the AO-PTMSP membranes.

decrease, while the CO_2/N_2 selectivity increases as a function of AO grafting content. When these values are plotted on a 2008 Robeson plot (Figure 7.7), all AO-PTMSP membranes showed much better overall CO_2/N_2 separation performance than that of pure PTMSP. Furthermore, the highest performing membrane, AO-31-PTMSP, has achieved separation performance very close to the Robeson upper bound.

7.3.4 Effect of AO Group Incorporation on Gas Diffusivity

The effect of AO group incorporation into PTMSP membranes on gas diffusivity was investigated by evaluating density, FFV, and gas permeability, and the results are summarized in Figure 7.3. The measured density and FFV of neat PTMSP are 0.79 g/cm^3 and 0.25, respectively, which are consistent with previously reported values.[45] With higher AO incorporation, the density increased while FFV showed a monotonic decrease. For example, AO-31-PTMSP, the membrane with the highest incorporation of AO at 31%, showed an increase in density (~20%) and decrease of FFV (~50%). The introduction of the bulkier AO group contributes to occupying excess free volume. Our results are consistent with a previous study where the AO functionality caused a decrease in surface area and pore size in other glassy materials[19]

The decrease of FFV exerts a negative effect on gas diffusivity, contributing to a decrease of gas permeability. Moreover, the formation of intermolecular H-bonding between the AO structures could also hinder gas diffusion in corresponding areas, leading to a further decrease of gas permeability. These two combined factors largely contribute to

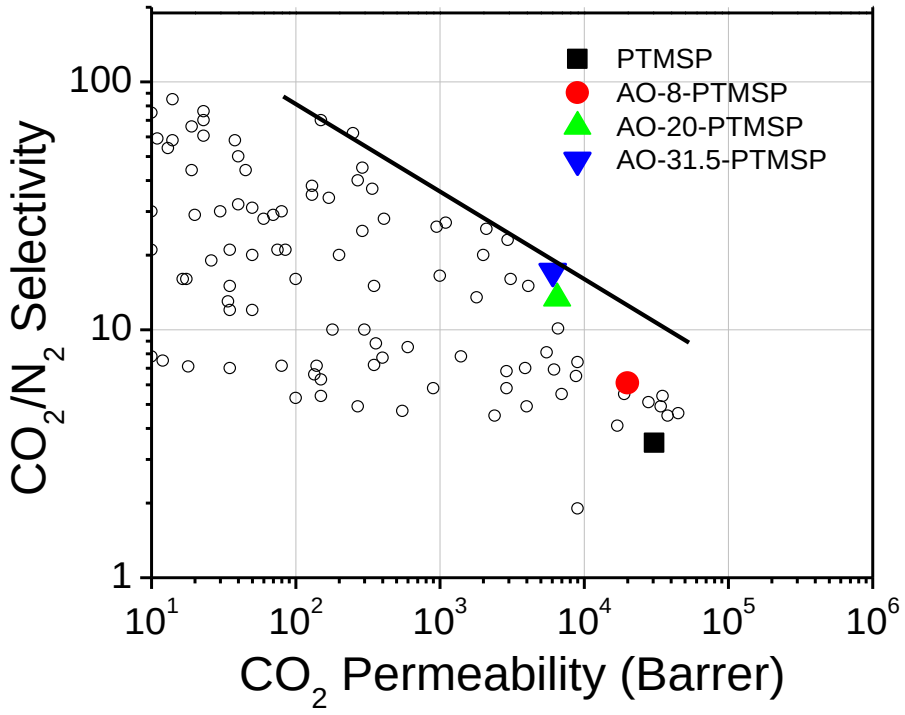

Figure 7.7. Summary of the AO-PTMSP membranes in a 2008 Robeson plot.[5]

the monotonic decrease of both CO_2 and N_2 permeability (~4 times for CO_2 and ~20 times for N_2) in AO-PTMSP membranes. Despite the decrease of gas permeability, the CO_2/N_2 selectivity demonstrates a five-fold increase. The enhancement of CO_2 selectivity by AO incorporation is attributed to the higher CO_2 affinity[17-20, 24], and it is further examined by sorption measurements and quantum chemical calculations.

7.3.5 Impact of AO Group Incorporation on Gas Solubility

The sorption isotherms for both CO_2 and N_2 in AO-PTMSP membranes are depicted in Figure 7.8. The sorption isotherms are described by the dual-mode model and the fitting parameters are summarized in Table 7.4.

The N_2 sorption of AO-31-PTMSP is much lower than other samples and was very close to the lower detection limit of the instrument. Thus, the potential error may lead to a deviated dual-mode model fit. For each polymer, the fitting parameters k_D and b (Eq 3) were constrained to a range which correlated to the critical temperature of permeating gas.[47] The neat PTMSP data (Table 7.4) is consistent with reported values.[9, 47-49] A slight variability of sorption data compared with previously reported values is likely from the film preparation process and processing history of the sample.[50-51]

The high sorption efficiency in PTMSP polymers is typically attributed to their high FFV and microporosity.[9] For AO functionalized membranes, the decrease of gas sorption capability is expected due to the reduction of FFV. When comparing the Henry's law parameter, k_D, an increasing trend with higher AO content is observed. More than 70%

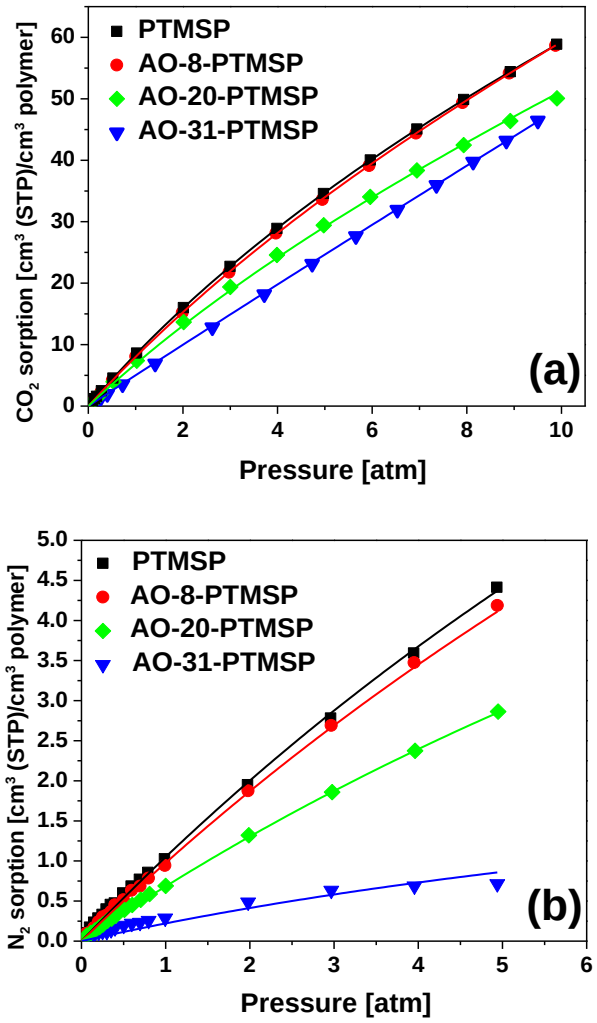

Figure 7.8. (a) CO_2 and (b) N_2 sorption isotherms for AO-PTMSP membranes. The black curves show the fits to the dual-mode sorption model.

Table 7.4. Summary of dual-mode model parameters, gas solubility and solubility selectivity for AO-PTMSP membranes.

Sample code	k_D $\left[\frac{cm^3(STP)}{cm^3\ atm}\right]$		C'_H $\left[\frac{cm^3(STP)}{cm^3}\right]$		b $[atm^{-1}]$		S $\left[\frac{cm^3(STP)}{cm^3\ atm}\right]$		$\alpha[S_A/S_B]$
	CO_2	N_2	CO_2	N_2	CO_2	N_2	CO_2	N_2	
PTMSP	2.71	0.01	66	22	0.094	0.050	8.49	1.07	7.9
AO-8-PTMSP	3.06	0.02	61	20	0.088	0.050	8.09	0.98	8.3
AO-20-PTMSP	3.10	0.01	43	14	0.095	0.050	6.86	0.68	10.0
AO-31-PTMSP	4.64	0.01	5	3	0.080	0.050	5.02	0.15	32.4

increase is achieved from neat PTMSP to AO-31-PTMSP. Typically, k_D describes penetrant dissolution into the densified equilibrium regions of a polymer matrix. For membranes with no gas-polymer interaction, k_D is generally related to the critical temperature of permeating gas. In our study, the k_D values of CO_2 and N_2 in pure PTMSP are comparable with previously reported data. However, the AO-PTMSP membranes show much higher CO_2 k_D values than that of PTMSP. The high CO_2 k_D values clearly indicate that the dissolution of CO_2 into the polymer are significantly enhanced, which should originate from the strengthened CO_2-polymer interaction/philicity by the presence of the AO moiety. On the other hand, the Langmuir capacity parameter, C'_H, represents the maximum number of penetrant molecules that can be accommodated in the excess free volume of a glassy polymer. With functionalizing PTMSP to AO-PTMSP membranes in C'_H showed the decreasing trend, clearly reflecting the decreased amount of gas absorbed via Langmuir sorption. The amidoximation of the PTMSP matrix causes a great reduction of FFV, therefore it imparts a deleterious effect on Langmuir sorption.

The solubility selectivity could be calculated using the following equation[47]:

$$\alpha[S_A/S_B] = \frac{[(C_2 - C_1)/(P_2 - P_1)]_A}{[(C_2 - C_1)/(P_2 - P_1)]_B} \quad (5)$$

Where $\alpha[S_A/S_B]$ are solubility selectivity, C the penetrant concentrations, p the pressure. When P_2-P_1=0, the solubility can be calculated as:

$$\lim_{\Delta p \to 0} \left(\frac{C_2 - C_1}{p_2 - p_1}\right) = k_D + \frac{C'_H b}{(1 + bp)^2} \quad (6)$$

The calculated solubility values for all AO-PTMSP membranes are summarized in (Table 7.4). When considering the overall CO_2 sorption (Henry's law plus Langmuir), it is higher (~40%) in the pure PTMSP than in AO-31-PTMSP. However, for N_2 sorption, due to the relative low k_D values for all PTMSP samples, the Langmuir sorption becomes the predominant factor. Thus, the N_2 sorption of AO-31-PTMSP show significant (~85%) decrease compared with pure PTMSP. Overall, when focusing on the sorption capability, although both CO_2 and N_2 sorption capacity show decreases to some extent, the decreasing percentage in N_2 is much higher than in CO_2. Thus, the overall solubility selectivity shows a four-fold enhancement after amidoximation. The solubility selectivity value of AO-31-PTMSP (~32) is comparable with several previously reported CO_2-philic materials.[52-53]

7.3.6 Noncovalent Interactions Between CO_2/N_2 and AO-PTMSP

DFT calculations were performed to further elucidate the observed IR spectra and gas-polymer interactions. The broad O-H stretch band of AO-PTMSP was examined. Analysis of this IR band provides valuable information for the reliable modeling of the noncovalent interactions between the gas molecules and the AO functional groups.

The AO monomer, dimer and trimer geometries were considered. Two different conformations were optimized for the AO dimer geometry, and two for the trimer geometry. For both dimers and trimers, the first conformer includes hydrogen bonds formed only with the oxygen atoms of the hydroxyl groups (O-H···O mode), while the second conformer considers a hydrogen bond formed by a nitrogen atom (O-H···N mode).

The calculated O-H vibration frequency for a free, non-hydrogen bonded H is ~3716 cm^{-1} (Table 7.5). This value was obtained from the monomer and conformer 1 of the dimer structure. The O-H···O mode is redshifted and ranges between 3315 and 3550 cm^{-1}. The O-H···N mode was found at even lower wavenumbers, at 3273 and 2938 cm^{-1} for the second conformer of the dimer and trimer geometries, respectively. The broad O-H peak of the experimental IR spectrum of AO-PTMSP (Figure 7.3 (b)) ranging between ~3100 and 3600 cm^{-1} indicates the presence of both O-H···O mode and O-H···N mode.

The comparison between the computational O-H vibration frequencies and the broad O-H peak in Figure 7.3 shows that the O-H···N mode is less favorable for the polymeric material, even if the dimer and trimer structures that are bound via the O-H···N mode have a stronger interaction (Table 7.5). On the other hand, the peak at 2938 cm^{-1} is covered by alkyl C-H stretch in Figure 7.3 and does not show apparent variation, while a shoulder peak at ~2940 cm^{-1} was observed in our previously reported AO-PDMS system,[23] which suggests the existence of O-H···N mode in these AO-functionalized membranes.

The noncovalent interactions of CO_2 and N_2 with the AO functional groups were further studied by means of DFT. Supersystems between the gas molecules and one, two, and three AO groups were considered. Based on the IR frequency analysis, the dimer and trimer geometries without the O-H···N mode were used as initial geometries for the optimized CO_2-AO and N_2-AO supersystems. Table 7.6 summarizes the strength of interaction between the two gas molecules and the AO groups. Comparison of the ΔH^{298} shows that the CO_2-AO interaction is about four to five times stronger than the N_2-AO.

Table 7.5. IR peaks of the O-H stretch mode (in cm^{-1}) with a short description, dissociation energies (in kJ/mol), and relative energies between the different dimer and trimer conformers (in kJ/mol).

	Monomer	Dimer (Conformer1)	Dimer (Conformer2)	Trimer (Conformer1)	Trimer (Conformer2)
O-H stretch	3718 (free O-H)	3714 (free O-H)	3273 (O-H···N)	3550 (O-H···O)	3381 (O-H···O)
		3471 (O-H···O)		3484 (O-H···O)	3336 (O-H···O)
				3315 (O-H···O)	2938 (O-H···N)
$\Delta E_{\text{Dissociation}}$	-	-10.3	-25.2	-36.7	-76.9
$\Delta E_{\text{Conformer}}$ [a]	-	14.9	0	40.2	0

[a] Relative energy difference between conformers

Table 7.6. Electronic energies and enthalpies of adsorption (in kJ/mol) for CO_2 and N_2 with one, two, and three AO groups.

Repeating units	CO_2		N_2	
	ΔE (kJ/mol)	ΔH^{298} (kJ/mol)	ΔE (kJ/mol)	ΔH^{298} (kJ/mol)
1 AO	-25.9	-19.7	-8.4	-4.3
2 AO	-30.2	-26.2	-10.3	-6.4
3 AO	-15.1	-12.0	6.6	1.2

Two AO are involved in cooperative binding of a gas molecule, an effect that further increases the interaction strength of the AO-PTMSP materials. This effect is larger for CO_2 (about 5 kJ/mol) than N_2 (about 2 kJ/mol), which can explain the increase of CO_2 selectivity upon larger AO loading (Table 7.3). Finally, the reason for the less favorable CO_2 or N_2 interaction with the three AO functional groups is due to the hydrogen bond network formed by the OH groups; the three AO are strongly bonded and it is less favorable to break the hydrogen bond network in order to cooperatively bind a CO_2 or N_2 molecule, which suggests that further AO functionalization might impede gas separation performance. Unfortunately, higher than 31 % AO functionalization could not be prepared due to the steric hindrance, and this prevents verification of the predicted decrease in the membrane performance.

7.4 Conclusion

We have successfully incorporated AO functionality into PTMSP membranes via hydrosilylation, followed by coupling reaction between active Si-Cl-containing chemical reagent and carbanion. The AO grafting significantly enhances the CO_2/N_2 selectivity, mainly due to the increase of CO_2-polymer interaction, while the gas permeability showed a decreasing trend due to the reduction of FFV and the formation of H-bonding. Compared with neat PTMSP, the highest performing membrane AO-31-PTMSP showed a factor of five increase in CO_2/N_2 selectivity, while maintaining high CO_2 permeability. The achieved performance was very close to the current Robeson upper bound line. DFT calculations

indicate that hydrogen bond networks affect the CO_2/N_2 interactions with the AO functional groups. This combination of experimental and theoretical work provides strong support that careful tuning of CO_2-philicity can strongly impact gas separation performance. This systematic study of the impact of CO_2-philic content provides insights for fundamental understanding of structure-property relationships for the development of gas separation membranes. These findings provide important knowledge for CO_2 separation materials development and foster fundamental understanding of the gas transport mechanism in polymer membranes.

7.5 References

1. Metz, B.; Davidson, O.; De Coninck, H.; Loos, M.; Meyer, L., Carbon dioxide capture and storage. In *IPCC*, Cambridge University Press: Cambridge, 2005; p 5.

2. Pachauri, R. K.; Allen, M.; Barros, V.; Broome, J.; Cramer, W.; Christ, R.; Church, J.; Clarke, L.; Dahe, Q.; Dasgupta, P., Climate Change 2014: Synthesis Report. Contribution of Working Groups I, II and III to the Fifth Assessment Report of the Intergovernmental Panel on Climate Change. 2014.

3. Materials for Separation Technologies—Emissions and Energy Reduction Opportunities. 2005.

4. Robeson, L. M., *J. Membr. Sci.* **1991,** *62*, 165-185.

5. Robeson, L. M., *J. Membr. Sci.* **2008,** *320*, 390-400.

6. Freeman, B. D., *Macromolecules* **1999,** *32*, 375-380.

7. Merkel, T. C.; Lin, H. Q.; Wei, X. T.; Baker, R., *J. Membr. Sci.* **2010,** *359*, 126-139.

8. Masuda, T.; Isobe, E.; Higashimura, T.; Takada, K., *J. Am. Chem. Soc.* **1983,** *105*, 7473-7474.

9. Srinivasan, R.; Auvil, S. R.; Burban, P. M., *J. Membr. Sci.* **1994,** *86*, 67-86.

10. Lin, H.; Freeman, B. D., *J. Membr. Sci.* **2004,** *239*, 105-117.

11. Jue, M. L.; Lively, R. P., *React. Funct. Polym.* **2015,** *86*, 88-110.

12. Mason, C. R.; Maynard-Atem, L.; Heard, K. W.; Satilmis, B.; Budd, P. M.; Friess, K.; Lanc, M.; Bernardo, P.; Clarizia, G.; Jansen, J. C., *Macromolecules* **2014,** *47*, 1021-1029.

13. Du, N.; Robertson, G. P.; Song, J.; Pinnau, I.; Guiver, M. D., *Macromolecules* **2009,** *42*, 6038-6043.

14. Du, N.; Park, H. B.; Robertson, G. P.; Dal-Cin, M. M.; Visser, T.; Scoles, L.; Guiver, M. D., *Nat. Mater.* **2011,** *10*, 372-375.

15. Du, N.; Robertson, G. P.; Dal-Cin, M. M.; Scoles, L.; Guiver, M. D., *Polymer* **2012,** *53*, 4367-4372.

16. Zulfiqar, S.; Karadas, F.; Park, J.; Deniz, E.; Stucky, G. D.; Jung, Y.; Atilhan, M.; Yavuz, C. T., *Energ Environ Sci* **2011,** *4*, 4528.

17. Zulfiqar, S.; Awan, S.; Karadas, F.; Atilhan, M.; Yavuz, C. T.; Sarwar, M. I., *RSC Adv.* **2013,** *3*, 17203.

18. Mahurin, S. M.; Gorka, J.; Nelson, K. M.; Mayes, R. T.; Dai, S., *Carbon* **2014,** *67*, 457-464.

19. Swaidan, R.; Ghanem, B. S.; Litwiller, E.; Pinnau, I., *J. Membr. Sci.* **2014,** *457*, 95-102.

20. Patel, H. A.; Yavuz, C. T., *Chem Commun (Camb)* **2012,** *48*, 9989-91.

21. Wang, S.; Li, X.; Wu, H.; Tian, Z.; Xin, Q.; He, G.; Peng, D.; Chen, S.; Yin, Y.; Jiang, Z.; Guiver, M. D., *Energy Environ. Sci.* **2016,** *9*, 1863-1890.

22. Car, A.; Stropnik, C.; Yave, W.; Peinemann, K.-V., *J. Membr. Sci.* **2008,** *307*, 88-95.

23. Hong, T.; Chatterjee, S.; Mahurin, S. M.; Fan, F.; Tian, Z.; Jiang, D.-e.; Long, B. K.; Mays, J.; Sokolov, A. P.; Saito, T., *J. Membr. Sci.*

24. Zulfiqar, S.; Karadas, F.; Park, J.; Deniz, E.; Stucky, G. D.; Jung, Y.; Atilhan, M.; Yavuz, C. T., *Energ Environ Sci* **2011,** *4*, 4528-4531.

25. Zulfiqar, S.; Awan, S.; Karadas, F.; Atilhan, M.; Yavuz, C. T.; Sarwar, M. I., *RSC Adv.* **2013,** *3*, 17203-17213.

26. Mahurin, S. M.; Gorka, J.; Nelson, K. M.; Mayes, R. T.; Dai, S., *Carbon* **2014,** *67*, 457-464.

27. Mulder, J., *Basic principles of membrane technology*. Springer Science & Business Media: 2012.

28. Bondi, A., *J. Phys. Chem.* **1964,** *68*, 441-451.

29. Van Krevelen, D. W.; Te Nijenhuis, K., Properties of polymers: their correlation with chemical structure; their numerical estimation and prediction from additive group contributions. Elsevier: 2009.

30. Mahurin, S. M.; Lee, J. S.; Baker, G. A.; Luo, H.; Dai, S., *J. Membr. Sci.* **2010,** *353*, 177-183.

31. Koros, W. J.; Chan, A. H.; Paul, D. R., *J. Membr. Sci.* **1977,** *2*, 165-190.

32. Adamo, C.; Barone, V., *J. Chem. Phys.* **1999,** *110*, 6158-6170.

33. Grimme, S.; Antony, J.; Ehrlich, S.; Krieg, H., *J. Chem. Phys.* **2010,** *132*, 154104.

34. Grimme, S.; Ehrlich, S.; Goerigk, L., *J. Comput. Chem.* **2011,** *32*, 1456-1465.

35. Weigend, F.; Ahlrichs, R., *PCCP* **2005,** *7*, 3297-3305.

36. Vogiatzis, K. D.; Klopper, W.; Friedrich, J., *J Chem Theory Comput* **2015,** *11*, 1574-1584.

37. Mavrandonakis, A.; Vogiatzis, K. D.; Boese, A. D.; Fink, K.; Heine, T.; Klopper, W., *Inorg. Chem.* **2015,** *54*, 8251-8263.

38. NIST Computational Chemistry Comparison and Benchmark DataBase. http://cccbdb.nist.gov/vibscalejust.asp.

39. Frisch, M.; Trucks, G.; Schlegel, H.; Scuseria, G.; Robb, M.; Cheeseman, J.; Scalmani, G.; Barone, V.; Mennucci, B.; Petersson, G., *Gaussian09, Revision D 1*.

40. Rajkumar, A. B.; Boudjouk, P., *Organometallics* **1989,** *8*, 549-550.

41. Chauhan, M.; Chauhan, B. P. S.; Boudjouk, P., *Tetrahedron Lett.* **1999,** *40*, 4127-4128.

42. Eloy, F.; Lenaers, R., *Chem. Rev.* **1962,** *62*, 155-183.

43. Nizam El‐Din, H.; Badawy, S.; Dessouki, A., *J. Appl. Polym. Sci.* **2000,** *77*, 1405-1412.

44. Brown, S.; Chatterjee, S.; Li, M.; Yue, Y.; Tsouris, C.; Janke, C. J.; Saito, T.; Dai, S., *Ind. Eng. Chem. Res.* **2015,** *55*, 4130-4138.

45. Nagai, K.; Masuda, T.; Nakagawa, T.; Freeman, B. D.; Pinnau, I., *Prog. Polym. Sci.* **2001,** *26*, 721-798.

46. Matteucci, S.; Kusuma, V. A.; Sanders, D.; Swinnea, S.; Freeman, B. D., *J. Membr. Sci.* **2008,** *307*, 196-217.

47. Merkel, T.; Bondar, V.; Nagai, K.; Freeman, B., *J. Polym. Sci., Part B: Polym. Phys.* **2000,** *38*, 273-296.

48. Ichiraku, Y.; Stern, S.; Nakagawa, T., *J. Membr. Sci.* **1987,** *34*, 5-18.

49. Nakagawa, T.; Fujisaki, S.; Nakano, H.; Higuchi, A., *J. Membr. Sci.* **1994,** *94*, 183-193.

50. Nagai, K.; Nakagawa, T., *J. Membr. Sci.* **1995,** *105*, 261-272.

51. Nagai, K.; Mori, M.; Watanabe, T.; Nakagawa, T., *J. Polym. Sci., Part B: Polym. Phys.* **1997,** *35*, 119-131.

52. Mahurin, S. M.; Górka, J.; Nelson, K. M.; Mayes, R. T.; Dai, S., *Carbon* **2014,** *67*, 457-464.

53. Bondar, V. I.; Freeman, B. D.; Pinnau, I., *J. Polym. Sci., Part B: Polym. Phys.* **1999,** *37*, 2463-2475.

Chapter 8 Conclusions and Future Work

8.1 Conclusions

In this dissertation, we tried to demonstrate various applications of heteroatom-containing functional polymers. We also want to know: how can we apply heteroatom containing functional polymers to solve currently challenging problems.

We designed and synthesized novel polymer electrolytes and polymerized ionic liquids based on soft polydimethylsiloxanes. To investigate the effect of side groups on the ion transport, we attached cyclic carbonate, sulfonate, and triethylene oxide unit to the soft PDMS backbone. The PHMS-*g*-VEC improved the ion dissociation and showed highest ionic conductivity of 9.58×10^{-6} S/cm at room temperature. On the other hand, PHMS-*g*-TES exhibits interesting behavior when different lithium salts were added. It was found in this work there was a significant increase in ion conductivity at ambient temperature of 10^{-4} S/cm. Furthermore, we synthesized polymerized ionic liquids using PDMS as a backbone, in which imidazolium was covalently bonded to the polymer backbone and TFSI anion was able to move freely. The room temperature ionic conductivity up to 3.3×10^{-5} S/cm was obtained. High pressure dielectric measurements revealed that the PIL was closely packed, causing the conductivity to be reduced. The results from dielectric measurements provide insights for better understanding the ion transport mechanism. It also showed that siloxane-based polymer could be one of the ideal polymer electrolyte matrices.

In this dissertation, we also introduced the synthesis of well-defined poly(2-isopropenyl-2-oxazoline) homopolymers and block copolymers via living anionic polymerization. By tuning the compositions and molecular weight of (PIPOx-*b*-PS-*b*-

PIPOx), different morphologies were observed. Inspired by the versatility of 2-isopropenyl-2-oxazoline, we further prepared AuNPs using PIPOx homopolymer as template in aqueous medium. TEM results revealed that the size of these AuNPs is in the range of 3.8±1.0 nm.

In the final chapter, we introduced application of amidoxime modified PTMSP on CO_2/N_2 gas separation. Due to strong CO_2 interaction with the amidoxime moiety, the modified PTMSP exhibited enhanced CO_2/N_2 selectivity while maintaining rather high permeability.

8.2 Future work

PILs have been becoming the promising candidates for applications in polymer electrolytes. They show superior ionic conductivity comparing with conventional ambipolar polymer electrolytes. Our future goal is to prepare single lithium-ion conducting polymer electrolytes. The fluorosulfonyl imide could facilitate the ion dissociation as discussed in the introduction (chapter 1.2.4). To further facilitate ion dissociation, fluorosulfonyl imide will be selected as the anion and covalently bonded the PDMS backbone (Scheme 8.1).

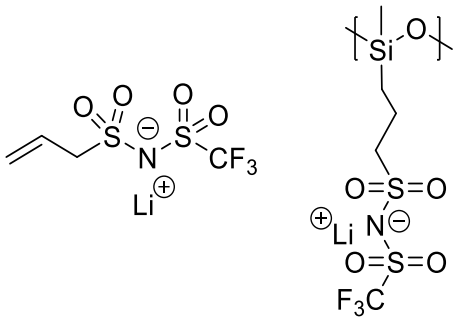

Scheme 8.1. Single lithium-ion conducting electrolytes.

Furthermore, due to the versatility of PIPOx and PIPOx containing block copolymers, advanced architectures such as bottle brush and "dumbbell" shaped brush-linear-brush could be achieved, as illustrated in Scheme 8.2.

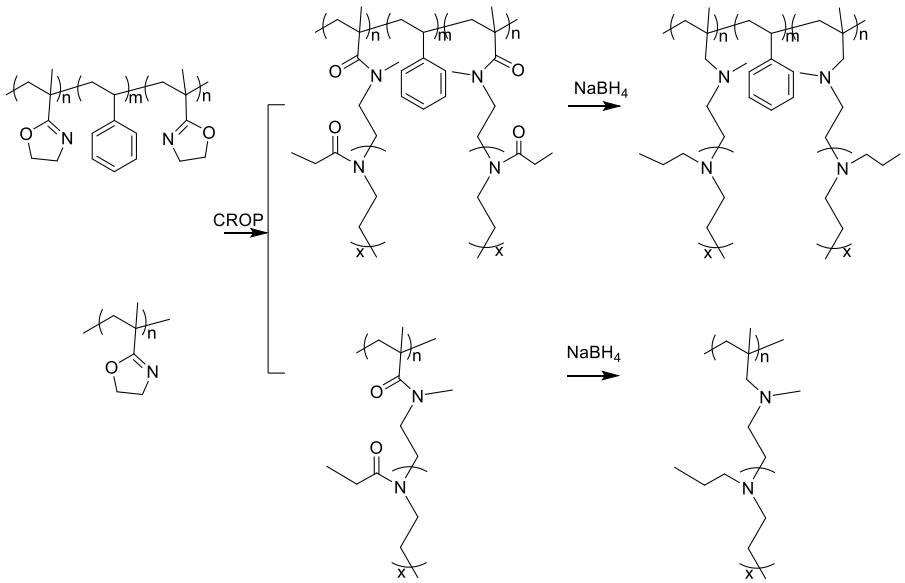

Scheme 8.2. Synthesis of P(IPOx-*g*-EtOx)-*b*-PS-*b*- P(IPOx-*g*-EtOx) and P(IPOX-*g*-EtOx).

Vita

Hongbo Feng was born in Zhengzhou, China. He obtained his B.S. in Zhengzhou University, majoring in applied chemistry. In August 2012, he entered the Department of Chemistry, University of Tennessee to pursue the PhD degree under the guidance of Professor Jimmy Mays. On March 30th, 2017, Hongbo successfully defended his dissertation.